Fate and Transport Investigations Update for Chromium Contamination from Sandia Canyon

Los Alamos
NATIONAL LABORATORY
EST.1943

Prepared by the Environmental Programs Directorate

Fate and Transport Investigations Update for Chromium Contamination from Sandia Canyon

July 2008

Responsible project leader:

Danny Katzman		Project Leader	Environmental Programs	7·30·08
Printed Name	Signature	Title	Organization	Date

Responsible LANS representative:

Susan G. Stiger		Associate Director	Environmental Programs	7/30/08
Printed Name	Signature	Title	Organization	Date

Responsible DOE representative:

David R. Gregory		Project Director	DOE-LASO	7/29/08
Printed Name	Signature	Title	Organization	Date

EXECUTIVE SUMMARY

This update report presents new results for investigations that assess the fate and transport of chromium in the environment, including numerical modeling, laboratory experiments and field observations. This work is an extension of, and update to, the "Fate and Transport Modeling Report for Chromium Contamination from Sandia Canyon" published in 2007. Development of the fate and transport models helps refine the conceptual model of how various physical, hydrological, and geochemical elements lead to the present-day distribution of chromium in the subsurface. In addition, model development, experimental studies, and data collected from monitoring wells and characterization coreholes are used together to integrate site knowledge about chromium migration at Los Alamos National Laboratory. This report presents the results of several ongoing studies, including hydrologic, geochemical, and hydrogeological modeling numerical/analytical studies. Hydrologic studies include an updated surface-water balance for Sandia Canyon, an analysis of alluvial water levels, and a summary and analyses of regional water levels and water-level responses to pumping. Geochemical studies include an analysis of stable chromium isotopes, an interpretation of the reductive capacity of Cr(VI) on various rock types, and a study of the stability of Cr(III) in wetland sediments. Finally, modeling studies estimate net infiltration rates in Sandia Canyon, investigate the potential for lateral flow in the vadose zone, determine potential entry locations for chromium arriving at the regional aquifer that give rise to the current distribution of chromium observed in the regional aquifer beneath Sandia and Mortandad Canyons, and estimate the current spatial distribution of chromium in the environment.

The models simulating the fate and transport of chromium in the subsurface were successfully calibrated to observed water levels and chromium concentrations at the monitoring wells in the regional aquifer. The calibrated models were applied to estimate the area in the regional aquifer that may be affected by the contamination. The estimated distribution of chromium mass in the regional can be used to site new monitoring wells. The calibration process also effectively constrained the potential locations of chromium arrival at the top of the regional aquifer. The chromium-concentration and water-level data observed at the new regional monitoring wells (R-42, SCI-2/R-43, R-44, and R-45) will further reduce the uncertainty in the model estimates of chromium mass in the regional aquifer.

The estimated entry points at the top of the regional aquifer suggest complex three-dimensional (3-D) flow paths in the vadose zone. The flow paths may be subject to lateral diversion to the south of Sandia Canyon. The mechanism of lateral diversion may be flow along dipping hydrostratigraphic contacts, as discussed in Appendix J of this report. In addition, the heterogeneity in hydrostratigraphic units and transients in infiltration recharge (caused by long-term changes in discharge rates or stormwater) may cause preferential flow paths in the vadose zone (sometimes called "fingers") that have complicated 3-D geometry (the formation of such preferential flow path is also discussed in Appendix J). Further complications in the spatial and temporal behavior of the flow paths through the vadose zone may be caused by geochemical characteristics of the hydrostratigraphic units and soil horizons between them.

Future work will further improve the developed models. The model estimates will be spatially and temporally constrained by applying the data collected at the new monitoring wells. The models will also be applied to estimate the potential chromium mass that may have reached the regional aquifer before the current monitoring network in the regional aquifer was established; this analysis will include historical observations of chromium concentrations where available. The 3-D model will be enhanced to investigate the effect of heterogeneity in hydrostratigraphic units and transients in infiltration recharge on the contaminant flow paths.

CONTENTS

Figures

Tables

Appendixes

Appendix A   Review of Chromium Fate and Transport Model Updates

Appendix B   Chromium Project Technical Working Sessions with the Citizens' Advisory Board and Other Stakeholders

Appendix C   Sandia Canyon Surface Water Balance and Alluvial Water-Level Responses

Appendix D   Chromium Isotope Investigation

Appendix E   Preliminary Analyses of the Water-Level Data Observed at Monitoring Wells R-35a, R-35b, and R-36

Appendix F   Analysis of Transient Water Levels Observed at Regional Aquifer Monitoring Wells Near Sandia Canyon

Appendix G   Estimation of Calibration Targets for the Chromium Concentration at the Regional Monitoring Wells

Appendix H   Maps of the Regional Water Table

Appendix I   Estimation of Mounding of the Regional Aquifer from Recharge Along Sandia Canyon

Appendix J   Numerical Simulations of Chromium Transport in the Subsurface

Appendix K   Hexavalent Chromium Attenuation on Vadose Zone and Regional Aquifer Materials: Application of X-ray Absorption Near-Edge Spectroscopy

Appendix L   Status Summary of Sandia Canyon Wetland Dewatering Experiments

Appendix M   A Geochemical Conceptual Model for Fate and Transport of Chromium at Los Alamos National Laboratory

Acronyms and Abbreviations

1-D   one-dimensional

2-D   two-dimensional

3-D   three-dimensional

AOC   area of concern

asl   above sea level

CAB	Citizens' Advisory Board
cfs	cubic feet per second
CME	corrective measures evaluation
CRM	chromium site model
DEM	digital elevation map
EES-6	Earth and Environmental Sciences (Laboratory Group)
Eh	oxidation-reduction
EPA	Environmental Protection Agency (U.S.)
ET	oxidation reduction
DI	deionized
DO	dissolved oxygen
FEHM	Finite Element Heat and Mass (transfer code)
GFM	geologic framework model
HDPE	high-density polyethylene
HFO	hydrous ferric oxide
ICPMS	inductively coupled plasma mass spectrometry
ICPOES	inductively coupled plasma optical emission spectroscopy
IRMS	isotope ratio mass spectrometry
IW	interstitial water
LANL	Los Alamos National Laboratory
LDCC	Laboratory Data Communications Center
MCL	maximum contaminant level (EPA)
NIST	National Institute of Standards and Technology
NPDES	National Pollutant Discharge Elimination System
ORP	oxidation-reduction potential
ppb	parts per billion
ppm	parts per million
QA	quality assurance
RF	retardation factor
RPF	Records Processing Facility
rpm	revolution per minute
SOM	solid organic matter
SSC	Strategic Computing Complex
SWMU	solid waste management unit

SWSC   Sanitary Wastewater Systems Consolidation (plant)

TA   technical area

TOC   total organic carbon

UIUC   University of Illinois Urbana-Champaign

WQDB   Water Quality Database

XAFS   x-ray absorption near-edge structure

XANES   x-ray absorption fine structure

1.0   INTRODUCTION

This report presents updated results for investigations that characterize the fate and transport of chromium in the environment, including numerical modeling, laboratory experiments and field observations. Numerical models are developed to predict the fate and transport of chromium in the subsurface and specifically in the regional groundwater where contaminants have been detected at several existing monitoring wells. This work is an extension of that described in the "Fate and Transport Modeling Report for Chromium Contamination from Sandia Canyon" (the Fate and Transport Report) (LANL 2007, 098938). This work also satisfies a request for an updated modeling report by the New Mexico Environment Department (NMED) in its letter of October 17, 2007 (NMED 2007, 097586). Development of the fate and transport models helps refine the conceptual model of how various physical, hydrological, and geochemical elements lead to the present-day distribution of chromium in the subsurface. The models become important tools for guiding site characterization and making quantitative assessments, including uncertainty, about the fate and transport of chromium. In the previous Fate and Transport Report (LANL 2007, 098938), the simulations provided results that are consistent with some aspects of the conceptual model of chromium transport, but the results did not agree with key observations of chromium contaminant distributions in the regional aquifer (Appendix A of this report). Model development, experimental studies, and data collection from monitoring wells and characterization coreholes are used together to integrate site knowledge about chromium migration at Los Alamos National Laboratory (the Laboratory). In this report, new data are analyzed to update conceptual model elements, and these updates are implemented in the numerical models.

The ultimate goal of the fate and transport modeling work is to provide probabilistic depictions of the current and future chromium mass distribution in the subsurface to help inform decisions regarding potential site characterization activities, corrective measures, and groundwater monitoring. These distributions estimate the chromium mass residing in the upper (within the tuff units) and lower (within the fanglomerate and basalt) portions of the vadose zone, and the temporal and spatial distribution of chromium within the regional aquifer. Models should be calibrated to agree with field data. To support this goal, several important conceptual model elements were analyzed and key components implemented in updated numerical models presented in this investigation update.

1. Hydrologic data analyses

   - The surface-water balance investigation expands on the investigations conducted as part of the "Interim Measures Work Plan for Chromium Contamination in Groundwater" (LANL 2006, 091987) and the Fate and Transport Report (LANL 2007, 098938) to better constrain the temporal and spatial variations in surface water loss throughout Sandia Canyon (Appendix C section C-1).

   - The correlation between alluvial water-level fluctuations and surface water losses was examined to better estimate net infiltration rates (including transients and spatial variability) from the alluvial system into the underlying vadose zone (Appendix C section C-2).

   - A summary and analyses of regional water levels and water-level responses to water-supply pumping was performed (Appendixes E, F, and H). These analyses help define the effects of that water-supply pumping and recharge on regional aquifer flow and refine the conceptual model of the regional aquifer.

2. Geochemical data analyses

- The analyses of stable chromium isotopes (δ^{53}Cr) (LANL 2007, 098938) have continued, and new results are presented in Appendix D of this report. This study is used to determine whether isotopic variations in δ^{53}Cr occur along surface water and groundwater flow paths within the Sandia and Mortandad watersheds; such variations may be used to evaluate reduction of Cr(VI) to Cr(III) along transport pathways.

- The adsorptive and reductive capacity of Cr(VI) for various rock samples is being investigated in laboratory experiments. Preliminary spectroscopy results relevant to the experiments are presented in Appendix K.

- A significant mass of chromium (mean estimate of 15,000 kg) is located in sediment in the wetland environment as Cr(III), which is relatively immobile and nontoxic. The stability of Cr(III) in wetland sediment samples is being investigated through laboratory experiments on field samples. These experiments will help define the stability of Cr(III) under current wet conditions and under drier conditions. The preliminary results are presented in Appendix L.

3. Model analyses

- Estimate the spatial heterogeneity of net infiltration rates into the vadose zone by calibrating to moisture content and contaminant concentration data measured on core samples collected from the SCC boreholes (Appendix J section J-4).

- Develop a coupled three-dimensional (3-D) vadose zone/regional aquifer model based on an updated geologic model for the area around Sandia Canyon. Use the model to identify the hydrogeologic controls for lateral diversion of groundwater flow through the vadose zone and to estimate the spatial extent of lateral diversion (Appendix J sections J-2, J-3, and J-6).

- Estimate the potential breakthrough locations for chromium entering the regional aquifer and detected in monitoring wells near Sandia and Mortandad Canyons (Appendix J section J-5). The locations must result in predicted chromium distributions that are consistent with observed distributions in the regional aquifer.

- Estimate the current spatial distribution of chromium concentrations in the regional aquifer using a probabilistic approach (Appendix J section J-5). The concentrations must be calibrated so they are consistent with observed chromium concentrations in regional groundwater samples.

- Update the current estimated distribution of chromium mass in the wetland, the alluvium, the vadose zone (upper and lower), and the regional aquifer based on field data and update predictions made in the previous Fate and Transport Report (LANL 2007, 098938) and the analyses presented in this report.

Further revisions to the model will be included as part of the Sandia Canyon investigation report, which is scheduled to be submitted to NMED by December 15, 2008, as data are collected at existing and newly installed regional and intermediate wells intended to further define the nature and extent of chromium contamination (LANL 2008, 101643). Models developed for that report will be calibrated against existing data and will be used to generate probabilistic maps of future chromium distributions based on conditions consistent with current conditions. The results of chromium geochemistry analyses, including laboratory batch and column studies, studies of wetland materials, and analysis of field (core) samples, will further define the geochemical conceptual model for chromium. This new understanding of geochemical

processes and the associated parameter distributions will be included in any future revisions to the models. The models will also incorporate other conceptual model and parameter updates resulting from continued field observations. Specific goals for the investigation report include the following:

1. Continue to define vadose zone flow and transport processes by using a combination of one-dimensional (1-D) and 3-D models. The effects of transient and nonuniform infiltration, 3-D spreading within the vadose zone, and coupling to the regional aquifer will be studied. The vadose zone simulations will be calibrated to field data (moisture content and chromium concentrations) and take into account conceptual model and parameter uncertainties.

2. Update the possible breakthrough locations for chromium entering the regional aquifer and the current spatial distribution of chromium concentrations in the regional aquifer based on chromium samples collected at existing and newly installed wells. The simulations will be calibrated to field data (water levels and chromium concentrations) and take into account conceptual model and parameter uncertainties.

3. Refine the estimated distribution of chromium mass in the Sandia Canyon wetland, the alluvium, the vadose zone (upper and lower), and the regional aquifer based on updated field data and updated modeling results.

4. Evaluate the monitoring network efficiency based on a monitoring network that includes newly installed wells R-35a, R-35b, R-36, SCI-2/R-43, R-42, and possibly R-44 and R-45 (Figure 1.0-1).

A corrective measures evaluation (CME) process will follow the investigation report. At that time, more characterization data will be available, and the numerical models should be sufficiently developed to support a focused evaluation of remedial alternatives.

2.0   SUMMARY OF PHYSICAL SYSTEM CONCEPTUAL MODEL

This section summarizes the main elements of the physical system conceptual model for chromium transport in Sandia Canyon that was first presented in the Interim Measures Investigation Report for Chromium Contamination in Groundwater (LANL 2006, 094431) and updated in the Fate and Transport Modeling Report for Chromium Contamination from Sandia Canyon (LANL 2007, 098938). In this report, elements of that conceptual model have been revised or expanded based on new data and information collected for this investigation. The primary focus of this section is to summarize the source(s) of chromium and other key contaminants found in the regional groundwater at wells R-11 and R-28. A discussion of the physical, chemical, and hydrologic processes that govern the fate and transport of chromium and associated contaminants, including molybdenum (Mo), nitrate (NO_3), sulfate (SO_4), chloride (Cl), and phosphate (PO_4) is also presented in this section. Figure 2.0-1 illustrates key aspects of the physical system conceptual model. The conceptual model forms the basis for identifying pathways, defining model assumptions, and bounding parameters used for modeling. Appendix M presents a detailed geochemical conceptual model for the fate and transport of Cr in the Sandia wetland and subsurface environments beneath Sandia and Mortandad Canyons.

2.1   Sources

A review of archival records and interviews with operators identified the cooling towers associated with the Technical Area 03 (TA-03) power plant (TA-3-22) at the head of Sandia Canyon as the main source of chromium contamination at the Laboratory (Figures 1.0-1 and 2.0-1). Chromium usage for the TA-03 power plant appears to have averaged 16.3 kg/d (35.9 lb/d) from circa 1956 to 1972, resulting in an estimated total release of 31,000 to 72,000 kg of Cr(VI) as potassium dichromate into the south fork of

upper Sandia Canyon, with the lower and upper bounds estimated to be 26,000 to 105,000 kg, respectively (LANL 2007, 098938, Appendix A). Effluent averaging from 7 to 18 mg/L Cr(VI) was discharged to Sandia Canyon at a rate of 380 to 1090 m^3/d (100,000 to 288,000 gal./d). In addition to potassium dichromate, other cooling water additives were used at the power plant, as summarized in Table 2.0-1 of the Interim Measures Investigation Report for Chromium Contamination in Groundwater (LANL 2006, 094431). Specifically, phosphate was probably used from 1951 to 2001, and sodium molybdate (Na$_2$MoO$_4$) was used from 1993 to 2001.

Effluent water releases to Sandia Canyon have occurred since the early 1950s and continue today, with the primary sources being treated sanitary wastewater and cooling tower blowdown. Since 1992, the TA-46 Sanitary Wastewater Systems Consolidation (SWSC) plant has routed effluent to TA-03 and released this effluent to upper Sandia Canyon through National Pollutant Discharge Elimination System (NPDES) outfall 01A001 (LANL 2006, 094431). Currently, total releases to the canyon are approximately 530 to 1500 m^3/d (140,000 and 400,000 gal./d) (Appendix B). These long-term discharges, along with stormwater runoff, have supplied a sufficient water volume to facilitate chromium transport in the Sandia watershed.

Other sources of Cr(VI) at the Laboratory include the former cooling tower at the Omega West Reactor (TA-02) in Los Alamos Canyon and solid waste management units (SWMUs) and areas of concern (AOCs) at TA-03, TA-35, and TA-48 in the Mortandad watershed, as summarized in previous reports (LANL 2007, 098938; LANL 2006, 094431; LANL 2006, 091987). However, these sites are thought to be relatively small sources of chromium releases compared with sites in Sandia and Los Alamos Canyons, both in terms of total chromium mass released and associated discharge volumes that may have served as a hydrologic driver. Sediment investigations indicate that TA-48 at the head of the Effluent Canyon tributary was the primary source of chromium contamination in the Mortandad watershed, and the downcanyon extent of residual chromium contamination in sediment is limited spatially (LANL 2006, 094161).

The total chromium mass released and effluent discharge volumes in Sandia Canyon were more than an order of magnitude greater than those released in Los Alamos and Mortandad Canyons. Nonetheless, data from archival core show that Cr(III) occurs above background concentrations in the upper vadose zone, indicating vertical migration of chromium in all three canyons (LANL 2006, 094431). Elevated concentrations of dissolved Cr(VI) in perched intermediate groundwater beneath Mortandad Canyon provide additional evidence that this metal is being transported within the vadose zone at that site. Thus, while Sandia Canyon is the hypothesized primary source of Cr(VI) observed at R-11 and R-28, contributions of chromium from Los Alamos and Mortandad Canyon sources cannot be ruled out for these or other wells.

The remaining discussion in this section focuses on the fate and transport of contaminants released from the TA-03 power plant at the head of Sandia Canyon (Figure 1.0-1). Many elements of the conceptual model discussed below also apply to the fate and transport of chromium in Los Alamos and Mortandad Canyons. However, Sandia Canyon is the assumed source of chromium for the modeling studies presented in this report.

2.2   Surface Water and Sediment Transport

Initially, dissolved Cr(VI) was released from the TA-03 power plant. Some Cr(VI) was adsorbed onto soils and sediments near the outfall, but most was transported by surface flow down the south fork drainage at the head of Sandia Canyon to the wetland located just below the confluence of the south and north forks (Figure 1.0-1). At the time of the initial releases, the wetland was not at its current size, but it is known to

have been substantial in size (LANL 1999, 064617). At all stages of its evolution, the wetland contained abundant solid organic matter (SOM) that served both as a chemical reductant and as an adsorbent; as a result, much of the Cr(VI) was reduced to its trivalent state. The reduced chromium precipitated as $Cr(OH)_3$ and/or was adsorbed onto SOM, hydrous ferric oxide (HFO), and clay minerals as Cr(III). Evidence for this process is based on elevated concentrations of Cr(III) in sediments found within the wetland and low concentrations of dissolved Cr(VI) in present-day alluvial groundwater within the wetland. Additionally, present-day surface water (filtered samples) entering the wetland contains higher concentrations of Cr(VI) than does surface water exiting the wetland (filtered samples, see Figure 2.0-1). Thus, the wetland is an effective geochemical sink that inhibits the migration of chromium, and a significant portion of the chromium released to the canyon likely remains within the sediments there. (Appendix L presents a discussion of chromium stability with respect to Fe(II) within the Sandia Canyon wetland and on initial experimental results evaluating chromium releases during drying of wetland material.) A previous report, Summary of Sandia Canyon Phase I Sediment Investigations (LANL 2007, 098127), provided a mean estimate of 15,000 kg of chromium stored in sediments of the wetland, almost entirely (~99.8%) as Cr(III). This value represents approximately 84% of the chromium stored in canyon-floor sediments and 21% to 49% of the total estimated chromium mass released to Sandia Canyon (LANL 2007, 098939, Appendix A); however, large uncertainties are associated with these values. The Phase I sediment investigation report provides a discussion of uncertainties associated with the estimate of chromium inventory in sediments (LANL 2007, 098127).

It is apparent that not all Cr(VI) discharged from the TA-03 power plant was immobilized within the Sandia Canyon wetland. Stream concentrations of 2.4 to 7.3 mg/L (as chromate) were reported below the wetland from 1969 to 1971 (Purtymun 1975, 011787), indicating that some of the Cr(III,VI) was transported downcanyon by surface flow, probably both as a dissolved phase and adsorbed onto suspended material. Chromium(VI) has also been detected in sediment samples downcanyon as far as reach S-5E, immediately west of NM 4 (Figures 1.0-1 and 2.0-1), although at low concentrations (LANL 2007, 098127).

Redistribution of chromium by surface water, sediment transport, and groundwater is an ongoing process within the Sandia watershed. Once adsorbed onto SOM and sediment particles in the wetland, chromium-bearing sediments are transported downcanyon by floods that erode headcuts along the channel, scour the streambed, and mobilize the bed sediment. These floods also erode banks in historical floodplains where much of the chromium in sediment deposits is stored in downcanyon reaches (Figure 2.0-1). Data reported in the Phase I sediment investigations (LANL 2007, 098127) indicate chromium concentrations of up to 22.5 mg/kg (or approximately twice background) occur as far east as reach S-5E at NM 4. Reoxidation of Cr(III) to Cr(VI) associated with suspended material and stream sediments could be significant in the absence of chemical reductants as surface water moves from the organic-rich environment of the wetland to less reducing conditions in downcanyon reaches. Reoxidation and colloidal Cr(III) may account for the observed increase of dissolved chromium concentrations in surface water at the eastern terminus of surface water flow relative to surface water exiting the wetland near gaging station E123 (Figures 1.0-1 and 2.0-1).

The transport of contaminants by surface water is facilitated where thin alluvium overlies relatively impermeable bedrock in the stream channel, limiting the amount of infiltration along the stream channel and resulting in greater movement of surface water downcanyon (Figure 2.0-1). The downcanyon extent of surface water flow varies with discharge from the TA-03 power plant, treated sewage effluent discharge rates, runoff from storm events and snowmelt, and previous moisture conditions along the channel. The effects of these variables were highlighted in changing infiltration patterns deduced from gaging data collected in 2007 and 2008 (LANL, 098939, Appendix B; Appendix C of this report).

Based on surface water data collected from September 2007 to June 2008, an estimated 0 to 39 acre-ft/yr, consisting primarily of effluent, infiltrates deeply into bedrock units beneath the wetland, an area that includes the Rendija Canyon fault zone (Figure 2.0-1 and Appendix C). This volume represents at most 11% of the effluent released to the canyon during this period and indicates that faults and fractures in this area are probably, at best, secondary pathways for deep infiltration. The volume of potential deep infiltration beneath the wetland is much smaller than that of infiltration east of D123.6, where nonwelded Bandelier Tuff underlies the canyon bottom. Possibly the fractures become filled by secondary minerals with depth, or they die out in less brittle tuffs below.

Much of the remaining effluent flow infiltrates bedrock units between gaging stations D123.6 and D123.8. This part of the canyon is steep and has a narrow canyon bottom where the stream incises through increasingly less welded tuffs in the lower part of Qbt 2 and then through the nonwelded units Qbt 1v and Qbt 1g (Figure 2.0-1). The remaining effluent largely infiltrates into the alluvium between D123.8 and the next downcanyon gaging station, E124, in an area where the canyon flow broadens and the alluvium thickens. Effluent flow only occasionally makes it downcanyon past E124 during times of high alluvial groundwater levels, such as in fall 2007 following an unusually rainy period in September. Runoff from storm events sometimes causes ephemeral flow and episodic infiltration to occur through the remaining portion of Sandia Canyon on Laboratory property, and possibly as far to the east as the Rio Grande, but these events are infrequent.

2.3   Geology

Recent drilling at the Laboratory has provided a basis for improved understanding of site geology. The models used in this report for predicting the fate and transport of chromium use an updated 3-D geologic model that represents the principal stratigraphic units encountered in drilling (Appendix J section J-2). The development of a 3-D geologic model from borehole geologic data is based on concepts of tectonic, sedimentary, volcanic, and erosional processes that have been active in the southwestern Española Basin. Figure 2.0-1 illustrates the integration of this history into a conceptual geologic model in a cross-section that honors borehole data from Los Alamos, Sandia, and Mortandad Canyons to show the vertical distribution and relationships of geological components in the fate and transport predictions. A comparable cross-section extracted directly from the updated 3-D geologic model is shown in Appendix J, Figure J-2.0-1.

Dipping strata may divert moisture along geologic contacts or internal bedding features as water travels through the vadose zone, possibly affecting the distribution of contaminants in the vadose zone and the location of entry points for contaminants into the regional aquifer (Appendix J). The basal contact of the Guaje Pumice Bed dips south to southwest and that of the Cerros del Rio basalt dips south to south-southeast beneath the zone of maximum infiltration in Sandia Canyon. The upper contact of the Cerros del Rio basalt dips primarily to the west and southwest. Near the water table, Miocene sedimentary rocks dip primarily to the south and southwest. Although there are large uncertainties, these relationships suggest that vadose zone pathways may include southerly and southwesterly to moderately southeasterly components. Paleosoils within or at the contacts between geologic units may also divert moisture in the vadose zone. For example, perched groundwater occurs in zones 3 m to greater than 9 m thick beneath Los Alamos Canyon within the Guaje Pumice Bed and the underlying Puye Formation fanglomerate. Clay-rich soils developed within the top of the Puye Formation are the apparent perching horizons for these groundwaters. In Sandia Canyon, coreholes encountered thick sequences of massive brown silt beds and subordinate intercalated gravels in the Puye Formation above the Cerros del Rio basalt. These deposits, which may represent intercalated aeolian and fluvial deposits, host the perched intermediate groundwater encountered in the SCI coreholes.

The conceptual geologic model allows for the possibility of some downward focused recharge along the Rendija Canyon fault zone, which forms the down-to-the-west canyon segment (SW1) that supports the Sandia Canyon wetland. Water balance studies (Appendix C) indicate that migration of dissolved chromium into this fault zone is limited. Migration of chromium-bearing surface water into the underlying Bandelier Tuff is likely to be controlled by whether fractures associated with the fault zone are plugged or lined by secondary minerals such as clay and calcite. Matric suction is expected to limit flow along fractures with little or no secondary minerals in unsaturated porous subunits of the Bandelier Tuff.

Thick Tschicoma dacitic lavas contemporaneous with the Cerros del Rio basalt occur beneath the western portion of Sandia Canyon. Borehole data indicate these dacitic lavas are massive, without multiple flow and interflow units observed in the Cerros del Rio. This difference in structure suggests that perched horizons are less likely to occur within the Tschicoma dacite, although the upper surface could support perching similar to that found above the Cerros del Rio basalt. Borehole data are lacking to test this inference, but Figure 2.0-1 shows a possible configuration where the dacite and the basalts do not overlap, creating a gap between lavas. Such a gap could provide a location where perched water above the lavas could find a pathway for deeper infiltration through Puye sedimentary deposits. Whether such a gap exists, or the dacite and basalts overlap, is currently unknown.

The regional water table is close to, or at the angular unconformity between, Puye Formation gravels and underlying Miocene sediments. The Puye Formation sediments have only modest and irregular dips, but the Miocene sediments have dips of several degrees consistently to the west, southwest, or south. There is no evidence for significant soil development at the eroded top of the tilted Miocene strata. The hydrologic effect of the angular unconformity is uncertain, but differences in bedding orientations and hydraulic properties of rocks may influence groundwater flow directions across this feature. The Miocene pumiceous rocks are particularly well-stratified, and the individual beds are generally highly porous and thin. These properties probably result in large differences between hydraulic horizontal and vertical anisotropies for these rocks.

The regional water table beneath canyon segment SW4 is commonly within or just above a highly transmissive interval of unaltered Miocene pumice deposits attributed to Peralta sources south of the Laboratory. Because of the dip orientation of the Miocene section, movement of groundwater in the regional aquifer to the east and southeast, toward the Rio Grande, encounters progressively older strata of the Santa Fe Group, including Miocene basalt flows. Miocene sediments were encountered at unusually high elevations at R-36, and the structural relief is likely related to faulting. The faulting does not displace Cerros del Rio basalt and overlying units. Groundwater movement in the regional aquifer may thus be affected both by passage through tilted sediments and lavas with highly heterogeneous properties and by passage across fault zones that may be significant features in the saturated zone yet without significant expression in overlying younger units of the vadose zone.

2.4   Alluvial Groundwater

Alluvial groundwater in Sandia Canyon is recharged daily by surface water flow, largely supplied by effluent from the 01A-001 outfall, and periodically by stormwater. It generally accumulates in the lower part of the alluvial deposits that fill the canyon bottom, most often perching on or within shallow bedrock units. The alluvial groundwater system extends farther downcanyon (roughly more than 1 km [0.6 mi] farther east) than do the daily stream-flow events. Because alluvial groundwater acts as a primary source of infiltrating water into the deeper tuff units, the extent of this water helps define infiltration zones within the canyon. This area exists approximately between stream gage E123.8 and alluvial well SCA-5, with the thickest, most persistent perched alluvial groundwater occurring between alluvial wells SCA-2 and SCA-4 (Figure 2.0-1 and Appendix C). Water-level measurements indicate that alluvial groundwater is

lost to bedrock units beneath the canyon floor in this area (Appendix C). This interpretation is supported by the results of analyzing transient, alluvial water-level responses to surface flow events. Analyses of the alluvial water-level data indicate that recharge to the alluvium, and flow within the alluvium and to the suballuvium bedrock are both spatially and temporally heterogeneous with infiltration rates potentially as high as a few meters per year (Appendix C). Lateral flow within the alluvium and infiltration of alluvial groundwater provide a driving force for subsurface transport of soluble chromium (and other mobile constituents including nitrate, sulfate, molybdenum, and chloride) along the length of the canyon and into the deeper subsurface.

2.5   Vadose Zone Transport

Infiltration of alluvial groundwater to bedrock units results in the vertical transport of mobile contaminants into suballuvium bedrock units. Movement of moisture and contaminants probably occurs as gravity and moisture-gradient-driven porous flow. Infiltration patterns are heterogeneous and probably transient; calibration to moisture data indicates that infiltration rates are on the order of 1 to 6 m/yr (Appendix J section J-4). Transport of contaminants to these deeper zones is generally limited to soluble constituents such as Cr(VI), Mo(VI), nitrate, chloride, and sulfate. The results reported in the Interim Measures Investigation Report for Chromium Contamination in Groundwater (LANL 2006, 094431) suggest that most of the dissolved chromium beneath the middle reaches of the canyon has been flushed out of the upper 122 m (400 ft) of the vadose zone by chromium-free water following cessation of the releases. Residual concentrations of chromium are observed in pore water and adsorbed onto mineral surfaces within the unsaturated zone, but the concentrations are generally low (<0.050 mg/L) and the occurrence of elevated concentrations (>0.1 mg/L) is sporadic. Molybdenum and phosphate are also observed in pore water and adsorbed onto mineral surfaces within the unsaturated zone (LANL 2006, 094431).

A thin zone of perched intermediate groundwater occurs within the Puye Formation atop the Cerros del Rio basalt between SCI-1 and SCC-4 (Figure 2.0-1). This perched system appears to thicken westwards, and it is probably recharged by percolation of moisture from the overlying rocks. The intermediate-zone water levels of SCI-1 (when corrected for barometric pressure changes) have varied by approximately 1 ft from February 2007 to February 2008 (Appendix C). The variation may be correlated with the variation of outfall fluxes, but the intermediate groundwater levels do not appear to be correlated to runoff events in Sandia Canyon. Concentrations of dissolved chromium in groundwater samples collected for this perched zone range from 13.5 to 22.1 μg/L. These data, combined with the generally low concentrations of contaminants in the overlying pore waters, suggest that years of recharge and high hydraulic fluxes have flushed large amounts of most soluble contaminants [nitrate, sulfate, Cr(VI), Mo(VI), and chloride] out of the upper vadose zone and into deeper rock units of the lower vadose zone. Most likely, moisture carrying these dissolved contaminants percolated into the lower vadose zone with some portion entering the regional groundwater system, which lies approximately 253 m (830 ft) below the canyon floor west of R-11 (Figure 2.0-1). The effects of anisotropy of vadose zone units may also be influenced by transients in recharge that become more pronounced during high-infiltration events.

Observations at SCI-2 will provide information concerning the presence of perched intermediate zones in the lower Cerros del Rio basalt or the underlying Puye Formation beneath Sandia Canyon segment SW4 (Figure 2.0-1). This location is of interest because the borehole data available from Los Alamos, Sandia, and Mortandad Canyons indicate a south-southeast dip for the base of the Cerros del Rio lavas in this area. This orientation may provide a vadose zone pathway from Sandia Canyon towards Mortandad Canyon, possibly accounting for a fraction of the high chromium contents found in the regional aquifer at R-28.

Perched intermediate groundwater was not encountered at regional wells R-11, R-35a, and R-35b, suggesting that the perched system west of R-11 is not connected with the known perched-intermediate system(s) to the east at R-10/10a, R-12, and R-36. The inferred connection between the perched intermediate systems at R-10/10a, R-12, and R-36 is based on their similar elevations and relatively close proximity. Based on water-quality data, it appears that the perched groundwater east of R-11 does not play a significant role in the transport of chromium in the Sandia Canyon area.

2.6   Transport in the Regional Aquifer

Currently, chromium concentrations in the regional aquifer are above background concentrations (~5–6 parts per billion [ppb]) at wells R-28, R-11, and R-15. The chromium concentration data for some of the key monitoring wells near Sandia Canyon are plotted versus time in Figure 2.6-1. In addition, other dissolved-phase contaminants including nitrate, perchlorate (ClO_4), sulfate, chloride, and tritium, are also detected in the regional aquifer beneath Sandia Canyon. As discussed in section 2.1, most of the anthropogenic chromium detected in the regional aquifer beneath Sandia and Mortandad Canyons is probably derived from releases from the TA-03 power plant at the head of Sandia Canyon. However, the other dissolved-phase contaminants collocated with the chromium were probably derived from potential contaminant sources in Los Alamos and Mortandad Canyons, suggesting a commingling of contaminant plumes. At R-11, for example, chromium is collocated with elevated concentrations of nitrate, perchlorate, and tritium that were derived from sources other than Sandia Canyon. At R-15, chromium is associated with tritium, nitrate, and perchlorate, suggesting a component of groundwater influenced by TA-50 wastewater discharges to Mortandad Canyon, based on chemical and isotope signatures. Differences in nitrogen isotopic ratios for some wells (e.g., R-28 vs. R-11) further indicate that contamination in regional groundwater beneath Sandia Canyon includes contributions from mixed sources. Tritium concentrations (180 pCi/L) measured at R-28 provide additional evidence for Mortandad Canyon-derived contaminants at the well.

Geochemical data from newly installed wells R-35a and R-35b (Figure 1.0-1) indicate that dissolved chromium is at background concentrations in the vicinity of water supply well PM-3 (LANL 2007, 098129). Chromium is also detected at slightly above background concentrations (8.8 μg/L) during the only round of sampling at the newly installed R-36 (Figure 1.0-1). R-36 is potentially downgradient of R-28 (Figures H-1 and H-2), and the chromium data from this well help to constrain the present-day extent of the chromium plume in the regional aquifer.

Figure 2.6-1 shows some transients in the observed chromium concentrations. At R-11 and R-28, the fluctuations seem to be somewhat seasonal, with higher concentrations in the spring (March to May) and lower concentrations in the fall (October and November). This analysis is considered very preliminary based on the short period of the chromium concentration record for these wells, but any seasonal effect may be associated with fluctuations of the water levels. Figure 2.6-2 compares the water-level and chromium-concentration data for R-28. A correlation between the water levels and chromium concentrations could mean that the fluctuations of the regional water table affect the portion of the subsurface that is saturated. During times of higher water levels, chromium could be mobilized from the lowermost part of the vadose zone. This less-mobile reserve of chromium may be flushed by regional aquifer water, resulting in a higher measured concentration at the monitoring wells. Conversely, when the water table drops, chromium comes from continuously saturated strata, which potentially results in more dilute concentrations.

Analytical results for stable isotopes of chromium ($\delta^{53}Cr$) show that various fractions of Cr(VI) have been reduced to Cr(III) in surface water and groundwater within Sandia and Mortandad Canyons. At well MCOI-5, $\delta^{53}Cr$ ratios for Cr(VI) indicate that up to 50% of Cr(VI) has been reduced to Cr(III), probably

within the Cerros del Rio basalt. Solid organic matter in wetlands and ferrous iron within the Cerros del Rio basalt are thought to be the two most important reductants for Cr(VI). The wetlands and Cerros del Rio basalt may contribute to natural attenuation of chromium to a greater extent than does the regional aquifer at R-11 and R-28. Variations in δ^{53}Cr ratios of Cr(VI) in perched intermediate groundwater and the regional aquifer are controlled by background isotope ratios, groundwater mixing, groundwater flow paths, groundwater residence times, kinetics of Cr(VI) reduction, and the reductive capacity of aquifer material.

The regional aquifer is a complex heterogeneous system that includes confined and unconfined zones. The degree of hydraulic communication between these zones is thought to be spatially variable. The shallow portion of the regional aquifer (near the water table) is predominantly under phreatic (unconfined) conditions and has limited thickness (approximately 30 to 50 m [98 to 164 ft]). Groundwater flow and contaminant transport directions in this zone generally follow the gradient of the regional water table; the flow is generally east/southeastward. The direction and gradient of flow at the regional water table are predominantly controlled by areas of recharge (e.g., the Sierra de los Valles and variably within some Pajarito Plateau canyons) and discharge (White Rock Canyon springs and the Rio Grande). The ambient regional groundwater flow gradients are relatively high, varying between 0.003 and 0.01 m/m in the area beneath Sandia Canyon. Water table contour maps characterizing the shape of the regional water table are presented and analyzed in Appendix H. As discussed above, a substantial amount of water has been released in Sandia Canyon, and most of this water is expected to be recharging the regional aquifer. The potential effect of this local and potentially focused infiltration is discussed in Appendix I; additional information is also provided in Appendixes H and J. Based on this information, it is possible that the water table is locally raised by infiltration along Sandia Canyon.

The deep portion of the regional aquifer is predominantly under confined conditions, and it is stressed by Pajarito Plateau water-supply pumping. The intensive pumping causes small water-level fluctuations in the phreatic zone (seasonally less than 0.2 m [0.6 ft] at R-28 and R-11; the largest seasonal fluctuations are observed at R-15: ~0.8 m or less than 3 ft [see Appendix F]). These low-magnitude responses in the phreatic zone from municipal well pumping are in sharp contrast to the larger responses at monitoring wells completed in deeper parts of the aquifer, indicating that the hydraulic communication between the phreatic zone and deeper parts of the aquifer is poor. The small scale fluctuations in the phreatic zone may be from drawdowns and/or strata compaction (Appendix F). However, the water-level fluctuations do not seem to affect the magnitudes and directions of groundwater flow. Capture of contaminants by supply well PM-3, which is screened approximately 56 to 536 m (183 to 1759 ft) below the regional water table, is probably unlikely because of this poor vertical hydraulic communication. This interpretation is supported by the contrasting water levels and drawdown responses observed in R-35a and R-35b during pumping of PM-3 (Appendix E). The analysis presented in Appendix E supports the conclusion that the pumping at PM-3 probably does not affect the hydraulic gradients in the phreatic zone of the regional aquifer in the vicinity. As a result, it can be expected that contaminant migration follows the ambient water-table gradients rather than diverting toward the pumping water-supply wells based on hydraulic data.

Poor hydraulic communication does not preclude the possibility that some contaminant migration may occur between the shallow and deep zones. Between the two zones, the hydraulic gradient has a strong downward vertical component because of water-supply pumping, creating the possibility that downward contaminant flow may occur along "hydraulic windows," although these have not been directly observed.

In the regional aquifer, the advective flow paths of contaminant migration might not be perpendicular to the equipotential water table lines. Deviations from the flownet conformity rule may occur because of the anisotropy/heterogeneity of aquifer materials. Flow- and head-gradient vectors do not coincide in an anisotropic medium when the flow gradient is not coincident with the principal directions of the permeability tensor (Freeze and Cherry 1979, 088742, Chapter 5). As a result, the south-southwest dips

of aquifer rock units in this area may influence the flow vectors. Large-scale permeability along the sedimentary layering is expected to be 1 to 4 orders of magnitude higher than large-scale permeability perpendicular to the layering.

3.0 METHODOLOGY FOR MODEL DEVELOPMENT

In the previous flow and transport modeling study (LANL 2007, 098938), Monte Carlo simulations were used to predict the transport of chromium and molybdenum from their source at the outfall through the unsaturated zone and through the regional aquifer. The simulations considered the effects of transport processes and geochemical interactions in surface water, the wetland, alluvial groundwater, the unsaturated zone and the regional aquifer. The implementation of assumptions, boundary conditions, and parameter distributions made in the models honored the conceptual model for chromium transport. However, some simplifications were made in that study (e.g., solving vadose zone transport with a series of 1-D columns), and the simulations were not calibrated to match field data. Simplifications often yield models that satisfactorily solve the problem at hand, but this was not the case with the previous study.

The modeling studies presented in Appendix J of this report explore different numerical techniques to determine whether predictions of chromium fate and transport can be improved upon from those made in the previous flow and transport modeling report (LANL 2007, 098938). In the current report, the different numerical techniques evaluated include calibrating predictions to better match field data (inverse modeling) and investigating 3-D effects for transport in the vadose zone.

3.1 Model Calibration and Inverse Analysis

Model calibration is a key component of model development. Calibration is a formal process of model adjustment against observed data. In this way, the model inputs (conceptualizations, parameters) are adjusted so that the model outputs (predictions) match the observations. Because the inputs are adjusted based on the outputs, this process is also called inverse modeling or inverse analysis. A large body of peer-reviewed scientific papers and technical reports summarizes existing theoretical developments and practical applications related to model calibration (Carrera and Hidalgo 2005, 102410).

Various analytical and numerical approaches are available to calibrate models. Most of them are based on optimization techniques. The Levenberg-Marquardt technique is one of the most widely used and powerful optimization methods; it is implemented in popular calibration codes such as PEST, DACOTA, and UCODE. Optimization techniques are applied to calibrate the numerical models (Appendix J).

The observed data applied to calibrate the model are called calibration targets. The process of selecting and quantifying calibration targets is very important and depends on various factors (e.g., uncertainty of data measurements, simulated problem, and representation of the problem in a numerical model). For the vadose zone model, the calibration targets include moisture content and chromium and molybdenum concentrations measured vertically along the SCC boreholes (Appendix J section J-4). For the regional aquifer model, the calibration targets include the water levels and measured chromium concentrations at the monitoring wells near Sandia Canyon (Appendix G). The calibrations targets are applied to calibrate the numerical models (Appendix J sections J-4 and J-5).

3.2 Uncertainties in Model Predictions

The predictions produced by any mathematical model are associated with uncertainties (also called predictive uncertainties). In the same way that the model inputs and the model itself are uncertain, the model outputs are also uncertain. The predictions and their uncertainties are commonly treated as

statistical variables (e.g., Beven and Freer 2001, 102321), and much like frequently used statistical measures such as mean and variance, these variables are associated with confidence levels. The statistical properties (uncertainty, confidence) of the model predictions are generally dependent on the statistical properties (uncertainty, confidence) of the model inputs. Various analytical and numerical approaches are available to evaluate statistical properties, such as uncertainty and confidence intervals, of model predictions. A large body of peer-reviewed scientific and technical reports summarizes existing theoretical developments and practical applications related to uncertainties in model predictions (e.g., Beven and Freer 2001, 102321; Neuman 2003, 102319; Gaganis and Smith 2006, 102322). In general, the existing methods can be divided into two groups, and the methods in each group have their strengths and weaknesses.

The first group of methods is based on the Monte Carlo analysis. In this case, a series of random realizations of model inputs are generated; the model predictions based on these random inputs are applied to evaluate predictive uncertainties. A substantial number of realizations may be required to evaluate uncertainty in the model predictions with an acceptable level of confidence (e.g., Ballio and Guadagnini 2004, 102315). The Monte Carlo approach is frequently used when no observational data can be used for model calibration. If calibration targets are available, typically a very small subset of the Monte Carlo realizations may be consistent with the observations. The second group of methods avoids this limitation by direct coupling of model calibration with estimation of uncertainties in model predictions (e.g., Vecchia and Cooley 1987, 102323; Cooley 1993, 102324; Blasone et al. 2008, 102320). In this case, the model is constrained to be calibrated (within predefined calibration ranges) during estimation of statistical properties of model predictions. The second method is used in the analysis presented in Appendix J.

3.3   Identification of Locations of Contaminant Arrival to the Regional Aquifer

Various analytical and numerical approaches can be used to estimate the potential locations of contaminant arrival to the regional aquifer based on monitoring data (e.g., Atmadja and Bagtzoglou 2001, 102325). One frequently used approach employs "reverse" simulation (backward in the time) of contaminant migration from the detection points back to the potential entry locations (e.g., Neupauer and Wilson 2002, 102326). This fate and transport report uses a different approach based on "forward" simulation (that is, forward in the time) of contaminant migration from multiple potential entry points at the regional aquifer coupled with inverse analyses. Some of the benefits of using the forward approach compared with the reverse approach are related to better numerical stability and computational efficiency. In addition, the forward approach allows for simpler representation of transients and nonlinear effects in the groundwater flow and contaminant migration. Application of the forward approach to estimate the potential locations of contaminant arrival based on regional aquifer data near Sandia Canyon is discussed in Appendix J section J-5.3. The results are presented in section 4.2.

3.4   3-D Spreading Effects in the Vadose Zone

Finally, a 3-D vadose zone model based on an updated geologic model for the area around Sandia Canyon was used to identify potential hydrogeologic controls for lateral diversion of groundwater flow through the vadose zone and to estimate the spatial extent of lateral diversion, especially toward Mortandad Canyon (Appendix J sections J-2, J-3, and J-6). This study is preliminary and evaluates the potential for lateral diversion based on geologic and hydrologic controls but is not formally calibrated, as discussed above. In addition, the 3-D model addresses issues related to the effects of infiltration (and transients in infiltration) along Sandia Canyon on groundwater flow directions in the regional aquifer near the water table.

4.0   INVESTIGATIONS RESULTS

The key results from modeling work presented in Appendix J are summarized in this section. The modeling results are consistent with available site observations and support refinement of the conceptual model of chromium transport through the vadose zone and regional aquifer presented in this report. A detailed discussion of the sensitivity of various model estimates to (1) model parameters and (2) conceptual-model elements is presented in Appendix J.

4.1   Vadose Zone Modeling

The vadose zone model is calibrated with data observed in boreholes SCC-2, SCC-3 and SCC-4 to estimate the current-day water-content and chromium and molybdenum concentrations in the vadose zone and the concentrations of chromium arriving at the regional aquifer (Appendix J section J-4). The results suggest that infiltration rates are spatially variable, high (potentially 1 to 6 m/yr), and probably time dependent. Chromium concentrations predicted at the base of the vadose zone are consistent with the concentrations predicted at the entry points based on the regional aquifer modeling.

4.2   Regional Aquifer Modeling

The regional aquifer model is calibrated to estimate the currently observed water levels and chromium concentrations at the monitoring wells in the regional aquifer. As a result of the calibration, it is possible to estimate the potential contaminant-arrival locations at the top of the regional aquifer (Appendix J section J-5). In addition, the calibration allows the estimation of the uncertainty ranges in the regional aquifer concentrations at the contaminant-arrival locations. The uncertainties in the locations of contaminant arrival and the contaminant concentrations at these locations are applied to estimate the uncertainty in the model prediction of contaminant distribution in the regional aquifer. Probabilistic assessments of the predicted current (circa 2007) distributions of chromium mass in the regional aquifer (in terms of concentrations) are presented in Figures 4.2-1 and 4.2-2. The concentrations represents the most probable values (the best estimates) based on the existing uncertainties. The two figures are based on two alternative conceptual models of the water table (presented in Figures J-5.1-2 and J-5.1-3, respectively; see also Appendix H). The potential locations of contaminant arrival identified in Appendix J-5 for the case of the two water table maps are considered to be equally probable and averaged to compute the data presented in the figures.

Figures 4.2-1 and 4.2-2 also show the area where the model indicates that regional groundwater chromium concentrations might exceed the current water-quality standards. The U.S. Environmental Protection Agency (EPA) maximum contaminant level (MCL) for Cr(VI) is 100 ppb and the New Mexico Human Health Standard is 50 ppb. The areas where the concentrations may exceed 100 ppb are contoured with pink lines (Figures 4.2-1 and 4.2-2); the green area defines where the concentrations may exceed 50 ppb. In the case of the first water table map (Figure 4.2-1), this area lies between Sandia and Mortandad Canyons, with R-28 located in the middle. In the case of the second water table map (Figure 4.2-2), the area extends along Mortandad Canyon, downgradient of R-28; in this case, R-28 is predicted to be very close to the potential contaminant arrival location. Figure 4.2-2 also demonstrates the effect of plume dispersion in the regional aquifer. The simulations are based on constant dispersivity coefficients (longitudinal 50 m; transverse 5 m) that might be underestimating the expected plume dispersion.

Table 4.2-1 compares chromium concentrations as defined in calibration ranges (Appendix G) and the model predicted ranges. In the table, model prediction 1 is based on the water table map presented in Figure H-1, and model prediction 2 is based on the water table map presented in Figure H-2. The results

demonstrate that, in general, the models are well calibrated and consistent with the observations. It is important to note that the estimated chromium concentrations do not include the background. Therefore, background concentrations should be added to the model-predicted concentrations to compare with the actual chromium measurements.

The inverse models can be applied to estimate the model-predicted chromium concentrations at the locations of the new monitoring wells that are currently being drilled or are planned to be drilled (Table 4.2-2). These wells (R-42, SCI-2/R-43, R-44, and R-45) are shown as purple circles in Figures 4.2-1 and 4.2-2. According to the models, the chromium concentration in the regional aquifer at R-42 may be at background or around 40 ppb (Figures 4.2-1 and 4.2-2), depending on the conceptual model of the water table used in the model. These values are best estimates. The entire uncertainty range, as predicted by the inverse model, is between 0 and 120 ppb (not shown in the figures). Similarly, the chromium concentration in the regional aquifer at SCI-2/R-43 may be at background or around 10 ppb; the entire uncertainty range, as predicted by the inverse model, is between 0 and 14 ppb (Table 4.2-2).

Figures 4.2-1 and 4.2-2 can also be used to inform the siting of the proposed wells R-44 and R-45. These analyses will be refined with the new data (water levels and chromium concentrations) that will be collected at R-42 and SCI-2/R-43.

4.3   3-D Coupled Modeling of Vadose Zone and Regional Aquifer

The 3-D modeling analysis demonstrates that lateral diversion of contaminants within the vadose from Sandia Canyon toward Mortandad Canyon may occur along dipping interfaces between hydrostratigraphic units. The potential locations where it might occur are the base of Guaje Pumice Bed, and on the top, within, and at the base of Cerros del Rio basalts. However, the simulations show that lateral diversion may be of limited extent with lenses of higher moisture building up on lower permeability interfaces causing some spreading but still leading to predominantly vertical flow. The 3-D modeling analysis demonstrates that recharge along Sandia Canyon may cause a mound at the water table in the regional aquifer that may result in off-axis spreading.

4.4   Distribution of Chromium Mass

Tables 4.4-1 and 4.4-2 summarize the results for the current-day distributions of chromium mass in the vadose zone presented in the previous chromium flow and transport report (LANL 2007, 098938). The tables list estimates of the mass of chromium that entered the unsaturated zone and the amount predicted to arrive at the regional aquifer to date, assuming the two infiltration models described in the previous report. These results still represent the best estimates of chromium distribution in the vadose zone. The estimated mass distributions are shown for the entire canyon and for four canyon segments (SW1 to SW4 in Figure 2.0-1). In addition, the estimates are further segregated by depth into two sections. The first section (UZ1) is the upper portion of the unsaturated zone that lies between the base of the alluvium (or the surface if no alluvium is present) and the base of the Guaje Pumice Bed. The second section (UZ2) is the lower portion of the unsaturated zone that lies between the base of the Guaje Pumice Bed and the regional water table. The table also presents inventories within the two vadose zone bins where the chromium is estimated to be present (in pore water, adsorbed on nonbasalt units, or reacted with the Cerros del Rio basalt) (Tables 4.4-1 and 4.4-2). These distributions may provide information to guide remedial options.

The regional aquifer analyses presented in section J-5 of Appendix J evaluate the current mass of chromium in the regional aquifer and the potential mass flux at the contaminant arrival locations. The

mass of chromium estimated to be within the area defined by 10 ppb and above in the aquifer (originating from the Sandia Canyon source) is less than 100 kg (between 50 and 90 kg) (Figures 4.4-1 and 4.4-2). The chromium mass flux at the contaminant-entry points is estimated to range between 3 and 18 kg/yr of chromium. If the current values were persistent for the last 50 yr, the total mass of chromium that may have reached the regional aquifer since 1956 varies between 150 and 900 kg. These values are lower than the estimates presented in Tables 4.4-1 and 4.4-2 (between 5500 and 50,000 kg). All the estimates for the regional aquifer are based on a model that assumes no reduction of chromium in the regional aquifer. The predicted chromium concentrations represent the mass in the groundwater. If chromium reduction occurs [including precipitation of Cr(III)], the estimated mass in the aquifer would be much higher. For example, if a 50% reduction occurs in the regional aquifer, the mass estimates would be approximately doubled.

4.5   Geochemical Studies

The chromium isotope study (Appendix D) shows that reduction of Cr(VI) to Cr(III) occurs within various media along the groundwater pathway. The greatest degree of reduction appears to be associated with ferrous iron, with the Cerros del Rio basalt being particularly important in this regard. The majority of water samples have chromium isotope values indicative of approximately 15% to 30% reduction of Cr(VI) to Cr(III). High dissolved concentrations of chromium coupled with low levels of Cr(VI) reduction at R-28 suggest that chromium may be entering the regional aquifer near R-28. X-ray absorption near-edge structure (XANES) spectroscopy was used in to identify chromium oxidation state(s) and to quantify the ratio of Cr(III)/Cr(VI) for rock samples exposed to solutions containing Cr(VI) (Appendix K). Results indicate that Cr(III) is precipitated on basalt samples and that approximately 50% Cr(VI) and 50% Cr(III) coexist on a sample from R-35a. Specific attenuation processes (adsorption versus precipitation) for chromium are being investigated further.

Initial results from dewatering experiments (Appendix L) suggest that both Cr(III) and Cr(VI) can be leached from wetland sediments upon drying and oxidation. Detectable concentrations of total dissolved chromium and Cr(VI) in leachates range from 5 to 1690 ppb and from 0.06 to 14.49 ppb, respectively. Preliminary stability calculations based on the amount of ferrous iron in the wetland, which will tend to keep chromium in its reduced form [Cr(III)], suggest that under current conditions 4 out of 11 samples do not contain sufficient Fe(II) to prevent oxidation of Cr(III) to Cr(VI). These calculations are preliminary because they do not account for the reduction capacity of organic carbon in the system.

5.0   CONCLUSIONS AND RECOMMENDATIONS

The models simulating the fate and transport of chromium in the subsurface were successfully calibrated to observed water levels and chromium concentrations at the monitoring wells in the regional aquifer. The calibrated models were applied to estimate the area in the regional aquifer that may be affected by the contamination. The estimated distribution of chromium mass in the regional can be used to site the new monitoring wells. The calibration process also effectively constrained the potential locations of chromium arrival at the top of the regional aquifer. The chromium-concentration and water-level data observed at the new regional monitoring wells (R-42, SCI-2/R-43, R-44, and R-45) will further reduce the uncertainty in the model estimates of chromium mass in the regional aquifer.

The estimated entry points at the top of the regional aquifer suggest complex 3-D flow paths in the vadose zone. The flow paths may be subject to lateral diversion to the south of Sandia Canyon. The mechanism of lateral diversion may be flow along dipping hydrostratigraphic contacts as discussed in Appendix J. In addition, the heterogeneity in hydrostratigraphic units and transients in infiltration recharge

(caused by long-term changes in discharge rates or stormwater) may cause preferential flow paths in the vadose zone (sometimes called "fingers") that have a complicated 3-D geometry (the formation of such preferential flow path is also discussed in Appendix J). Further complications in the spatial and temporal behavior of the flow paths through the vadose zone may be caused by geochemical characteristics of the hydrostratigraphic units and soil horizons between them.

Future work will further improve the developed models. The model estimates will be spatially and temporally constrained by applying the data collected at the new monitoring wells. The models will also be applied to estimate the potential chromium mass that may have reached the regional aquifer before the current monitoring network in the regional aquifer was established; this analysis will include historical observations of chromium concentrations where available. The 3-D model will be enhanced to investigate the effect of heterogeneity in hydrostratigraphic units and transients in infiltration recharge on the contaminant flow paths.

As the chromium investigation evolves into the CME phase, additional geochemical studies may be considered to assess different remedial options.

6.0   ACKNOWLEDGEMENTS

The following are the primary contributors to this report.

- Project Leaders: Danny Katzman and Kay Birdsell

- Flow and Transport Modeling: Velimir Vesselinov, Kay Birdsell, and Terry Miller

- Geochemistry and Geochemical Modeling: Patrick Longmire, Jeff Heikoop, Mei Ding, June Fabryka-Martin

- Chromium Isotope Investigation: Jeff Heikoop and Patrick Longmire

- Sediment and Surface Water Investigations: Steven Reneau and Greg Kuyumjian

- Regional Water-Level Analysis: Velimir Vesselinov, Rich Koch, and Dylan Harp

- Alluvial Water Investigation: Kay Birdsell and Rich Koch

- Geology and Geologic Model Update: David Broxton, David Vaniman, and Dan Strobridge

- Archival Source: Kay Birdsell

- Document Preparation: Pamela Maestas, Meena Sachdeva, Saundra Martinez, and Nicole Valerio

7.0   REFERENCES

The following list includes all documents cited in this report. Parenthetical information following each reference provides the author(s), publication date, and ER ID number. This information is also included in text citations. ER ID numbers are assigned by the Environmental Programs Directorate's Records Processing Facility (RPF) and are used to locate the document at the RPF and, where applicable, in the master reference set.

Copies of the master reference set are maintained at the NMED Hazardous Waste Bureau; the U.S. Department of Energy–Los Alamos Site Office; the U.S. Environmental Protection Agency, Region 6; and the Directorate. The set was developed to ensure that the administrative authority has all material

needed to review this document, and it is updated with every document submitted to the administrative authority. Documents previously submitted to the administrative authority are not included.

Atmadja, J., and A.C. Bagtzoglou, 2001. "State of the Art Report on Mathematical Methods for Groundwater Pollution Source Identification," *Environmental Forensics,* Vol. 2, pp. 205–214. (Atmadja and Bagtzoglou 2001, 102325)

Ballio, F., and A. Guadagnini, 2004. "Convergence Assessment of Numerical Monte Carlo Simulations in Groundwater Hydrology," *Water Resources Research,* Vol. 40, W04603, 5 pp. (Ballio and Guadagnini 2004, 102315)

Beven, K., and J. Freer, 2001. "Equifinity, Data Assimilation, and Uncertainty Estimation in Mechanistic Modelling of Complex Environmental Systems Using the GLUE Methodology," *Journal of Hydrology,* Vol. 249, pp. 11–29. (Beven and Freer 2001, 102321)

Blasone, R.-S., J.A. Vrugt, H. Madsen, D. Rosbjerg, B.A. Robinson, and G.A. Zyvoloski, 2008. "Generalized Likelihood Uncertainty Estimation (GLUE) Using Adaptive Markov Chain Monte Carlo Sampling," *Advances in Water Resources,* Vol. 31, pp. 630–648. (Blasone et al. 2008, 102320)

Carrera, J., and J. Hidalgo, 2005. "Inverse Problem in Hydrogeology," *Hydrogeology Journal,* Vol. 13, pp. 206–222. (Carrera and Hidalgo 2005, 102410)

Cooley, R.L., January 1993. "Exact Scheffé-Type Confidence Intervals for Output from Groundwater Flow Models, 1. Use of Hydrogeologic Information," *Water Resources Research,* Vol. 29, No. 1, pp. 17–33. (Cooley 1993, 102324)

Freeze, R.A., and J.A. Cherry, January 1979. *Groundwater*, Prentice-Hall, Inc., Englewood Cliffs, New Jersey. (Freeze and Cherry 1979, 088742)

Gaganis, P., and L. Smith, 2006. "Evaluation of the Uncertainty of Groundwater Model Predictions Associated with Conceptual Errors: A Per-Datum Approach to Model Calibration," *Advances in Water Resources,* Vol. 29, pp. 503–514. (Gaganis and Smith 2006, 102322)

LANL (Los Alamos National Laboratory), September 1999. "Work Plan for Sandia Canyon and Cañada del Buey," Los Alamos National Laboratory document LA-UR-99-3610, Los Alamos, New Mexico. (LANL 1999, 064617)

LANL (Los Alamos National Laboratory), March 2006. "Interim Measures Work Plan for Chromium Contamination in Groundwater," Los Alamos National Laboratory document LA-UR-06-1961, Los Alamos, New Mexico. (LANL 2006, 091987)

LANL (Los Alamos National Laboratory), October 2006. "Mortandad Canyon Investigation Report," Los Alamos National Laboratory document LA-UR-06-6752, Los Alamos, New Mexico. (LANL 2006, 094161)

LANL (Los Alamos National Laboratory), November 2006. "Interim Measures Investigation Report for Chromium Contamination in Groundwater," Los Alamos National Laboratory document LA-UR-06-8372, Los Alamos, New Mexico. (LANL 2006, 094431)

LANL (Los Alamos National Laboratory), September 2007. "Fate and Transport Modeling Report for Chromium Contamination from Sandia Canyon," Los Alamos National Laboratory document LA-UR-07-6018, Los Alamos, New Mexico. (LANL 2007, 098938)

LANL (Los Alamos National Laboratory), September 2007. "Summary of Sandia Canyon Phase 1 Sediment Investigations," Los Alamos National Laboratory document LA-UR-07-6019, Los Alamos, New Mexico. (LANL 2007, 098127)

LANL (Los Alamos National Laboratory), September 2007. "Completion Report for Regional Aquifer Wells R-35a and R-35b," Los Alamos National Laboratory document LA-UR-07-5324, Los Alamos, New Mexico. (LANL 2007, 098129)

LANL (Los Alamos National Laboratory), April 2008. "Drilling Work Plan for Nature and Extent of Chromium Contamination in Groundwater Investigations," Los Alamos National Laboratory document LA-UR-08-2611, Los Alamos, New Mexico. (LANL 2008, 101643)

Neuman, S.P., 2003. "Maximum Likelihood Bayesian Averaging of Uncertain Model Predictions," *Stochastic Environmental Research and Risk Assessment,* Vol. 17, pp. 291–305. (Neuman 2003, 102319)

Neupauer, R.M., and J.L. Wilson, 2002. "Backward Probabilistic Model of Groundwater Contamination in Non-Uniform and Transient Flow," *Advances in Water Resources,* Vol. 25, pp. 733–746. (Neupauer and Wilson 2002, 102326)

NMED (New Mexico Environment Department), October 17, 2007. "Notice of Disapproval, Fate and Transport Modeling Report for Chromium Contamination from Sandia Canyon," New Mexico Environment Department letter to D. Gregory (DOE LASO) and D. McInroy (LANL) from J.P. Bearzi (NMED HWB), Santa Fe, New Mexico. (NMED 2007, 097586)

Purtymun, W.D., December 1975. "Geohydrology of the Pajarito Plateau with Reference to Quality of Water, 1949-1972," Informal Report, Los Alamos Scientific Laboratory document LA-UR-02-4726, Los Alamos, New Mexico. (Purtymun 1975, 011787)

Vecchia, A.V., and R.L. Cooley, July 1987. "Simultaneous Confidence and Prediction Intervals for Nonlinear Regression Models with Application to a Groundwater Flow Model," *Water Resources Research,* Vol. 23, No. 7, pp. 1237–1250. (Vecchia and Cooley 1987, 102323)
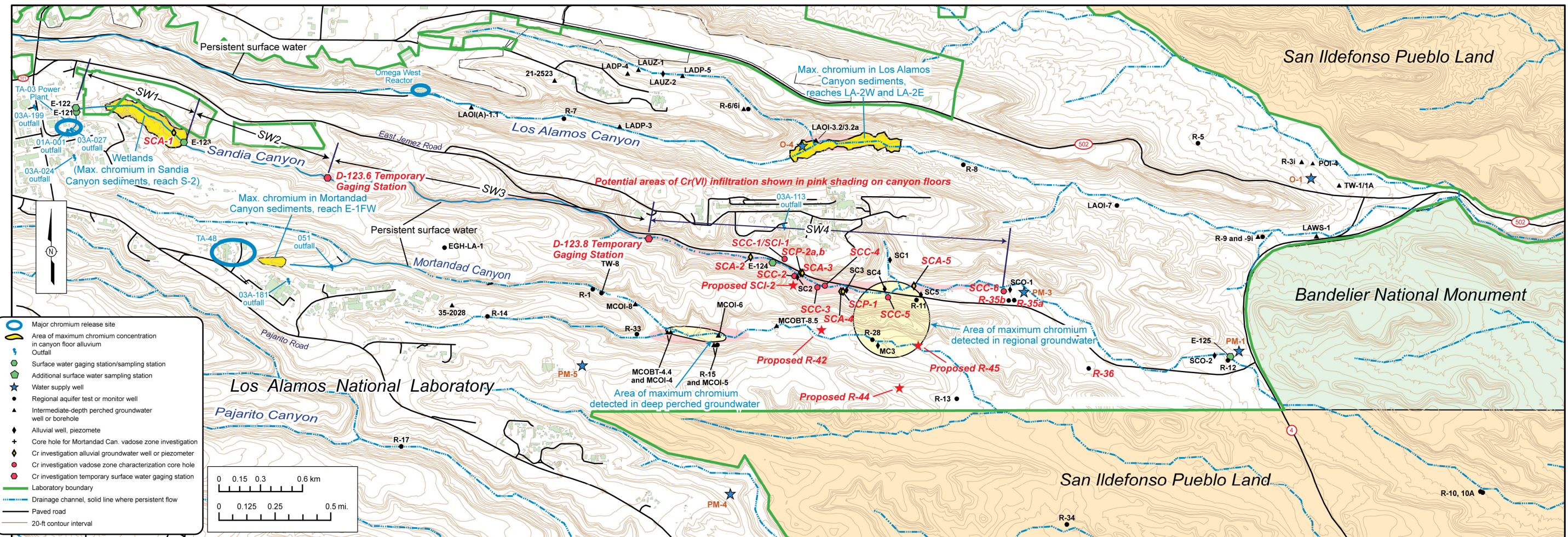
Figure 1.0-1   Location of Sandia, Los Alamos, and Mortandad Canyons showing major chromium release sites, stream-flow gages, infiltration reaches, boreholes and wells, and conceptual locations of proposed wells
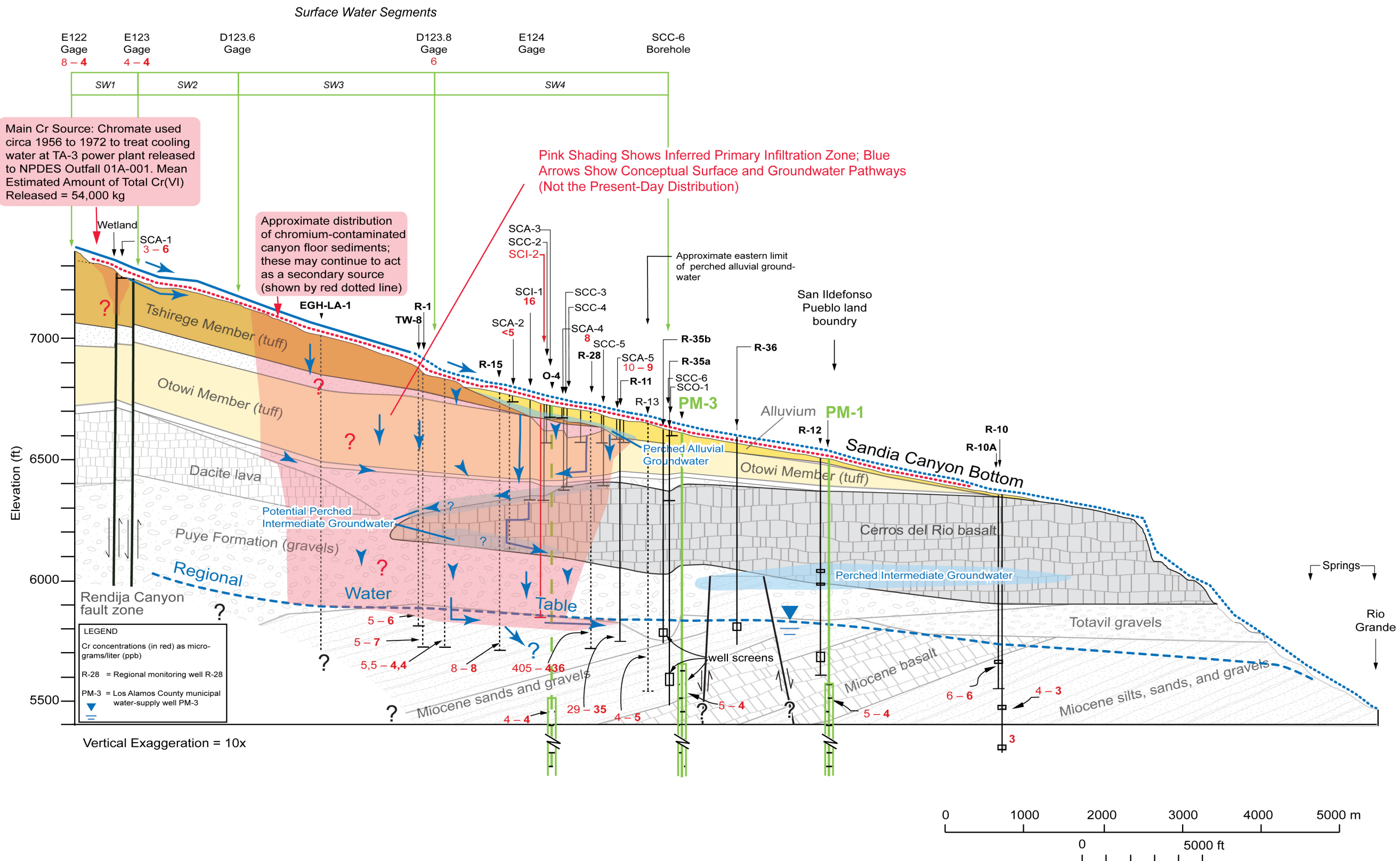
Figure 2.0-1   Conceptual hydrogeologic cross section showing potential chromium transport pathways and dissolved hexavalent chromium for surface water, monitoring wells, and water supply wells in the vicinity of Sandia Canyon
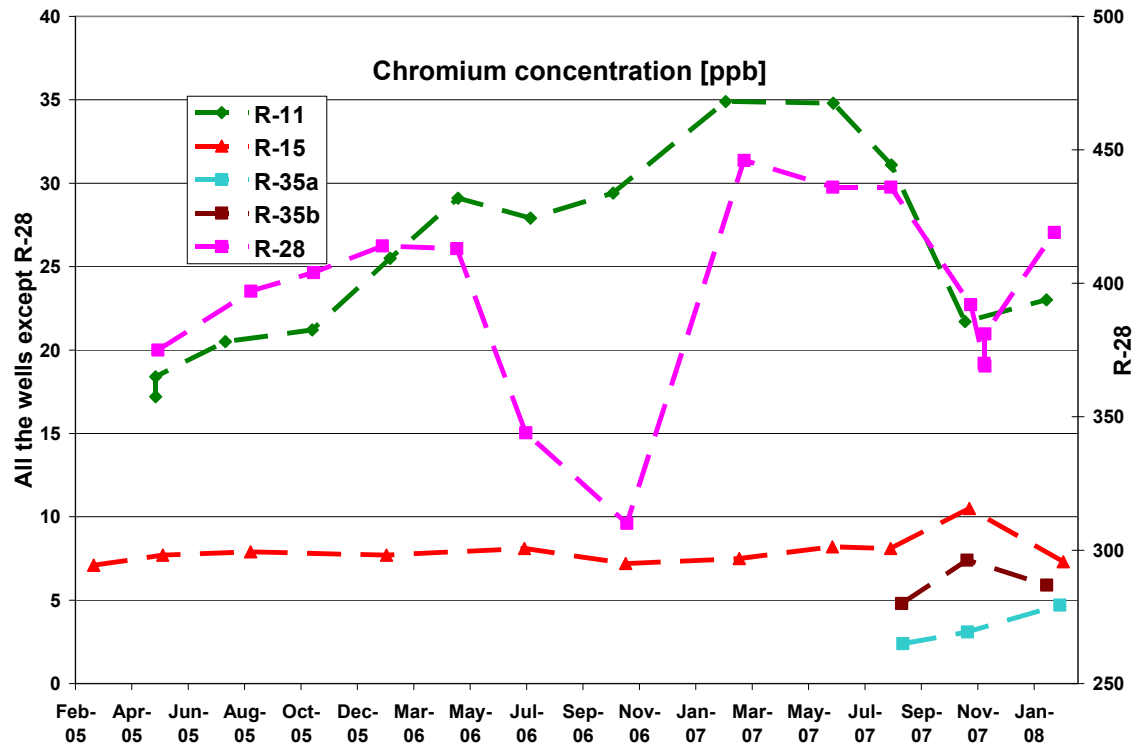
Figure 2.6.1   Total dissolved chromium concentrations observed at some of the wells near Sandia Canyon
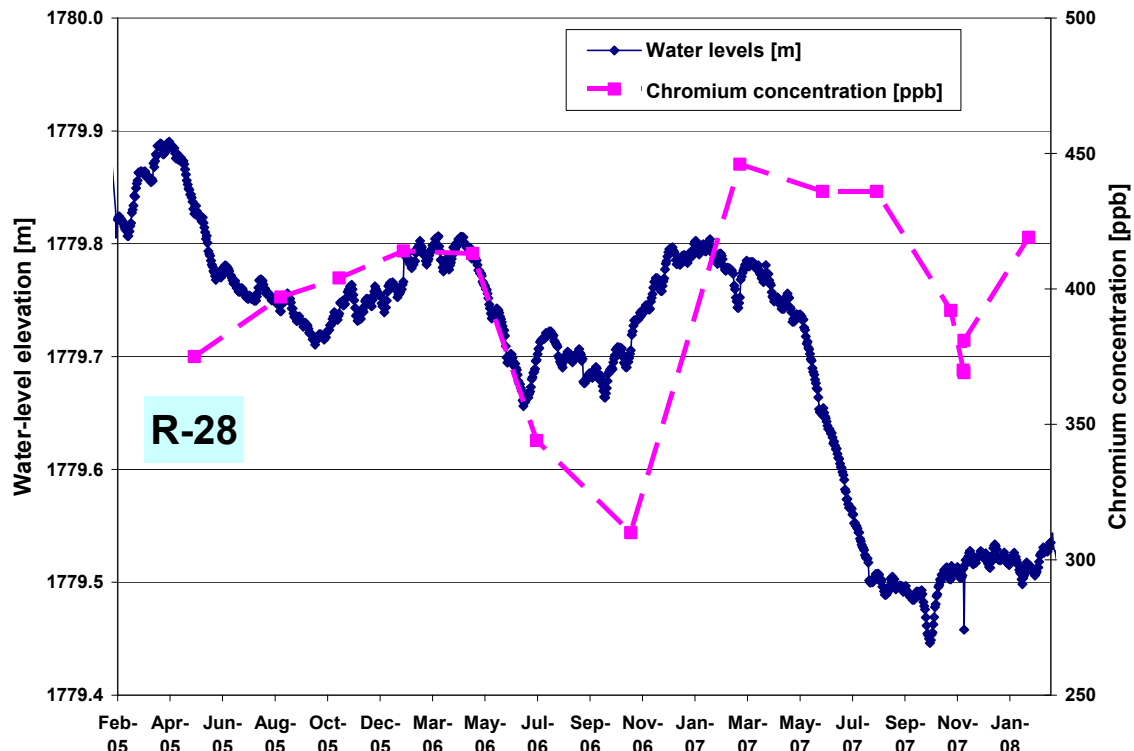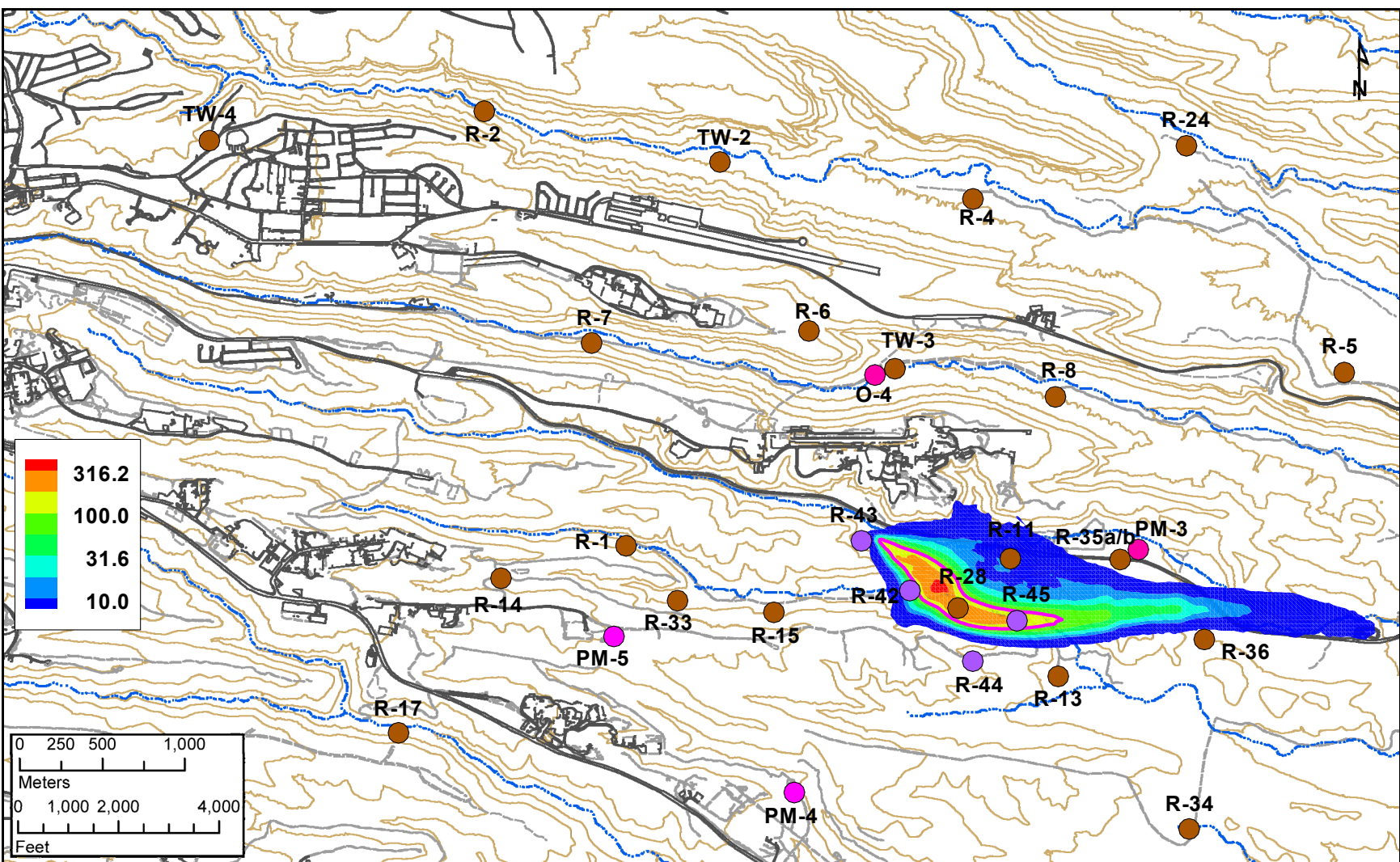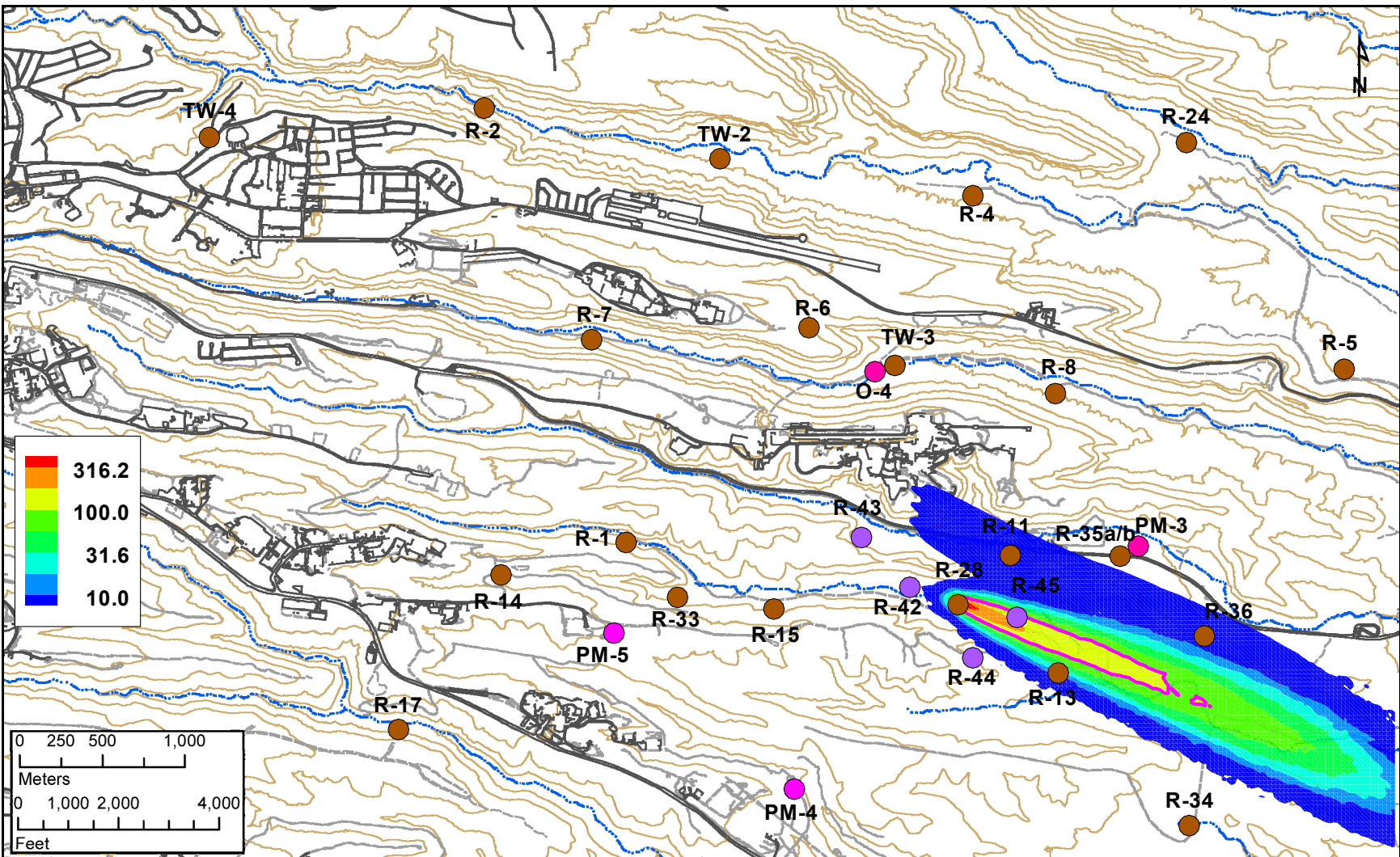
Figure 2.6.2   Comparison between transients in the water levels and total dissolved chromium concentrations observed at R-28

Fate and Transport Update for Chromium from Sandia Canyon

Notes: The simulations are based on constant dispersivity coefficients (longitudinal 50 m; transverse 5 m) that might be underestimating the expected plume dispersion. The thick pink line contours an area where the chromium concentrations are expected to be above 100 ppb with 50% probability. The model uses water table map 1 presented in Figure H-1. All the potential locations of contaminant arrival identified in Appendix J-5 are considered to be equally probable.

Figure 4.2-1   Most probable estimates of the spatial distribution of chromium concentrations based on probabilistic analysis of uncertainty in model predictions

Notes: The simulations are based on constant dispersivity coefficients (longitudinal 50 m; transverse 5 m) that might be underestimating the expected plume dispersion. The thick pink line contours an area where the chromium concentrations are expected to be above 100 ppb with 50% probability. The model uses water table map 2 presented in Figure H-2. All the potential locations of contaminant arrival identified in Appendix J-5 are considered to be equally probable.

Figure 4.2-2   Most probable estimates of the spatial distribution of chromium concentrations based on probabilistic analysis of uncertainty in model predictions

Fate and Transport Update for Chromium from Sandia Canyon

Table 4.2-1
Chromium Concentration (ppb) Predicted at Existing
Monitoring Wells Based on the Two Alternative Water Table Maps

Well	Calibration Range			Model Prediction 1			Model Prediction 2		
	Min	Average	Max	Min	Average	Max	Min	Average	Max
R-28	300	400	700	110	300	1100	590	600	610
R-11	5	30	50	1	10	32	3	8	40
R-15	0	10	30	0	0	0	0	0	0
R-35a/b	0	5	15	0	0	0	0	0	0
R-36	0	5	15	0	0	0	1	4	7
R-13	0	5	15	0	0	0	10	11	12
R-34	0	5	15	0	0	0	0	0	0

Notes: Model prediction 1 is based on the water table map in Figure H-1; model prediction 2 is based on the water table map in Figure H-2. Background concentrations should be added to the calibration ranges and model-predicted concentrations to compare with the actual chromium measurements.

Table 4.2-2
Chromium Concentration (ppb) Predicted at Monitoring Wells Currently
Being Drilled or Planned to be Drilled Based on the Two Alternative Water Table Maps

Well	Model Prediction 1			Model Prediction 2		
	Min	Average	Max	Min	Average	Max
R-42	0	40	120	0	0	0
R-43	0	2	14	0	0	0
R-44	0	0	0	0	0	0
R-45	83	180	450	124	125	126

Notes: Model prediction 1 is based on the water table map in Figure H-1; model prediction 2 is based on the water table map in Figure H-2.

Table 4.4-1
Simulated Present-Day Distribution of Cr(VI) (kg)
in the Vadose Zone Assuming Conceptual Infiltration Model 1

Cr(VI) (kg)	Total Mean [Minimum-Maximum]	SW1 Wetland Mean [Minimum-Maximum]	SW1 Fault Mean [Minimum-Maximum]	SW2 Mean [Minimum-Maximum]	SW3 Mean [Minimum-Maximum]	SW4 Mean [Minimum-Maximum]
Input	35879 [9640–69046]	3730 [995–6914]	413 [3.7–1332]	2666 [638–6879]	9856 [2720–17835]	19215 [4821–36439]
Output to Regional Aquifer	24027 [5504–48255]	877 [0–5956]	413 [3.7–1332]	2665 [638–6878]	6768 [173–15350]	13303 [2517–30173]
UZ1 Porewater	1803 [47–5311]	1479 [29–4084]	0	0.34 [0–3.8]	245 [0.9–2140]	79 [1–1364]
UZ1 Adsorbed	1042 [2–4644]	837 [1–2699]	0	0.1 [0–2]	156 [0–1757]	50 [0–983]
UZ2 Porewater	1175 [52–4289]	223 [0.5–904]	0 [0–0.03]	0.1 [0–1.65]	677 [0.6–3000]	277 [0.4–2580]
UZ2 Adsorbed (Nonbasalt)	2529 [9–15204]	318 [2–1243]	0	0.2 [0–4.7]	1527 [0.2–7405]	683 [0–7794]
Cerros del Rio Basalt	5282 [1442–13433]	0	0	0	459 [2.7–1308]	4823 [2189–5990]

Note: Simulation results are from vadose zone modeling presented in LANL 2007, 098938.

Table 4.4-2
Simulated Present-Day Distribution of Cr(VI) (kg)
in the Vadose Zone Assuming Conceptual Infiltration Model 2

Cr(VI) (kg)	Total Mean [Minimum-Maximum]	SW1 Wetland Mean [Minimum-Maximum]	SW1 Fault Mean [Minimum-Maximum]	SW2 Mean [Minimum-Maximum]	SW3 Mean [Minimum-Maximum]	SW4 Mean [Minimum-Maximum]
Input	36026 [9650–69141]	3695 [334–10425]	13 [4–23]	9 [3–16]	23197 [5840–48878]	9111 [147–36538]
Output to Regional Aquifer	28124 [6411–49554]	1009 [0–6199]	13 [4–23]	0	21778 [5565–46841]	5324 [0–25595]
UZ1 Porewater	1937 [261–6194]	1350 [51–3429]	0	6 [1–13]	8 [0–36]	574 [1–3681]
UZ1 Adsorbed	1086 [4–6201]	728 [4–2463]	0	3 [0–9]	3 [0–18]	351 [0–4722]
UZ2 Porewater	641 [1–3104]	225 [0–1217]	0 [0–2]	0	37 [0–498]	380 [0–2604]
UZ2 Adsorbed (Nonbasalt)	1138 [1–5201]	387 [0–2800]	0	0	78 [0–1035]	673 [0–4294]
Cerros del Rio Basalt	3105 [401–11350]	0	0	0	1293 [273–2001]	1812 [0–10100]

Note: Simulation results are from vadose zone modeling presented in LANL 2007, 098938.

Appendix A

Review of Chromium Fate and Transport Model and Updates

Appendix A provides a summary of the approach used in the predecessor modeling report (LANL 2007, 098938) and details the key changes made in this report as part of a process to further refine the model simulations for fate and transport of chromium originating from Sandia Canyon.

Numerical flow and transport models of the unsaturated zone and the regional aquifer in the Sandia Canyon area are developed to inform and enhance the understanding of the fate and transport of chromium in the environment. Some of the goals of these studies are to develop groundwater flow and contaminant transport models that can be used to predict chromium mass distributions in the regional aquifer and subsequent chromium transport to monitoring and potentially nearby water-supply wells. Such models can also be used to evaluate corrective measures alternatives or help define current contaminant distributions within different portions of the subsurface.

Preliminary models of chromium fate and transport were developed and documented in the "Fate and Transport Modeling Report for Chromium Contamination from Sandia Canyon" (LANL 2007, 098938). The flow and transport simulations predicted the migration of chromium from its presumed source in Sandia Canyon into and through the regional aquifer. The model simulated flow and chromium transport in surface water, alluvial groundwater, the unsaturated (vadose) zone, and the regional aquifer. The model also accounted for the effects of geochemical interactions of contaminants with wetland sediments and with various rock and sedimentary layers along the flow paths. Monte Carlo simulations that addressed uncertainty in input parameters (e.g., permeability, porosity, retardation factors, infiltration rates) were run to constrain the range of likely transport behaviors. The implementation of assumptions, boundary conditions and parameter distributions made in the models was conducted to mathematically simulate the conceptual model of chromium transport described in the report. The modeling results illustrated key aspects of the conceptual model of chromium transport through the vadose zone and regional aquifer. However, model runs that were intended to simulate present-day observations in the regional aquifer did not yield results that adequately matched field data. For example, key discrepancies between the model results and the chromium observations in the regional aquifer included simulations that overestimated chromium concentrations and overstated the area with elevated chromium. The model did not yield a chromium concentration pattern that is consistent with concentrations observed at key monitoring locations (i.e., incorrect predictions of spatial profile of chromium concentrations in the regional groundwater). That report concluded that further model development and calibration were required before the simulations could be used to describe chromium nature and extent or to assess the efficiency of the monitoring well network for detecting contaminants in Sandia Canyon.

Some simplifying assumptions were made in the previous modeling study (for example, solving vadose-zone transport with a series of one-dimensional columns). Simplifications often yield models that satisfactorily solve the problem at hand, but this was not the case with the previous study. Therefore, the modeling studies presented in the main body and in Appendix J of this report explore different numerical techniques to determine how the model can be improved. New techniques evaluated include (1) model calibration through inverse modeling to better match field data and (2) investigation of the effects of three-dimensional modeling on flow in the vadose zone. In addition, data analyses that further define the complex hydrologic system and refine the conceptual model are included in several of the appendixes of this report. Table A-1 summarizes some of the key assumptions and approaches used in the 2007 chromium transport modeling studies (LANL 2007, 098938) that are updated in this report to improve the capability of the numerical models to predict the current and future chromium observations. Several of these potential problems were also discussed in meetings with stakeholders, as described in Appendix B.

REFERENCE

The following list includes all documents cited in this appendix. Parenthetical information following each reference provides the author(s), publication date, and ER ID number. This information is also included in text citations. ER ID numbers are assigned by the Environmental Programs Directorate's Records Processing Facility (RPF) and are used to locate the document at the RPF and, where applicable, in the master reference set.

Copies of the master reference set are maintained at the NMED Hazardous Waste Bureau; the U.S. Department of Energy–Los Alamos Site Office; the U.S. Environmental Protection Agency, Region 6; and the Directorate. The set was developed to ensure that the administrative authority has all material needed to review this document, and it is updated with every document submitted to the administrative authority. Documents previously submitted to the administrative authority are not included.

LANL (Los Alamos National Laboratory), September 2007. "Fate and Transport Modeling Report for Chromium Contamination from Sandia Canyon," Los Alamos National Laboratory document LA-UR-07-6018, Los Alamos, New Mexico. (LANL 2007, 098938)

Table A-1
Summary of Simplifications in Los Alamos National
Laboratory 2007 Modeling Study and Resulting Analyses in This Report

Conceptual Model Element	Assumption/Approach Used in 2007,Modeling Study (LANL 2007, 098938)	Potential Problem Related to Previous Modeling Assumption/Approach	Approaches in 2008 report to Improve Numerical and Conceptual Models
Source	Cr mass calculated as 01A-001 outfall water volume multiplied by recorded surface water concentrations	Too much Cr mass is defined as a model input in some simulations.	Calibrate to measured Cr concentrations in vadose-zone profiles and throughout the regional aquifer to constrain infiltration rates and Cr mass (Appendix J)
Vadose-zone flow and transport	Modeled with series of 1-D columns with fixed cross-sectional areas, which forces vertical flow; uniform and nearly steady infiltration assumed; deep infiltration assumed to be based on surface water balance; only water source considered is 01A-001 outfall	Poor matches to Sandia Canyon corehole (SCC) core data (moisture content; Cr/Mo concentrations); deep infiltration controlled by spreading in alluvial groundwater in lower section of canyon, rather than by surface flow, which distributes water farther down the canyon; stormwater effects not taken into account; transient effluent and stormwater flows cause nonuniform surface water and alluvial groundwater flow and infiltration patterns; 3-D spreading effects, particularly at geologic contacts, not captured	Perform longer-term surface water study and include estimates of stormwater volumes (Appendix C) Analyze alluvial water levels and their relationship to outfall discharges, stormwater events and gage flows (Appendix C) Calibrate to SCC core data to infer infiltration rates, Cr/Mo concentrations and hydrologic parameters (Appendix J) Develop 3-D vadose-zone model to determine potential lateral spreading (Appendix J)
Regional-aquifer flow and transport	Entry points of chromium contamination are constrained by the location of one-dimension vadose models. Contaminant mass fluxes estimated by the vadose-zone transport model are applied as boundary conditions at the regional water table; A single water table map controls the directions of flow and transport; heterogeneity not explicitly included	Absolute and relative Cr concentrations do not match observed concentrations. Regional aquifer model predicted northerly groundwater flow from potential entry points beneath upper section of Sandia Canyon that does not agree with field observations.	Calibrate to measured Cr concentrations throughout the regional aquifer to constrain locations where Cr may have arrived at the water table (Appendix J) Include alternative water table map in analyses of groundwater flow directions (Appendixes G and J) Analyze water levels to better determine flow directions, pumping effects, and media heterogeneity (Appendixes E through I)

Table A-1 (continued)

Conceptual Model Element	Assumption/Approach Used in 2007,Modeling Study (LANL 2007, 098938)	Potential Problem Related to Previous Modeling Assumption/Approach	Approaches in 2008 report to Improve Numerical and Conceptual Models
Geochemistry	Cr Kd based on literature values; Cr reduction and subsequent uptake in vadose-zone basalt treated as simple % loss for any 1-D column having Tb4 present; Mo K_d = 1/3 Cr K_d	Cr K_d literature values may not reflect adsorption capacity of local rocks; simple % loss may not capture Cr reduction accurately; assumed Mo K_d values probably do not reflect adsorption capacity of local rocks	Use Cr isotopes to help define Cr reduction in different media (e.g., alluvial water, intermediate-perched water, regional groundwater) (Appendix D) Determine adsorptive and reductive capacities through experiments with local rocks (Appendix K) Calibrate to SCC core data to infer information about K_d ranges (Appendix J)

Appendix B

Chromium Project Technical Working Sessions
with the Citizens' Advisory Board and Other Stakeholders

B-1.0 INTRODUCTION

Los Alamos National Laboratory staff held three working sessions with the Citizens' Advisory Board (CAB) and other members of the public (collectively, the stakeholders) to discuss and receive input to the conceptual model for chromium transport from Sandia Canyon and numerical modeling approaches for simulating the fate and transport of chromium. The sessions were held on February 27, 2008, March 12, 2008, and June 11, 2008. In the first two meetings, the stakeholders provided comments on data collection, the conceptual model, and numerical implementation. In the third session, the key stakeholder comments were discussed, and representatives of the Laboratory presented how the comments will be addressed in this report. These comments and the responses are presented in Attachment B-1.

Attachment B-1

Chromium Project Technical Working Session—Q & A

GOAL OF WORKING SESSIONS
Integrate stakeholder input into models of subsurface chromium fate and transport while acknowledging uncertainty in our understanding of the system and in the parameters that control fate and transport.

Include the public and the CAB in:
> **1) assessing our approach including an evaluation of the data used to set up and calibrate the fate and transport models**
> **2) capturing a range of conceptual models of fate and transport**
> **3) capturing a range of parameter values**
> **4) evaluating model results**

To date, meetings with the CAB and the public, herein referred to as stakeholders, have yielded the following list is issues and questions. Each issue or question is followed by a LANL response. These responses are a basis for discussion to make sure the questions/issues have been correctly understood so the input can be considered in the conceptual and numerical model development. The modeling work will be presented in the following upcoming reports due to the NMED: Fate and Transport Modeling Report (July 2008) and the Sandia Canyon Investigation Report (December 2008).

Note that: Actions that have resulted in part from these working session discussions are underlined in the text below.

SOURCE OF CHROMIUM

Background

The model will not focus solely on the chromium mass currently in the regional aquifer. It captures the nature and timing of the historical releases as well as the present and potential future migration of chromium. In this effort, bounding the water volumes and mass of chromium released to Sandia Canyon and the timing of these releases are critical.

> S.1   *Clarification is sought about the nature and the estimated range of chromium mass released into Sandia and adjacent canyons.*

Potassium dichromate was used as a corrosion inhibitor in the TA-03 power plant cooling towers from approximately 1956 through April 1972. The dichromate solution did not coat the cooling tower parts, rather its presence in solution kept the acidic cooling water from attacking the metal parts of the towers. Based on archival review, the most likely mass of Cr(VI) released to the canyon in effluent is 31,000 to 72,000 kg (with a possible range of 26,000 to 105,000 kg). This range in mass was calculated by multiplying reported release volumes by reported release concentrations for the entire possible range. The likely range used one standard deviation on reported volumetric flow rates, and assumed that concentration values reported by two or more sources (historic references) were more reliable than those reported by only one source. In all, 8 references were relied upon for this study. This source is almost certainly the largest source of

chromium released at the Laboratory. The second largest chromium source at the Laboratory is thought to be from cooling towers for the Omega West Reactor (in Los Alamos Canyon, circa 1957 to 1973), which released approximately 3000 kg of Cr(VI).

In addition, chromium from the TA-03 power plant cooling tower was released directly to the air. Up to 1/3 more Cr(VI) could have been dispersed as droplets as part of the evaporative cooling process. However, the estimated range described above captures this mass because several of the sources reported only total chromium usage. Air dispersion estimates predict that these droplets would have dispersed within a 1- to 2-km radius of the cooling towers, potentially mixing with soil or surface water. If this mass of Cr(VI) mixed with the upper few inches of surface soil, its concentration would be difficult to detect above background. Soil samples collected at the heads of Mortandad and Los Alamos Canyons (two neighboring canyons to Sandia Canyon) do not differ substantially from background. For Sandia Canyon fate and transport simulations, estimates of mobile Cr(VI) are based on historic surface water contributions which included both effluent and the airborne contributions via surface runoff.

Effluent has been continuously released to upper Sandia Canyon since about 1950. Currently, treated sewage effluent and cooling tower blow down are released at roughly 300,000 to 400,000 gal/day. The TA-3 power plant operates only on an as-needed basis and cooling effluent from that facility no longer contributes significantly to flow in Sandia Canyon. Future simulations may consider the effects of transient surface water flow due to storm water and fluctuations in effluent volumes.

PATHWAYS

Background

Understanding migration pathways is key to every aspect of the chromium problem from assessing nature and extent to monitoring to remedy selection. We heard the following major questions or issues from the CAB and the public about migration pathways.

> P1. *How does chromium that is discharged into Sandia Canyon end up in the groundwater beneath Mortandad Canyon?*

Sandia Canyon and Mortandad Canyon are adjacent, parallel-running canyons that are approximately 1500 feet apart, with Mortandad Canyon to the south. Water entering the subsurface in Sandia Canyon may migrate away from the canyon axis due to geologic controls in the vadose zone. For example, in the unsaturated zone beneath Sandia Canyon, geologic data indicate that the base of the Guaje Pumice Bed, and the top and the base of the Cerros del Rio basalts have either a southerly or south-westerly dip that may divert water toward the south. In the regional aquifer, local gradients and other spatial variability of the aquifer properties may also divert groundwater flow in a south/south-east direction. Numerical models developed for the upcoming deliverables will account for these geologic and hydrologic controls, including a three-dimensional vadose zone model and alternative water-table maps that are consistent with water-level data in the study area.

> P2.   *There is a potential fast pathway for contaminant transport in the regional aquifer that is not being captured in the fate and transport modeling, and the contaminant concentrations along the fast pathway are unknown.*

It is assumed that the fast pathways being referred to are associated with more permeable strata that are interbedded within the aquifer in the area and downgradient of the known chromium contamination. The geologic setting that now comprises the regional aquifer is a highly spatially variable sequence of channel (coarser, more permeable) deposits, and inter-channel (finer, generally relatively less permeable) deposits. Therefore, the lateral continuity of the more permeable deposits is expected to be relatively limited. For example, the generally tight zone encountered near the water table at R-13 does not occur at R-28 (see below for further discussion on R-13). Additionally, the strata dip at an angle that is across the general groundwater gradient meaning that water will encounter multiple strata along the flow path.

The new wells downgradient to the east and southeast of R-28 will help constrain the question about the migration of chromium away from R-28.

> P3.   *The combined influence of drilling-fluid effects and not placing the well screens within the most permeable units near the water table could result in not identifying potential fast flow paths. For example, the screen of R-13 is 125 feet below the top of the water table and below confining beds.*

R-13 was a difficult well to design because of several operational and hydrological factors unique to this location. A potentially productive zone was indicated at the water table. However, the target zone for a screen at the water table would have been very thin (about 12 ft), and potentially not in good hydraulic communication with up-gradient contaminant sources due to locally dipping beds. In addition, a short screen at the water table might result in a short service life for the well because of draw down from nearby municipal supply wells. Ultimately, a decision was made to target the highest productive zone identified in the open-hole geophysical logs, and interpreted as containing the greatest effective porosity and estimated hydraulic conductivity (the zone 145–187 ft below the water table).

Additionally, a sample of groundwater collected at the water table from the borehole during drilling showed no indication of Laboratory contaminants, including chromium and tritium.

Ultimately, the importance of shallow pathways along the water table and the downgradient extent of Laboratory contaminants, including chromium, will be specifically addressed by two planned regional wells that will be located midway between R-28 and R-13; the goal of both wells is to monitor water quality at the top of the regional groundwater system and at a depth of an additional permeable zone up to 100 ft within the aquifer.

> P4.   *It was stated that contaminants may get forced to travel in fast pathways not far below the top of the water table. For example, it was suggested that the fast pathway is apparent in the nature of the water chemistry from R-35.*

LANL agrees that rapid transport along the water table may occur. <u>This pathway is one of the conceptual models that will be explored in our fate and transport analyses.</u> R-35a and b and the two new downgradient wells from R-28 were designed considering this conceptual model. Note also that the two new downgradient wells will also have screens set deeper in the aquifer to evaluate possible deeper migration pathways.

> *P5. The natural setting of the regional aquifer may be very effective for slowing downward migration of contamination.*

We agree with this statement. The chromium plume observed at R-28 might never manifest itself down-gradient at unacceptable concentrations due to reduction associated with iron in the aquifer sediments, adsorption, or dispersion due to the high groundwater flux in the vicinity of R-28. <u>These possibilities are part of the conceptual models that will be explored in our fate and transport analyses.</u>

> *P6. There was concern expressed that the modeling was forcing fixed pathways and not allowing flow in some critical directions.*

In the unsaturated (vadose) zone, the previous one-dimensional modeling reported in September 2007 did not depict lateral flow along geologic contacts or vertically within locally saturated "fingers" in the vadose zone. <u>To address this for the July 2008 report, the potential for lateral flow along geologic contacts will be included, thus providing a three-dimensional fate and transport aspect to the vadose zone. Spatially-variable infiltration patterns that allow for preferential flow will also be included.</u>

In the regional aquifer, the flow is assumed to be pseudo-three-dimensional: predominantly lateral (2-dimensional) along the water-table but with additional vertical downward components toward water-supply wells through hypothetical hydraulic "windows". The water-supply wells near the chromium plume (O-4, PM-1, PM-2, PM-3, PM-4 and PM-5) have screens in the deep section of the aquifer. In general, the well screens are about 150 ft or more below the regional water-table. The pumping stresses the deep portion of the aquifer producing drawdowns on the order of 50 ft. However, the pumping causes very subdued drawdowns at the monitoring-well screens located close to the water table. As a result, the water-supply pumping might not substantially affect the direction and magnitude of groundwater flow in the shallow aquifer zones near the water table. Nevertheless, the fact that the pressures (water levels) are lower in the deeper aquifer when compared to the water-table elevations creates the potential for downgradient flow, especially vertically along potential hydraulic windows. For example, the hydraulic windows might be caused by local heterogeneities or hydrostratigraphic discontinuities. The identification of properties of hydraulic windows or proving/disproving their existence is a difficult task. <u>As a result, the problem will be treated stochastically, considering the properties of potential hydraulic windows as random model parameters.</u>

> *P7. Explain the treatment of faults and fractures in the modeling.*

In the previous one-dimensional vadose-zone model, the fault zone near the downstream end of the wetland was treated in two ways, as either a fracture zone allowing for rapid transport all the

way to the regional aquifer, or a porous media acting similarly to surrounding media. Based on the existing data, we cannot reject either of these two alternatives. The July report will still treat the fault zone as a potential pathway for migration, and the results will be assessed against the calibration criteria discussed below.

The amount of water potentially currently entering the fault zone is constrained by the difference in the amount of water entering and leaving the wetland as estimated from outfall records and gaged surface-water flow at the downstream end of the wetland. The surface water study reported in September 2007 concluded that the majority of surface water that infiltrates in the wetland re-emerges as surface flow in the next downcanyon segment, indicating that very little net infiltration (approximately 0.03 cfs [ft^3/s] from more than 0.4 cfs) occurs in the fault zone in upper Sandia Canyon. Significantly more gaging data are now available, and this more comprehensive data set will be analyzed as part of the July report. The results will be used for constraining infiltration patterns in the vadose-zone model.

> *P8. More information was requested about which LANL contaminants are being used as tracers to identify pathways, specifically if bromide is being used.*

Several of the constituents that were released in Sandia Canyon and that could serve as tracers were also released in the adjacent LA/Pueblo, and Mortandad Canyons. Concentrations of some of these constituents including molybdenum and bromide occur in the regional groundwater beneath Pueblo, Los Alamos, Sandia, and Mortandad Canyons. In the case of bromide, the widespread occurrence limits its use as a tracer unique to the pathways that originate in and beneath Sandia Canyon.

> *P9. It was requested that a planned perched-intermediate well (SCI-2) be extended to the regional aquifer to help define pathways.*

This year two wells are being installed upgradient of well R-28 to help define where chromium is entering the regional aquifer. Well SCI-2 is located in Sandia Canyon in an area where a significant proportion of the available surface and alluvial groundwater in the canyon is lost to the underlying vadose zone. Well R-42, located in Mortandad Canyon, will help define regional groundwater pathways and the extent of Cr contamination in an area about a 0.5 mi up gradient of well R-28.

Well SCI-2 will consist of a core hole to the regional aquifer and a well installed in a second borehole. Samples from the initial core hole will provide information about (1) the distribution and concentrations of chromium in the lower vadose zone, (2), the presence of perched-intermediate groundwater and associated contaminants, and (3) chromium concentrations in regional groundwater near the water table. Based on data from samples collected in the initial core hole, well SCI-2 will be installed in a second borehole targeting either perched-intermediate groundwater or regional groundwater.

> *P10. What is being done to address sediment transport in Sandia Canyon?*

Ongoing investigations of sediment deposits along Sandia Canyon are being used to determine the distribution of chromium and other contaminants resulting from past sediment transport. This work has shown that the process of sediment mixing during transport results in substantial downstream decreases in the concentration of chromium in sediment, such that levels are near background at the eastern Laboratory boundary. Analyses of stormwater samples at a series of gaging stations in Sandia Canyon are also used to monitor concentrations of chromium and other contaminants in runoff events. Because runoff from most storm events naturally infiltrates into the alluvium within the Laboratory, off-site sediment transport in Sandia Canyon is rare. For example, no runoff event extended from TA-3 to the Laboratory's eastern boundary in 2007. Results of these ongoing studies will be presented in the two upcoming reports.

WETLAND

Background
Understanding the wetland is a key to a number of issues related to chromium in groundwater. Specifically, how much of the original source of chromium is still present in the wetland sediments, and is the chromium currently in the wetland a significant secondary source under current or future hydrologic conditions.

> W1. *What is the mass of chromium in the wetland?*

The best estimate for the total mass of chromium stored in sediments in and adjacent to the wetland is about 15,000 kg, and the uncertainty of this estimate is about 5,700 to 27,000 kg (using the 10th and 90th percentiles of a probabilistic statistical distribution). This is compared to the best estimate for the amount of chromium released into Sandia Canyon of 31,000 to 72,000 kg. (Note that much of the volume of chromium-bearing sediment is adjacent to but outside the boundaries of the current true wetland setting, and this entire area of sediment is included when informally referring to "the wetland".)

> W2. *Why is there no monitoring well in the wetland?*

There is an alluvial well in the wetland. This well does not produce very much water due to the low permeability of the high organic-content, wetland sediments. The chemistry of water in this alluvial well indicates interaction between surface water and the wetland environment.

> W3. *How stable is the chromium in the wetland?*

In the Sandia Canyon wetland, the majority of chromium is stable as chromium(III), in the form of solid chromium hydroxide ($Cr(OH)_3$), with very small amounts of chromium(VI) present, mainly as chromate. Chromium hydroxide has a low solubility that is less than 50 μg/L under near-neutral pH (6 to 9) conditions. The high abundance of solid organic matter present in the Sandia Canyon wetland helps to keep chromium(III) stable. The presence of reactive manganese(IV), stable as manganese dioxide, however, supports (re)oxidation of some of the chromium(III) to chromium(VI). Most of the chromium(III) should remain in a stable, reduced phase as long as the current wetland conditions are maintained. Experiments are being run with

wetland materials to determine the stability of chromium(III) under different wetting conditions in the event that effluent disposal practices are changed in the future.

> *W4. Does contamination in the wetlands pose an ecological risk?*

As part of this project, LANL is conducting a comprehensive ecological investigation in the wetland and throughout the remainder of Sandia Canyon that will be included in the December report. This study is consistent in nature to ecological investigations that have been completed in the LA/Pueblo, Mortandad, and Canon de Valle watersheds. In addition to chromium, the wetland contains PCBs and mercury which may pose an unacceptable ecological risk. Examples of ecological elements of the current investigation include bluebird studies, earthworm analysis, small mammal studies, and direct measurements of toxicity of site waters to aquatic organisms.

GEOCHEMICAL CONTROLS ON CHROMIUM MIGRATION AND STABILITY

Background

Geochemistry plays a major role in migration of chromium and, more importantly, transforming mobile and toxic hexavalent chromium into less mobile and less toxic trivalent chromium.

> *G1. What are the geochemical controls on chromium sorption and what experiments is LANL performing to determine the degree of sorption or reduction?*

The main geochemical parameters that control chromium adsorption include pH, oxidation-reduction potential, concentration of competing anions, and concentration of total dissolved chromium(III, VI). Chromium(VI) does not adsorb as strongly under basic pH (>7.0) conditions as it does under acidic pH (<7) conditions. Important adsorbents include ferric hydroxide (rust), clay minerals such as smectite, and possibly calcium carbonate (calcite). Chromium(VI) is stable under relatively oxidizing conditions (indicative of most groundwater at LANL) whereas chromium(III) is stable under relatively reducing conditions (indicative of some groundwater and pore water within wetland). Adsorption of chromium(III) is enhanced under basic pH conditions, which differs from that of chromium(VI). Presence of competing anions including phosphate and sulfate decreases chromium adsorption onto solid surfaces. Adsorption of chromium(III, VI) is enhanced at concentrations less than 10 μg/L of total dissolved chromium.

LANL is conducting both batch and column adsorption experiments for chromium to be used as site-specific input parameters (distribution coefficient or Kd) in geochemical and fate and transport modeling. The results of these experiments will not be completed for the July 2008 report but will be used as available to guide the model and help determine parameter ranges. LANL is also measuring stable isotopes of chromium in surface water and groundwater samples. These isotope ratios can indicate if chromium reduction occurs along flow paths due to interactions with iron-bearing minerals or organic materials. Results from these isotope studies will be presented in the July report and can inform parameter ranges used in the modeling studies.

MODELING - CALIBRATION, SENSITIVITY, AND UNCERTAINTY

Background

LANL is using fate and transport models to aid in the definition of the nature and extent of chromium and in remedy selection. Stakeholders were interested in how models are formulated, how they will be calibrated, what data will be used in calibration, and what type of processing will be performed on the model results.

> *M1. How will conceptual model uncertainty be treated in the modeling?*

Conceptual model uncertainty, or the fact that alternative assumptions can be made about the hydrogeologic system that are consistent with all of the data, is a key issue. The process being used for this report is to elicit input from both LANL and stakeholders on alternative conceptual models. Simulations will then be performed using a series of alternative conceptual models.

For the unsaturated zone modeling, conceptual model uncertainty will be explored for several transport mechanisms. In the previous modeling report submitted in September 2007, relatively uniform, vertical flow and transport was modeled. In the next modeling phases, including for the July 2008 report, more complex conditions will be modeled. These include preferential and transient flow due to factors such as variations in surface-water flow in the canyon, spatially non-uniform infiltration, geologic controls and variable hydrologic properties. Three-dimensional effects (such as dipping or discontinuous geologic units) that can disperse contaminants laterally will also be explored. Alternate geochemical effects will also be explored (such as reversible vs. nonreversible oxidation or adsorption of Cr(VI). Model results will be compared to field and laboratory data.

For the regional aquifer modeling, some of the conceptual model uncertainties that will be considered in the upcoming reports are: flow directions and magnitudes (including potential transients due to water-supply pumping and preferential recharge along the canyons), heterogeneity (e.g. existence of highly-permeable channels in the Puye Formation, stratification, effect of discontinuities such as faults and non-conforming contacts between different hydrostratigraphic units), effect of heterogeneity on contaminant dispersion and existence of fast flow paths, and geochemical effects on chromium concentrations.

> *M2. Which parameters are to be used in model calibration and how are acceptable ranges set for these parameters?*

For the vadose zone, observations of moisture content, and chromium and molybdenum concentrations measured in the SCC coreholes drilled in 2006 will be used. For the regional aquifer, observation of water levels and chromium concentrations measured in the R-wells will be used. Acceptable ranges for all the observations (regional and unsaturated) are being defined taking into account various factors: transients in the measurements, location and geochemical performance of monitoring screens, hydrostratigraphy, heterogeneity within strata, scaling effects and computational grid resolution.

M3. Please explain how the vadose zone will be modeled.

A combination of one-dimensional and three-dimensional modeling will most likely be used. First, a limited number of three-dimensional runs will be used to explore three-dimensional spreading and other effects (see #M1) within the unsaturated zone. Depending on the results and complications with computing, either further three-dimensional simulations will be run or the nature of the three-dimensional effects will be captured with a series of vertical columns that describe unsaturated-zone transport rates but potentially disperse (increase the footprint from that occurring near the surface) or spatially translate the arrival of contaminants at the water table. These vadose zone simulations will take into account the conceptual and parameter uncertainties.

M4. What is the overall value of models in addressing the chromium problem especially in light of a perceived lack of data to support model development and evaluation, and what is the role of sensitivity and uncertainty analysis?

The goals of the chromium study are to: (1) define the nature and extent of chromium in the regional aquifer and the vadose zone; (2) to assess the potential future impact of secondary chromium sources in the wetland and the vadose zone; (3) to assess remedial alternatives; and (4) to quantitatively evaluate the performance of the groundwater monitoring network. Numerical models of flow and transport are a quantitative mean of addressing these goals. They couple processes governing groundwater flow and transport with available observations to predict present and future conditions.

A fundamental challenge of the hydrogeology is dealing with incomplete knowledge. Hydrogeologists do not have and never will have data on the geologic and hydrologic properties of all rocks at all locations. This lack of complete knowledge results in conceptual model and parameter uncertainties that will be addressed in the analyses. Conceptual model uncertainty arises from differing views on, for example, the geometry of the domain, the site boundary conditions, and the governing physical and chemical reactions. The desire in the chromium project is to solicit from LANL staff and stakeholders the definitions of a set of conceptual models that describe the potential range of chromium migration and behavior. In addition to conceptual model uncertainty, parameters controlling the rates and directions of chromium transport are uncertain. Therefore LANL staff and stakeholders will define distributions of possible values for each parameter. Predicted concentrations will be compared to existing measurements. The uncertainty analysis will produce sets of results that will be used to help determine a path forward with respect to remedy selection, potential additional data collection, and groundwater monitoring.

Another tool employed in the LANL decision support process is sensitivity analysis. Sensitivity analysis will be used to define parameters that may need further study and refinement in order to reduce the types of uncertainties that affect decisions for remedial actions. For example, it may turn out that given both conceptual model and parameter uncertainty that the optimum remedy is to pump chromium contaminated groundwater and treat it at the surface. On the other hand, it may turn out that given the current uncertainty the choice of a remedy is not clear and therefore

additional characterization is required prior to remedy selection. Formal decision analysis will allow us to make this determination.

> M5. Concern was expressed that numerical models cannot help us (1) identify the source of chromium observed in the regional aquifer and (2) predict fate of plume downgradient from R-28.

Current data inform the potential locations where chromium enters the regional aquifer and modeling is being used, not to absolutely define these locations, but to reduce the uncertainty in where these locations are.

With respect to predicting downgradient concentrations from R-28, we recognize that our knowledge of where and how fast the chromium will migrate is uncertain, and to some degree, always will be. The question is – can we understand the existing nature and extent and the potential future migration well enough to select a remedy and design a monitoring well network that is protective even if the remedy fails? In this regard, modeling can help us to make informed decisions. If the uncertainties are too large to allow for a confident remedy selection (as stated above), then additional data may be needed to refine the models and re-evaluate remedy selection.

REMEDIATION OPTIONS

Background

The goal of the chromium project is to select a remedy from a list of potential remedies.

> R1. *Is LANL considering removing the chromium in the wetland?*

Potential remedial actions will be considered for all parts of the system including the wetland, the vadose zone, and the regional groundwater. Remedial actions may be driven by exceedance of groundwater or surface-water standards, protection against potential future impacts to groundwater, or identification of concentrations in the surface environment that are unacceptable for human health or cause adverse ecological effects.

Appendix C

Sandia Canyon Surface Water
Balance and Alluvial Water-Level Responses

C-1.0 SURFACE WATER STUDY

This appendix section summarizes the results from investigations of surface water in Sandia Canyon, revising the conceptual model of surface water loss presented in previous reports (LANL 2006, 094431; LANL 2007, 098938) based on new data collected from September 2007 to June 2008. Investigations focused on four areas with perennial or common surface water supplied from effluent discharges:

1. the approximately 0.6 km (0.4 mi) long Sandia wetland (reach S-2 of Katzman 2000, 064349; LANL 2007, 098127), between the confluence of the south fork and the north fork of Sandia Canyon (gaging stations E121 and E122, respectively) and the east end of the wetland (collocated gaging stations D123 and E123);

2. an approximately 0.9 km (0.6 mi) section of canyon east of the wetland, between gaging stations D123 and D123.6;

3. an approximately 2.6 km (1.6 mi) section of canyon between gaging stations D123.6 and D123.8; and

4. an approximately 0.9 km (0.6 mi) section of canyon between gaging stations D123.8 and E124.

Less frequent surface water also occurs downcanyon from E124, occasionally reaching the next downstream gaging station, E125, located above the eastern boundary of Los Alamos National Laboratory (LANL or the Laboratory). Gaging stations E121, E122, E123, E124, and E125 are part of the main stream gaging network at the Laboratory (Romero et al. 2007, 100140), and D123, D123.6, and D123.8 are temporary stations installed for this study. The temporary stations consist of portable 6-in. Parshall flumes, as discussed in the previous reports (LANL 2006, 094431; LANL 2007, 098938). The gaging station locations are shown in Figure C-1.0-1.

The Sandia wetland is in a broad, relatively low gradient area that occurs upcanyon of exposures of resistant unit Qbt 2 of the Bandelier Tuff (Gardner et al. 1999, 063492). The nonwelded lower part of unit Qbt 3 probably underlies most of the wetland, and down-to-the-west splays of the Rendija Canyon fault zone also cross Sandia Canyon in this area. The second investigation area is steeper and has a narrower canyon bottom where the stream incises through the most welded part of unit Qbt 2. The third area also has a narrow canyon bottom, and the stream here incises through the less-welded lower part of Qbt 2 and the nonwelded underlying units Qbt 1v and Qbt 1g (Gardner et al. 1999, 063492; Lavine et al. 2003, 092527). The fourth area includes the transition to a broader canyon bottom with thicker alluvium. Drainage areas are 234 acres (0.95 km^2), 358 acres (1.45 km^2), 824 acres (3.33 km^2), and 956 acres (3.87 km^2) above the lower ends of the four investigation areas.

Surface water in Sandia Canyon originates from discharges from outfalls, stormwater runoff, and snowmelt runoff, the latter being a relatively minor component. Most of the outfall discharges at present originate from National Pollutant Discharge Elimination System (NPDES) outfall 01A001 in Technical Area 03 (TA-03), which discharges effluent predominantly from the Laboratory's TA-46 Sanitary Wastewater Systems Consolidation (SWSC) plant and the TA-03 steam plant. Smaller discharges occur from NPDES outfalls 03A027 and 03A199, also in TA-03. These effluent discharges result in perennial flow through the wetland and for several kilometers downcanyon and are discussed in more detail in sections 2.1 of this report and C-2.2.1 of this appendix. Stormwater runoff supplements effluent discharges, and in some months can be a major contributor to the total surface water flow. Much of the headwaters of Sandia Canyon in TA-03 are either paved or occupied by buildings, and rapid runoff from these areas occurs during storms. Stormwater runoff also occurs from developed areas farther east, such as at TA-53, resulting in short-duration ephemeral flow in downcanyon reaches.

Comparison of outfall data with discharge data immediately below the wetland, at gaging station D123, from fall 2007 and 2008 indicate a net surface water loss through the wetland for all periods, which is consistent with the earlier observations from investigations conducted in 2006 and 2007 (LANL 2006, 094431; LANL 2007, 098938). However, comparison of records at D123 and D123.6 from September 2007 to June 2008 indicate more variability than observed in summer 2007. Specifically, whereas the summer 2007 data indicated a net gain between D123 and D123.6, the later data show either a net gain or no net change (within measurement errors) between these stations. Examples for April 21–23, 2008, and June 23–29, 2008, are shown in Figures C-1.0-2 and C-1.0-3. The reason for this variability between measurement periods is uncertain. Nevertheless, the most important aspect for this study is the amount of water lost to deeper bedrock units beneath the wetland, which can be estimated by subtracting the discharge at D123.6 from the outfall discharges for given periods and subtracting the estimated loss to evapotranspiration (ET), as done in a previous report (LANL 2007, 098938).

Estimated net daily losses between the outfalls and D123.6 for select periods from July 2007 to June 2008 are shown in Table C-1.0-1. Periods were chosen when discharge estimates at both stations were considered to be reliable and not significantly affected by precipitation events. The difference between average daily discharge at these stations, subtracting ET, is assumed to approximate the loss into deeper bedrock. Equivalent annual loss using these data ranges from 0 to 22 acre-ft/yr, averaging 12 acre-ft/yr. This is somewhat lower than estimated previously for July and August 2007 (LANL 2007, 098938), suggesting that less water infiltrates into bedrock beneath the wetland than indicated by the earlier, smaller data set.

Comparison of discharge records at D123.6 and D123.8 indicate either net loss or no net change downstream through this canyon segment from September 2007 to June 2008, depending on the measurement period. Previous data had indicated consistent loss through this section of canyon (LANL 2006, 094431; LANL 2007, 098938). As examples, Figure C-1.0-4 shows a period with net loss, June 7–30, 2008, and Figure C-1.0-5 shows a period with no significant net change, November 16–19, 2007. These variations in surface water loss can be attributed to variable stormwater runoff and the resulting saturation of alluvium. Specifically, September 2007 was unusually wet, having the second highest monthly precipitation of the last 3 yr, as shown in Table C-1.0-2. The infiltration of stormwater runoff into alluvium below D123.6 raised the water table, as shown by alluvial groundwater levels presented in section C-2.1.3 (e.g., well SCA-4), reducing surface water loss between D123.6 and D123.8 and allowing effluent to flow farther downcanyon. As discussed in a previous report (LANL 2007, 098938), the downcanyon extent of effluent-derived surface flow is also related to the total effluent volume, such that flow extended farther in 2006 than in 2007 because of the larger effluent releases in 2006. Variations in outfall discharge volumes since October 2005 are also presented in Table C-1.0-2, showing the unusually low discharges in summer 2007.

Estimated net daily surface water losses between D123.6 and D123.8 for selected periods from July 2007 to June 2008 are shown in Table C-1.0-3. These periods were chosen when discharge volumes at both stations were considered to be reliable and not significantly affected by precipitation events. Total loss from the stream channel between D123.6 and D123.8 for these periods averages 119 acre-ft/yr, which is similar to that estimated for summer 2007 (110 acre-ft/yr) when effluent discharges were less (LANL 2007, 098938). This estimate can be considered a first approximation of infiltration rates from alluvium into bedrock in this part of the canyon, although actual infiltration into bedrock could be either higher or lower.

Flow is intermittent at the next downcanyon gaging station, E124, located approximately 0.9 km (0.6 mi) downcanyon from D123.8, and indicates infiltration of most of the remaining effluent into alluvium in this reach. For example, Figure C-1.0-5 shows the very low flow at E124 during November 2007 when alluvial

groundwater levels were unusually high. Data from E124 for the period July 2007 to June 2008 suggest a total discharge of about 36 acre-ft, mostly from stormwater runoff events, although the rating curve for E124 is not as reliable as at other stations because the channel bed is not stable in this area. Discharge estimates here should be considered "poor," with an uncertainty of at least ± 25%. Surface water that passes E124 usually infiltrates alluvium on Laboratory land, upcanyon from E125. In 2007, for example, no runoff events were recorded at E125.

Table C-1.0-4 presents a summary of the surface water budget for upper Sandia Canyon for the period from July 2007 to June 2008, as estimated from the data discussed above. Some simplifying assumptions were made here, including the assumption that relatively little water is contributed by stormwater runoff downcanyon from the E123 gaging station and that ET is relatively unimportant along the narrow canyon bottom away from the wetland. There are also some problems with data quality, especially at E124, as discussed above. Therefore, this surface water budget should be considered an approximation because of various assumptions that had to be made and incomplete records; nevertheless, it shows the general magnitude of relative gains and losses along the canyon.

Surface water in the upper part of Sandia Canyon is primarily supplied by discharges from NPDES outfalls at TA-03, constituting approximately 75% of the total flow from July 2007 to June 2008 (Table C-1.0-4). The total amount of runoff is estimated using discharge records at E123 and varies from year to year, depending on precipitation events. For example, runoff is estimated as about 19% of the total flow in water year 2006 (October 2005 to September 2006) and about 28% of the total flow in water year 2007.

Table C-1.0-4 indicates that more than 60% of the total surface water loss from July 2007 to June 2008 occured in the area between D123.8 and E124, and that roughly 5% to 10% of the surface water was lost downcanyon from there. A relatively small amount of water was lost in the area of the wetland through ET and infiltration to deeper bedrock units, and a larger amount between D123.6 and D123.8 where nonwelded tuff occurs beneath the alluvium. The surface water losses in the downcanyon segments may be different from volumes that infiltrate into bedrock in these areas because of lateral flow within the alluvium, as discussed in section C-2.1.3, although both surface water data and alluvial groundwater data indicate the importance of the area between D123.8 and E124. The total amount of flow past E124 in particular is expected to vary from year to year with the size of precipitation events and associated runoff events as well as with total effluent discharges.

C-2.0 ALLUVIAL WATER-LEVEL RESPONSES TO SURFACE WATER FLOW

Alluvial wells SCA-1, SCA-2, SCA-3, SCA-4 and SCA-5 and piezometer nests SCP-1a,b,c and SCP-2a,b were installed in Sandia Canyon during October 2006 as part of the chromium investigation work defined in the "Interim Measures Work Plan for Chromium Contamination in Groundwater" (LANL 2006, 091987). The locations of these wells and piezometers are shown on the location map in Figure 1.0-1 of this report. Completion information is included in Appendix B of the "Interim Measures Investigation Report for Chromium Contamination in Groundwater," (LANL 2006, 094431). Water-level (transducer) data from these wells and piezometers have been gathered since October 2006, and mean-daily levels are shown in Figure C-2.0-1. Data for SCA-5 are not shown because the water level is generally below the well screen. In addition to the alluvial water levels, corresponding mean-daily outfall volumes, mean-daily surface water flow rates measured at gaging stations E123 and E124 showing storm events, and daily maximum and minimum temperatures at Laboratory meteorological tower TA-06, are also shown in Figure C-2.0-1, so the response of the perched alluvial groundwater can be investigated in relation to these surface flow events and weather effects. In addition to the full records, the data are shown for a shorter, more-detailed time period in Figure C-2.0-2. The shorter time period illustrates hourly water levels

and 5-min gage flow rates; it was chosen to better illustrate alluvial water-level responses during an active storm period. Both time periods are useful for understanding transients in the alluvial system and their potential spatial and time-dependent effects on deeper percolation to the underlying bedrock units. Additionally, the groundwater-level of the perched-intermediate zone beneath Sandia Canyon in well SCI-1 (Figure 1.0-1) is plotted in Figure C-2.0-1 to determine whether the hydrologic response of this deeper system (approximately 300 ft below ground) is related to surface and near-surface events.

C-2.1 Data Summary

C-2.1.1 Water Sources

Figure C-2.0-1a shows daily and monthly average outfall volumes recorded for NPDES outfall 01A001 in upper Sandia Canyon (Figure 1.0-1) from October 1, 2006, to April 30, 2008. This outfall discharges effluent predominantly from the Laboratory's TA-46 SWSC plant and the TA-03 steam plant (TA-3-SM22). Effluent for cooling of the TA-03 power plant is also discharged here, but currently the power plant produces power only infrequently and adds little to the effluent volume. Outfall 01A001 is the main effluent source of water to Sandia Canyon, and average discharges are close to 300,000 gal./d. It is noteworthy that the TA-03 steam plant was taken out of service for maintenance of the steam system from May 31, 2007, to early August 2007. During that period, discharges dropped to roughly 160,000 gal./d. This discharge rate is close to the estimated discharge rate while chromium was being released in the late 1950s to early 1970s (LANL 2007, 098938, Appendix A). Also, discharges are greatest, averaging nearly 400,000 gal./d, from mid-January to mid-March 2008, probably from an increase in the steam-heating requirements. These observations indicate that the steam plant discharges add significantly to the outfall 01A-001 releases. Daily records for two NPDES outfalls (03A027 and 03A199) associated with facility cooling of the Strategic Computing Complex and the Lab Data Communications Center (LDCC), both at TA-03, from August 1, 2008 through April 30, 2008, are also plotted in Figure C-2.0-1. Together, these outfalls contribute less than 50,000 gal./d of cooling water effluent to the canyon. Runoff from summer thunderstorm events are also shown for selected stream gages in Sandia Canyon in Figure C-2.0-1a; runoff contributes a significant volume of surface water as compared to effluent volume, as described in section C-1.

C-2.1.2 Stream Gage Data

Stream gaging station data for permanent gages E121, E122, E123 and E124 and temporary gage D123 (Figure 1.0-1 and Figure C-1.0-1) are shown in Figure C-2.0-1b. These data have not undergone the scrutiny discussed above in Section C-1. They are used here to understand the relative magnitude and timing of flow variations rather than their absolute magnitude. In terms of the alluvial water-level responses to surface flow events, E123, D123, and E124 are most informative because they describe surface water flow out of the wetland (E/D123) and farther downcanyon where the canyon bottom has a significant thickness of alluvium (E124). These data are repeated on the plots for SCA-2 and SCA-4 (Figures C-2.0-1d and C-2.0-1f) to better illustrate alluvial-water-level responses to surface flow events observed at these two gage locations. In general, surface flow at the eastern end of the wetland responds about 1.5 hr after releases at outfall 01A001. The gages respond quickly to storm events as well. Surface flow at gage E124 generally occurs only as a result of storms (or sustained heavy snowmelt), but not all storms yield flow at the gage. During storm runoff events in September 2007, the runoff front arrived at gage E124 about 1.5 hr after arriving at gage E123.

C-2.1.3   Alluvial Groundwater Levels

Alluvial well SCA-1 is located in upper Sandia Canyon in the eastern part of the wetland. The well is shallow and fully saturated (LANL 2006, 094431). The mean daily water level reported at this location is shown in Figure C-2.0-1c; it is effectively the surface water level because the well is fully saturated to above the ground surface. Over the full period of record, the mean water level has declined just over 1 ft. Most notably, the lowest levels were measured during January and February 2008 when outfalls volumes were highest. This finding seems counterintuitive but may be to the result of icing in the stream channel during this colder period, as evidenced by the low temperatures (below 0°C) shown in Figure C-2.0-1c. The hourly data in Figure C-2.0-2a show that the water level at SCA-1 rises and falls diurnally in concert with flow at gage E123 with approximately a 0.5-ft variation. The water-level variations at this location are minor, suggesting that storage volume and/or conductive capacity of the wetland area are sufficiently large to dampen out the transients.

Alluvial well SCA-2 is located in the narrow stretch of Sandia Canyon just west of where the alluvial floor in the canyon floor begins to thicken and is 2.3 m above the active stream channel (LANL 2006, 094431). The mean-daily water level reported at this location is shown in Figure C-2.0-1d. Here the water level fluctuates approximately diurnally in response to the effluent releases. Over the full period of record, variations of over 4 ft have occurred over time periods of approximately 2 mo. The highest levels at SCA-2 occur during active storm periods and also during cold weather. The cold weather may cause icing in the upstream channel, which, in turn, routes surface water farther down the canyon, resulting in greater infiltration into the alluvium down stream. The hourly data depicted in Figure C-2.0-2b show that the water level at SCA-2 rises and falls diurnally, with the peak water level occurring approximately a half-day after peak flow occurs at gage E123, and the variations are 1 ft or more. The lag suggests the water flow below E123 predominantly occurs through the alluvial system. When surface water reaches gage E124, SCA-2 water levels rise more quickly (about one-quarter-day lag) because in this case the water flow below E123 occurs as surface flow as well. In this way, the surface water might be recharging the alluvium closer to SCA-2. The peak is broader under this condition because presumably two water sources contribute to the release: the more rapid surface water recharge followed by slower groundwater flow through the alluvial system below E123. At SCA-2, the rapid, diurnal changes in water level imply small storage and high conductive capacity of the alluvial system. The high conductive capacity might be enhanced by the steep slope of the canyon bottom in this section (Figures 1.0-1 and 2.0-1 in the main body of this report and Appendix J section J-2), which likely promotes downcanyon lateral flow in the alluvium rather than infiltration into bedrock.

Alluvial well SCA-3 and the two nested piezometers SCP-2a and SCP-2b are located next to each other in a broad stretch of Sandia Canyon, east of SCA-2, and just off the active stream channel near stream gage E124 (LANL 2006, 094431). Mean daily water levels for these are shown in Figure C-2.0-2e. There was considerable difficulty during drilling of SCA-3, and the screen placement is generally too high to measure alluvial water levels, except for a period during December 2007 when alluvial groundwater levels were elevated. However, the two nested piezometers are deeper and have complete records that adequately cover the water-level fluctuations. For the period of record, water-level fluctuations vary over longer time scales (months) and overall by up to 10 ft. This behavior is very different from the one observed at SCA-2. It appears that long-term rises at SCP-2a and SCP-2b correspond to similar long-term rises at SCA-2 (e.g., during December 2006 through January 2007, late August and September 2007, December 2007 to January 2008). Again, icing in the upstream portion of the channel may cause more infiltration into the alluvium downstream. The lowest groundwater levels were measured during August 2007, following the approximately 2-mo, low-release period at the 01A001 outfall. The hourly data in Figure C-2.0-2c show that the water levels at SCP-2a and SCP-2b rise in response to runoff after summer thunderstorms. When surface water reaches gage E124, the water levels in the alluvium rise at a

faster rate (inflections in the curves), often within a day, because the surface water seeps into the alluvium closer to the wells than under conditions when runoff does not reach stream gage E124. However the response in the alluvial groundwater to storm runoff events is subdued. At this location, response times are slow because a significant volume of surface water and runoff generally infiltrates into the alluvium between SCA-2 and SCA-3/SCP-2. The groundwater at SCA-3/SCP-2 also responds to lateral flow through the alluvium, which has a large storage volume and shallow slope at this location in the canyon (Figures 1.0-1 and 2.0-1 of this report and Appendix J section J-2). Near SCP-2a and SCP-2b, groundwater levels decline during periods of low runoff, indicating that infiltration into bedrock likely occurs in this part of the canyon.

Alluvial well SCA-4 and the three nested piezometers SCP-1a, SCP-1b, and SCP-1c are located next to each other in a broad stretch of Sandia Canyon east of SCA-3 and about 1200 ft east of E124 (LANL 2006, 094431). Mean daily water levels for these are shown in Figure C-2.0-1f. The well and the three piezometers have nearly complete records. Water levels have varied by up to 5 ft here. The fluctuations occur over longer time periods than at SCA-2, but response to runoff events at E124 is quicker than at SCP-2a and SCP-2b, despite their location farther down the canyon. The long-term rises and falls follow those at SCA-2, although lag times are not consistent. Here also, low groundwater levels were measured during August 2007, following the low release period at the 01A001 outfall and a period when significant runoff did not reach E124. The hourly data shown in Figure C-2.0-2d indicate the overall water levels rise during the summer runoff period in discrete steps. When runoff reaches gage E124, the water levels rise steeply (1.5 to 2 ft abrupt change) within a day, apparently because of nearby surface water recharge. Between runoff events, however, the water levels stay constant or decline slowly. This behavior shows that the alluvial groundwater at this location is tied more directly to the surface water system than near SCA-3/SCP-2. Overall, however, groundwater levels are low and response times are slow when runoff does not reach E124; this segment is generally recharged by lateral flow through the extensive alluvium. The decline in the alluvial groundwater level between runoff events suggests slow leakage of the groundwater from the alluvium system. Because alluvial groundwater does not extend much farther downcanyon, it can be expected most of the groundwater loss is from seepage into underlying units. Therefore, infiltration into bedrock is very likely in this part of Sandia Canyon.

C-2.1.4 Perched-Intermediate Water Levels

Perched-intermediate well SCI-1 (Figure 1.0-1) is located on the north side of the road in Sandia Canyon between alluvial wells SCA-2 and SCA-3 (LANL 2006, 094431). It is screened in the Puye Formation just above the contact with the Cerros del Rio basalt at approximately 300 ft depth below the base of the alluvium. The mean-daily water level at SCI-1 is shown in Figure C-2.0-1g, along with the water level corrected for barometric pressure effects for the period from February 2007 to March 2008. The corrected water levels vary by approximately 1 ft over the period of record. The water-level variation is smooth; the highest levels are in February and the lowest are in October 2007. The variation may be somewhat correlated with the variation of outfall fluxes (Figure C-2.0-1a), but the intermediate groundwater does not indicate a correlation with runoff events in Sandia Canyon. The relatively short period of groundwater-level data for this well preclude additional analyses at this time.

C-2.2 Estimating Infiltration Based on Alluvial Water Levels and Piezometer Nests

C-2.2.1 Piezometer Analyses

Vertical gradients and seepage velocities in the alluvium were reported in the interim measures investigation report for chromium contamination (LANL 2006, 094431) based on the two piezometer sets for a short time after their initial installation (October 13, 2006 to November 6, 2006). That report also

notes that the alluvium is quite heterogeneous (from well-sorted coarse sand to silty, clayey sand) having large variations in hydraulic conductivity and porosity.

At SCP-2a and SCP-2b, the vertical gradients were downward at that time, and the trend remains the same with the upper piezometer measuring water levels consistently 2 to 2.5 ft higher than the lower (Figure C-2.0-1e). These strong vertical gradients result in an estimated downward seepage velocity of 46 to 49 cm/day (1.5 to 1.6 ft/day), which yields an average annual infiltration loss of 172.5 m/yr (LANL 2006, 094431) based on the lower reported hydraulic conductivity measured at these two locations.

At the nested piezometers SCP-1a, SCP-1b and SCP-1c, the vertical gradients are variable in time (Figure C-2.0-1f) with the water level at SCP-1a often below that piezometer's screen. Generally, the lowest piezometer (SCP-1c) measures the highest water level, which indicates upward flow. However, the gradient between the two higher piezometers (when measureable at SCP-1a) frequently, but not always, indicates downward flow. The piezometer seepage velocities reported in the previous report were 12 to 61 cm/day (0.4 to 2 ft/day) downward between the upper two and 116 to 155 cm/day (3.8 to 5.1 ft/day) upward between the lower two (LANL 2006, 094431).

The seepage velocities, from 12 (down) to 155 (up) cm/day (0.4 (down) to 5.1 (up) ft/day) calculated for these piezometer sets, are extreme and are not in line with the effluent disposal volumes entering the canyon. The analysis assumes that the differences in the pressures observed at the piezometers drive vertical flow. However, the pressure gradients may instead cause lateral flow through very heterogeneous strata characterized by multiple layers with contrasting hydraulic properties. As a result, rather than representing lumped seepage velocities from the alluvial system to the underlying bedrock, these piezometer-based values probably represent small-scale flow patterns within the alluvium, including the extreme heterogeneity and transient nature of the system. For this reason, the same alluvial water-level data are examined in terms of longer-term storage losses to determine if analyzing the data in that light yields more reliable, integrated seepage velocities from the alluvium to the underlying bedrock.

C-2.2.2 Storage Analysis

A mass-balance analysis of alluvial groundwater based on the alluvial-groundwater levels can also be used to constrain infiltration rates from the alluvium into the underlying tuff units. An alluvial water balance is considered for the portion of the canyon between stream gage D123.8 and borehole SCC-6 (Figure 1.0-1). Over this canyon length, it can be assumed that almost no flow as alluvial groundwater enters or exits the system because very little alluvium is present at the gage on the western end of the section, and perched groundwater is not observed at SCC-6 to the east. If this is the case, then the water balance can be written as Equation C-1 below. For a subsection of the canyon, the flow of alluvial groundwater must be included, and Equation C-1 can be expanded in the form of Equation C-2.

For the entire segment:

Δ(alluvial groundwater storage)/Δt = volumetric flow rate measured at Gage E123.8 – volumetric infiltration rate into the tuff **Equation C-1**

For a subsection of the alluvial segment:

Δ(alluvial groundwater storage) /Δt = volumetric flow rate at Gage E123.8 – volumetric infiltration rate into the tuff + volumetric flow rate of alluvial water entering laterally – volumetric flow rate of alluvial water exiting laterally **Equation C-2**

Where Δ(alluvial groundwater storage)/Δt = (Δh/Δt)*specific yield*area **Equation C-3**

Equation C-1 can be applied with some simple assumptions to yield first-order approximations of infiltration rates. If Equation C-1 is applied over the entire segment for a period with relatively steady water levels, then the overall infiltration rate for the segment is calculated directly from the gage data. Here, two time periods are evaluated.

For the period October 24 to November 19, 2007, the approximate average flow at gage D123.8 was 1.4×10^{-2} m^3/s (324,000 gal./day) (see section C-1), and piezometers SCP-2a and SCP-2b measure nearly steady water levels (Figure C-2.0-1e). Assuming an infiltration area of approximately 100,000 m^2 (1.1×10^6 ft^2), this yields an estimated infiltration rate of 4.5 m/yr (15 ft/yr). However during this same period, the water level declines approximately 0.15 m (0.5 ft) at SCA-4 (Figure C-2.0-1f). Including this change in alluvial groundwater storage (Equation C-3) and assuming a value of 0.2 for the specific yield (Freeze and Cherry 1979, 088742, p. 61), an estimated infiltration rate of 4.9 m/yr (16 ft/yr) is obtained.

For the period July 29 to August 29, 2007, water levels at piezometers SCP-2a and SCP-2b and at well SCA-4 are fairly level. If surface water flow to the alluvial segment is assumed to be approximately 7.6×10^{-3} m^3/s (175,000 gal./d) (based on the effluent discharge records, Figure C-2.0-1a), this yields an infiltration rate of 2.4 m/yr (7.9 ft/yr). This value reflects a potential infiltration rate following the lower discharge period that occurred while the steam plant was shut down.

These estimates assume that the water-level changes over time measured at given locations apply over the entire segment (i.e., from gage D123.8 to SCC-6). The rates are quite high compared to other estimates for net infiltration rates across that Pajarito Plateau (Birdsell et al. 2005, 092048; Kwicklis et al. 2005, 090069), but they are required in to accommodate the approximately 1.3×10^{-2} m^3/s (300,000 gal./d) of effluent discharged to the canyon. The infiltration rates calculated here agree well with vadose-zone calibration runs presented in Appendix J section J-4. Therefore, it appears that estimating infiltration rates based on longer-term (weeks) water-level variations may yield integrated values that are more representative than those obtained from analyses of piezometer data (section C-2.2.1), which may be sampling small-scale flow patterns and short-term fluctuations in flow within the alluvium..

If one assumes that measured water-level changes are more local than representative of the entire segment, Equation C-2 can be applied. The mass-balance analysis presented here can be expanded and solved using a numerical model of the alluvial groundwater system that is calibrated using alluvial water levels and stream-gage data to estimate spatial and temporal estimates of seepage (infiltration) from the alluvium into the underlying tuffs.

C-3.0 REFERENCES

The following list includes all documents cited in this appendix. Parenthetical information following each reference provides the author(s), publication date, and ER ID number. This information is also included in text citations. ER ID numbers are assigned by the Environmental Programs Directorate's Records Processing Facility (RPF) and are used to locate the document at the RPF and, where applicable, in the master reference set.

Copies of the master reference set are maintained at the NMED Hazardous Waste Bureau; the U.S. Department of Energy–Los Alamos Site Office; the U.S. Environmental Protection Agency, Region 6; and the Directorate. The set was developed to ensure that the administrative authority has all material needed to review this document, and it is updated with every document submitted to the administrative authority. Documents previously submitted to the administrative authority are not included.

Birdsell, K.H., B.D. Newman, D.E. Broxton, and B.A. Robinson, 2005. "Conceptual Models of Vadose Zone Flow and Transport beneath the Pajarito Plateau, Los Alamos, New Mexico," *Vadose Zone Journal,* Vol. 4, pp. 620-636. (Birdsell et al. 2005, 092048)

Freeze, R.A., and J.A. Cherry, January 1979. *Groundwater*, Prentice-Hall, Inc., Englewood Cliffs, New Jersey. (Freeze and Cherry 1979, 088742)

Gardner, J.N., A. Lavine, G. WoldeGabriel, D. Krier, J., D.T. Vaniman, F.A. Caporuscio, C.J. Lewis, M.R. Reneau, E.C. Kluk, and M.J. Snow, March 1999. "Structural Geology of the Northwestern Portion of Los Alamos National Laboratory, Rio Grande Rift, New Mexico: Implications for Seismic Surface Rupture Potential from TA-3 to TA-55," Los Alamos National Laboratory report LA-13589-MS, Los Alamos, New Mexico. (Gardner et al. 1999, 063492)

Katzman, D., February 2000. "Summary Status of Environmental Restoration Project Investigations in Upper Sandia Canyon," Los Alamos National Laboratory document LA-UR-00-777, Los Alamos, New Mexico. (Katzman 2000, 064349)

Kwicklis, E., M. Witkowski, K. Birdsell, B. Newman, and D. Walther, August 2005. "Development of an Infiltration Map for the Los Alamos Area, New Mexico," *Vadose Zone Journal,* Vol. 4, pp. 672-693. (Kwicklis et al. 2005, 090069)

LANL (Los Alamos National Laboratory), March 2006. "Interim Measures Work Plan for Chromium Contamination in Groundwater," Los Alamos National Laboratory document LA-UR-06-1961, Los Alamos, New Mexico. (LANL 2006, 091987)

LANL (Los Alamos National Laboratory), November 2006. "Interim Measures Investigation Report for Chromium Contamination in Groundwater," Los Alamos National Laboratory document LA-UR-06-8372, Los Alamos, New Mexico. (LANL 2006, 094431)

LANL (Los Alamos National Laboratory), September 2007. "Fate and Transport Modeling Report for Chromium Contamination from Sandia Canyon," Los Alamos National Laboratory document LA-UR-07-6018, Los Alamos, New Mexico. (LANL 2007, 098938)

LANL (Los Alamos National Laboratory), September 2007. "Summary of Sandia Canyon Phase 1 Sediment Investigations," Los Alamos National Laboratory document LA-UR-07-6019, Los Alamos, New Mexico. (LANL 2007, 098127)

Lavine, A., C.J. Lewis, D.K. Katcher, J.N. Gardner, and J. Wilson, June 2003. "Geology of the North-central to Northeastern Portion of Los Alamos National Laboratory, New Mexico," Los Alamos National Laboratory report LA-14043-MS, Los Alamos, New Mexico. (Lavine et al. 2003, 092527)

Romero, R.P., D. Ortiz, and G. Kuyumjian, August 2007. "Surface Water Data at Los Alamos National Laboratory: 2006 Water Year," Los Alamos National Laboratory report LA-14328-PR, Los Alamos, New Mexico. (Romero et al. 2007, 100140)
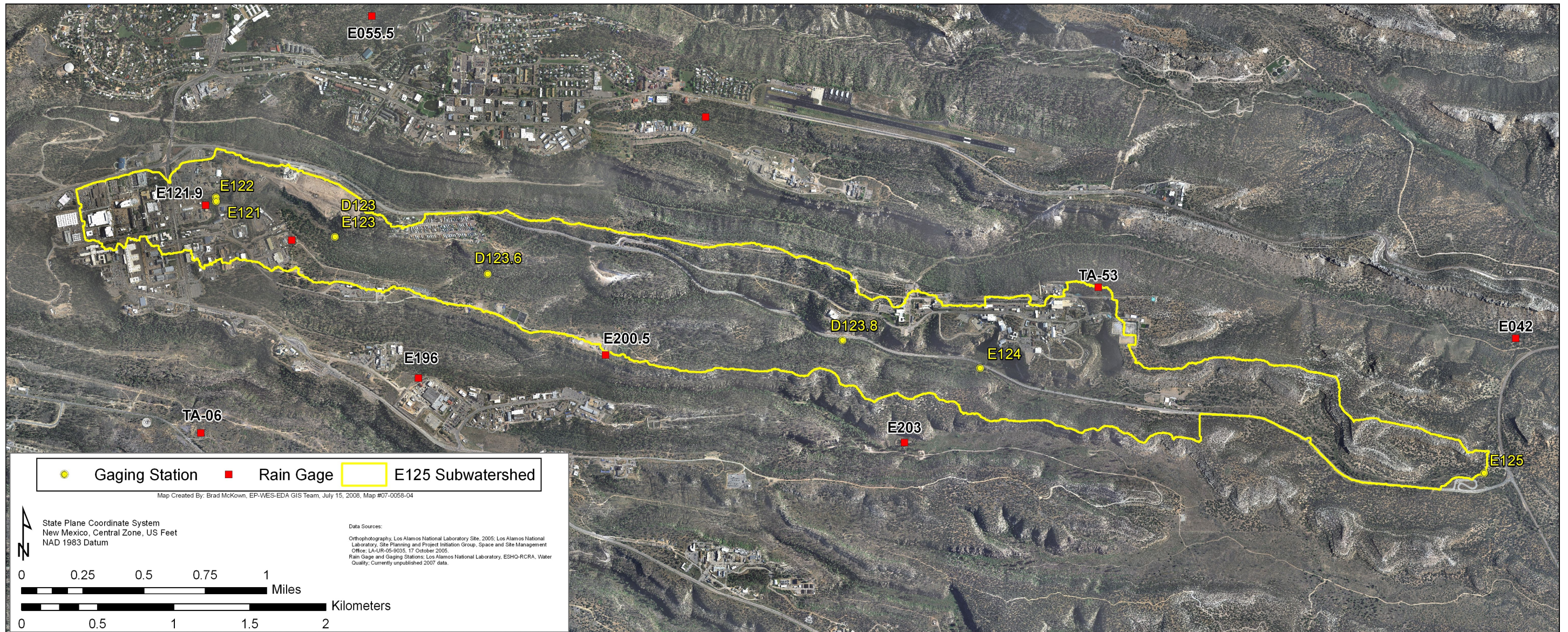
Figure C-1.0-1 Orthophotograph of Sandia Canyon on Laboratory land showing locations of gaging stations and precipitation stations discussed in this appendix and the extent of the drainage basin upcanyon from gaging station E125
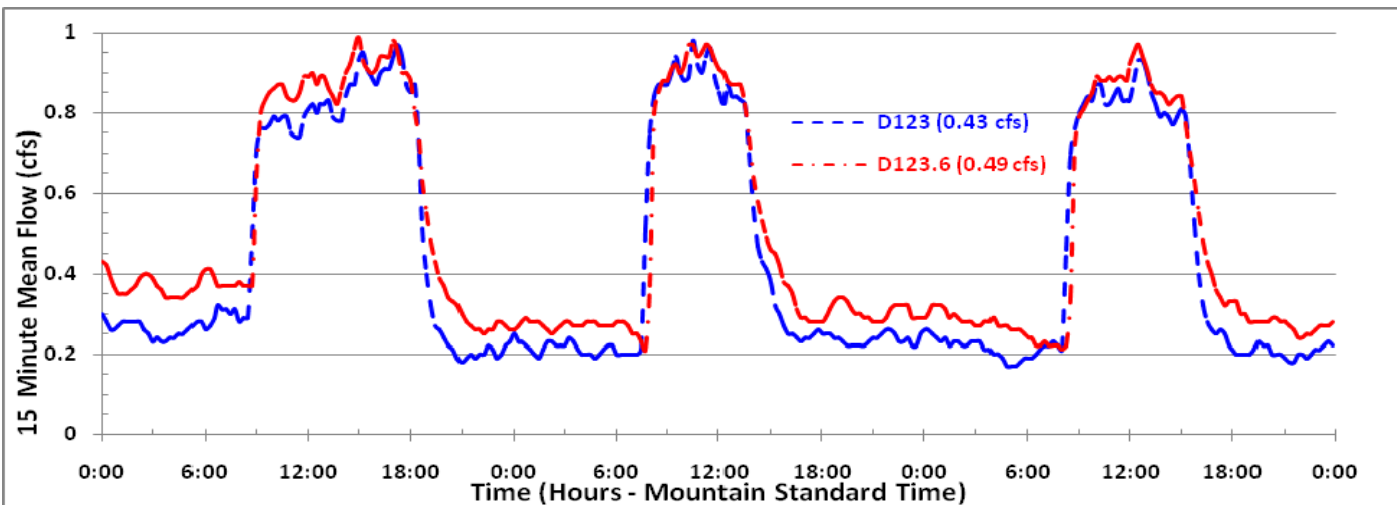
Figure C-1.0-2 Hydrographs from gaging stations D123 and D123.6 from April 21 to April 23, 2008, with time of D123.6 hydrograph shifted by 1.5 hr to better show relationship with D123; average daily discharge at gages shown in parentheses; average discharge from NPDES outfalls = 0.55 cfs for this period

Figure C-1.0-3 Hydrographs from gaging stations D123 and D123.6 from June 23 to June 28, 2008, with time of D123.6 hydrograph shifted by 1.5 hr to better show relationship with D123; average daily discharge at gages shown in parentheses; average discharge from NPDES outfalls = 0.61-0.62 cfs for this period
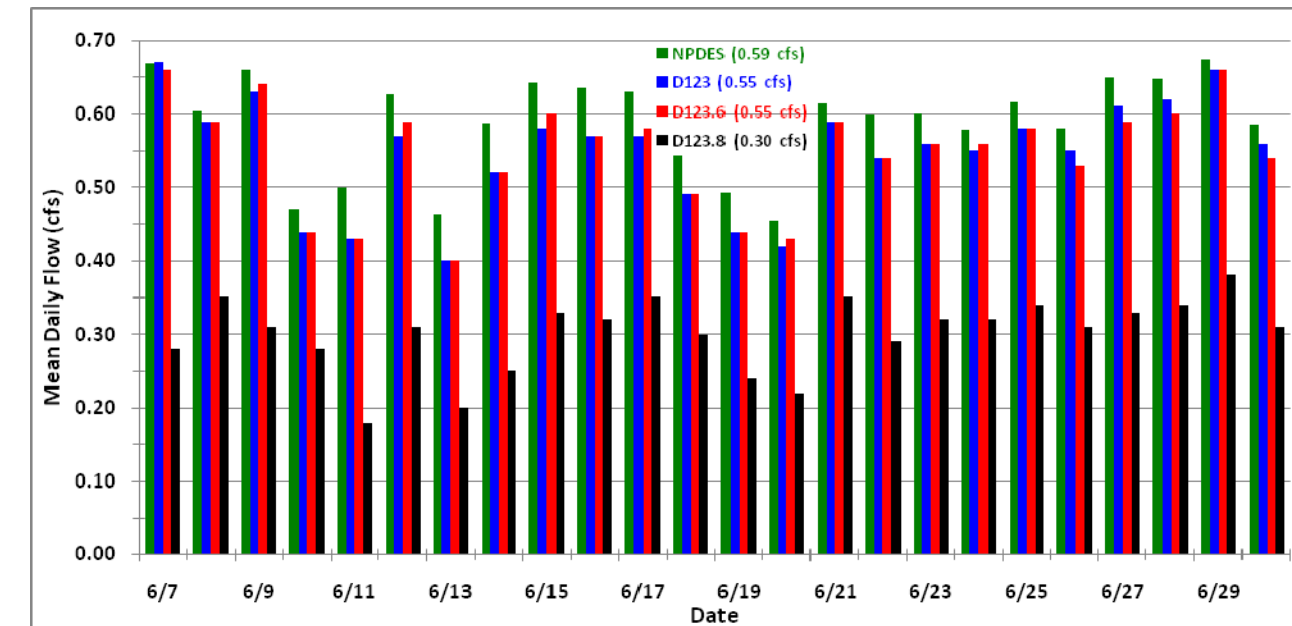
Figure C-1.0-4 Bar graphs showing mean daily flow for NPDES outfalls and gaging stations D123, D123.6, and D123.8 from June 7 to June 30, 2008, with average daily discharge shown in parentheses
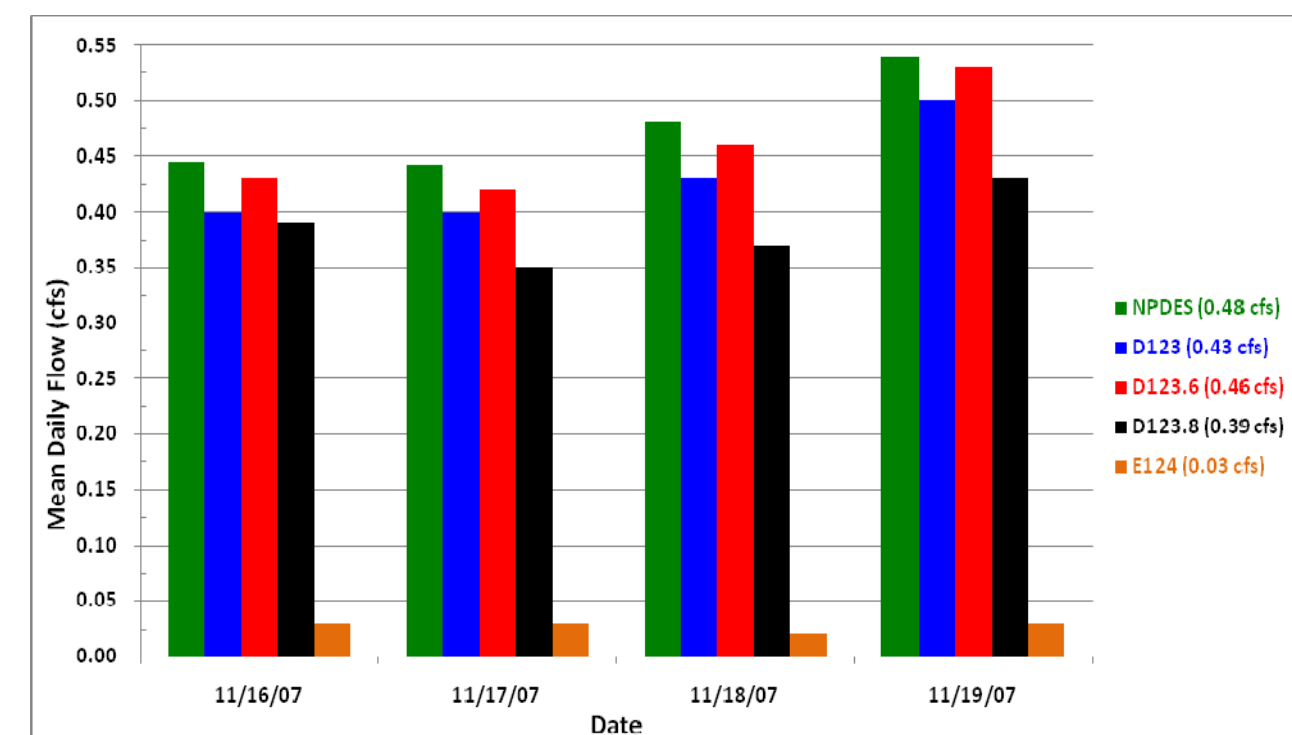
Figure C-1.0-5 Bar graphs showing mean daily flow for NPDES outfalls and gaging stations D123, D123.6, D123.8, and E124 from November 16 to November 19, 2007 (average daily discharge shown in parentheses)
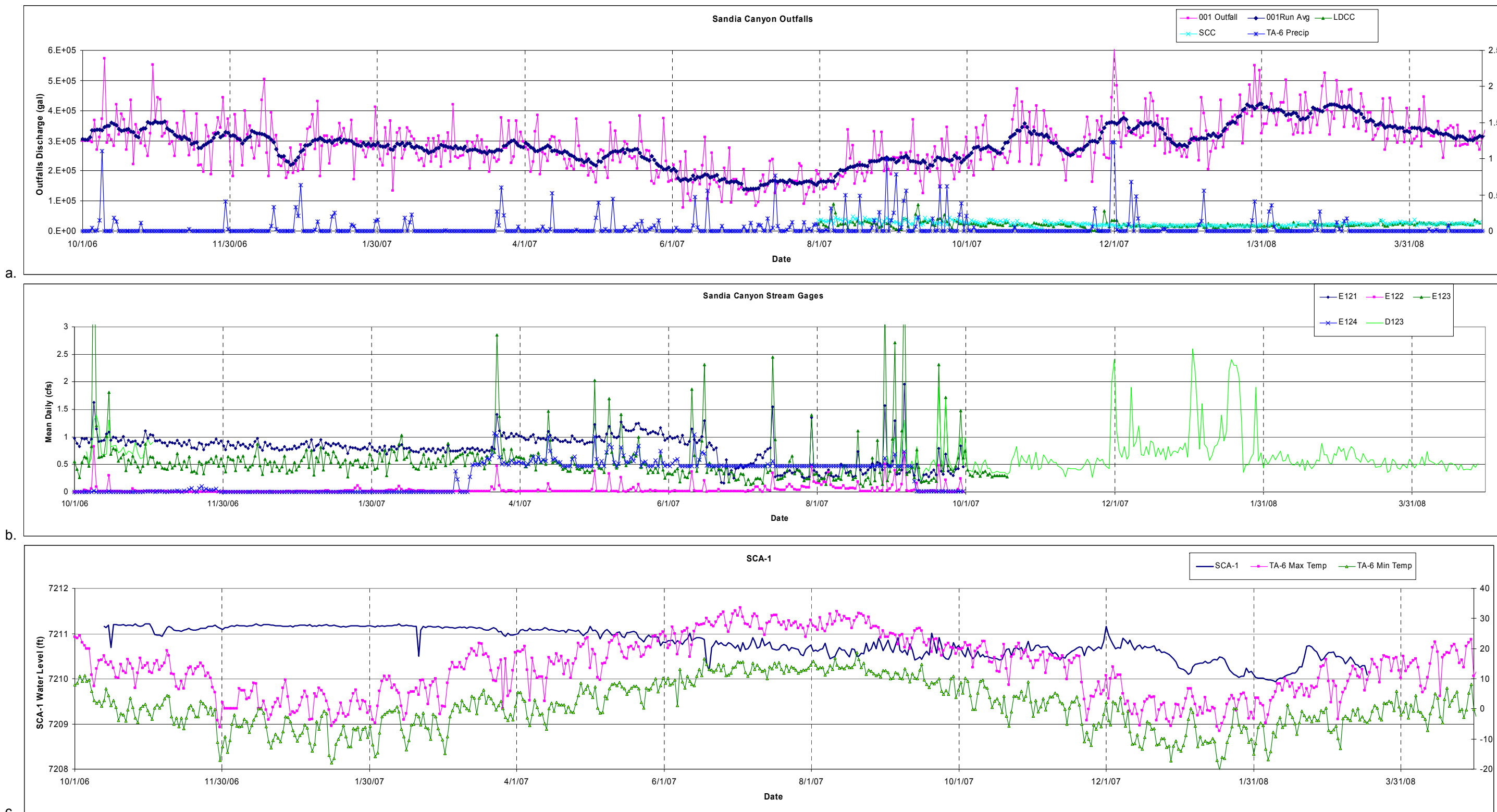
Figure C-2.0-1 Mean-daily alluvial water levels measured in wells SCA-1, SCA-2, SCA-3, and SCA-4 and piezometers SCP-1a,b,c and SCP-2a,b for the period of record, October 2006 to April 2008. Also shown are data for Sandia Canyon outfall volumes and stream gage, and TA-06 precipitation and temperature records

d.

e.

f.
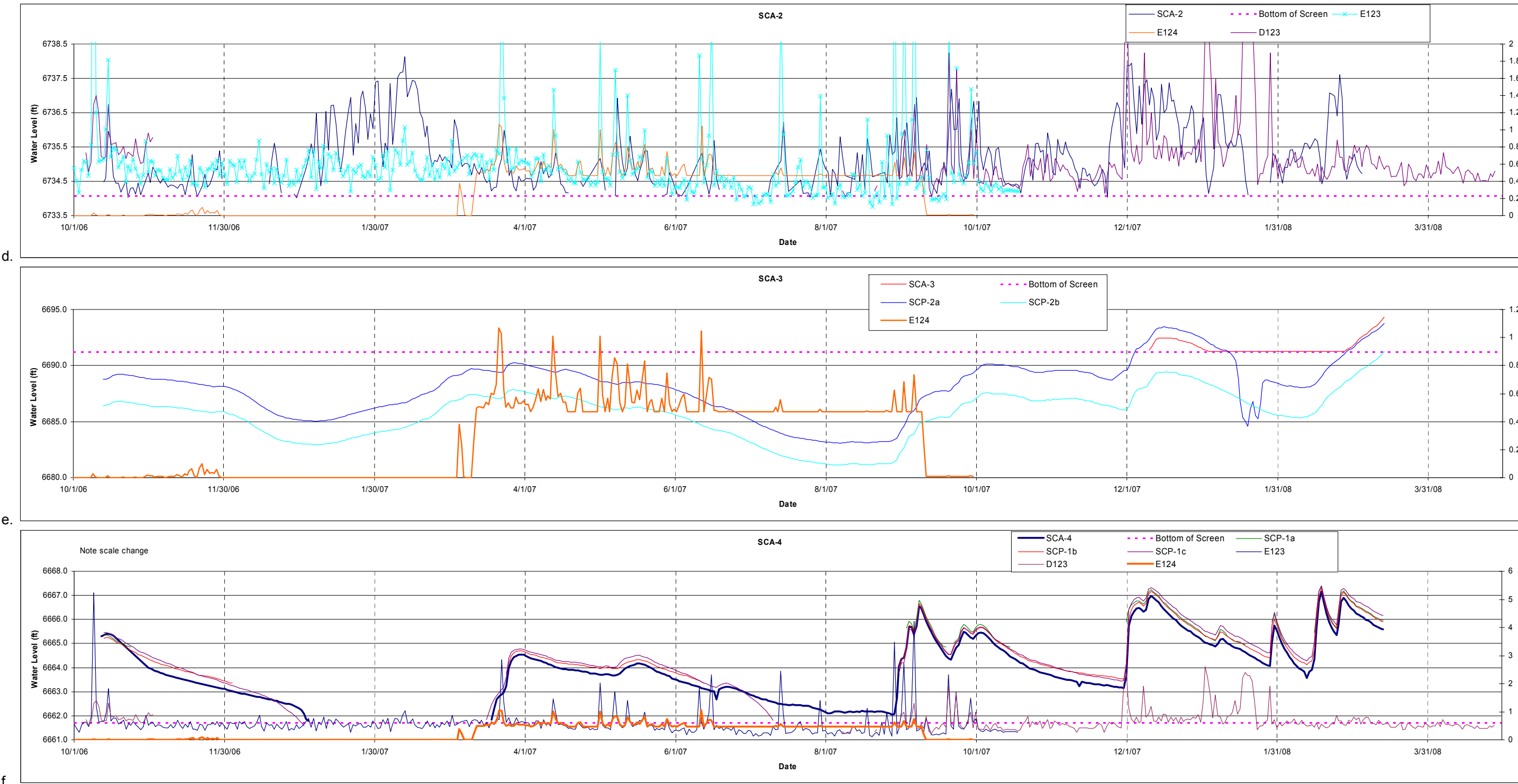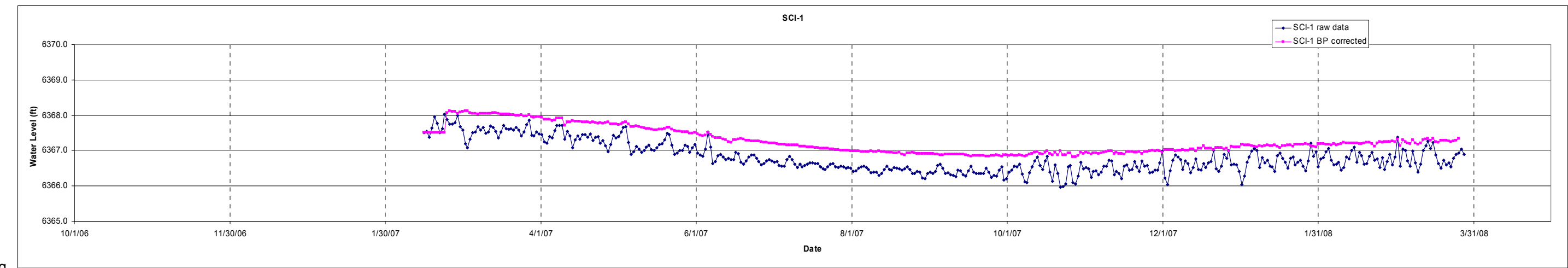
Figure C-2.0-1 (continued)   **Mean-daily alluvial water levels measured in wells SCA-1, SCA-2, SCA-3, and SCA-4 and piezometers SCP-1a,b,c and SCP-2a,b for the period of record, October 2006 to April 2008. Also shown are data for Sandia Canyon outfall volumes and stream gage, and TA-06 precipitation and temperature records**

g.

Figure C-2.0-1 (continued)   Mean-daily alluvial water levels measured in wells SCA-1, SCA-2, SCA-3, and SCA-4 and piezometers SCP-1a,b,c and SCP-2a,b for the period of record, October 2006 to April 2008. Also shown are data for Sandia Canyon outfall volumes and stream gage, and TA-06 precipitation and temperature records
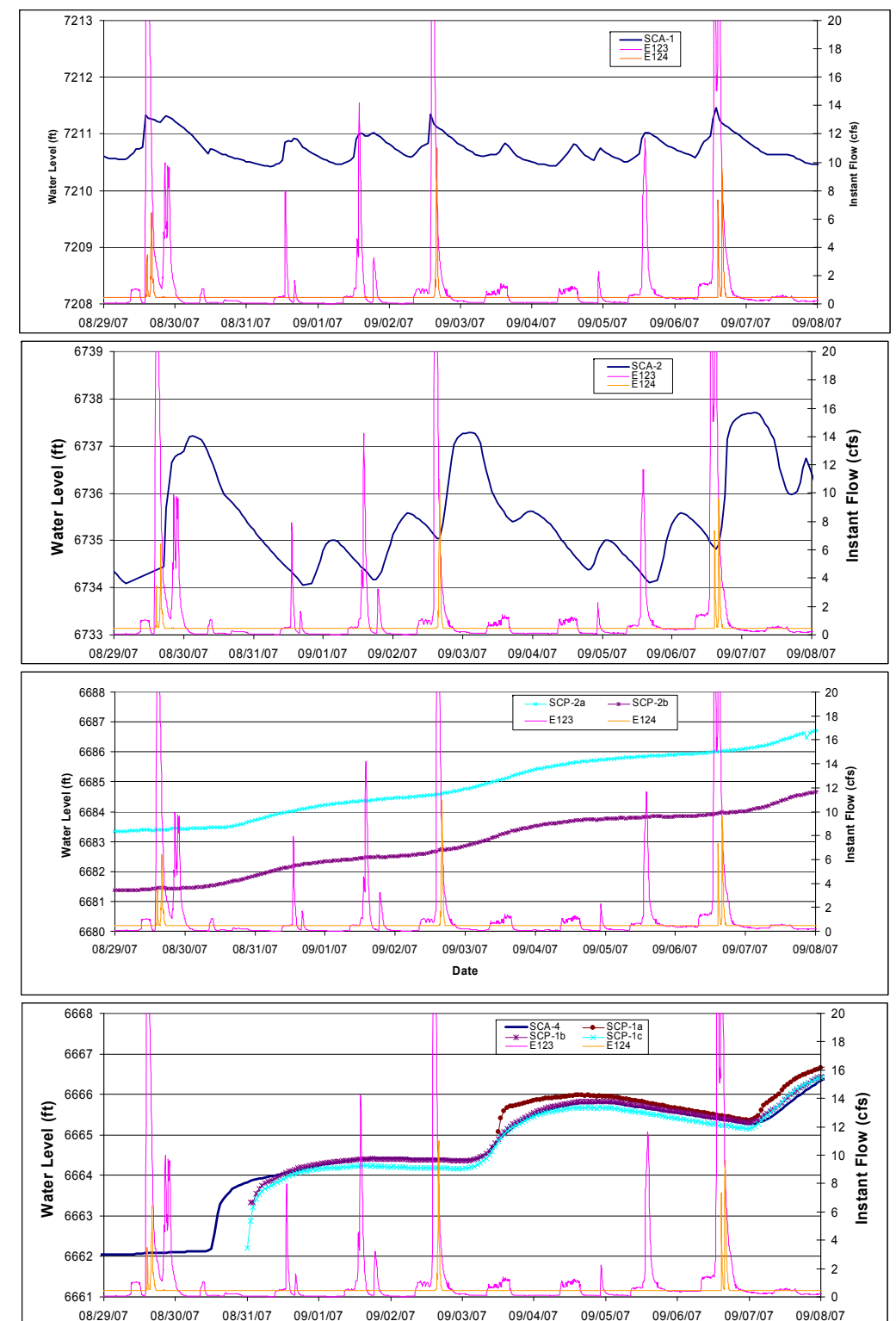
Figure C-2.0-2 Hourly alluvial water levels measured in wells SCA-1, SCA-2, SCA-3, and SCA-4 and piezometers SCP-1a,b,c and SCP-2a,b and 5-min gage data for gaging stations E123 and E124 for the period August 29, 2007, to September 8, 2007

Table C-1.0-1
Estimated Losses Between Outfalls and
Gaging Station D123.6 for Select Periods from July 2007 to June 2008

Period	Number of Days	Estimated Average Daily Discharge from Outfalls (cfs)	Estimated Average Daily Discharge at D123.6 (cfs)	Estimated Daily Loss to ET (cfs)[a]	Estimated Net Loss to Bedrock Between Outfalls and D123.6 (cfs)[b]	Equivalent Annual Loss Rate (acre-ft/yr)[c]
July and August 2007[d]	7	0.37	0.31	0.04	0.03	21
10/27/07 to 11/6/07	11	0.56	0.57	0.02	0	0
11/7/07 to 11/19/07	13	0.47	0.43	0.01	0.03	22
4/21/08 to 5/12/08	22	0.54	0.47	0.04	0.03	22
6/7/08 to 6//30/08	24	0.59	0.55	0.05	0	0
All	**77**	**0.53**[e]	**0.49**[e]	**0.04**[e]	**0.02**[e]	**12**[e]

[a] ET based on monthly evaporation pan data from Santa Fe (downloaded from http://weather.nmsu.edu/Pan_Evaporation/santa_fe_evap.htm) and assumption that ET is 70% of pan evaporation (LANL 2006, 094431, p. 11).

[b] Negative values replaced by zero.

[c] Daily loss extended to 365 d; average daily loss in cfs x 1.984 = average daily loss in acre-ft.

[d] Values for July and August 2007 from LANL 2007, 098938.

[e] Value is a weighted average, weighting value for each period by the number of days in that period.

Table C-1.0-2
NPDES Outfall Discharges into Upper Sandia Canyon and
Precipitation at TA-06, Water Years 2006 to 2008 (October 2005 to June 2008)

Month	Year	Monthly Discharge (gal.)	Monthly Discharge, (acre-ft)	Average Daily Discharge, (cfs)	Precipitation at TA-06 (in.)
October	2005	11,922,600	36.6	0.60	1.11
November	2005	10,482,000	32.2	0.54	0.07
December	2005	11,479,900	35.3	0.57	0.01
January	2006	12,809,200	39.3	0.64	0.15
February	2006	10,365,600	31.8	0.57	0.02
March	2006	12,524,000	38.4	0.62	0.63
April	2006	10,803,000	33.1	0.56	0.51
May	2006	11,203,400	34.4	0.56	0.22
June	2006	10,953,000	33.6	0.56	1.76
July	2006	11,897,800	36.5	0.59	2.26
August	2006	13,178,100	40.4	0.66	5.85
September	2006	11,211,000	34.4	0.56	1.36
October	2006	11,672,000	35.8	0.60	1.73
November	2006	11,196,200	34.4	0.56	0.47
December	2006	9,980,800	30.6	0.50	1.62
January	2007	11,264,700	34.6	0.56	1.06
February	2007	9,286,800	28.5	0.51	0.54
March	2007	10,427,200	32.0	0.52	1.23
April	2007	9,179,200	28.2	0.54	0.62
May	2007	9,430,100	28.9	0.47	1.70
June	2007	7,005,800	21.5	0.36	1.34
July	2007	6,839,600	21.0	0.34	1.93
August	2007	8,342,580	25.6	0.42	2.93
September	2007	8,827,320	27.1	0.46	4.35
October	2007	10,681,530	32.8	0.53	0.32
November	2007	9,926,770	30.5	0.51	1.61
December	2007	11,635,100	35.7	0.58	2.74
January	2008	12,182,030	37.4	0.61	1.39
February	2008	12,533,130	38.5	0.67	1.11
March	2008	13,070150	40.1	0.65	0.46
April	2008	11,074,950	34.0	0.57	0.13
May	2008	10,690,630	32.8	0.53	1.66
June	2008	10,842,500	33.3	0.56	0.04

Table C-1.0-3
Estimated Surface Water Losses Between Gaging
Stations D123.6 and D123.8 for Select Periods from July 2007 to June 2008

Period	Number of Days	Estimated Average Daily Discharge at D123.6 (cfs)	Estimated Average Daily Discharge at D123.8 (cfs)	Estimated Average Daily Surface Water Loss Between D123.6 and D123.8 (cfs)	Equivalent Annual Loss Rate (acre-ft/year)[a]
July and August 2007[b]	13	0.42	0.26	0.15	110
10/27/07 to 11/19/07	24	0.51	0.47	0.04	26
4/4/08 to 5/5/98	32	0.54	0.33	0.21	153
5/17/08 to 5/21/08	5	0.51	0.35	0.16	119
5/24/08 to 5/27/08	4	0.47	0.26	0.21	148
6/11/08 to 6/30/08	20	0.54	0.30	0.24	174
All	**98**	**0.51**[c]	**0.35**[c]	**0.16**[c]	**119**[c]

[a] Daily loss extended to 365 days; average daily loss in cfs x 1.984 = average daily loss in acre-ft.

[b] Values for July and August 2007 from LANL 2007, 098938.

[c] Value is a weighted average, weighting value for each period by the number of days in that period.

Table C-1.0-4
Approximate Surface Water Budget in
Upper Sandia Canyon from July 2007 to June 2008

Process and Area	Estimated Gain or Loss (acre-ft/yr)	Percent of Total
Discharges from Outfalls	389	75%
Runoff above E123	130	25%
ET in Wetland	−18	−3%
Deep Infiltration Beneath Wetland	−12	−2%
Deep Infiltration Between Wetland and D123.6	0	0%
Surface Water Loss Between D123.6 and D123.8	−119	−23%
Surface Water Loss Between D123.8 and E124	−334	−64%
Surface Water Loss Between E124 and E125	−36	−7%
Total	**0**	**0**

Appendix D

Chromium Isotope Investigation

D-1.0   INTRODUCTION

Samples of surface water in Mortandad and Sandia Canyons and groundwater beneath Sandia Canyon, Mortandad Canyon, and Cañada del Buey were collected and analyzed for stable isotopes of chromium (^{52}Cr and ^{53}Cr, δ^{53}Cr). Samples were collected per the "Addendum to the Work Plan for Sandia Canyon and Cañada del Buey, Revision 1" (LANL 2007, 095454, Table B-1) and a revision to the sampling plan presented in the recommendations section of the September 2007 "Fate and Transport Modeling Report for Chromium Contamination from Sandia Canyon" (LANL 2007, 098938). The purpose of this investigation, conducted by Los Alamos National Laboratory (the Laboratory), is to evaluate possible reduction of Cr(VI) to Cr(III) along surface water and groundwater flow paths. Stable isotopes of chromium may provide quantitative information on biological and/or chemical conditions that control the extent of Cr(VI) reduction in surface and subsurface environments. Key reductants include solid organic matter (SOM) (especially abundant in the Sandia Canyon wetland) and ferrous iron [Fe(II)] concentrated in reactive minerals and glass, which is particularly abundant at depth within the Cerros del Rio basalt. Analyses of δ^{53}Cr in water samples should advance the geochemical conceptual model for chromium, particularly with regard to where in the system reduction of Cr(VI) may be occurring.

D-2.0   CHROMIUM ISOTOPE FRACTIONATION

Chromium has four stable isotopes: ^{50}Cr (4.35%), ^{52}Cr (83.8%), ^{53}Cr (9.50%), and ^{54}Cr (2.37%). Ratios of ^{53}Cr to ^{52}Cr have been demonstrated to reflect the degree of reduction of dissolved Cr(VI) to Cr(III) along surface water and groundwater flow paths (Ellis et al. 2002, 098081; Kitchen et al. 2004, 098088; Sikora et al. 2004, 098101). During both abiotic and biotic reduction of Cr(VI) to Cr(III), a kinetic isotope effect occurs in which the lighter isotope, ^{52}Cr, reacts preferentially, leaving the remaining dissolved Cr(VI) enriched in the heavier isotope, ^{53}Cr.

This process is represented mathematically as follows (Ellis et al. 2002, 098081):

Equation D-1

$$\delta^{53}Cr=[(\delta^{53}Cr_{ini} + 10^3)f^{(\alpha-1)}]-10^3$$

where δ^{53}Cr is the isotopic composition of residual dissolved Cr(VI) and f is the fraction of Cr(VI) remaining.

In Equation D-1, alpha (α) is the instantaneous fractionation factor. A range of environmentally relevant values from approximately 0.9957 (i.e., an instantaneous fractionation of 4.3‰ resulting from microbial reduction [Sikora et al. 2008, 102411]) to 0.9975 (i.e., an instantaneous fractionation of 2.5‰, abiotic reduction [Ellis et al. 2002, 098081; Kitchen et al. 2004, 098088; Johnson and Berna 2008, 102464]) have been observed. Fractionation factors do not appear to vary with Cr(VI) concentration, at least in the case of microbial reduction (Sikora et al. 2008, 102411). The isotopic fractionation factor for oxidation of solid Cr(III) to Cr(VI) is considered to be negligible (Ellis et al. 2004, 098086). Chromium isotopes are not fractionated significantly by adsorption processes (Ellis et al. 2004, 098086).

The initial chromium isotope composition of the dissolved chromate before reduction is δ^{53}Cr$_{ini}$. Chromite ores, from which industrial chromium is derived, have an average δ^{53}Cr of -0.082 ± 0.058 ‰ (2 σ) (Schoenberg et al. 2008, 102413). Because of the high temperature and efficiency of extraction, industrial chromium should have very similar δ^{53}Cr values (Ellis et al. 2002, 098081; Schoenberg et al. 2008, 102413). The highest values measured for industrial reagent chromium is 0.37 ‰ (Ellis et al. 2002, 098081). An initial value for potassium dichromate released from cooling towers of 0.3 ‰ is assumed. If

actual values were lower (i.e., closer to that of chromite ores), the calculated values for reduction will be slightly underestimated (i.e., assuming a source value of 0.3 ‰ is a conservative assumption). The chromium isotopic composition of background chromate should be equal to that of chromium-bearing minerals (i.e., ~0 ‰, Schoenberg et al. 2008, 102413) as weathering of solid Cr(III) does not appear to fractionate chromium (Ellis et al. 2004, 098086). A value of 0.3 ‰ for $\delta^{53}Cr_{ini}$ of both contaminant and background chromate is used because it is not always known if contaminant or background chromate is being measured, or a mixture of the two. In addition, 0.3 ‰ is within the 2 σ analytical precision of zero ‰ and represents a conservative assumption for calculated fraction Cr(VI) reduced. Before any reduction of Cr(VI), f will be equal to 0, and $\delta^{53}Cr$ will be equal to $\delta^{53}Cr_{ini}$.

It has been hypothesized that for naturally derived Cr(VI) some reduction, and resultant enrichment of ^{53}Cr of Cr(VI), may occur on mineral surfaces subsequent to weathering and oxidation of Cr(III) from chromium-bearing minerals to Cr(VI) but before Cr(VI) is released to solution (Izbicki et al. 2008, 102412). This would require that some portion of Cr(VI) produced during weathering and oxidation diffuse back to reducing zones associated with ferrous iron, for example (Johnson 2008, 102461). It is not known if this effect occurs in the Laboratory groundwater system. If this process does occur, the resulting enriched values could be taken as $\delta^{53}Cr_{ini}$. However, this approach was not taken. It is likely, given the oxidizing nature of groundwater beneath the Pajarito Plateau, that most observed reduction of Cr(VI) occurs on mineral surfaces containing ferrous iron (see section D-6.5) as opposed to reduction because dissolved oxygen in groundwater is lacking. It will be difficult, therefore, to distinguish reduction that occurred immediately following weathering-related production of Cr(VI) from subsequent reduction of Cr(VI) on mineral surfaces elsewhere along the groundwater flow path. Moreover, any initial reduction on mineral grains is likely to be highly heterogeneous, making it impossible to assign a single value for $\delta^{53}Cr_{ini}$ for background Cr(VI). In addition, assuming initial reduction on mineral grains occurs, background chromate concentrations would be higher in the absence of this process, so it seems reasonable to use a value for $\delta^{53}Cr_{ini}$ of approximately zero ‰, and to count this initial reduction as part of the calculated fraction Cr(VI) reduced.

The delta (δ) notation is as follows:

Equation D-2

$$\delta^{53}Cr = \{[(^{53}Cr/^{52}Cr_{sample})/(^{53}Cr/^{52}Cr_{standard})-1)]*1000\}$$

in units of per mil (‰) or parts per thousand.

The standard used in this study was National Institute of Standards and Technology (NIST) SRM 979, a chromium nitrate compound sold by the NIST as an isotopic standard.

D-3.0   SAMPLE COLLECTION AND PRESERVATION

Surface water samples and groundwater samples were collected in 1-L high-density polypropylene bottles for chromium isotope analyses. The nonacidified samples were filtered through 0.45-micrometer membranes. The chromium isotope analyses were conducted at the University of Illinois Urbana-Champaign (UIUC), Department of Geology.

D-4.0   ANALYTICAL METHODOLOGY

The sample preparation process consisted of purifying chromium and removing interfering elements such as titanium (Ti), vanadium (V), and iron. A measured amount of the $^{50}Cr+^{54}Cr$ double isotope spike

solution (see section D-4.1) was added and thoroughly mixed with an aliquot of the water. Chromium(VI) was separated from the sample matrix and purified using an anion exchange process. Chromium(VI) was adsorbed onto an anion exchange resin, sample matrix species were rinsed from the resin with hydrochloric acid, the chromium was converted to Cr(III) form, and Cr(III) was eluted from the resin.

With most of the samples containing less than 30 μg/L of chromium, some iron was not fully separated from chromium in the purification process described above. It is possible that the iron occurred as complex ions bound to dissolved and suspended organic species. Excessive iron was removed using a second ion exchange step in which iron was adsorbed onto anion exchange resin as $FeCl_4^-$ and chromium passed through.

D-4.1 Double Isotope Spike

Multicollector inductively coupled plasma mass spectrometer (ICPMS) instruments impart a large bias to the measured ratios; measured $^{53}Cr/^{52}Cr$ ratios differ from true ratios by approximately 3%. This measurement bias was determined precisely and corrected for using the double isotope spike approach. A solution containing ^{50}Cr and ^{54}Cr in a known ratio was added to each sample and mixed thoroughly with it. When the sample-spike mixture was analyzed, the measured $^{50}Cr/^{54}Cr$ ratio was used to determine the measurement bias. The measured $^{53}Cr/^{52}Cr$ was then corrected for this bias. Any isotopic fractionation that occurred during sample preparation after addition of the double spike was corrected for as part of the overall bias. More detail about the double spike approach can be found in recent publications (Beard and Johnson 1999, 098076; Johnson et al. 1999, 098087) and references therein.

D-4.2 Mass Spectrometry

Isotopic ratios for chromium were determined using a Nu Plasma HR multicollector ICPMS. The argon-(Ar-) based inductively coupled plasma generates ArC+, ArN+ and ArO+ ions with masses close to, but slightly greater than, those of ^{52}Cr, ^{53}Cr, ^{54}Cr, and ^{56}Fe. The instrument is operated in a high-resolution mode that allows measurement of ^{50}Cr, ^{52}Cr, ^{53}Cr, ^{54}Cr, and ^{56}Fe while excluding ArC+, ArN+, and ArO+. Interferences from ^{54}Fe, ^{50}Ti, and ^{50}V were corrected for by measuring ^{56}Fe, ^{49}Ti, and ^{51}V; calculating the ^{54}Fe, ^{50}Ti, and ^{50}V interference intensities using natural $^{54}Fe/^{56}Fe$, $^{50}Ti/^{49}Ti$, and $^{50}V/^{51}V$ ratios, and subtracting the calculated interference intensities from the measured chromium isotope intensities. A thoroughly tested calculation routine was used to correct for interferences, determine the instrumental bias, mathematically subtract the double spike chromium from the sample chromium, and calculate a final $^{53}Cr/^{52}Cr$ result.

Because the measured changes in the $^{53}Cr/^{52}Cr$ ratios are small (<1%), the isotopic composition is reported in δ notation. $\delta^{53}Cr$ expresses the parts-per-thousand (per mil or ‰) deviation of a measured isotope ratio relative to the NIST SRM 979 standard (see Equation D-2).

D-4.3 Quality Control and Uncertainty of Method

Standard solutions were run through the sample preparation procedure along with batches of samples. The results from these standards all differed from unprocessed standards by less than 0.1‰ and show no statistically significant offset from unprocessed standards. Field duplicate samples were analyzed to assess precision. Offsets between duplicate pairs was always less than 0.2‰, except for a surface water sample from location E123.4, which ran at lower precision (2 σ precision of 0.5 ‰) because of the high concentrations of dissolved organics (Table D-4.3-1). The root-mean-square difference for all the pairs of samples having precision of less than 0.2 ‰ was 0.09 ‰. Between sampling rounds, $\delta^{53}Cr$ also appears

to be quite consistent, particularly for regional aquifer locations (for example, data from R-11 and R-28 (Table D-4.3-1)).

Recent (2007) water-quality samples collected from the regional aquifer locations listed in Table D-4.3-1 were evaluated for residual effects from drilling following the general protocol described in the Well Screen Analysis Report, Revision 2 (LANL 2007, 096330). These evaluations concluded those wells retained for sampling are fully capable of providing reliable and representative data for chromium (LANL 2007, 099128, Table B-1; LANL 2008, 101897, Table F-2.0-1). The possible exception is R-14 screen 1, in which chromium concentrations could potentially be biased low because of slightly reducing conditions; however, it is also possible this condition is representative of site conditions. If residual drilling fluid effects were present in a screened interval and resulted in reducing conditions, it is possible that Cr(VI) reduction unrelated to surrounding aquifer geochemical conditions could occur. For this reason, screens 1 and 2 from well R-33 were sampled for only one round, although it should be noted that δ^{53}Cr of Cr(VI) from these screens was similar to other regional aquifer locations (Table D-4.3-1). It is unlikely that residual drilling fluid effects have impacted the sampled wells, based on relatively oxidizing conditions occurring within perched intermediate zones and the regional aquifer. Concentrations of oxidized forms of nitrogen (nitrate), iron (ferric iron), sulfur (sulfate), and total inorganic carbon (bicarbonate) dominate over reduced forms of these solutes. Measurable dissolved oxygen and positive noncorrected oxidation-reduction potential (ORP) measurements recorded during sampling also provide evidence for oxidizing groundwater not being impacted by residual drilling fluid effects. Fractionated or more positive δ^{53}Cr values measured in groundwater samples collected from perched intermediate zones and the regional aquifer probably result from naturally occurring reductants, including ferrous iron and/or organic-rich treated sewage effluent.

Surface water and groundwater samples are typically filtered through 0.45-micrometer membranes to determine dissolved concentrations of major ions and trace elements. It has been established, however, the colloidal material smaller than 0.45 micrometer occurs in natural systems, potentially biasing concentrations of solutes or dissolved species. Three surface water samples were collected from the Sandia wetland and separately filtered through 0.02, 0.22, and 0.45-micrometer membranes before total chromium analysis to address the potential occurrence of colloids. Sample ID EF070800PSFS60 contained 0.017, 0.020, and 0.012 parts per million (ppm) of total chromium filtered through 0.45, 0.22, and 0.02-micrometer membranes, respectively. Sample ID EF070800P12301 contained 0.015, 0.018, and 0.012 ppm of total chromium filtered through 0.45, 0.22, and 0.02-micrometer membranes, respectively. Total filtered chromium concentrations are approximately 33% to 40% lower in these two samples when filtered through 0.02-micrometer membranes as opposed to a 0.45-micrometer membrane, suggesting some of the chromium present in the 0.02- to 0.22-micrometer range could be colloidal Cr(III) [in the form of $Cr(OH)_3$] or soluble Cr(III)-humate-fulvate complexes most likely present in organic-bearing surface water within and downstream of the Sandia wetland. Sample ID EF070800PMSC60 contained 0.023, 0.022, and 0.025 ppm of total chromium filtered through 0.45-, 0.22-, and 0.02-micrometer membranes, respectively. Concentration distributions of total chromium in this sample suggest that colloidal material is not present to a significant extent.

Cr(III) cationic complexes are not anticipated to affect determination of δ^{53}Cr of Cr(VI) because these complexes would have to bind to the anion exchange resin-like Cr(VI) and then not get dissolved and flushed from the column before Cr(VI) is extracted (Johnson 2008, 102459). As a future check, aliquots of groundwater samples from two locations will be separately filtered through 0.45- and 0.02-micrometer membranes, and the δ^{53}Cr values will be compared. In addition, because of a lack of Cr(VI) recovery following the Cr(VI) extraction procedure at UIUC from a sample collected from R-35a (GWR35a-08-8632; Table D-4.3-2; section D-6.4) that had a total dissolved chromium value of 5.9 μg/L, the potential for loss of Cr(VI) during storage is being investigated. All samples from the May 2008 sampling round will

have Cr(VI) concentrations determined within 24 hr of sampling and then again immediately before isotopic analysis. Sample CASA-08-11172 from well R-36 had a Cr(VI) concentration measured at the Laboratory within 24 hr of sampling of 5 µg/L. This same sample, measured at UIUC yielded a Cr(VI) concentration of 4.9 µg/L (Table D-4.3-1). These values are identical within analytical error, suggesting no loss of Cr(VI) during storage. It should further be noted that UIUC has found δ^{53}Cr of Cr(VI) to be stable during storage for several years (Johnson 2008, 102460).

D-5.0   PROOF OF CONCEPT

Initial samples collected for chromium stable isotope analyses were taken in February, March, and August 2007. Data were evaluated to determine whether isotopic fractionation associated with reduction of Cr(VI) to Cr(III) was evident in surface water and groundwater samples. Based on results from these initial scoping analyses, isotopic fractionation was observed, suggesting that chromium isotope analysis could be a viable tool for quantifying reduction of Cr(VI). Initial scoping analyses also indicated that several surface water and alluvial well locations proposed in the "Addendum to the Work Plan for Sandia Canyon and Cañada del Buey, Revision 1" (LANL 2007, 095454) were not amenable to chromium isotope measurement because of the high concentrations of dissolved organic matter and/or iron, coupled with low concentrations of Cr(VI) (Tables D-4.3-2).

Additional analytical results for chromium isotopes will be presented in the Sandia Canyon investigation report, to be released in December 2008.

D-6.0   RESULTS AND DISCUSSION

The analytical results provided in Table D-4.3-1 are listed by watershed, generally organized from upgradient to downgradient along the flow path within each aquifer zone. The fraction of Cr(VI) reduced versus δ^{53}Cr values is shown in Figure D-6.0-1 and provided in Table D-4.3-1. All values for fraction Cr(VI) reduced presented herein assume a fractionation factor of 3.5 ‰ (i.e., an alpha of 0.9965).

D-6.1   Sources of Uncertainty in Interpreting δ^{53}Cr Data

In addition to uncertainty associated with isotopic fractionation factors and the chromium isotopic composition of source potassium dichromate, sources of uncertainty in *interpreting* the calculated fraction of Cr(VI) reduced from δ^{53}Cr data include (1) the relative position of a sampling location within a plume (i.e., center of plume versus margins), and (2) mixing of water with different chromium isotopic compositions related to differing amounts of Cr(VI) reduction.

It is expected that chromium isotopic enrichment will be highest where the supply of reductants [e.g., Fe(II) and dissolved organic carbon] is highest relative to the mass of Cr(VI) available for reduction. The lateral and leading edges of a plume, therefore, are expected to have the highest δ^{53}Cr values, whereas the core of the plume, where Cr(VI) concentrations are highest, may show the lowest δ^{53}Cr values. In the core of a plume, reductants can more easily be overwhelmed by elevated concentrations of oxidants and Cr(VI).The trailing edge of a plume is expected to have lower δ^{53}Cr values relative to the leading edge if available reductants have been quantitatively consumed as the plume migrates. For example, little enrichment would be expected as the trailing edge of a plume moves past a given location if available reactive Fe(II) and/or dissolved organic carbon has been previously consumed through reaction with Cr(VI). This potential spatial heterogeneity within a plume makes interpretation of chromium isotope results more difficult in terms of defining discrete pathways. If sampling locations were located right along the primary axis of a plume and if reductants were largely consumed during plume migration,

downgradient locations within a discrete plume would have progressively enriched δ^{53}Cr values. Because these conditions may often not be met, it is best not to compare δ^{53}Cr values between locations to define discrete pathways, particularly within a complex, heterogeneous subsurface system such as that found at the Laboratory. Rather, δ^{53}Cr measurements can be used to help determine where overall in the system Cr(VI) reduction is occurring and which reductants promote transformation of Cr(VI) to Cr(III). It should be emphasized that a single δ^{53}Cr value only yields the total amount of reduction that occurred *somewhere* along the upgradient flow path. Measurements at different locations are needed to determine where in the system reduction actually occurs.

A mixed plume consisting of converging groundwater pathways derived from either one source or from multiple sources will have an intermediate δ^{53}Cr value, and the calculated fraction of Cr(VI) reduced will be intermediate to the actual value for both end members. There will always be some mixing between contaminant and background Cr(VI). For locations like R-28 (~400 μg/L) where chromate concentrations are 2 orders of magnitude above background, mixing with background will have little effect on the calculated fraction of Cr(VI) reduced. At locations only slightly elevated above background for Cr(VI), however, the effect of mixing on calculated values could be significant. The isotopic composition of background Cr(VI) in the Laboratory groundwater is poorly defined. Wells R-1, R-10, and R-16r are representative of background chromate, suggesting that naturally occurring δ^{53}Cr (ranging from 0.68 to 1.37 ‰ at these wells) has similar δ^{53}Cr values relative to most locations associated with chromate contamination (Table D-4.3-1). Natural chromate δ^{53}Cr values of up to 5.1 ‰ have been observed in alluvial aquifers of the Mojave Desert in California (Izbicki et al. 2008, 102412). It could be argued that background chromate may be expected to have higher δ^{53}Cr because of lower initial Cr(VI) concentrations relative to potential supply of reductants. Well R-35a is possibly an example of such a location. Total dissolved Cr concentrations are in the background range for the regional aquifer at this well, while the initial δ^{53}Cr value is high (3.93 ‰; Table D-4.3-1). It should be noted, however, that assuming all of the Cr(VI) at R-35a is natural, and the initial δ^{53}Cr is representative, the initial natural concentration of Cr(VI) before reduction in the groundwater system would have been approximately 17 μg/L, based on the calculated fraction of Cr(VI) reduced [this calculation assumes no initial reduction of Cr(VI) on mineral grains subsequent to weathering/oxidation but before release]. Background concentrations of this order of magnitude have not been measured in groundwater at the Laboratory. At R-35a, δ^{53}Cr of Cr(VI) has decreased in the most recent sampling round reported here (Table D-4.3-1), suggesting that δ^{53}Cr values may not have stabilized at this location.

D-6.2 Surface Water and Alluvial Aquifer

Surface water and alluvial groundwater within Mortandad Canyon were generally not amenable to δ^{53}Cr determinations because of the high concentrations of organic compounds and/or colloidal iron and the low concentrations of Cr(VI). A single δ^{53}Cr value from alluvial well MCO-7.5 yielded a fraction Cr(VI) reduced of 0.28, suggesting that some reduction can occur in the surface water and/or alluvial systems. Potential reductants present in alluvial groundwater include dissolved organic carbon in the form of humic and fulvic acids and dissolved organic nitrogen in the form of amino acids and total Kjeldahl nitrogen.

Surface water samples collected within Sandia Canyon have fractions of Cr(VI) reduced ranging from zero to 0.31. Two possibilities exist that could explain the fact that δ^{53}Cr of Cr(VI) at E123.5, located approximately 3 km downstream of the Sandia wetland, has an essentially identical value (0.14 and 0.3 ‰; Table D-4.3-1) to the presumed isotopic composition of source potassium dichromate (0.3 ‰), and therefore a calculated fraction Cr(VI) reduced of zero. It is possible, however unlikely, that Cr(VI) in this water sample escaped reduction in the upstream Sandia wetland and its δ^{53}Cr value is identical to that of source potassium dichromate. This hypothesis suggests that no reduction of Cr(VI) occurred during storage within the Sandia wetland or other parts of the alluvial system in Sandia Canyon subsequent to

cessation of cooling tower Cr(VI) releases. The second possibility is that the Cr(VI) measured at this location results from reoxidation of Cr(III) within Sandia wetland sediments. The chromium isotopic composition of Cr(III) in the Sandia wetland is not known, but it could be equal to the source potassium dichromate, provided all Cr(VI) entering the wetland alluvial system was quantitatively reduced. Quantitative reduction is very likely given the large Cr(III) inventories (LANL 2007, 098127) and the prevalence of reducing conditions maintained by SOM concentrated within the wetland. It is also possible the δ^{53}Cr value for the wetland is lighter than the source isotopic composition, if only a portion of the Cr(VI) entering the alluvial system of the wetland was reduced. During Cr(VI) reduction, the light isotope (^{52}Cr) preferentially accumulates in the reduced form of Cr(III). Because oxidation of solid Cr(III) appears to be a nonfractionating process (Ellis et al. 2004, 098086), Cr(VI) derived from reoxidation of Cr(III) in the Sandia wetland would have a δ^{53}Cr value of less than or equal to 0.3 ‰. If Cr(III) reoxidized within the wetland is actually less than 0.3 ‰, then some subsequent reduction would have had to occur to bring the initial observed value at E123.5 back to 0.3 ‰, or some Cr(VI) would need to have been immediately rereduced following oxidation in the wetland (cf., Izbicki et al. 2008, 102412). Isotopic analysis of Cr(III) in wetland sediments could be performed to distinguish among these possibilities. It is not known why surface water locations farther upstream in Sandia Canyon have δ^{53}Cr values indicative of reduction of Cr(VI) to Cr(III) whereas E123.5 does not.

Both dissolved and solid organic carbon and Fe(II) are the most viable reductants concentrated in the surface water/alluvial systems of Sandia Canyon.

D-6.3 Intermediate-Depth Perched Groundwater

Samples collected from the intermediate-depth aquifers have among the lowest and the highest δ^{53}Cr values observed. Well SCI-1 in Sandia Canyon has δ^{53}Cr only slightly higher than source potassium dichromate. The same possibilities exist as presented above for surface water location E123.5, although the possibility that Cr(VI) discharged from the cooling tower essentially bypassed the Sandia wetland (in terms of chemical interaction) as surface flow, with subsequent storage in the vadose zone without reduction is a somewhat more plausible hypothesis. Well SCI-1 is completed above the Cerros del Rio basalt, whereas MCOI-5 in Mortandad Canyon is completed within the basalt. The fraction of Cr(VI) reduced for MCOI-5 is up to 0.53. Samples from the other Mortandad Canyon intermediate wells also have relatively high δ^{53}Cr (Table D-4.3-1). The isotopic difference between these two locations suggests that reduction occurs within the basalts, which is consistent with high ferrous iron contents. Chemical reduction of Cr(VI) by Fe(II) concentrated within the Cerros del Rio basalt and associated fracture fill is confirmed by x-ray absorption near edge structure (XANES) spectroscopic analysis conducted at Stanford University using crushed samples of Cerros del Rio basalt and chromate concentrations exceeding 1000 μg/L (Appendix K presents a more detailed discussion).

D-6.4 Regional Aquifer

With the exception of R-35a and R-33 screen 1, the regional aquifer wells in Sandia and Mortandad Canyons have δ^{53}Cr ranging from 0.9 ‰ to 1.37 ‰ or a fraction of Cr(VI) reduction of 0.16 to 0.24, respectively. These relatively low and consistent values suggest that most reduction occurs in the surface/alluvial system and in the vadose zone. R-28 is at the low end of the range for chromium reduction, which is not surprising given the high and relatively steady Cr(VI) concentrations observed at this well. This location is either close to the center of mass of a plume where the availability and reactivity of reductants are insufficient to reduce the Cr(VI) present, or is near a "drip point" from the vadose zone that is constantly supplying fresh chromate. In either case, the relatively constant δ^{53}Cr values over time at this location are consistent with a stable situation in terms of contaminant supply versus degradation,

dispersion, and dilution. The single δ^{53}Cr value measured to date at R-36 has a value of 0.94 ‰, essentially identical to that of R-28 but also within the range of background δ^{53}Cr of Cr(VI).

The highest δ^{53}Cr value in the present data set was found for an initial characterization sample at R-35a. As mentioned above, the possibility that this δ^{53}Cr value is not representative because of the unlikely possibility of reduction during storage is being investigated. During initial characterization sampling, this well had higher concentrations of suspended iron than any other regional aquifer well included as part of this study. The concentration of suspended iron is determined from subtracting the dissolved fraction of iron from total iron in the nonfiltered aliquot. This iron, however, is likely in the form of Fe(III) oxide-hydroxide, the stable form of iron under oxidizing conditions, which would not lead to reduction of Cr(VI) during sample storage. Assuming the high initial δ^{53}Cr at R-35a is representative, it would suggest a fraction of Cr(VI) reduced on the order of 0.64. Analytical results using XANES suggest that both Cr(III) and Cr(VI) are present in R-35a cuttings collected from 1060 to 1065 ft and experimentally exposed to a chromate solution, suggesting in situ reduction and precipitation of chromium might occur at this location in Santa Fe Group sediments. The initial sample was taken soon after well development; however, δ^{53}Cr values may be changing over time. The most recent value for δ^{53}Cr of Cr(VI) at this location is 2.1 ‰ (Table D-4.3-1). This latter value is similar to δ^{53}Cr of Cr(VI) from intermediate depth perched aquifers completed in the Cerros del Rio basalt. If δ^{53}Cr values stabilize at around 2 ‰ at R-35a, it might suggest reduction along the flow path to this well is greater in the overlying basalt than in Santa Fe Group sediments. Even if δ^{53}Cr at R-35a stabilizes, the chromium isotope values cannot be used to uniquely and independently distinguish whether Cr(VI) at R-35a, is natural or anthropogenic.

D-6.5 Sources and Types of Reductants

Ferrous iron present in aquifer material is hypothesized to be the most important naturally occurring reductant for removing Cr(VI) from groundwater at Los Alamos. Reduction of Cr(VI) by Fe(II) leads to the precipitation of insoluble $Cr(OH)_3$ under circumneutral pH conditions. Ferrous iron is concentrated in silicate minerals including biotite, amphiboles, and pyroxenes and silica glass present in the Cerros del Rio basalt, the Puye Formation, and the Santa Fe Group. Reduction of Cr(VI) to Cr(III) occurs as Fe(II) oxidizes to Fe(III) forming ferric hydroxide, a common alteration product of Fe(II)-bearing minerals. Figure D-6.5-1 shows δ^{53}Cr values versus concentrations of suspended iron [most likely present as Fe(III)] and total organic carbon in groundwater. Increasing concentrations of suspended iron correlate reasonably well with increasing δ^{53}Cr values ($p<0.001$), supporting the importance of oxidation-reduction processes involving iron and Cr(VI). While Fe(III) cannot lead to reduction of Cr(VI), much of the suspended iron was probably derived from oxidation of Fe(II) produced during weathering of the minerals mentioned above. Oxidation of Fe(II) to Fe(III) resulting in reduction of Cr(VI) to Cr(III) could explain the observed correlation. Figure D-6.5-1 suggests that total organic carbon is not an important reductant for Cr(VI) within perched intermediate groundwater and the regional aquifer.

D-7.0 SUMMARY

Surface water in Mortandad and Sandia Canyons and groundwater beneath Sandia and Mortandad Canyons and Cañada del Buey were analyzed for stable isotopes of chromium (δ^{53}Cr) to evaluate isotope fractionation resulting from Cr(VI) reduction. Based on analytical results, isotope fractionation of Cr(VI) is occurring to a varying degree within surface and subsurface environments. The greatest degree of Cr(VI) reduction is likely to occur under the following conditions:

1. where the dissolved mass of Cr(VI) is small relative to the available SOM and reactive Fe(II) in sediments and aquifer material, and

2. when groundwater-travel times are such that Cr(VI) remains in Fe(II)-bearing strata (e.g., the Cerros del Rio basalt) sufficiently long that a significant portion of the dissolved Cr(VI) pool can be reduced.

Chromium isotope variation, along with total dissolved-chromium-concentration data, may be used to define spatial variation of Cr(VI) reduction in contaminant plumes. High dissolved concentrations of chromium coupled with low levels of Cr(VI) reduction at R-28 are suggestive of a location near where chromium might be entering the regional aquifer. At that location, high chromium concentrations in groundwater overwhelm the ability of aquifer solids to reduce much of the Cr(VI).

The majority of water samples have δ^{53}Cr values indicative of approximately 15% to 30% reduction of Cr(VI) to Cr(III) (Figure D-6.0-1). While Cr(VI) reduction is relatively low at R-28, based on low δ^{53}Cr values near or at unity and concentrations of total dissolved Cr of approximately 400 μg/L, this location is clearly dominated by contaminant Cr(VI), demonstrating that some natural reduction of contaminant-derived Cr(VI) does occur. Comparison of results from MCOI-5 (completed in the Cerros del Rio basalt) and SCI-1 (completed in the Puye Formation overlying the Cerros del Rio basalt) demonstrate that reduction in Fe(II)-bearing basalts is important for natural reduction in the Laboratory groundwater system. Wetland and alluvial systems are also important in terms of natural reduction of Cr(VI), but the isotopic signal associated with these parts of the system is less clear. While observed reduction does not go to completion Cr(VI) reduction could still be important in attenuation of plume migration. Further evaluation of δ^{53}Cr data in terms of remedy selection will occur in the context of corrective measures evaluation investigations.

D-8.0 REFERENCES

The following list includes all documents cited in this appendix. Parenthetical information following each reference provides the author(s), publication date, and ER ID number. This information is also included in text citations. ER ID numbers are assigned by the Environmental Programs Directorate's Records Processing Facility (RPF) and are used to locate the document at the RPF and, where applicable, in the master reference set.

Copies of the master reference set are maintained at the NMED Hazardous Waste Bureau; the U.S. Department of Energy–Los Alamos Site Office; the U.S. Environmental Protection Agency, Region 6; and the Directorate. The set was developed to ensure that the administrative authority has all material needed to review this document, and it is updated with every document submitted to the administrative authority. Documents previously submitted to the administrative authority are not included.

Beard, B.L., and C.M. Johnson, 1999. "High Precision Iron Isotope Measurements of Terrestrial and Lunar Materials," *Geochimica et Cosmochimica Acta,* Vol. 63, 11/12, pp. 1653-1660. (Beard and Johnson 1999, 098076)

Ellis, A.S., T.M. Johnson, and T.D. Bullen, March 15, 2002. "Chromium Isotopes and the Fate of Hexavalent Chromium in the Environment," *Science,* Vol. 295, pp. 2060-2062. (Ellis et al. 2002, 098081)

Ellis, A.S., T.M. Johnson, and T.D. Bullen, 2004. "Using Chromium Stable Isotope Ratios to Quantify Cr(VI) Reduction: Lack of Sorption Effects," *Environmental Science & Technology,* Vol. 38, No. 13, pp. 3604-3607. (Ellis et al. 2004, 098086)

Izbicki, J.A., J.W. Ball, T.D. Bullen, and S.J. Sutley, 2008. "Chromium, Chromium Isotopes and Selected Trace Elements, Western Mojave Desert, USA," *Applied Geochemistry,* Vol. 23, pp. 1325–1352. (Izbicki et al. 2008, 102412)

Johnson, T., April 4, 2008. Re: Chromium isotope sample IDs. E-mail message to J. Heikoop (LANL) and J. Glessner from T. Johnson (University of Illinois), Urbana, Illinois. (Johnson 2008, 102459)

Johnson, T., June 17, 2008. Re: R-35a. E-mail message to J. Heikoop (LANL), J. Glessner, and P. Longmire (LANL) from T. Johnson (University of Illinois), Urbana, Illinois. (Johnson 2008, 102460)

Johnson, T., July 12, 2008. Re: need advice on report. E-mail message to J. Heikoop (LANL) and J. Glessner from T. Johnson (University of Illinois), Urbana, Illinois. (Johnson 2008, 102461)

Johnson, T.M., and E. Berna, 2008. "Cr Isotopes Reveal Progress of Natural Reduction of Contaminant Cr(VI) in a Groundwater System," *Goldschmidt Conference Abstracts,* p. A437. (Johnson and Berna 2008, 102464)

Johnson, T.M., M.J. Herbel, T.D. Bullen, and P.T. Zawislanski, 1999. "Selenium Isotope Ratios as Indicators of Selenium Sources and Oxyanion Reduction," *Geochimica et Cosmochimica Acta,* Vol. 63, No. 18, pp. 2775-2783. (Johnson et al. 1999, 098087)

Kitchen, J.W., T.M. Johnson, and T.D. Bullen, 2004. "Chromium Stable Isotope Fractionation During Abiotic Reduction of Hexavalent Chromium," *Eos Transactions, American Geophysical Union*, Vol. 85, No. 47, Fall Meeting Supplement, Abstract V51A-0519. (Kitchen et al. 2004, 098088)

LANL (Los Alamos National Laboratory), April 2007. "Addendum to the Work Plan for Sandia Canyon and Cañada del Buey, Revision 1," Los Alamos National Laboratory document LA-UR-07-2186, Los Alamos, New Mexico. (LANL 2007, 095454)

LANL (Los Alamos National Laboratory), May 2007. "Well Screen Analysis Report, Revision 2," Los Alamos National Laboratory document LA-UR-07-2852, Los Alamos, New Mexico. (LANL 2007, 096330)

LANL (Los Alamos National Laboratory), September 2007. "Fate and Transport Modeling Report for Chromium Contamination from Sandia Canyon," Los Alamos National Laboratory document LA-UR-07-6018, Los Alamos, New Mexico. (LANL 2007, 098938)

LANL (Los Alamos National Laboratory), September 2007. "Mortandad Canyon Groundwater Monitoring Well Network Evaluation, Revision 1," Los Alamos National Laboratory document LA-UR-07-6435, Los Alamos, New Mexico. (LANL 2007, 099128)

LANL (Los Alamos National Laboratory), September 2007. "Summary of Sandia Canyon Phase 1 Sediment Investigations," Los Alamos National Laboratory document LA-UR-07-6019, Los Alamos, New Mexico. (LANL 2007, 098127)

LANL (Los Alamos National Laboratory), May 2008. "2008 Interim Facility-Wide Groundwater Monitoring Plan," Los Alamos National Laboratory document LA-UR-08-3273, Los Alamos, New Mexico. (LANL 2008, 101897)

Schoenberg, R., S. Zink, M. Staubwasser, and F. von Blanckenburg, 2008. "The Stable Cr Isotope Inventory of Solid Earth Reservoirs Determined by Double Spike MC-ICP-MS," *Chemical Geology,* Vol. 249, pp. 294–306. (Schoenberg et al. 2008, 102413)

Sikora, E.R., T.M. Johnson, and T.D. Bullen, 2004. "Chromium Stable Isotope Fractionation During Bacterial Reduction of Hexavalent Chromium," *Eos Transactions, American Geophysical Union*, Vol. 85, No. 17, Joint Assembly Supplement, Abstract H43E-05. (Sikora et al. 2004, 098101)

Sikora, E.R., T.M. Johnson, and T.D. Bullen, 2008. "Microbial Mass-Dependent Fractionation of Chromium Isotopes," *Geochimica et Cosmochimica Acta,* Vol. 72, pp. 3631–3641. (Sikora et al. 2008, 102411)
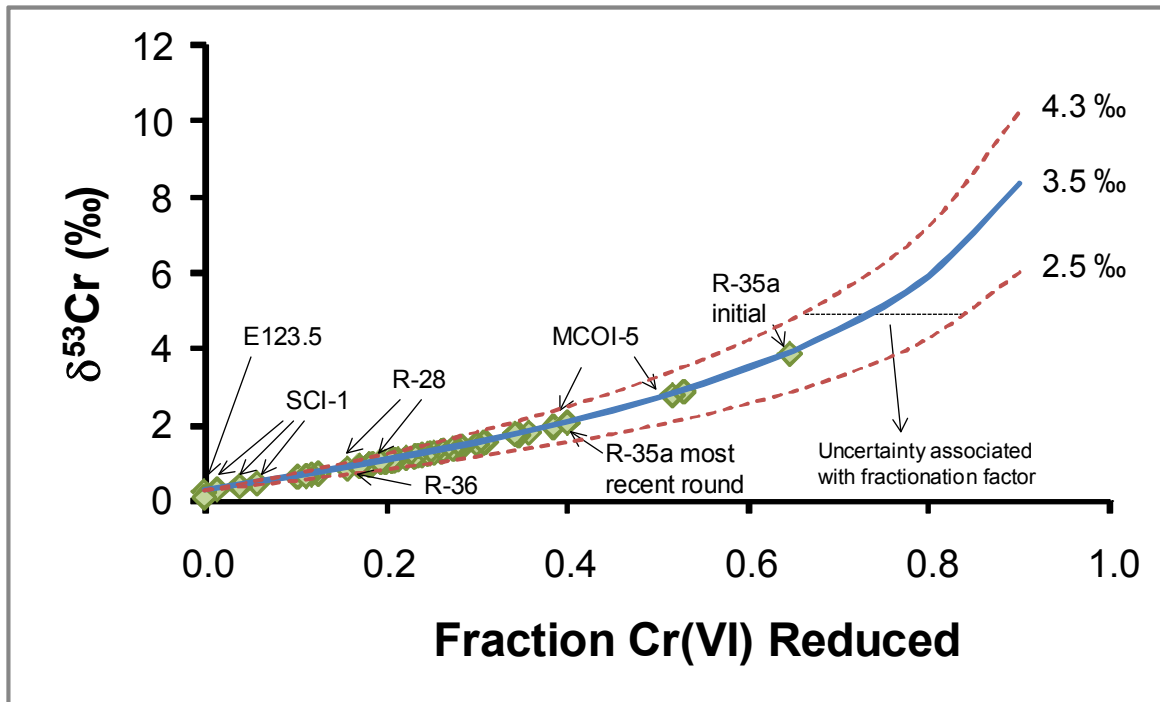
Figure D-6.0-1 Chromium isotope results from Sandia and Mortandad Canyons surface water and groundwater samples for a range of fractionation factors. The solid line is for a fractionation factor of 3.5‰ (i.e., an alpha of 0.9965), a typical fractionation factor approximately in the middle of the range of observed abiotic fractionation (Ellis et al. 2002, 098081).
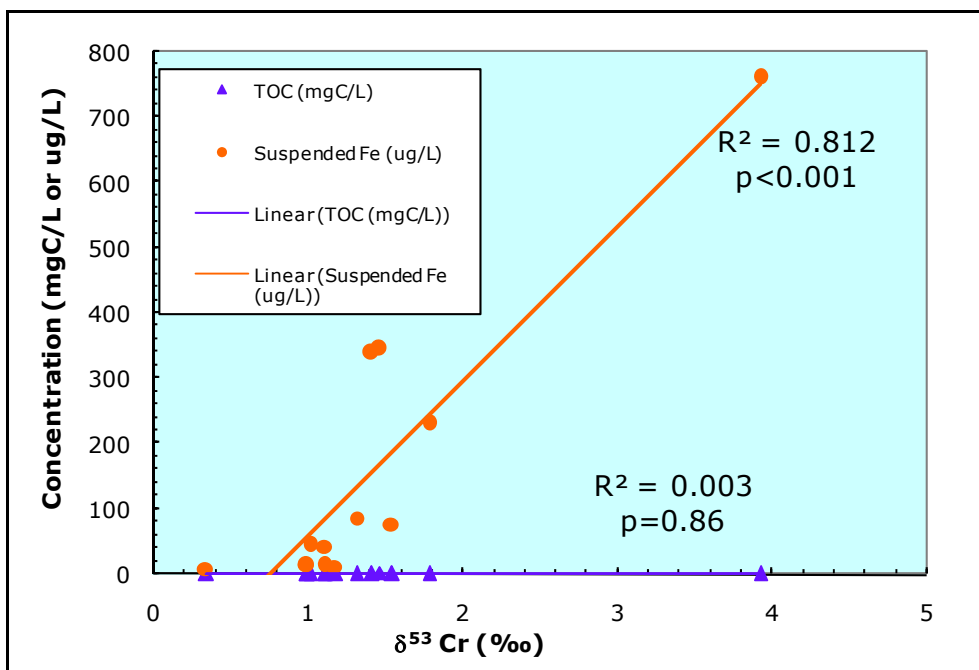
Figure D-6.5-1 δ^{53}Cr values versus concentrations of suspended iron [most likely present as Fe(III)] and total organic carbon in groundwater

Table D-4.3-1

Chromium Isotope Results from Sandia and Mortandad Canyons and Cañada del Buey Surface Water and Groundwater Samples

Canyon	Location	Aquifer Type	Sample ID	Collection Date	Total Filtered Cr (μg/L)	Cr(VI) (μg/L)	δ^{53}Cr ‰	Fraction Reduced
Mortandad	MCO-2	Alluvial	CAMO-08-10492	06-Feb-08	3.8	ND[a]	Pending[b]	ND
	MCO-7.5	Alluvial	UF070200G57M01	02-Mar-07	2.4	ND	1.47[c]	0.28
	MCO-7.5	Alluvial	CAMO-08-10484	06-Feb-08	10 (U)[d]	ND	Pending	ND
	MCO-7.5	Alluvial	CAMO-08-10486[e]	06-Feb-08	10 (U)	ND	Pending	ND
	MCOI-6	Intermediate	UF070200GMC601	26-Feb-07	29.4	ND	1.60	0.31
	MCOI-6	Intermediate	UF070200GMC620[e]	26-Feb-07	30.3	ND	1.44	0.28
	MCOI-6	Intermediate	CASA-08-7612	09-Nov-07	33.3	ND	1.55	0.30
	MCOI-6	Intermediate	CAMO-08-10425	22-Feb-08	34.2	ND	1.00	0.18
	MCOI-4	Intermediate	CAMO-08-8619	12-Nov-07	10.1	ND	1.85	0.36
	MCOI-5	Intermediate	UF070200GMC501	05-Mar-07	5 (U)	ND	2.93	0.53
	MCOI-5	Intermediate	CAMO-08-8625	12-Nov-07	1.1	ND	2.00[c]	0.38
	MCOI-5	Intermediate	CAMO-08-10422	13-Feb-08	4.6	ND	2.84[c]	0.52
	R-14 Screen 1	Regional	UF07020G14R101	01-Mar-07	2.4	ND	1.11[c]	0.21
	R-1	Regional	UF070200G01R01	07-Mar-07	4.6	ND	1.24	0.24
	R-1	Regional	CAMO-08-10453	22-Feb-08	7.2	ND	1.22	0.23
	R-1	Regional	CAMO-08-10455[e]	22-Feb-08	7.2	ND	1.13	0.21
	R-33 Screen 1	Regional	UF07020G33R101	13-Mar-07	NA	ND	1.79	0.35
	R-33 Screen 2	Regional	UF07020G33R201	13-Mar-07	NA	ND	1.36	0.26
	R-15	Regional	UF070200G15R01	18-Feb-07	7.5	ND	1.02	0.19
	R-15	Regional	CAMO-08-10436	25-Feb-08	7.3	ND	1.02	0.19
	R-28	Regional	UF070200G28R01	06-Mar-07	446	ND	1.00	0.18
	R-28	Regional	UF070200G28R20[e]	06-Mar-07	425	ND	0.90	0.16
	R-28	Regional	CAMO-08-8712	14-Nov-07	385	ND	1.00	0.18
	R-28	Regional	CAMO-08-10441	15-Feb-08	419	ND	1.08	0.20
	R-13	Regional	UF070200G13R01	28-Feb-07	3.8	ND	1.00	0.18

Fate and Transport Update for Chromium from Sandia Canyon

Table D-4.3-1 (continued)

Canyon	Location	Aquifer Type	Sample ID	Collection Date	Total Filtered Cr (µg/L)	Cr(VI) (µg/L)	δ⁵³Cr ‰	Fraction Reduced
	R-13	Regional	CAMO-08-10444	14-Feb-08	6.2	ND	1.14	0.21
	R-34	Regional	UF070200G34R01	13-Mar-07	5	ND	1.18	0.22
	R-34	Regional	CAMO-08-10450	19-Feb-08	4.6	ND	Pending	ND
Sandia	E122	Surface water	CASA-08-10848	14-Feb-08	2.6	ND	Pending	ND
	E122	Surface water	CASA-08-10851[e]	14-Feb-08	3.7	ND	Pending	ND
	E123	Surface water	UF070200P12301	20-Feb-07	2.7	ND	1.43	0.28
	E123	Surface water	CASA-08-10856	14-Feb-08	5.4	ND	Pending	ND
	E123.5	Surface water	UF070200PMSC01	22-Feb-07	7.6	ND	0.3	0.00
	E123.5	Surface water	CASA-08-10858	19-Feb-08	4.9	ND	0.14[c]	0.00
	E123.4	Surface water	UF0702E123.401	20-Feb-07	3.3	ND	1.59	0.31
	E123.4	Surface water	UF0702E123.420[e]	20-Feb-07	3.3	ND	1.01	0.18
	SCI-1	Intermediate	UF070800SCI101	22-Aug-07	22.1	ND	0.44	0.04
	SCI-1	Intermediate	CASA-08-7412	16-Nov-07	16.5	ND	0.35	0.01
	SCI-1	Intermediate	CASA-08-10569	22-Feb-08	17.1	ND	0.51	0.06
	R-12 screen 1	Intermediate	CASA-08-10573	20-Feb-08	10 (U)	ND	Pending	ND
	R-12 screen 2	Intermediate	CASA-08-10578	21-Feb-08	10 (U)	ND	1.77[f]	0.34
	R-11	Regional	UF070200G11R01	13-Feb-07	33.2	ND	1.18	0.22
	R-11	Regional	UF070200G11R20[e]	13-Feb-07	34.9	ND	1.13	0.21
	R-11	Regional	CASA-08-7433	07-Nov-07	21.7	ND	1.12	0.21
	R-11	Regional	CASA-08-10546	06-Feb-08	23	ND	1.36	0.26
	R-11	Regional	CASA-08-10553[e]	06-Feb-08	23	ND	1.30	0.25
	R-35a	Regional	UF07080GR35a01	30-Aug-07	2.4	ND	3.93	0.64
	R-35a	Regional	GWR35a-08-8632	10-Nov-07	5.9	ND	NA[g]	ND
	R-35a	Regional	CASA-08-10557	07-Feb-08	4.7	ND	2.1	0.40
	R-35b	Regional	UF07080GR35b01	29-Aug-07	4.8	ND	1.23	0.23
	R-35b	Regional	UF07080GR35b20[e]	29-Aug-07	4.8	ND	1.29	0.25

Fate and Transport Update for Chromium from Sandia Canyon

Table D-4.3-1 (continued)

Canyon	Location	Aquifer Type	Sample ID	Collection Date	Total Filtered Cr (µg/L)	Cr(VI) (µg/L)	δ53Cr ‰	Fraction Reduced
	R-35b	Regional	GWR35b-08-8639	10-Nov-07	7.4	ND	1.42	0.27
	R-35b	Regional	CASA-08-10558	07-Feb-08	5.9	ND	Pending	ND
	R-36	Regional	CASA-08-11172	12-Mar-08	8.8	5	0.94[f]	0.17
	R-10a	Regional	UF07020GR10A01	20-Feb-07	5.6	ND	1.32	0.25
	R-10a	Regional	CASA-08-10564	19-Feb-08	5.8	ND	1.33	0.25
	R-10 screen 1	Regional	UF07020GR10101	21-Feb-07	2.7	ND	1.26	0.24
	R-10 screen 2	Regional	UF07020GR10201	21-Feb-07	2.7	ND	1.37	0.26
Cañada del Buey	R-16r	Regional	UF07020GR16A01	14-Mar-07	6.3	ND	0.74	0.12
	R-16r	Regional	UF07020GR16A20[e]	14-Mar-07	6.4	ND	0.77	0.13
	R-16r	Regional	CAMO-08-10459	06-Feb-08	8	ND	0.70	0.11
	R-16r	Regional	CAMO-08-10460[e]	06-Feb-08	8	ND	0.68	0.10

[a] ND = Not determined.

[b] Pending = Further sample preparation needed to remove organics and/or iron; data not available for this report.

[c] 0.5 ‰ 2 σ error.

[d] U = Nondetect.

[e] Field duplicate.

[f] 0.3 ‰ 2 σ error.

[g] NA = No Cr(VI) recovered.

Table D-4.3-2
Samples Not Run Because of Organics and/or Iron Interference or Insufficient Cr(VI)

Canyon	Sampling Location	Sample ID	Notes
Mortandad	Surface Water at E1FW	UF07020PWF1E01	Interference from organics and/or iron
	SW at E200	UF070200P20001	Interference from organics and/or iron
	Surface Water at E1E	UF070200PE1E01	Interference from organics and/or iron
	MCO-0.6	UF070200GM0601	Interference from organics and/or iron
	MCO-4B = MCO 4.5 in plan	UF070300G4BM01	Interference from organics and/or iron
	MCO-4B = MCO 4.5 in plan	UF070300G4BM20	Field duplicate; Interference from organics and/or iron
	MCO-5	UF070200G5CM01	Interference from organics and/or iron
	R-14 (screen 2)	UF07020G14R201	Interference from organics and/or iron
Sandia	R-35a	GWR35a-08-8632	Insufficient Cr(VI)

Appendix E

Preliminary Analyses of the Water-Level Data
Observed at Monitoring Wells R-35a, R-35b, and R-36

A relatively short record of water-level data has been collected at the newly installed monitoring wells R-35a, R-35b, and R-36. These data will be further analyzed in the future using analytical and numerical modeling techniques.

Figure E-1 shows the time series of the R-35a and R-35b water-level data (corrected for atmospheric pressure fluctuations) and water temperature data. R-35a responds immediately to PM-3 pumping with a daily drawdown of 5 to 6 ft, while the typical daily drawdown at PM-3 is 25 to 27 ft. R-35b water levels show no discernable response to pumping at PM-3, suggesting a strong hydraulic separation between the shallow (R-35b) and the deep (R-35a) portions of the regional aquifer. It should be noted that the distance between R-35a/R-35b and PM-3 is only about 100 m (330 ft). The R-35a water temperature is about 25°C, while the R-35b water temperature is about 23.5°C. The temperatures are relatively steady at both screens and are not affected by the water-level and pumping fluctuations. (The isolated temperature spikes are caused by water-sampling events.) PM-3 was rested for a month before the R-35 data were collected. If the pumping at PM-3 was bringing groundwater from the shallow portion of the regional aquifer (R-35b), it could be expected that the temperature of R-35a would decrease during the observation period. On the contrary, R-35a temperature increased slightly during the observation period, suggesting that the formation was warmed because PM-3 was pumping warmer groundwater from the deep sections of the aquifer. The temperature measurements at R-35a and R-35b further suggest the lack of vertical flow between the shallow (R-35b) and deep (R-35a) portions of the regional aquifer both at ambient conditions and during PM-3 pumping.

Figure E-2 shows the PM-3 and R-35a water-level time series for the period from August 2007 to April 2008. Supply well PM-3 was in routine operation during this period, with a nonpumping water level about 3 to 4 ft lower than the water level at R-35a. Decreasing water levels (pressure heads) with depth may explain this observation. In contrast to the strong response between PM-3 pumping and R-35a water levels, R-35a water-levels show no discernable response to pumping at PM-1.

Figure E-3 shows the time-series data for PM-3 and R-35b for the period from August 2007 to April 2008. The water level at R-35b shows no apparent response to pumping at PM-3. Similarly, R-35b water levels show no discernable response to pumping at other surrounding supply wells such as PM-1, PM-4, and PM-5. More importantly, the lack of response to PM-3 pumping at R-35b suggests that potential flow along the PM-3 filter pack may have a negligible effect on water levels in the shallow portion of the regional aquifer.

Operation of PM-3 was curtailed from July 2, 2007, to August 6, 2007 (Figure F-2.0-1) to allow for relatively undisturbed aquifer testing of R-35a and R-35b (LANL 2007, 098129). During the cessation in operation of PM-3, the water level at PM-3 showed a daily fluctuation of about 1 ft in response to pumping at supply well O-4 (Figure E-4); during the same period, PM-1 was also pumped, but it did not seem to influence the PM-3 water level. The water level at R-35a showed a daily fluctuation of about 0.3 ft in response to pumping at O-4; no apparent response was observed at R-35b.

Since R-36 was drilled, a 3-mo record of water levels has been collected (Figure E-5). Water-level data are adjusted to account for the effects of barometric pressure. The residual fluctuations are negligible (less than 0.2 ft) and do not correlate with the pumping records of PM-1 and PM-3. R-36 is located between the two pumping wells. This result further demonstrates the strong hydraulic separation between the shallow and the deep portions of the regional aquifer in this area.

REFERENCE

The following list includes all documents cited in this appendix. Parenthetical information following each reference provides the author(s), publication date, and ER ID number. This information is also included in text citations. ER ID numbers are assigned by the Environmental Programs Directorate's Records Processing Facility (RPF) and are used to locate the document at the RPF and, where applicable, in the master reference set.

Copies of the master reference set are maintained at the NMED Hazardous Waste Bureau; the U.S. Department of Energy–Los Alamos Site Office; the U.S. Environmental Protection Agency, Region 6; and the Directorate. The set was developed to ensure that the administrative authority has all material needed to review this document, and it is updated with every document submitted to the administrative authority. Documents previously submitted to the administrative authority are not included.

LANL (Los Alamos National Laboratory), September 2007. "Completion Report for Regional Aquifer Wells R-35a and R-35b," Los Alamos National Laboratory document LA-UR-07-5342, Los Alamos, New Mexcio. (LANL 2007, 098129)
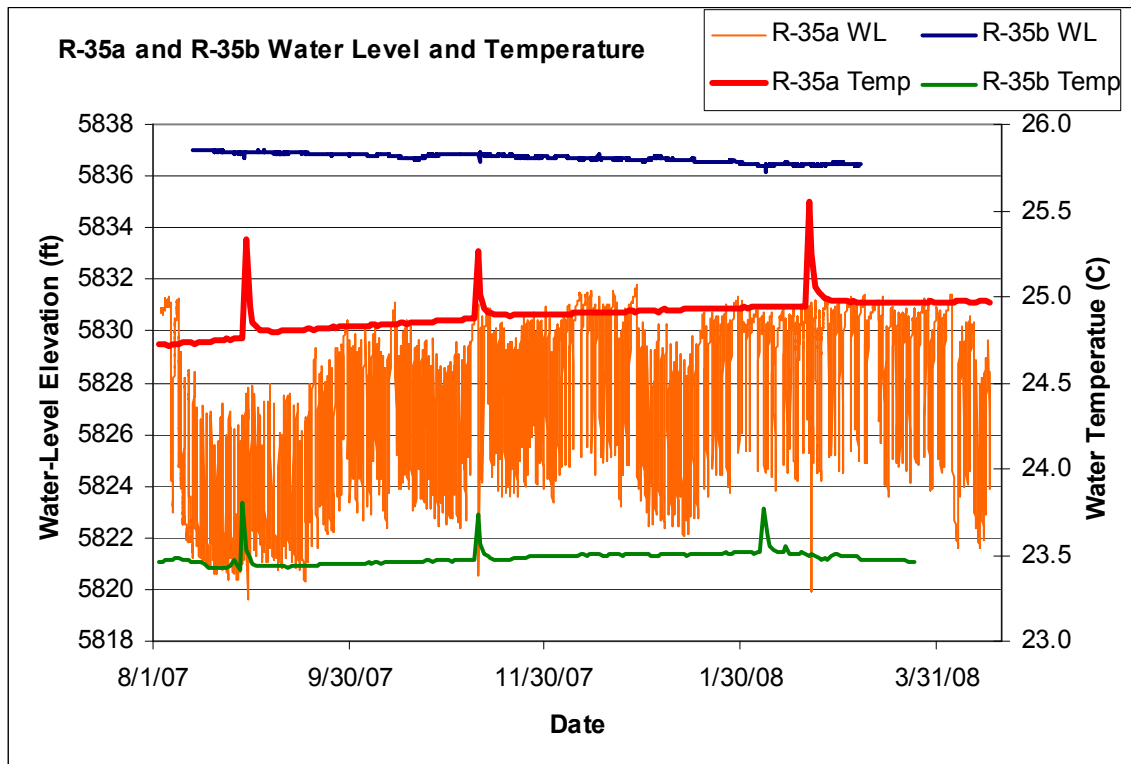
Figure E-1   Time series of R-35a and R-35b water levels and temperatures
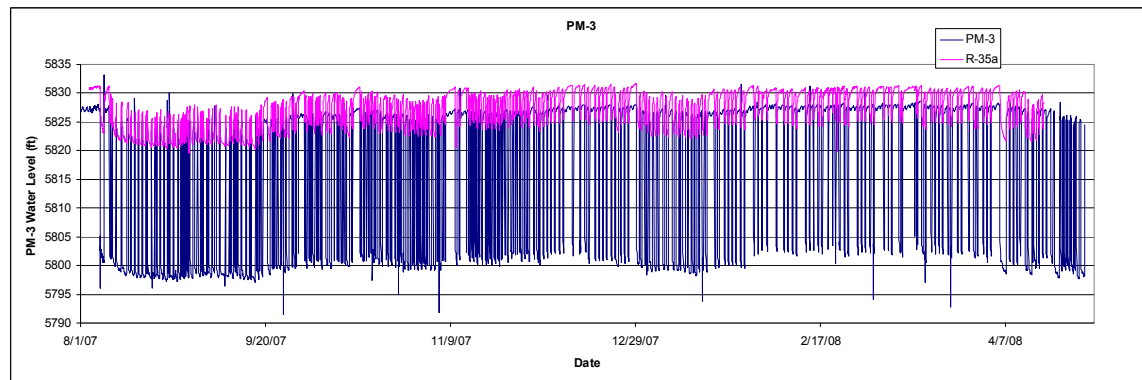
Figure E-2   Time series of water levels at PM-3 and R-35a from August 2007 to April 2008
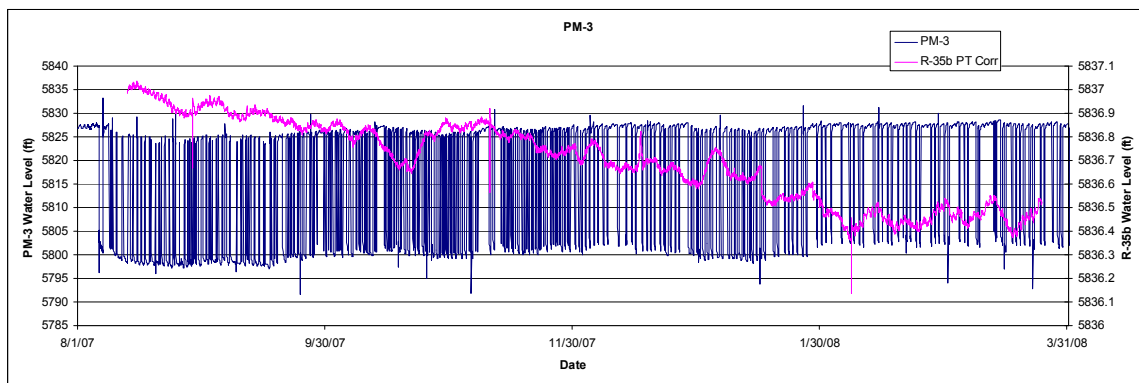
Figure E-3   Time series of water levels at PM-3 and R-35b from August 2007 to April 2008
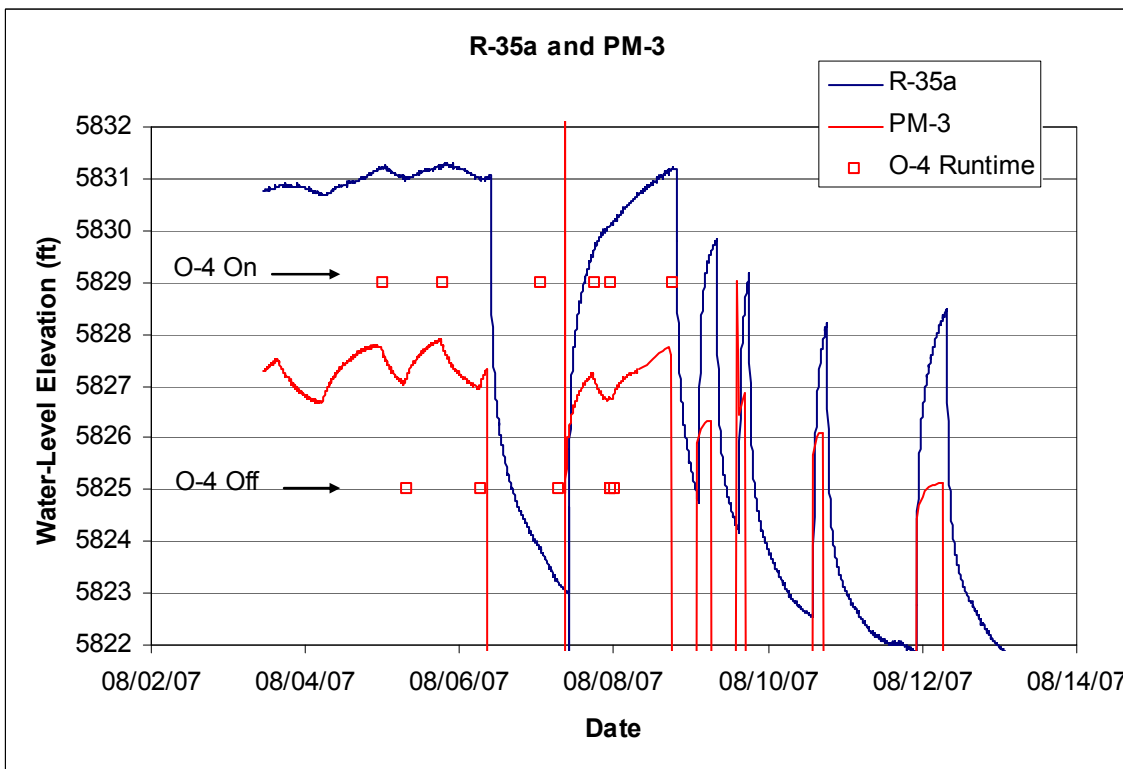
Figure E-4   PM-3 and R-35a water levels from August 2, 2007, to August 14, 2007, showing response to pumping at supply wells O-4 and PM-3
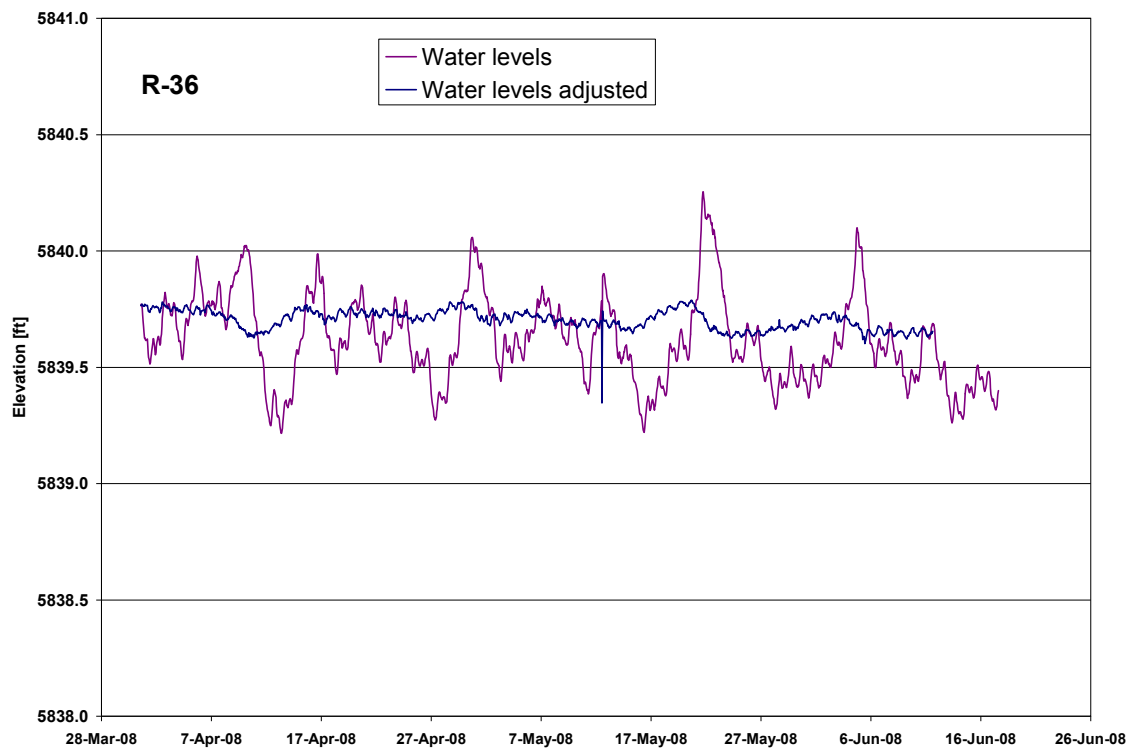
Figure E-5   Water levels observed at R-36; the water levels are adjusted to compensate for barometric pressure effects

Appendix F

*Analysis of Transient Water Levels Observed at
Regional Aquifer Monitoring Wells Near Sandia Canyon*

F-1.0   INTRODUCTION

Analysis of transient water levels observed in the regional aquifer at the monitoring wells near Sandia Canyon provides information about the magnitude of pumping drawdowns caused by the water-supply wells in the vicinity. The analysis also provides information about the hydrogeologic properties of the regional aquifer, the potential effect of local infiltration recharging the aquifer beneath Sandia Canyon, and water-supply pumping on groundwater flow directions. The complex hydrogeology present at the Los Alamos National Laboratory site and the relatively small magnitude of the observed water-level transients in the shallow portion of the regional aquifer present particular challenges for this analysis. This appendix discusses a hydraulic survey of transients observed at monitoring wells R-28, R-11, and R-15 using an analytical flow model. A preliminary analysis of water-level transients at R-35a, R-35b, and R-36 is presented in Appendix E.

F-2.0   WATER-LEVEL DATA

The observation wells in and near Sandia Canyon monitor water-level elevations in the shallow portion of the regional aquifer, which is predominantly under phreatic (unconfined) conditions (e.g., R-28, R-11, R-35a, R-35b, and R-36). Water-supply wells in the vicinity pump from the deeper portion of the aquifer, which is predominantly under confined conditions (e.g., O-4, PM-5, PM-3, and PM-1). The drawdown at the supply wells varies from 10 to 25 m. The gradients and flow directions in the phreatic zone exhibit a predominant influence from ambient flow, with a less pronounced influence from water-supply pumping. The ambient flow is controlled by areas of recharge (flanks of the Sierra de los Valles and along segments of some of the canyons on the plateau) and discharge to the east (the Rio Grande and the White Rock Canyon Springs). Maps of the regional water table are presented and discussed in Appendix H.

Figure F-2.0-1 presents groundwater levels (as absolute water-level elevations above the sea level) for the observation wells near Sandia Canyon. These wells include R-11 in Sandia Canyon and R-15 and R-28 in Mortandad Canyon. Along with raw water elevations (red), the figure shows groundwater elevations with barometric pressure fluctuations removed (black). The barometric pressure fluctuations are removed using constant coefficient methods assuming 100% barometric efficiency for all observation wells. The total fluctuation in groundwater levels over the approximately 3-yr period presented is small, around 1 ft for wells R-11 and R-28 and around 3 ft for R-15. Figure F-2.0-1 also presents the daily pumping (production) volumes from wells in the vicinity (PM-1, PM-2, PM-3, PM-4, PM-5, O-1, and O-4). Note that the pumping at all the wells, except PM-4, is cycled on a daily basis. PM-4 is pumped continuously during the summer season.

A visual comparison between the fluctuations in the groundwater levels and in the pumping volumes does not demonstrate clear correlations, except between R-15 and PM-4. However, a subtle correlation between general seasonal trends in water levels and pumping rates (i.e., high pumping rates and low water levels in the summer months) can be found at R-11 and R-28, suggesting the water-level changes are probably caused by water-supply pumping.

Other influences that may be present in the water-level records include (1) barometric effects (the total effect of barometric pressure fluctuations may not have been completely removed by the correction calculations), (2) variability in the ambient flux, (3) variability in local recharge beneath Sandia Canyon or other canyons (identification of such transients typically require much longer observation periods than the existing 3-yr water-level record), and (4) subsidence (pore-elastic effects) from water-supply pumping.

The following discussion analyzes transient water-level responses at R-28, R-11, and R-15 by estimating pumping drawdown using simple analytical techniques that account for pumping influences. This approach allows fingerprinting of pumping influences at observation well locations, given contrasting pumping records, estimation of potential drawdown effects associated with individual pumping wells, and estimation of effective hydraulic properties of the aquifer between pumping and observation wells. While the use of a simple analytical model does not allow the accurate estimation of the spatial properties of aquifer heterogeneity, it can provide information about the aquifer properties, for example nonuniform aquifer properties or aquifer anisotropy.

F-3.0   ANALYTICAL ESTIMATION OF POTENTIAL PUMPING EFFECTS

Pumping drawdown effects have been simulated using the Theis solution (Freeze and Cherry 1979, 088742, p. 317) defined as

$$s = \frac{Q}{4\pi T}W(u) = \frac{Q}{4\pi T}W\left(\frac{r^2 S}{4Tt}\right),$$

where s is the transient drawdown (L), Q is the discharge from the well ($L^3 T^{-1}$), T is the transmissivity ($L^2 T^{-1}$), $W(u)$ is the well function where $u = r^2 S/4Tt$, where r is the distance to the pumping well (L), S is the specific storage coefficient, and t is time since pumping commenced (T). The Theis solution is intended for homogeneous formations, precluding its ability to characterize spatial variation of hydraulic properties. Nevertheless, the equation can provide estimates for the pumping effects in heterogeneous formations if the effective properties of the aquifer are known.

The principle of superposition is used for the analysis to represent transient effects in pumping rates and to combine drawdown contributions from multiple water-supply wells in order to predict observed drawdown at a given monitoring well. In this way, the predicted drawdown at a monitoring well is a sum of drawdowns created by each production well during each pumping period:

$$s = \sum_{i=1}^{N}\sum_{j=1}^{M_i} \frac{Q_{ij} - Q_{ij-1}}{4\pi T_i}W\left(\frac{r_i^2 S_i}{4T_i\left(t - t_{Qij}\right)}\right),$$

where N is the number of pumping wells, M_i is the number of pumping periods (i.e., number of pumping rate changes), Q_{ij} is the pumping rate of well i during pumping period j, and t_{Qij} is the time when the pumping rate changed at well i during pumping period j. In these analyses, seven pumping wells are considered, and the maximum number of pumping rate changes (M_i) is 2035 (for O-4). The principle of superposition allows for different effective hydraulic properties between different water supply/observation well pairs (T_i, S_i). In this way, it is possible to estimate at what extent the heterogeneity affects the observed drawdowns in the monitoring wells. Furthermore, discrepancies between the simulated and observed pressures may suggest additional transients or heterogeneities that are currently not included in this model (e.g., transients in the ambient fluxes).

Inverse modeling is employed to identify effective hydraulic properties (transmissivity T and specific storage S), resulting in model predictions that are consistent with observed water-level elevations (calibration targets). The daily variations in the water supply production record, which include the daily pumping and recovery periods, are explicitly represented in the model.

This inverse analysis is similar to the analysis of pumping tests. However, in this case, the pumping test includes multiple pumping wells that have transient pumping records. The benefits of this approach are

that (1) there is no need to perform specially designed field tests (which should include a prolonged cessation of pumping at all the production wells before the test, although this might not be feasible), and (2) the effects of measurement errors may be mitigated given long water-level and pumping records.

F-4.0 RESULTS AND DISCUSSION

Figure F-4.0-1 presents results from inversions where a model is calibrated (as closely as possible) to simulate the water-level fluctuations observed at a particular monitoring well based on the production rate changes at a particular production well. This analysis determines the extent to which water-level fluctuations at a particular (single) monitoring location can be characterized by drawdown caused by a particular (single) production well. Each plot in Figure F-4.0-1 presents the results from a separate model inversion. Visual inspection of the figures suggests that PM-2, PM-3, PM-4, and PM-5 may be the primary wells that cause the observed water-level fluctuations. However, it also appears that the drawdown caused by an individual production well cannot characterize all the observed fluctuations. Therefore, further analysis combining the drawdowns from all the production wells is required.

Next, the model is updated to predict groundwater water-level elevations at single observation wells using the pumping records from all seven production wells. The resulting model predictions (black lines) and respective groundwater-level observations (red lines [water levels are corrected for barometric fluctuations]) at each monitoring well (R-11, R-15, and R-28) are shown in Figure F-4.0-2. The significant improvement in the correlation between the predicted water level and the observed water level from Figure F-4.0-1 to Figure F-4.0-2 indicates that the cumulative effect of water-supply well pumping has to be considered because individual production well pumping records do not allow for adequate predictions.

For each inversion model, the effective properties of the aquifer between the observation and pumping wells are estimated (Table F-4.0-1). In general, transmissivity estimates and specific storage estimates are at least an order of magnitude higher than previous estimates obtained through pumping tests (McLin 2005, 090073; McLin 2006, 092218; McLin 2006, 093670). The various transmissivity estimates listed in Table F-4.0-1 are similar (the same order of magnitude); however, certain variations suggest unique aquifer heterogeneity between each of the supply wells and monitoring wells, except for the effective properties related to PM-2 (Table F-4.0-1). PM-2 is located south of each of the monitoring wells; the similar effective parameters between each monitoring well and PM-2 indicates similar effective aquifer properties in this direction and this scale and substantiates the modeling. The specific storage estimates are also similar (the same order of magnitude), except for the estimate associated with the R-11 response to PM-3 pumping. Additional analyses involving more sophisticated models that can account for aquifer heterogeneity are required to further resolve these issues.

Figures F-4.0-3, F-4.0-4, and F-4.0-5 present the components of the drawdowns predicted by the modeling at R-11, R-15, and R-28, respectively, that are caused by pumping at each production well. The drawdown data are plotted with the associated daily production for each supply well. These figures illustrate the correlation between the pumping records and the predicted drawdowns at the observation wells. In general, the monitoring wells do not respond significantly to individual or daily pumping events at the supply wells but show a muted, subtle response to pumping stresses.

As illustrated by Figures F-4.0-3 and F-4.0-5, the drawdowns at R-11 and R-28 are caused by a similar set of wells: PM-2, PM-3, and PM-4. The magnitudes of drawdowns are also very similar. More importantly, the modeled transients in the pumping records of PM-1, PM-5, O-1, and O-4 do not appear to cause water-level fluctuations at R-11, R-15, and R-28. However, the model predicts a long-term decline of the water levels at R-28 and R-11. An important conclusion of the calibration analysis is that the model predicts a portion of the drawdown observed at R-11 and R-28 is caused by a water-level decline that is

not directly correlated with the transients created by the existing pumping rates. This decline is relatively small (~0.15 m) within the analyzed period but is similar in order of magnitude to the predicted pumping drawdowns (Figures F-4.0-3 and F-4.0-5). The decline may be associated with vertical leakage from the shallow into deep aquifer zones (potentially through hydraulic windows). It is also possible that other factors, such as reduced ambient flux or reduced local recharge not directly associated with the local water-supply pumping, are causing this water-level decline.

At R-15, drawdowns are caused by PM-2, PM-3, PM-4, and PM-5 (Figure F-4.0-4). The model predicts that the water-level fluctuations observed at R-15 can be explained by the transients in the production wells only; the model does not predict that additional factors control the observed long-term decline of the water levels. The model predicts that PM-3 pumping causes a drawdown at R-15 (Figure F-4.0-4) that is higher than the drawdowns at R-11 (Figure F-4.0-3) and R-28 (Figure F-4.0-5), even though R-11 and R-28 are much closer to PM-3 than R-15 is. This prediction suggests complex, three-dimensional hydrogeological heterogeneity.

In summary, the analysis indicates that the pumping at PM-2, PM-3, and PM-4 is causing the pressure response at R-11, R-15, and R-28. The water level at R-15 is also influenced by PM-5. None of the three monitoring wells seems to be influenced by pumping at PM-1, O-1 or O-4. In the case of O-1, this effect may be from the limited pumping of this well. However, O-4 is located relatively close to R-11, R-15, and R-28 when compared to PM-2 and PM-4, and is pumped significantly. The results of the modeling indicate major aquifer heterogeneity that may require further analyses.

F-5.0   CONCLUSIONS

A simple analytical model was used to extract groundwater information from production and water-level records about the properties of the regional aquifer beneath the Sandia Canyon area. It is apparent that the model inversions that consider only single water supply wells do not provide adequate predictions of water-level responses in monitoring wells. Model inversions that consider pumping of all water-supply wells provide predictions that correlate to observed groundwater levels. However, influences other than water-supply pumping may be attributed to the observed water levels at R-11 and R-28. The inverse analysis of pressure responses from pumping suggests that there may be large-scale hydrogeologic structures (e.g., faults or troughs) with properties that are different from the rest of the aquifer. For example, the lack of apparent pressure response to O-4 pumping may suggest the existence of a hydraulic barrier between the analyzed monitoring wells and O-4; another explanation could be that O-4 taps a highly permeable structure in the regional aquifer that provides most of the groundwater pumped at this well. Similarly, the observed pressure response from PM-2 pumping, but not from PM-1 pumping, may suggest a regional anisotropy with a southeastern orientation. Further analyses may address these issues. Future work may also include more sophisticated models, more monitoring wells, and longer data records to better characterize transients in the groundwater levels and aquifer heterogeneity.

It is important to note that during the PM-2 pump test (McLin 2005, 090073, p. 7) no drawdown was identified at R-15. However, the modeling and analysis presented here demonstrate there is a measurable response to PM-2 pumping at R-15. McLin (2005, 090073) also identifies a radius of influence around PM-2 that includes R-15 and R-28 but not R-11. The analysis presented here effectively increases the potential zone of influence by identifying a potential response of PM-2 pumping at R-11. The PM-4 pump test (McLin 2006, 092218) confirms that drawdowns at R-15 and R-28 can be attributed to PM-4 pumping. However, no data were collected at R-11 during the pump test. The PM-4 pump test report does not include estimates of aquifer properties based on R-15 and R-28 drawdowns. In this way, the presented modeling and analysis are consistent with, and improve on, existing work.

F-6.0   REFERENCES

The following list includes all documents cited in this appendix. Parenthetical information following each reference provides the author(s), publication date, and ER ID number. This information is also included in text citations. ER ID numbers are assigned by the Environmental Programs Directorate's Records Processing Facility (RPF) and are used to locate the document at the RPF and, where applicable, in the master reference set.

Copies of the master reference set are maintained at the NMED Hazardous Waste Bureau; the U.S. Department of Energy–Los Alamos Site Office; the U.S. Environmental Protection Agency, Region 6; and the Directorate. The set was developed to ensure that the administrative authority has all material needed to review this document, and it is updated with every document submitted to the administrative authority. Documents previously submitted to the administrative authority are not included.

Freeze, R.A., and J.A. Cherry, January 1979. *Groundwater*, Prentice-Hall, Inc., Englewood Cliffs, New Jersey. (Freeze and Cherry 1979, 088742)

McLin, S., July 2005. "Analyses of the PM-2 Aquifer Test Using Multiple Observation Wells," Los Alamos National Laboratory report LA-14225-MS, Los Alamos, New Mexico. (McLin 2005, 090073)

McLin, S., January 2006. "Analyses of the PM-4 Aquifer Test Using Multiple Observation Wells," Los Alamos National Laboratory report LA-14252-MS, Los Alamos, New Mexico. (McLin 2006, 092218)

McLin, S.G., May 2006. "A Catalog of Historical Aquifer Tests on Pajarito Plateau," Los Alamos National Laboratory document LA-UR-06-3789, Los Alamos, New Mexico. (McLin 2006, 093670)
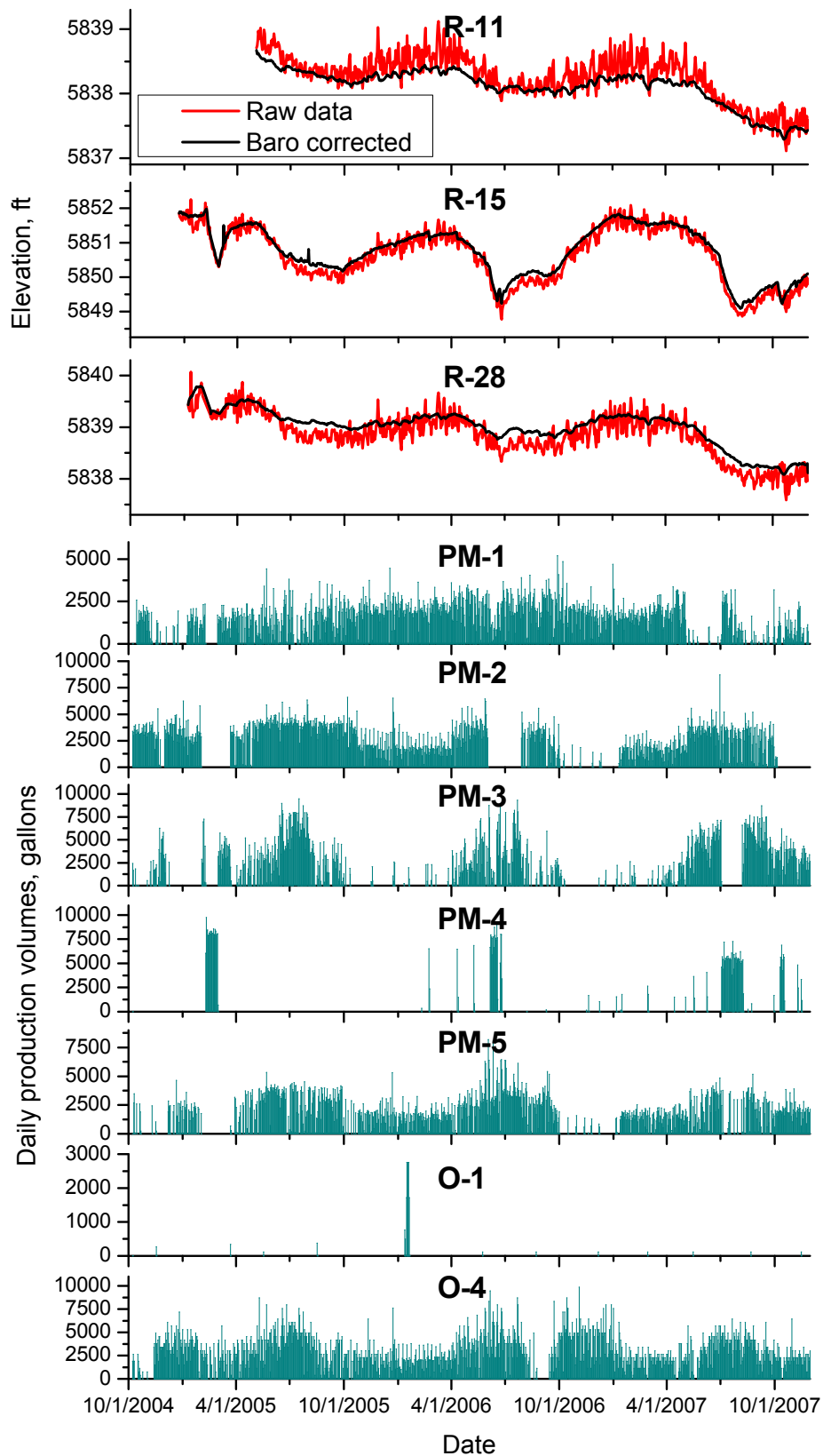
Figure F-2.0-1   Groundwater-level elevations at observation wells and supply-well pumping volumes for production wells near Sandia Canyon
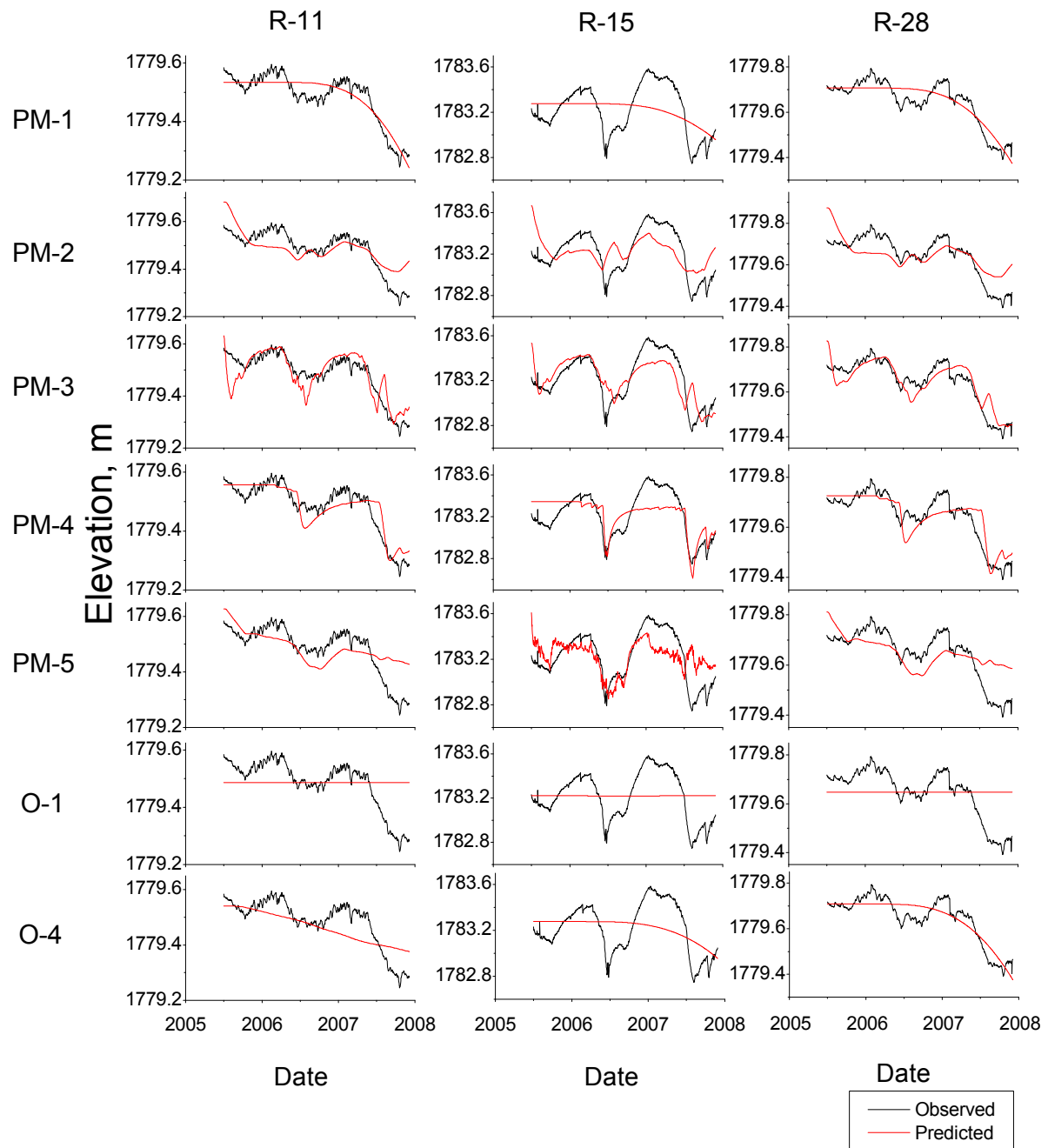
Figure F-4.0-1 Observed (black line) and model-predicted (red line) water levels at individual monitoring wells. Each plot presents the results from a separate model inversion. The row headings denote the production well and the column headings denote the observation well for the associated model inversion. In each case, the model predicts water-level elevations at a single observation well using the pumping record for a single production well.

R-11

R-15

R-28
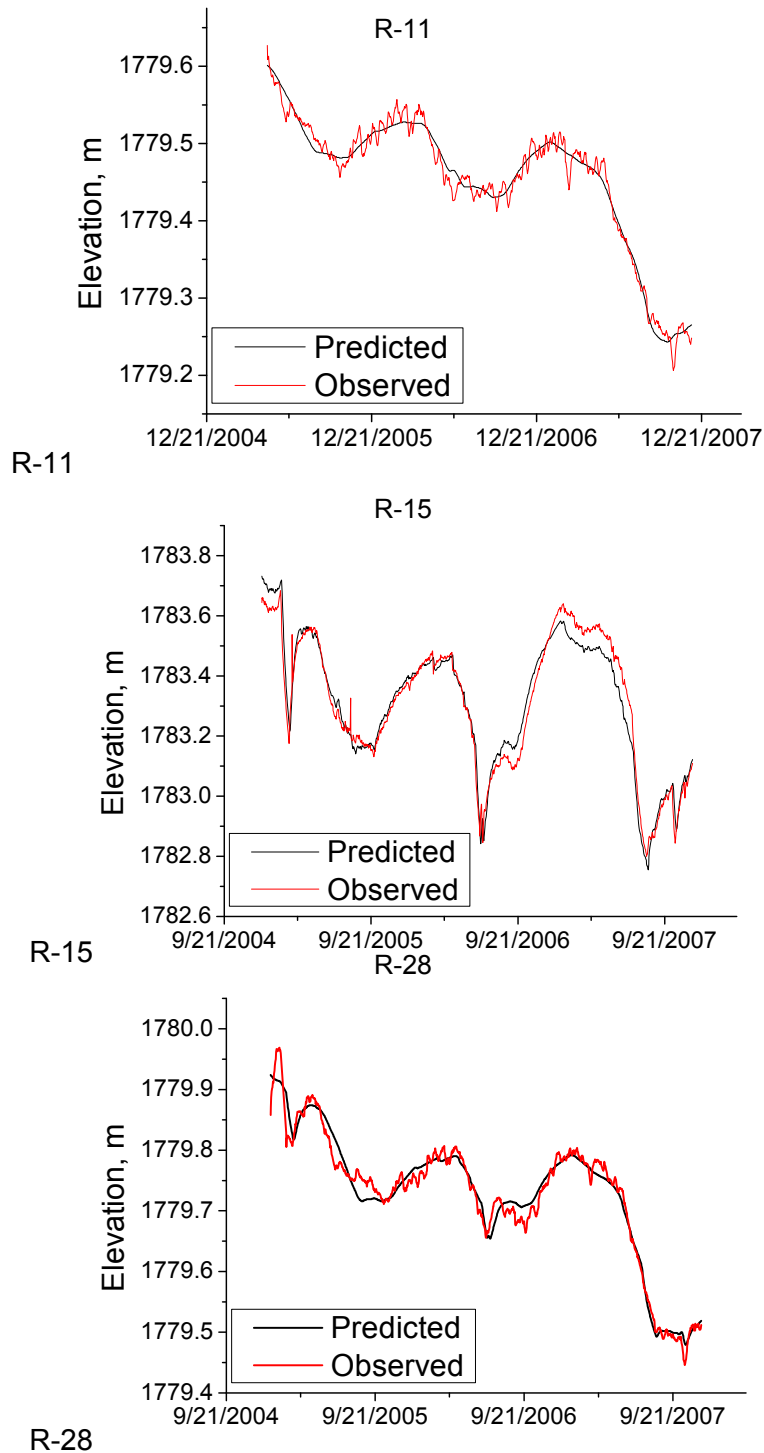
Figure F-4.0-2 Observed (red line) and model-predicted (black line) water levels at individual monitoring wells. Each plot presents the results from a separate model inversion. In each case, the model predicts water elevations at a single observation well using pumping records for all seven water-supply wells. Note differences in the y-axis scales on each plot.
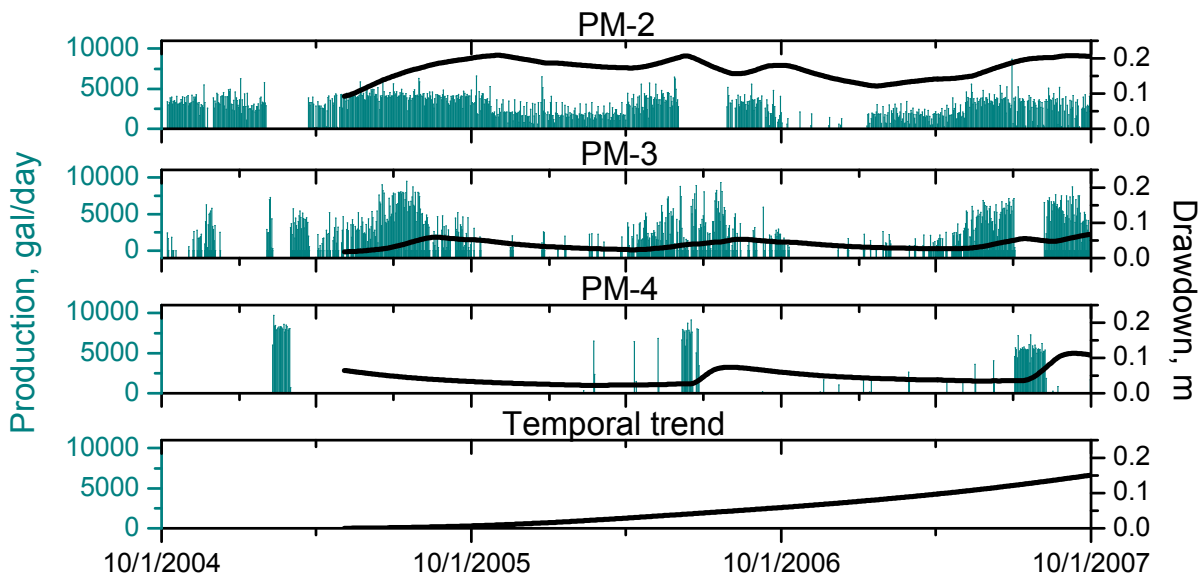
Figure F-4.0-3   Model-predicted drawdown contributions from each water supply well at R-11. The plots also present well production data and the estimated trend line of drawdown decline.
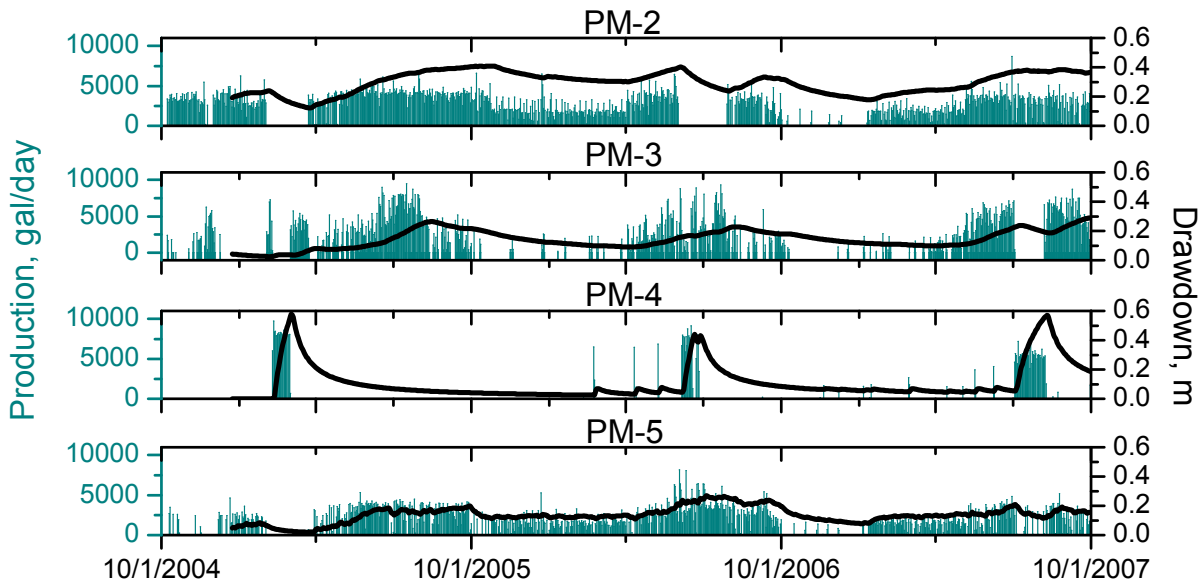
Figure F-4.0-4   Model-predicted drawdown contributions from each water supply well at R-15. The plots also present well production data. Note the different scale of drawdown axes compared to Figures F-4.0-3 and F-4.0-5. The model did not predict that there are transients in the water levels that are not related to the existing pumping; as a result, there is no plot of a trend line.
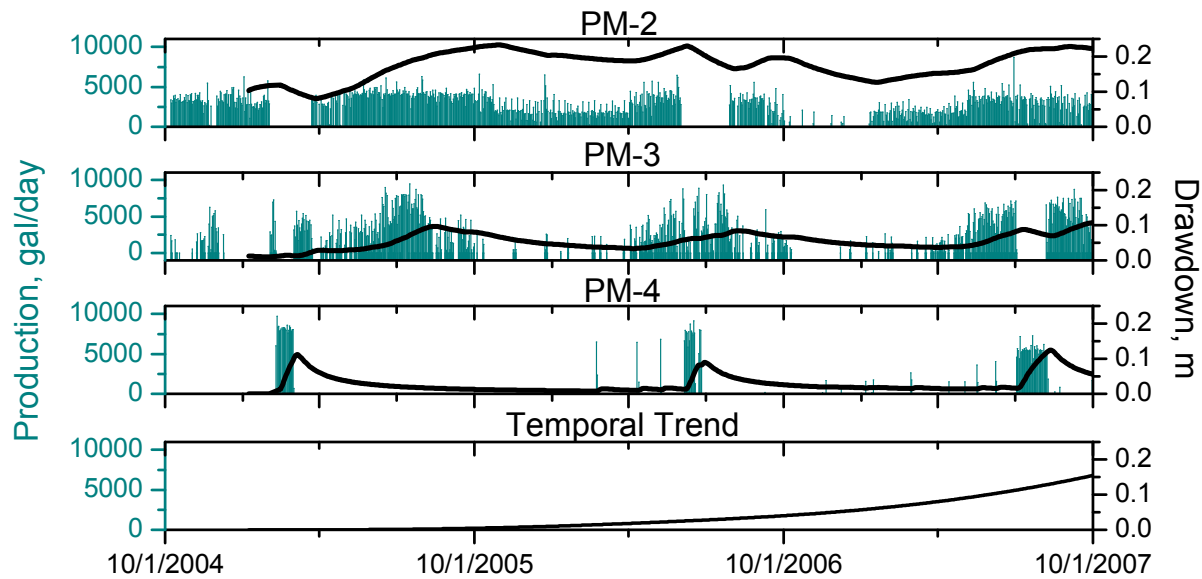
Figure F-4.0-5   Model-predicted drawdown contributions from each water supply well at R-28. The plots also present well production data and the estimated trend line of drawdown decline.

Table F-4.0-1
Estimates of Effective Aquifer Hydraulic Properties Based on Model Calibration

Well	Initial Head (m)	Hydraulic Property	PM-1	PM-2	PM-3	PM-4	PM-5	O-1	O-4
R-11	1779.8	Transmissivity [m^2/d]	—*	3000	8900	1500	—	—	—
		Specific storage [-]	—	0.033	1.4	0.078	—	—	—
R-15	1784.0	Transmissivity [m^2/d]	—	2200	2500	1500	5000	—	—
		Specific storage [-]	—	0.013	0.035	0.020	0.032	—	—
R-28	1780.0	Transmissivity [m^2/d]	—	3000	6600	4600	—	—	—
		Specific storage [-]	—	0.035	0.36	0.066	—	—	—

*— = Not estimated during calibration

Appendix G

Estimation of Calibration Targets for the
Chromium Concentration at the Regional Monitoring Wells

To perform the fate and transport modeling of chromium contamination in the subsurface, it is important to have a numerical model that produces predictions consistent with field data. This objective can be achieved through a formal process of model calibration (inversion) against existing data measurements. The data considered in the calibration process are called calibration targets. The chromium concentrations in the regional aquifer observed at the monitoring wells near Sandia Canyon are key calibration targets. The goal of the numerical modeling is to predict current chromium concentrations in the regional aquifer resulting from releases in Sandia Canyon (circa 1956 to 1972) that are consistent with current observations (circa 2007). However, the chromium concentrations that are used to calibrate the numerical model are uncertain. First, uncertainties occur as a result of transients in the data (section 2.6) and from uncertainty in the background chromium concentrations (Appendix J-5) (the chromium background is not explicitly simulated in the numerical model). In addition, the calibration targets need to take into account uncertainties related to (1) potential dilution within and above the screen where water samples are collected (between the screen and the water table) and (2) representation of monitoring screens in the numerical model. The calibration ranges are estimated using a formal process that follows the steps listed below. The implementation of the steps is also presented in Table G-1.

1. Minimum, arithmetic average, and maximum chromium concentrations are calculated for each monitoring well based on all the observed chromium concentrations (filtered samples) at the monitoring wells from 2005 to 2007 (using data extracted from the Los Alamos National Laboratory's Water Quality Database [WQDB]). The calculated raw values are presented in Table G-1.

2. The minimum, average, and maximum chromium concentrations are rounded to integers. (The minimum is rounded to the nearest smaller integer; the average and maximum are rounded to the nearest larger integer.)

3. Regional wells R-11, R-15, and R-28 have chromium concentration detected above background. The lower and upper limits for R-11, R-15, and R-28 are assigned to be close to the minimum/maximum concentration ranges. The lower limit is set to 0 µg/L for R-15 because chromium observed at this well may be associated with a source other than that from Sandia Canyon, and the scope of the model is to simulate excess chromium derived solely from the Sandia Canyon source.

4. For all the other wells, the lower limit is set at 0 µg/L, again because the background chromium concentrations are not explicitly simulated in the numerical model. The upper limit is set at 8 µg/L because concentrations greater than this value are considered clearly above background and indicative of contamination.

5. According to the screen-depth test, if the distance between the regional water table and the top of screen is greater than the 1.5 times the screen length, contaminant dilution above the screen may be significant. If dilution is expected, the maximum concentration is set at 15 µg/L. The selection of this upper limit is somewhat arbitrary; it is selected to be almost 2 times higher than the upper limit for the other wells. This is the case for some of the monitoring wells including R-4, R-5, R-6, R-10a, R-16r, R-13, R-18, R-19, R-20, R-21, R-27, R-32, R-33, R-34, R-35a, and R-35b.

6. According to the grid-resolution test, the upper limits are increased if the grid resolution of the numerical model may cause artificial contaminant dilution. To evaluate this effect, the actual screen lengths and the depths of the screens below the water table represented in the numerical model are analyzed. If the screen lengths and screen depths are underestimated in the model by more than 150%, the upper concentration range is increased to 15 µg/L to account for potential artificial dilution in the model. The selection of this upper limit is somewhat arbitrary; it is selected

to be almost 2 times higher than the upper limit for the other wells. This adjustment was required only for well R-9.

The final estimates of the calibration ranges are presented in Table G-1. These ranges are applied to calibrate the numerical model of the regional aquifer (section J-5).

Table G-1
Estimate of Chromium Calibration Ranges at Monitoring Wells Near Sandia Canyon

Well	Data Considered for Adjustment of Calibration Ranges											Chromium Concentrations (ppb)									
	Cr Plume Could be Expected to be Observed at this Location?	IDs of Screen Used for Raw Data Calculations	Distance Between Regional Water Table and Top of Screen (ft)	Screen Length (ft)	Need to Adjust the Upper Limit?	Number of Nodes in the Model Within the Screen	Screen Length in the 3-D Model (ft)	Need to Adjust the upper limit?	Distance Between Regional Water Table and Top of Screen in the 3-D Model (ft)	Number of Nodes in the Model above the Screen	Need to Adjust the Upper Limit?	Number of Samples Included in Raw Calculations	Raw Calculated Values			Values Adjusted by Truncation			Calibration Ranges		
													Min	Average	Max	Min	Average	Max	Lower	Best Estimate	Upper
R-01	No	single	27	25	No	1	41.01	No	41.0	2	No	6	4.2	5.5	7.2	4	6	8	0	5	8
R-02	No	single	13	25	No	1	41.0	No	20.5	1	No	3	4.3	5.4	6.9	4	5	7	0	5	8
R-04	Yes	single	61	25	Yes	2	20.5	No	61.5	3	No	3	3.2	4.8	6.2	3	5	7	0	5	15
R-05	Yes	3	-8	40	No	3	41.0	No	20.5	1	No	2	7.1	8.3	9.5	7	8	10	0	10	15
R-06	Yes	single	47	20	Yes	2	20.5	No	82.0	4	No	4	3.5	4.6	6.4	3	5	7	0	5	15
R-07	No	3	-7	40	No	2	41.0	No	0.0	0	No	3	1.32	2.56	4.06	1	3	5	0	5	8
R-08	No	1 and 2	-4	50	No	3	41.0	No	20.5	1	No	3	3.4	4.9	7.4	3	5	8	0	5	8
R-09	Yes	single	-4	65.5	No	3	41.0	Yes	123.0	6	No	2	2.3	2.3	2.3	2	2	3	0	5	15
R-10a	Yes	single	66	10	Yes	1	20.5	No	82.0	4	No	5	4.4	5.4	6.2	4	5	7	0	5	15
R-11	Yes	single	19	20	No	2	20.5	No	20.5	1	No	6	25.5	29.8	34.8	25	30	35	5	30	50
R-13	Yes	single	124	60	Yes	4	61.5	No	123.0	6	No	5	3.8	4.5	5.3	3	5	6	0	5	15
R-14	No	1	19	30	No	1	41.0	No	41.0	2	No	5	1.9	2.3	2.7	1	2	3	0	5	8
R-15	Yes	single	-5	60	No	4	61.5	No	0.0	0	No	5	7.2	7.7	8.2	7	8	9	0	10	30
R-16r	No	single	36	20	Yes	1	41.0	No	41.0	2	No	6	4.1	5.5	6.9	4	6	7	0	5	15
R-17	No	1 and 2	21	20	No	1	41.0	No	41.0	2	No	9	1.6	2.6	4.5	1	3	5	0	5	8
R-18	Yes	single	70	20	Yes	1	41.0	No	123.0	3	No	5	1.0	2.2	5.0	1	2	5	0	5	15
R-19	No	4	232	7	Yes	1	41.0	No	246.1	12	No	4	2.9	3.3	4.0	2	3	4	0	5	15
R-20	No	1	68	7	Yes	1	20.5	No	102.5	5	No	4	1.2	2.1	2.7	1	2	3	0	5	15
R-21	No	single	85	20	Yes	2	20.5	No	102.5	5	No	4	3.1	3.3	3.6	3	3	4	0	5	15
R-22	No	2 and 3	57	40	No	2	41.0	No	82.0	4	No	6	1.8	3.8	8.9	1	4	9	0	5	8
R-23	No	single	-13	55	No	2	41.0	No	0.0	0	No	4	1.9	3.0	5.0	1	3	5	0	5	8
R-24	No	single		20	No	2	20.5	No	123.0	6	No	4	1.5	2.8	5.0	1	3	5	0	5	8
R-26	No	1			No	1	164.0	No	0.0	0	No	3	2.0	3.6	6.4	2	4	7	0	5	8
R-27	No	single	41	20	Yes	1	41.0	No	82.0	3	No	4	1.6	2.7	3.8	1	3	4	0	5	15
R-28	Yes	single	45	20	Yes	2	20.5	No	41.0	2	No	6	310	394	446	310	394	446	300	400	700
R-31	No	2, 3 and 4	-7	30	No	1	20.5	No	0.0	0	No	6	1.0	2.4	4.4	1	2	5	0	5	8
R-32	No	1	85	10	Yes	1	20.5	No	102.5	5	No	3	1.9	3.4	5.8	1	3	6	0	5	15
R-33	No	1	17	20	Yes	2	20.5	No	20.5	1	No	3	4.1	6.8	9.7	4	7	10	0	5	15
R-34	No	single	88	20	Yes	2	20.5	No	102.5	5	No	5	3.4	4.9	6.4	3	5	7	0	5	15
R-35a	Yes	single	214.11	50	Yes	2	41.0	No	225.6	11	No	3	2.4	3.1	4.7	2	3	5	0	5	15
R-35b	Yes	single	34.4	20	Yes	2	20.5	No	41.0	2	No	3	4.8	6.0	7.4	4	6	8	0	5	15
R-36	Yes	single	17.8	20	No	2	20.5	No	20.5	1	No	1	7.1	7.1	7.1	7	7	8	0	5	8

Appendix H

Maps of the Regional Water Table

As discussed in section 2.6, the regional aquifer beneath Los Alamos National Laboratory is a complex hydrogeological system. The top of the aquifer is predominantly under phreatic (water-table) conditions, but there are zones of local confinement as well. The shape of the regional water table is predominantly controlled by the areas of regional recharge to the west (flanks of Sierra de los Valles) and discharge to the east (the Rio Grande and the White Rock Canyon Springs). The structure of the phreatic flow is also impacted by (1) infiltration zones (predominantly along western faults and along the floors of wet canyons); (2) geologic heterogeneity (lithological variations, bedding characteristics, and faults); and (3) discharge zones (water-supply wells and springs). The river stage is not explicitly used to evaluate the water-table contours. The regional water table is located approximately 300 to 400 m below ground surface across the Pajarito Plateau.

Information about the elevation of the top of the regional aquifer (the regional water table) is provided by existing data from monitoring wells and by the discharge elevation for springs that are believed to issue from the regional groundwater system. Well data are primarily used; spring discharge elevations are used only in the vicinity of White Rock Canyon. Water-table elevation data are shown in Figures H-1 and H-2; these represent monthly averaged water levels from January, 2006. The data are analyzed to create two alternative water-table maps (Figures H-1 and H-2) by making different conceptual-model assumptions.

In the contouring process, water-level data from some of the wells have been excluded in these analyses because they may only represent local conditions. Water levels at R-9 and R-12 are substantially lower than water levels at the nearby wells. Because R-9 and R-12 are located very close to water-supply wells PM-1 and O-1, their low water levels suggest there could be cones of drawdown around the production wells. However, the lack of water-level variability at R-9 and R-12 from pumping suggests that the low heads at R-9 and R-12 are not caused by the water-supply pumping. The low water levels may instead result from the screen locations of R-9 and R-12. The screens are located in Miocene basalt and may be substantially below the regional water-table; thus, the measured pressures characterize a deep compartmentalized zone that is in poor hydraulic connection with the rest of the aquifer. In addition, R-4 and R-24 are not explicitly included in the contouring process because both wells appear to tap a confined portion of the regional aquifer that may not represent the regional water-table elevation.

In previous reports (LANL 2007, 095364; LANL 2008, 101932), uncertainties in the water-table elevation at R-25 were discussed. These uncertainties still exist and revolve around the choice of using data from Screens 4 or 5 to define the water-table elevation. Here we use the Screen 5 data to create the water-table maps. This assumption is not important for the purposes of this report because R-25 is located far from Sandia Canyon.

In addition to the actual measurement data, a major constraint that controls the shape of the water-table contours comes from the conformity rules. According to these rules (1) the contour lines should be perpendicular to the groundwater flow paths and (2) the lengths and the widths of the cells formed by the contour lines between two adjacent flow paths should have similar ratios. These rules are valid in the case of uniform isotropic medium in areas with no recharge/discharge sources. The heterogeneity/anisotropy of the aquifer and the presence of recharge/discharge sources in the area of interest are expected to affect the conformity rules. The water-table contours are defined by attempting (1) to simultaneously match the observed water-level data at the wells and (2) to preserve flow-net conformity rules. Both goals are not perfectly achieved in the maps included in this appendix. However, the maps represent a balance between those two goals. The contouring of water-table maps is performed using manual and automated techniques. The automated contouring is performed using the Minimum Curvature Method as implemented in the software Surfer, Version 8, developed by Golden Software.

To address uncertainty in the hydrogeologic conditions, two alternative water-table maps have been created. These maps are similar to those presented in the 2008 General Facility Information report (LANL

2008, 101932). The first map emphasizes the potential mounding of the regional water table due to preferential recharge along the canyons on the Pajarito Plateau, especially near TW-1 and R-8 (Figure H-1). However, the water levels at TW-1 and R-8 may not characterize actual mounding of the regional water table. The relatively high water levels at the two wells may result from problems associated with well construction (particularly in the case of TW-1) and/or to local, small-scale, elevated pressures caused by aquifer heterogeneity and compartmentalization (R-8). As a result, a second water-table map has been created (Figure H-2). This map features (1) no mounding near TW-1, (2) spatially limited mounding near R-8, and (3) reduced effects of preferential recharge along the canyons. The second water-table map can be viewed as a smoothened version of the map presented in Figure H-1. The second water-table map deviates more from the water-level well data but more accurately follows the conformity rules than the map presented in Figure H-1. Based on the existing information, both maps are equally probable.

It is important to note that the maps were created before water-level elevations were measured at R-35b and R-36. (Those data only became available after the analyses presented in this report were underway.) The water-level elevation at R-35b (~5837 ft) is consistent with the maps and does not require recontouring of water levels. However, the water-level elevation at R-36 (~5840 ft) is somewhat higher than predicted (~5836 ft) by the maps in Figures H-1 and H-2; the water level at R-36 is even slightly higher than the water levels at R-28 (~5839) and R-11 (~5839). The higher water level at R-36 suggests that the direction of groundwater flow downgradient from R-28 has a southern component; this flow direction is already captured in the two water-table maps (Figures H-1 and H-2). Further analysis of the R-36 water level is underway and will be discussed in the Sandia Canyon investigation report. That analysis may include further interpretation of water-level transients and of potential hydrogeologic controls, such as faults, hydrostratigraphy, and heterogeneity.

The water-table maps shown in Figures H-1 and H-2 suggest that the horizontal components of the hydraulic head gradient tend to have an easterly/southeasterly direction across the plateau, and the gradients range from 0.0026 to 0.162 m/m. The gradients near Sandia Canyon are on the order of 0.005 m/m (ranging from 0.003 to 0.1 m/m). Generally, gradients are higher at the western portion of the central portion of the study area, lower in the central portion, and higher again at the eastern portion near the Rio Grande. The mounding at the water table along Los Alamos, Pueblo, Sandia, and Water Canyons, and Cañon de Valle (as described above) is evident in Figure H-1. In the area near Sandia Canyon, the map suggests that the infiltration causes a mound on the order of 2 to 3 ft. Analytical and numerical analyses of potential mounding are also presented in Appendixes I and J. It is important to note that Figures H-1 and H-2 indicate that the shape of the regional water table is not affected by intensive water-supply pumping in the deep zone of the regional aquifer on the Pajarito Plateau.

The numerical models discussed in Appendix J are calibrated to represent the two water-table maps shown in Figures H-1 and H-2.

REFERENCES

The following list includes all documents cited in this appendix. Parenthetical information following each reference provides the author(s), publication date, and ER ID number. This information is also included in text citations. ER ID numbers are assigned by the Environmental Programs Directorate's Records Processing Facility (RPF) and are used to locate the document at the RPF and, where applicable, in the master reference set.

Copies of the master reference set are maintained at the NMED Hazardous Waste Bureau; the U.S. Department of Energy–Los Alamos Site Office; the U.S. Environmental Protection Agency, Region 6;

and the Directorate. The set was developed to ensure that the administrative authority has all material needed to review this document, and it is updated with every document submitted to the administrative authority. Documents previously submitted to the administrative authority are not included.

LANL (Los Alamos National Laboratory), March 2007. "2007 General Facility Information," Los Alamos National Laboratory document LA-UR-07-1839, Los Alamos, New Mexico. (LANL 2007, 095364)

LANL (Los Alamos National Laboratory), March 2008. "2008 General Facility Information," Los Alamos National Laboratory document LA-UR-08-1538, Los Alamos, New Mexico. (LANL 2008, 101932)
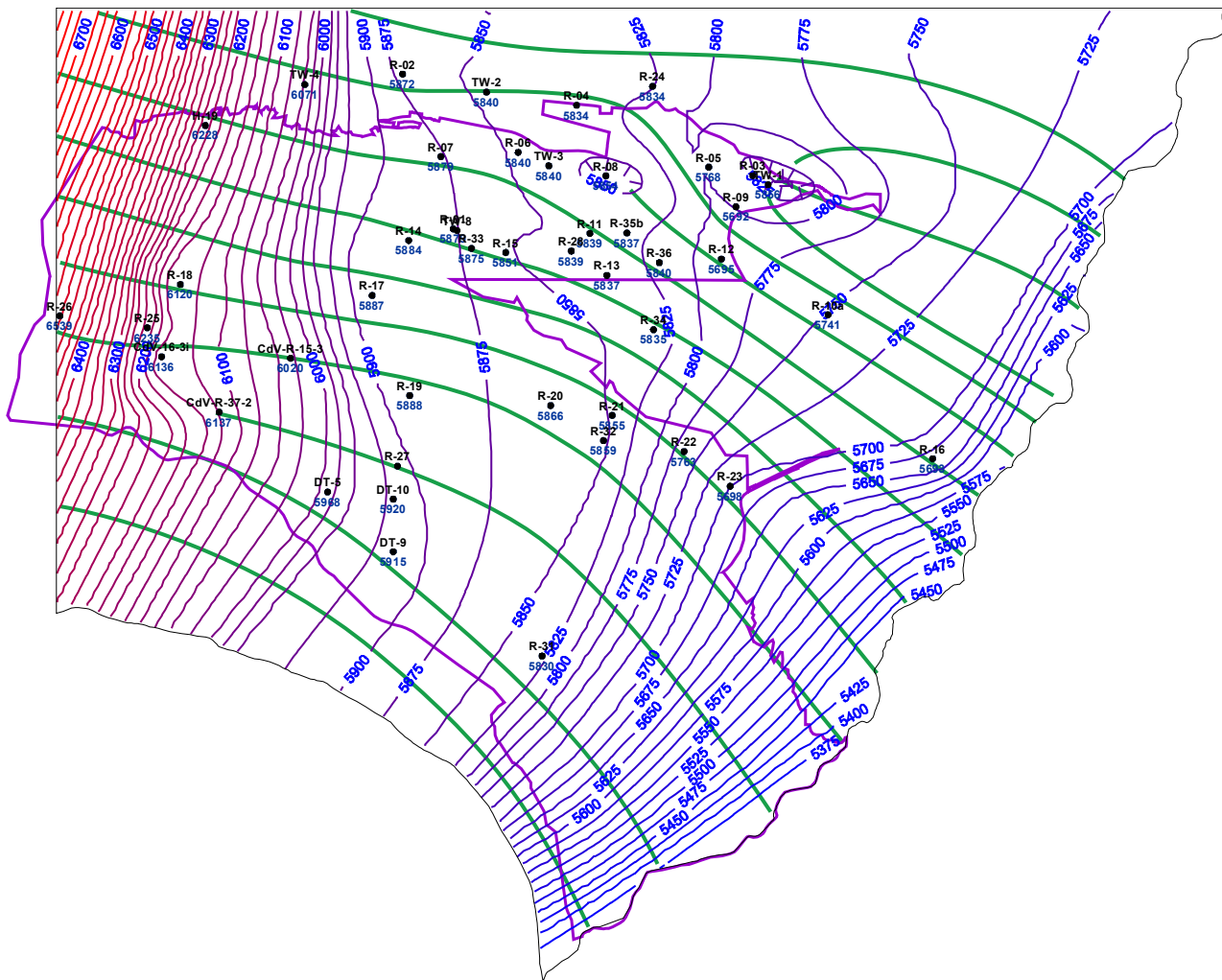
Figure H-1 **Alternative water-table map 1, based on average water-table elevations in January 2006. More recent water levels observed at R-35b and R-36 are also shown.**
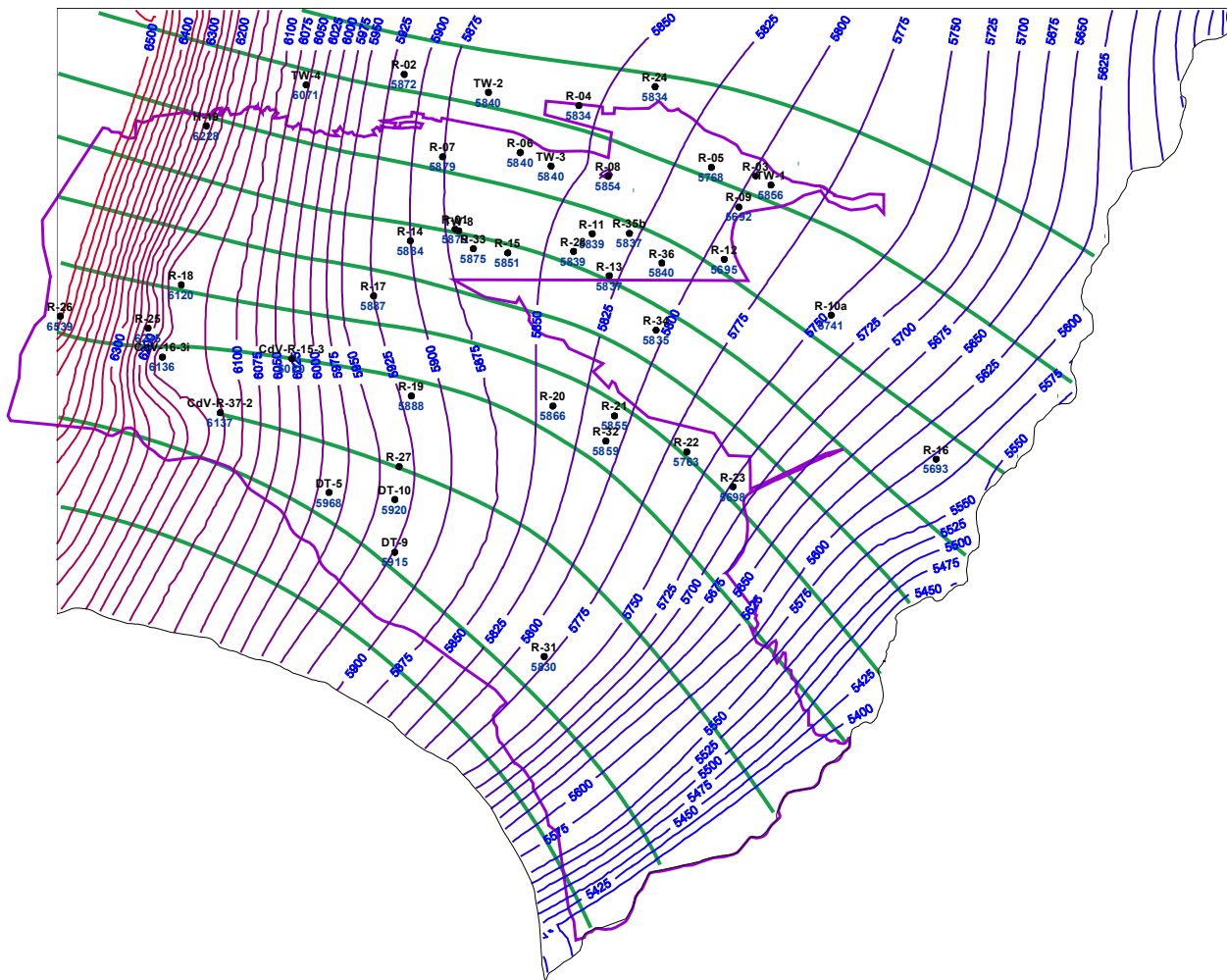
**Figure H-2   Alternative water-table map 2, based on average water-table elevations in January 2006. Generated by modifying alternative map 1 by (1) smoothing the contour lines, (2) reducing mounding near R-8, and (3) excluding the mounding near TW-1. More recent water levels observed at R-35b and R-36 are also shown.**

Appendix I

Estimation of Mounding of the
Regional Aquifer from Recharge Along Sandia Canyon

A mound in the water table beneath Sandia Canyon may result from the significant effluent discharges to the canyon since approximately 1950 (Appendix B and section 2.1). Depending on the height of the mound, water-level gradients could change enough to affect flow directions (Appendix H). For example, significant mounding beneath the canyon could divert flow locally from following the ambient, southeasterly gradient to approximately perpendicular to the canyon axis over the area where the mounding occurs. This analysis estimates the potential mounding that might occur beneath Sandia Canyon.

There are simple analytical approaches to evaluate a potential mound at the regional water table due to recharge along Sandia Canyon. For example, Hantush (1967, 102161) proposed the following equations for predicting the maximum height of the water table beneath a rectangular recharge area for the case of a constant infiltration rate:

$$h_m^2(t) = h_i^2 + \frac{2Rat}{ABk} W\left(\frac{A}{2\sqrt{4at}}, \frac{B}{2\sqrt{4at}} \right)$$

$$a = \frac{kb}{S}$$

$$b = \frac{1}{2}\left[h_i + h_m(t) \right]$$

where h_m [L] is maximum height of a mound above the aquifer base (i.e., the maximum saturated thickness of the aquifer beneath the recharge area; the maximum occurs in the center of the recharge area); h_i [L] is initial height of water table above the aquifer base (i.e., the initial saturated thickness of aquifer); k [L/T], S [–] and a [L^2/T] are hydraulic conductivity, storativity (specific yield) and hydraulic diffusivity of the aquifer, respectively; R [L^3/T] is constant infiltration rate within a rectangular recharge area of length A [L] and width B [L]; b [L] is a linearization constant; and the function W is an integral expression (for more details see Hantush 1967, 102161). The aquifer is assumed to be unconfined (phreatic), to be two-dimensional, and to have infinite lateral extent. The problem is nonlinear, and the solution is obtained using successive iterative approximations. The solution is valid when the water-level increase in the mound (h_m - h_i) is less than 50% of the initial saturated thickness of the aquifer (h_i). If infiltration is applied for a limited period of time, the principle of superposition can be applied to compute the decay of the mound after the infiltration has ceased. If a similar approach is used, the solution can be applied even if substantial transients occur in the recharge.

To estimate the potential ranges in aquifer mounding, the following values for parameters are assumed: k = 20 to 40 m/d (based on the R-11 and R-28 pumping test data), S = 0.1 to 0.3, h_i = 10 to 30 m, R = 662 to1041 m^3/d (175,000 to 275,000 gal./d based on potential ranges discussed in Appendix J section J-6), A = 100 to 3000 m, B = 100 to 1000 m, t = 1 to 100 yr (range of times since the recharge occurred). The parameter ranges above represent potential uncertainty. It should be noted that the range for aquifer thickness (h_i = 10 to 30 m) represents the potential thickness of the uppermost phreatic portion of the regional aquifer. As discussed in section 2.6, hydraulic separation may occur between the shallow and deep sections of the regional aquifer, which will potentially not allow the pressures created by mounding to propagate in the deep portions of the aquifer. Assuming the parameters above, the maximum increase of water-table elevation at the center of the mound can be evaluated for a series of recharge area sizes.

It is important to note that the recharge area is defined at the top of the regional aquifer, not at the top of the vadose zone (ground surface). As a result, the size of the recharge area should capture any diversion and dispersion of recharge flux during flow through the vadose zone (and any potential perching

horizons). Furthermore, in reality the recharge is expected to be spatially heterogeneous and transient. In our analyses, recharge is assumed to be spatial uniform and constant in time. A range of recharge areas is considered. The case of a 100 × 100 m^2 recharge area represents a case of extremely focused recharge along preferential-flow pathways ("fingers") through the vadose zone. The maximum recharge area case (3000 × 1000 m^2) represents a case of highly distributed flow paths through the vadose zone and a potential maximum in the recharge area. Based on the current Sandia Canyon data (surface flow and water-level observations), a recharge area with a size on the order of 1000 × 100 m^2 may be the most probable case. In this way, the analyses are expected to address potential uncertainties in the spatial distribution of recharge and in the resulting uncertainties in potential mounding.

Figure I-1 shows how the water levels are predicted to increase in time for four different recharge areas. Within the explored uncertainty range, the maximum water-level increase might be about 3 m (~10 ft). The computed values represent the maximum increase of water-table elevation at the center of the mound. However, depending on the recharge area and the model parameters, the water-levels decay away from the center of the mound.

It should be noted that the mound is not expected to reach steady-state conditions for 60 yr or more (the time since the intensive discharge started in Sandia Canyon in 1950, Figure I-1). Nevertheless, the transients in the water levels are not substantial. The smaller the recharge area, the larger the mound and the faster the mound approaches steady-state conditions. If the recharge area is large, the mound is more subdued and could still be growing as a result of enhanced recharge in Sandia Canyon since the 1950s. The existing water-level data observed at the monitoring wells may suggest the existence of up to 10 ft of groundwater mounding near areas of local recharge along the canyons (Appendix H). The transients in the water levels at some of the monitoring wells near Sandia Canyon (R-28, R-11, and R-15) are influenced by the pumping of water-supply wells in the vicinity (see Appendix F). However, the long-term (annual, decadal) transients at these wells may be influenced by long-term transient recharge along Sandia Canyon as well. Currently, the data are insufficient to characterize the potential impact of canyon recharge, but future analyses of existing and new data may provide additional constraints about the potential for mounding in this area.

REFERENCE

The following list includes all documents cited in this appendix. Parenthetical information following each reference provides the author(s), publication date, and ER ID number. This information is also included in text citations. ER ID numbers are assigned by the Environmental Programs Directorate's Records Processing Facility (RPF) and are used to locate the document at the RPF and, where applicable, in the master reference set.

Copies of the master reference set are maintained at the NMED Hazardous Waste Bureau; the U.S. Department of Energy–Los Alamos Site Office; the U.S. Environmental Protection Agency, Region 6; and the Directorate. The set was developed to ensure that the administrative authority has all material needed to review this document, and it is updated with every document submitted to the administrative authority. Documents previously submitted to the administrative authority are not included.

Hantush, M.S., 1967. "Growth and Decay of Groundwater-Mounds in Response to Uniform Percolation," *Water Resources Research,* Vol. 3, No. 1, pp. 227–234. (Hantush 1967, 102161)
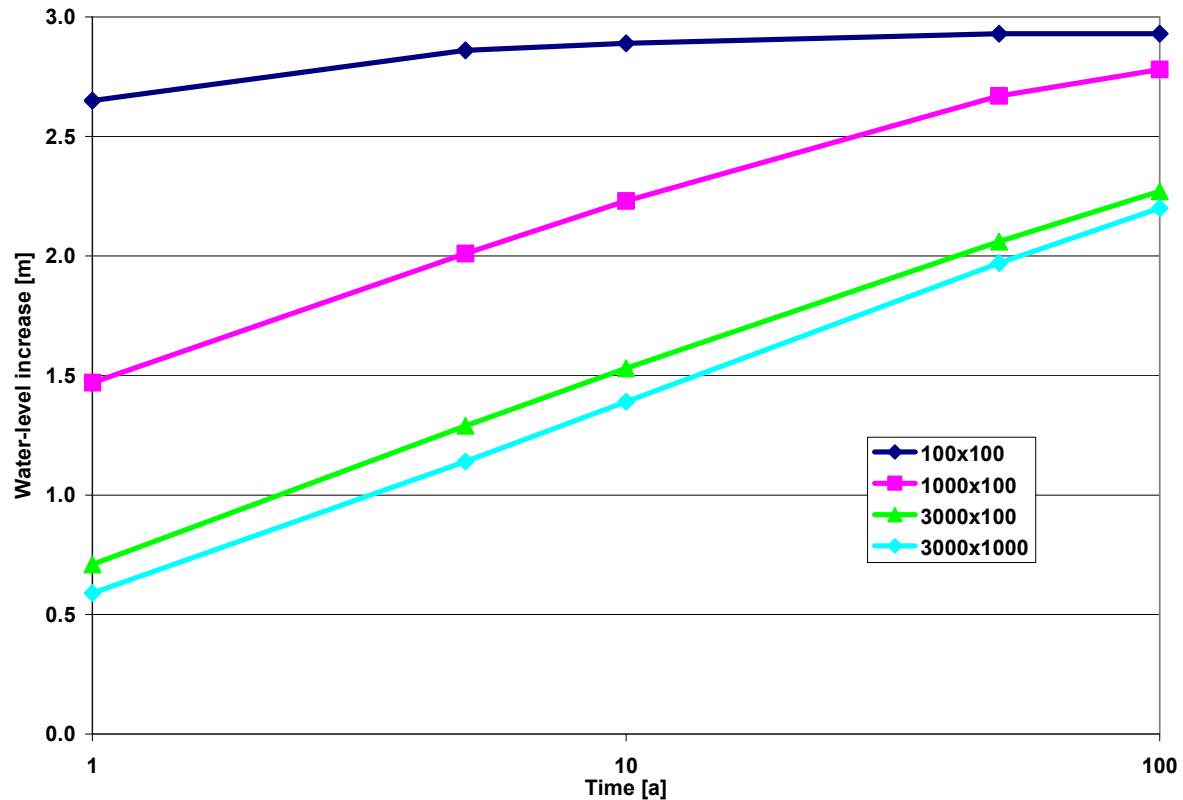
Figure I-1   **Maximum increase of water levels within a mound (at the center of the mound) caused by a constant recharge of 1041 m³/d (275,000 gal./d) distributed over four different recharge areas (*A×B*). The other parameters are *k* = 20 m/d, *S* = 0.1, h_i = 10 m.**

Table I-1
Maximum Water Level Increases Within the Recharge Mound

h_i (m)	k (m/d)	S (-)	R (m³/d)	A (m)	B (m)	$h_m - h_i$ (m)
10	20	0.1	1041	100	100	2.93
10	40	0.1	1041	100	100	1.56
30	20	0.1	1041	100	100	2.16
10	20	0.3	1041	100	100	2.91
10	20	0.1	663	100	100	1.94
10	20	0.1	1041	3000	1000	1.96

Note: Assumes various model parameter values after 50 yr of continuous uniform and constant recharge.

Appendix J

Numerical Simulations of
Chromium Transport in the Subsurface

J-1.0   INTRODUCTION

Numerical flow and transport models of the unsaturated zone and the regional aquifer in the Sandia Canyon area are developed to inform and enhance the understanding of the fate and transport of chromium in the environment. The goals of the Los Alamos National Laboratory (LANL or the Laboratory) study are to develop groundwater flow and contaminant transport models and to use the models to predict potential future contaminant concentrations at monitoring and municipal supply wells. This appendix describes the current state of the development of these models and discusses the modeling results.

Flow and transport simulations are used to predict the migration of chromium in the subsurface. The simulations consider groundwater transport in the unsaturated zone and the regional aquifer. The effects of geochemical interactions of contaminants with rocks along the flow paths are also considered. The implementation of assumptions, boundary conditions, and model parameters implemented in the models honors the conceptual model described in section 2 of this report.

The flow and transport simulations are run with the Finite Element Heat and Mass Transfer code (FEHM) (Zyvoloski et al. 1996, 054421; Zyvoloski et al. 1997, 070147). FEHM was developed by researchers at the Laboratory and is capable of simulating three-dimensional (3-D), time-dependent, multiphase, nonisothermal flow, and multicomponent reactive groundwater transport through porous and fractured media. FEHM has been used in a wide variety of applications. The software is mature, has users throughout the world, and has been certified through the Yucca Mountain Project Software Quality Assurance Program. FEHM is available to the public and operates under various operating systems.

J-2.0   HYDROSTRATIGRAPHIC MODEL

A 3-D hydrostratigraphic framework model was assembled to use as the basis for assigning material properties that govern simulations of groundwater flow and contaminant transport. The model, called the Weston-Cole Fiscal Year 2008 (WC08) model, was created by updating the Cole Fiscal Year 2005 (FY2005) geologic framework model (GFM) (Cole et al. 2006, 095079) to account for data that were either omitted from the FY2005 model or have been obtained since the FY2005 model was constructed. The size and basic geometry of the FY2005 GFM remain the same, but layer surfaces have been adjusted slightly to honor the additional data. This has resulted in some slight changes to the thickness and extent of many of the model layers. The primary difference between the FY2005 and WC08 geologic models is that they were created with different software. The FY2005 model was constructed using ArcINFO while the WC08 model was constructed using EarthVision' Version.7.5.3, developed by Dynamic Graphics. While the grid interpolation techniques are similar between these two software packages, the end products of the two packages are different. ArcINFO defines surfaces that represent the tops of the various geologic units. However, EarthVision uses the stack of layer surface grids to create 3-D solid-volume models, called faces files, for enhanced visualization of the site geology. Simulation results for variables such as saturation or contaminant distributions can be superimposed onto the solid geologic framework (using the EarthVision software) for visualization of results (section J-6). Throughout this section, the term "grid" refers to geologic surfaces defined by sets of regularly spaced points.

The WC08 modeling was conducted using the following generalized procedure:

1.   Assemble an updated database of borehole lithologic contacts and create a separate database of control points that will force pinch-outs of layers, where necessary, so discontinuous layers do not show up in borehole stratigraphic columns extracted from the model. This step is a quality assurance (QA) check.

2. Convert the FY2005 ArcINFO grids (Cole et al. 2006, 095079) to EarthVision's format and extract a database of FY2005 layer surface control points using a 1000-ft horizontal spacing.

3. Create an EarthVision compatible database of layer outcrop control points from the set of lines provided with the FY2005 GFM report (Cole et al. 2006, 095079).

4. Create vertical fault planes from shape files provided with the FY2005 GFM report (Cole et al. 2006, 095079).

5. Perform gridding of each model layer in two passes. The first pass creates a 200-ft resolution temporary grid from the FY2005 200-ft spaced surface control points. The second pass creates a 100-ft resolution final grid by flexing the temporary grid so that it honors (1) the borehole lithologic contacts, (2) the outcrop pattern control points, and (3) the pinch-out control points. Each gridding pass takes into account offsets present in both the "real" and the "control" data that straddle a fault line. The offsets present in the control data were established in the FY2005 geologic model (Cole et al. 2006, 095079).

6. Use a 100-ft resolution digital elevation map (DEM) based on the year 2000 LIDAR data (Carey and Cole 2002, 073784) to create the unconformity that forms the upper surface of the regional model.

7. Calculate model layer residuals and extract modeled borehole stratigraphy to compare with the observed stratigraphy.

8. Crop the WC08 regional Pajarito Plateau model to the groundwater model subdomains discussed below for focused 3-D visualizations of simulation results. A 20-ft resolution DEM is used for subdomain models.

9. Create ArcINFO grids for use in two-dimensional (2-D) mapping of WC08 zone top/bottom elevation and thickness.

10. Create cross-sections for 2-D visualizations of the model interior.

While the basic geometry of the FY2005 geologic model was left in tact, the number of model zones needed to create this geometry was reduced from 36 in the FY2005 model to 28 in the WC08 model. The model layering was simplified by exploiting EarthVision's ability to easily embed a model layer that crosscuts several others, for example the Bayo Canyon basalt unit (Tb 2). In the FY2005 model, any layer bisected by Tb 2 required two or more surfaces to form the portions of the unit above and below Tb 2. In the WC08 model, the stack of non-Tb 2 layers was used to create a temporary faces file, and then the regions occupied by Tb 2 were subsequently overridden by this zone. The Santa Fe basalt (Tb 1) was handled in this same way, although it only affected the Upper Santa Fe (Ts) zone. Figure J-2.0-1 shows a geologic cross-section down the axis of Sandia Canyon generated from the WC08 model. It compares favorably to the conceptual model cross-section shown in Figure 2.0-1 that was prepared manually by geologists from surface and borehole data. Differences between the cross-sections reflect alternative interpretations of structurally high Santa Fe Group sediments in the vicinity of R-36. The WC08 model treats this structural high as an erosional high, whereas Figure 2.0-1 treats it as a fault-bound horst block. Other differences between the two cross-sections arise from how the dips of the Pliocene and Miocene sedimentary units are treated. The WC08 model treats the geologic units as volumes defined by the interpolation of contacts between boreholes. Figure 2.0-1 honors the same borehole data but incorporates into the interpretation the available stratal-dip data from borehole Formation Microimager logs and includes the interpretation that Miocene sedimentary deposits were tilted to the southwest and eroded before the Puye Formation was deposited.

During the numerical simulations of vadose zone transport, special attention was given to the role of lateral diversion of moisture and chromium at dipping geologic interfaces. Diversion is expected to favor

those interfaces separating rocks with strongly contrasting lithologic properties. Examples of these dipping interfaces are given for the base of the Guaje Pumice Bed (Figure J-2.0-2) and the base of the Cerros del Rio basalt (Figure J-2.0-3). Two additional layers were added to the regional model to simulate the lateral diversion of moisture and chromium by internal stratigraphic features of the Otowi Member (Figure J-2.0-4) and the Cerros del Rio basalt (Tb 4) (Figure J-2.0-5). The internal Otowi surface is defined in borehole logs by an abrupt shift in gamma activity partway through the unit. This shift may represent a depositional boundary between ash-flow tuffs with different uranium, thorium, and potassium compositions. The internal surface for the Cerros del Rio basalt represents a stratigraphic contact between tholeiitic basalts in the upper part of the unit and alkalic basalts in the lower part. These basalts are chemically distinct and aerially extensive in the area of interest. Mapping of these basaltic subunits is facilitated by their distinctive borehole gamma signatures. The tholeiite-alkalic basalt interface was included in the modeling effort because it may mimic other interfaces between the numerous individual flow units that make up the Cerro del Rio basalt.

The WC08 model includes the addition of the Quaternary Alluvium (Qal) in portions of Mortandad, Sandia, and Los Alamos Canyons (Figure J-2.0-2). Its inclusion was important for this modeling effort because the numerical simulation of vadose zone infiltration begins at the base of alluvium. The difference in modeled lateral extent between this zone and the regional model causes rendering problems in the regional faces file so the Qal zone can be viewed only in the aforementioned subdomain faces files extracted from the regional model.

WC08 model residuals were calculated for each of the 1523 lithologic contacts in the updated database. Out of these data, 84% of the points were considered valid subsurface zone contacts for modeling. The 84% is composed of 79% "real" points and 5% control points used to force pinch-outs. Model residuals were less than 1 ft for 92% of these valid contacts. Of the remaining valid contacts, the maximum residual was 25 ft and 7% had residuals less than 3.5 ft. The remaining 1% (16 contacts) had an average residual of ~10 ft. Residual statistics for the valid lithologic contacts are summarized by zone in Figure J-2.0-6. This figure shows that the average residual was <1 ft for all but the Tt 1 top zone, which had only two real points to represent this steep surface that is otherwise based on control points. Approximately 14% of the contacts in the database are ground surface elevations where the layers outcrop and therefore do not represent the native, or uneroded, layer surface elevations that EarthVision requires. Another 4% of the data represent contacts with alluvium or regolith and are likewise handled through unconformities rather than deposition of unaltered top surfaces. Eight contacts (1%) were ignored during the gridding process because the data did not appear to agree with data from neighboring boreholes.

Residuals were also calculated for each of the FY2005 surface control points to illustrate areas where the WC08 model differs from the FY2005 model. The differences between the WC08 and FY2005 models over the entire domain and within the chromium study area are illustrated in Figures J-2.0-7 and J-2.0-8, respectively. These figures break the differences down by zone and show the percent of residuals below various residual thresholds. Figure J-2.0-7 shows that, with the exception of four zones (ts_t, tb2_b, tt1_t, and tt2_t), 90% of the differences between the WC08 and FY2005 models are less than 100 ft. The four zones with the greatest differences are also the four with the steepest slopes and the most new points added. The percentage of residuals less than 100 ft is lower within the chromium area because (1) the smaller area contains fewer points for comparison, and (2) this area contributes heavily to the differences observed over the entire model domain.

J-3.0   MODEL DOMAINS AND COMPUTATIONAL GRIDS

The dimensions and design of the computational grid needed for flow and transport simulations at a given site depend on understanding of the relationships between hydrogeology, contaminant-release history,

and site-specific details such as the locations of monitoring wells and water-supply wells. Also of great importance is the spatial scale of the process to be modeled. The focus of studies for this report is along and beneath Sandia and Mortandad Canyons, and the surrounding regions contributing to flow and transport to the regional aquifer. The highest resolution in computational-gridding details is needed along and below the two canyons where chromium was released and is observed at elevated levels in the regional aquifer. For the larger region models, details along the water-table surface are important. Increasing the number of grid nodes along areas of interest creates resolution in the grid that results in more accurate numerical solutions in that area. Increasing nodes in the vertical direction captures thin units and shallow gradients. Resolution in the horizontal direction can be used to capture sloping units and complicated geometries, such as the ground surface. Optimal grid design balances the high number of nodes for better resolution with the need to keep the total number of nodes within a computationally efficient size of fewer than 1 million. Therefore separate site-specific grids are built to the resolution and domain needs of the modeling simulations.

For this study, four grid types were developed. At the smallest domain, but with the greatest geologic accuracy, is a set of one-dimensional (1-D) columns representing the vadose zone along Sandia Canyon. This set of columns was used for the vadose zone modeling presented in the previous flow and transport modeling report (LANL 2007, 098938) and for simulations presented in section J-4. Three increasingly larger domains are used for computational grids as shown in Figure J-3.0-1. The smallest area domain is the 3-D chromium-site model (CRM) designed to perform 3-D simulations of groundwater flow and transport in the vadose zone and the regional aquifer below Sandia Canyon. Simulations using this grid are presented in section J-6. The other two model domains shown in Figure J-3.0-1, the 2-D LANL Groundwater site-scale grid (LGM2D) and the 3-D LANL Groundwater site-scale grid (LGM3D), are used to simulate flow and transport in the regional aquifer on the scale of Pajarito Plateau (section J-5).

The computer code LaGriT is used to create the computational grids used by FEHM. The LaGriT grid generation software is an integrated package for all the grid generation and setup for FEHM input and output, including import of geologic frameworks, grid optimization and refinement, postprocessing, evaluation tools, and data interpolation. LaGriT is also used to generate initial and boundary conditions for FEHM simulations that are mapped directly onto the computational grid. The grid generation approach (Miller et al. 2007, 102466) maintains the geometry and topology of the geologic framework while optimizing the computational grid to ensure accurate and efficient simulations. Once a grid of chosen domain and node spacing has been created, the geologic framework is mapped onto the grid. The EarthVision geologic framework used for all three computational grids is described in section J-2. The grid nodes are imported into the EarthVision software framework, and each point is located within an EarthVision volume representing the shape of the geologic units. These volumes are defined internally by EarthVision as intersecting surfaces th2,t delineate the bottom and top for each volume.

One-dimensional vadose zone simulations along Sandia Canyon were used to calibrate against moisture and contaminant profiles measured in cores from SSC-2, SSC-3, SCC-4 (section J-4). The domain for the 1-D columns is a line of selected wells in the vadose zone extracted at several locations along Sandia Canyon (LANL 2007, 098938). The western portion of the Sandia Canyon line, where no boreholes were completed, consists of points selected at an interval of approximately 1000 to 1200 ft. The eastern portion of the line consists of observed data locations spanning the distance from SCC-1 to PM-3. The columns provide top elevations for each lithologic unit, including the alluvium, in descending order from the ground surface to the water table.

The 3-D CRM domain is shown in green in Figure J-3.0-1. This is the smallest computational grid domain and has sufficient resolution to represent area geology and spans greater vertical depth than the LGM2D and LGM3D models. The grid is used to perform coupled simulations of unsaturated and saturated 3-D groundwater flow and transport along the expected contaminant flow paths in the subsurface below

Sandia Canyon (section J-6). The CRM grid has variable refinement with the finest resolution located along Sandia and Mortadad Canyons at a spacing of 15.62 m horizontal and 12.5 m vertical. The lateral extent of the computational grid is centered near Sandia Canyon while including important data locations such as monitoring well LAOI(A)-1.1 to the north in Los Alamos Canyon, water-supply well PM-1 to the east near NM 4, and R-13 in Mortadad Canyon. The resulting computational grid extends from UTM NAD83 coordinates 495000, 537750 m at the lower left corner to 503000, 542000 m at the upper right corner in the New Mexico State coordinate system. The grid bottom is truncated by a horizontal surface with elevation of 1124 m above sea level (asl) and at the top by the ground surface with a maximum elevation of 2324 m asl. The CRM grid has 404809 nodes and 2319806 tetrahedral elements (Table J-3.0-1).

The 3-D CRM computational grid is predominantly structured but includes zones of telescoping grid refinement to restrain the total number of nodes. The outside perimeter of the grid has 250 m horizontal node spacing; the resolution increases inward toward Mortadad Canyon to 125 m and 62.5 m. The region between the coarse outside grid and Sandia and Mortadad Canyons is refined inward to horizontal 62.5 m and 31.25 m spacing. The primary region of interest at the canyon bottoms surrounding lower Sandia and the confluence of Mortadad and Ten Site Canyons has the highest horizontal resolution with 15.62 m spacing. The vertical resolution increases from bottom to top in the same manner as the horizontal resolution. The vertical spacing starts with 200 m at the bottom and perimeter then decreases by halves to the high-resolution region of 12.5 m vertical spacing. Figures J-3.0-2 and J-3.0-3a show views of the CRM grid with the telescoping spacing. A selected group of well locations in the vicinity of the canyons helps reference important grid areas. The well group used in Figure J-3.0-2 includes R-15, R-13, R-28, R-11, R-35a, R-35b, PM-3, and O-4.

The EarthVision software used to build the geologic framework (section J-2) is also used for 3-D viewing of the geologic units, thus allowing comparisons of the resulting grid geology to the source geologic framework. For example, during inspection of the grid representation of hydrostratigraphic units, the Tschicoma unit north of the focus area was not represented because of a coarse grid spacing. To address this, the regions selected for refinement were extended further west to better capture a continuous unit and to maintain the rounded lobe shape of this formation, which was deemed to be a potentially important hydrologic control (Miller et al. 2007, 102466). During analysis of the grid it was found that the thin Guaje Pumice Bed (Qbog) layer was not captured adequately. This layer dips towards Mortadad Canyon and may divert flow laterally (Figure J-2.0-2). Much of the layer is less than 9 m thick (Figure J-2.0-1), too thin to be captured with the vertical grid resolution of 12.5 m. To represent this layer in the simulations, the nodes of the grid were reselected based on the intersection of the EarthVision Qbog surface grid in such a way that the grid layer consisted of at least one layer of nodes for the full domain, and as a continuous and connected volume through the high-resolution area. Figure J-3.0-3a shows this grid resolution by a cut along and perpendicular to Sandia Canyon. This figure shows the grid colored by the reselected Qbog and rest of unit materials as defined in the EarthVision WC08 framework (section J-2.0). The Guaje Pumice Bed is shown as the thin olive-colored layer above the red-colored Cerros del Rio basalt.

In addition to the normal FEHM setup files that include all grid and geologic definitions, grid nodes at the top of the model and within alluvium are located and provided as input for FEHM. These grid nodes are found by using the quaternary alluvium (Qal) boundary as defined in the EarthVision WC08 model (section J-2.0). The Qal outlines (Figures J-2.0-2 to J-2.0-5) were used to identify top grid nodes in each of the three canyons. The Sandia Canyon Qal nodes were further broken into four segments, as shown in Figure J-3.0-2b. The eastern boundary of each Qal segment from west to east are; gage station E123.8 (segment S4), gage station E124 (segment S5), the end of the refined grid at x = 500250 m (segment S6), and to the eastern end of the EarthVision alluvium boundary (segment S7). These segments are used to define the boundary fluxes that represent enhanced recharge in Sandia Canyon (section J-6).

The other two models in Figure J-3.0-1, LGM2D and LGM3D, are used to simulate 2-D or 3-D chromium transport in the regional aquifer on the scale of the Pajarito Plateau. These models cover a much larger domain than the CRM but preserve grid size by using larger horizontal spacing and a much smaller vertical extent. The model domains of LGM2D and LGM3D (Figure J-3.0-1) extend from the flanks of the Sierra de los Valles on the west to the Rio Grande on the east. The entire Laboratory, as well as existing monitoring and Los Alamos County water-supply wells, are within the boundaries of these domains. Both grids are truncated at the top by the shape of the regional water table.

LGM2D (Figure J-3.0-4) is designed to be a pseudo–3-D model with a single layer of uniformly spaced elements 25 m wide. Figure J-3.0-3c shows a close-up view of the grid resolution and units. The north edge of the grid is at y = 543150 m, the west edge is at x = 490750 m, and the rest of the grid has an irregular shape defined by the boundary of LGM3D with a southern tip at y = 526575 m. The computational grid is practically 2-D, characterizing the flow and transport along the phreatic zone of the regional aquifer. However, the computational model domain is pseudo–3-D by allowing contaminants to flow downward along vertical flow paths through hydraulic windows toward water-supply wells. Figure J-3.0-4 shows the hydrostratigraphy along the water table within LGM2D model domain. The total number of nodes and tetrahedral elements are 693948 and 2072862, respectively (Table J-3.0-1).

LGM3D is a 3-D model of the regional aquifer. Laterally, the grid cells are uniform and equal to 125 × 125 m. Vertically, the size of the grid cells vary from 6.25 m at the water table to 100 m at the bottom. The total vertical thickness of the grid is about 500 m below the water table defined by a flat bottom at 1000-m elevation. Vertical refinement is placed where hydrostratigraphic units have limited vertical thickness and to capture the sloping elevation of the water table surface and unit bottoms, such as the Cerros del Rio basalt. Figure J-3.0-3b shows a close-up view of the grid resolution and units. The 6-m vertical resolution along the grid top captures the curving shape of the Cerros del Rio basalt and Puye Formation better than the 12.5 m vertical spacing in the CRM grid (Figure J-3.0-3a) but represents fewer total number of units (Table J-3.0-1). The total number of nodes and elements are 520664 and 2965716, respectively (Table J-3.0-1).

The finer lateral grid resolution of LGM2D (25 × 25 m) when compared to LGM3D (125 × 125 m) allows for better simulation of lateral transport of contaminant plumes along the water table. It also allows for better representation of the location of monitoring and pumping wells. The vertical extent of LGM3D allows for better representation of the vertical spreading of the contaminant plumes (Figures J-3.0-3b and J-3.0-3c).

The 3-D geologic model described in section J-2 of this appendix defines the spatial distribution of various hydrostratigraphic units used in the construction of the computational grids. Table J-3.0-1 lists the hydrostratigraphic units identified in the three models and describes their spatial representation within each model domain. The computational grids of the 2-D and 3-D models are designed to sufficiently characterize medium heterogeneity, and the total number of nodes does not exceed 1 million; this limitation is caused by the size of the computer memory. Table J-3.0-2 lists the permeability and porosity ranges identified for each of the hydrostratigraphic units. The simulations presented in sections J-4 through J-6 use values from these ranges to represent the hydrologic properties.

J-4.0 1-D VADOSE ZONE CALIBRATION

One-dimensional vertical models (the computational grids are described in section J-3) located near the boreholes SCC-2, SCC-3, and SCC-4 are used to estimate the spatial heterogeneity of infiltration fluxes into the vadose zone by calibrating to moisture content and chromium and molybdenum concentration data measured on core samples collected from these boreholes. The calibrations also allow for the

estimation of uncertainty in other model parameters, such as permeability, porosity, and retention properties of various hydrostratigraphic units, to be constrained. The calibrated models are applied to estimate the uncertainty in the chromium concentrations at the bottom of the vadose zone (the top of the regional aquifer) at these three locations. These simulations use an inverse analysis to calibrate to the field data and subsequently yield information about the uncertainty in the predictions.

J-4.1 Methodology

The 1-D models are calibrated using the Levenberg-Marquardt optimization algorithm (as implemented in the code PEST). The objective function subject to minimization is defined as

$$\Phi = [\mathbf{c} - f(\mathbf{b})]^{\mathrm{T}} \mathbf{W}[\mathbf{c} - f(\mathbf{b})]$$

where c is a vector [N×1] of optimization targets, b is a vector [M×1] of model parameters, W is a diagonal weight matrix [N×M], and *f* is the model. If Φ is minimized, the algorithm searches for the maximum-likelihood parameter set **b** that provides the best fit between simulated $f(\mathbf{b})$ and measured **c** quantities. The vector of optimization targets includes (1) water-content and (2) chromium- and molybdenum-concentration data. **W** represents the relative weight of each optimization target defined subjectively based on the magnitude of the calibration data. The calibration targets for the three simulations, which are data collected at boreholes SCC-2, SCC-3, and SCC-4 (LANL 2006, 094431), and their weights are listed in Tables J-4.1-1, J-4.1-2, and J-4.1-3, respectively. These targets do not include data from the alluvium (Qal) because the 1-D grids start just below Qal. The vector **b** includes various model parameters considered in the inverse analysis, as described in section J-4.2.

Using the best estimates from inverse analysis, the model predicts the concentration of chromium at the bottom of the vadose zone (right above the regional water table). Because the model parameters are uncertain, this prediction is also uncertain. To evaluate the uncertainty in this model prediction, a predictive analysis is performed to determine the range of possible predictions, given parameter uncertainty and uncertainty in the calibration data. The basis for this analysis is as follows. In the following equation, prediction *p* is defined as

$$p = f'(\mathbf{b})$$

where *f'* is the model under predictive conditions, and unknown parameter set **b** that maximizes/minimizes *p* subject to

$$[\mathbf{c} - f(\mathbf{b})]^{\mathrm{T}} \mathbf{W}[\mathbf{c} - f(\mathbf{b})] = \delta\Phi_{min}$$

where Φ_{min} is defined for the best (maximum-likelihood) estimates $\mathbf{b}_{ML}$. For the maximum-likelihood case,

$$\delta = \frac{N}{N-M} F_{\alpha}(N, N-M) + 1$$

where *F* is the F-distribution and α is the confidence level. The constrained optimization of **b** is solved as an iterative nonlinear Lagrangian problem as proposed by Vecchia and Cooley (1987, 102323). The solution is obtained using the code PEST.

J-4.2   MODEL SET-UP

The vadose zone calibration simulations use the assumptions and boundary conditions from the previous modeling study (LANL 2007, 098938). The simulation approach here, however, is different from in that study. The previous study used Monte Carlo sampling from parameter distributions to predict many sets of flow and transport results using 18 1-D vadose zone columns representing Sandia Canyon. The results from that study did not adequately match field data from the SCC boreholes. For that reason, an inverse approach is being investigated to identify input parameter ranges that satisfy the calibration targets in Tables J-4.1-1 through 4.1-3. The simulations are run with FEHM coupled with the PEST code, which performs parameter estimation and evaluation of uncertainty in the model predictions.

Many of the model-input parameters are estimated by the inverse models for the three SCC boreholes; the calibration ranges set for these parameters are shown in Table J-4.2-1. These are grouped as water fluxes (watflux); chromium and molybdenum mass fluxes (crflux, moflux); hydrologic properties (perm, alpha, por); dispersivity (vz_disp); and adsorption coefficients (k_d). These parameters apply to the numerical model set-up as described below.

J-4.2.1   Boundary Conditions

Water Source: An initial steady-state flow field is calculated for each of the simulations by defining the water flux at the upper boundary to be equivalent to a 50 mm/yr infiltration rate. Once steady state is achieved, higher fluxes representing two time periods (q1 and q2 in Table J-4.2-1) characterize discharge to Sandia Canyon from National Pollutant Discharge Elimination System (NPDES) outfall 01A-001 (see section 2.1 of this report). The first time period is 1950 to 1991, when the Technical Area (TA-03) power plant cooling towers used treated sewage effluent as their primary water source. The second time period is 1992, when the Laboratory's TA-46 Sanitary Wastewater Systems Consolidation (SWSC) plant came on line, to the present day. The consolidated effluent is discharged to Sandia Canyon at TA-03, and its volume is larger than the previous effluent volume. The bottom boundary of the 1-D columns is located just above the water table, and it is held at a constant saturation of 0.98 throughout the simulations.

Contaminant Source: Chromium mass fluxes are described using four time periods (cr1, cr2, cr3, and cr4 in Table J-4.2-1). These are derived from the product of measured surface water concentrations and outfall volumes, as described in detail in a Laboratory report (LANL 2007, 098938). The first period is from June 1956 to April 1972, which is the active period of chromium use at the power plant (LANL 2006, 094431). The second time period extends from April 1972 until 1989. It reflects decreased concentrations in response to discontinued chromium use. The third period is for 1990 and 1991 and assumes a further decrease in surface water concentration. The last is from 1992 (when water discharges increase) until 2007, and surface water concentrations remain low.

Molybdenum mass fluxes are described using two time periods (mo1 and mo2 in Table J-4.2-1) and are also derived from measured surface water concentrations and outfall volumes, as described in a Laboratory report (LANL 2007, 098938). Molybdenum was reportedly used at the power plant from 1993 to 2001 (LANL 2006, 094431), but elevated levels of molybdenum were detected in Sandia Canyon surface water between 1991 and 2001. The first time period is for 1991, and the second is for 1992 to 2007.

It is important to note that although the mass flux ranges were originally derived from the water fluxes and the surface water concentrations, this coupling was not maintained during the calibration exercise. Therefore, the final simulation results were checked to ensure the calculated mass fluxes were within reasonable ranges.

J-4.2.2 Hydrologic and Transport Properties

The simulations were run using unsaturated-zone hydrologic properties based on the van Genuchten formulation for the retention curve (Van Genuchten 1980, 063542). Ranges for the saturated permeability, van Genuchten alpha and the porosity are defined for all of the stratigraphic units present in the 1-D columns (Table J-4.2-1). These ranges are based on parameter distributions given in Appendix D of the previous flow and transport report (LANL 2007, 098938). However, as part of the calibration process some permeability ranges were made broader beyond those reported in the previous report. The inverse analyses demonstrated that broader permeability ranges for some of the parameters improved the match to calibration data. The minimum permeability for the Tpf was decreased from $10^{-12.2}$ to $10^{-13.2}$ m^2, and the maximum permeability values for the Qct and Qbt1g were increased from $10^{-12.5}$ and $10^{-11.4}$ m^2 to 10^{-11} and $10^{-10.5}$ m^2, respectively.

Ranges for adsorption coefficients for chromium and molybdenum adsorption onto tuff (kd_cr_tuff, kd_mo_tuff, Table J-4.2-1) were used as specified in Appendix D of the previous flow and transport report (LANL 2007, 098938). In addition, independent ranges for adsorption coefficients for the Qct (kd_cr_ct, kd_mo_ct) with higher maximums were defined because chromium concentrations measured in pore water and by acid digestion of Qct indicate that this rock may adsorb chromium more strongly than the other tuffs (LANL 2006, 094431). The dispersivity was also assumed to be an uncertain parameter (vs_disp, Table J-4.2-1).

J-4.3 Results and Discussion

Figures J-4.3-1 through J-4.3-3 show the calibration data and the optimized solutions for moisture content and chromium and molybdenum concentrations for SCC-2, SCC-3, and SCC-4, respectively. These figures show the solution over two scales, the depth of the respective SCC borehole and over the entire vadose zone beneath Qal to the regional aquifer. The figures also show the hydrostratigraphic units along the boreholes and their contacts. Tables J-4.3-1 through J-4.3-3 show the best estimates for the parameters that lead to these solutions. The mass fluxes given in Tables J-4.3-1 through J-4.3-3 are converted to equivalent infiltration rates, which are given in Table J-4.3-4. The estimated infiltration rates range between approximately 1 and 6 m/yr for these three SCC boreholes, which have the highest moisture contents of the six SCC boreholes. Resulting travel times to the regional aquifer for a conservative (e.g., nonsorbing) contaminant would be approximately 10 to 40 yr at these infiltration rates.

For the SCC-2 data, the optimized solution fits all three data sets reasonably well (Figure J-4.3-1). One chromium data point (2.56E-05 kg/kg measured at an elevation of 2042 m, Table J-4.1-1) was not used for calibration (it has a weight of zero) because it varied so much from the rest of the chromium profile and prevented a good solution. The data at this location are consistent with the conceptual model because chromium (which was released before molybdenum) is observed deeper than molybdenum.

For the SCC-3 data, the optimized solution fits the moisture content and the molybdenum profiles reasonably well, but it does not match the lower portion of the chromium profile (Figure J-4.3-2). The solutions for SCC-2 and SCC-3 predict that the chromium concentrations may be elevated below the depth of the boreholes (Figures J-4.3-1b and J-4.3-2b). At SCC-4, the model reproduces the elevated chromium concentration within Qct by predicting high levels of adsorption (high values for K_d) within this unit. There are other conceptual explanations of this behavior that do not invoke such a high level of adsorption in Qct (for example, 3-D flow effects or transient infiltration). In fact, conditions at SCC-4 do not fit the assumptions of the conceptual model applied for these simulations. The borehole is located near SCA-4 where alluvial water levels are largely controlled by stormwater runoff (see Appendix C). At this location, the infiltration rates and the contaminant concentrations are likely to be highly transient rather than mostly steady (with step changes) as the current model assumes.

The inverse model is applied to compute the sensitivity of model parameters related to calibration data along each borehole. The sensitivity coefficients are listed in Tables J-4.3-1 through J-4.3-3. The sensitivity coefficients associated with SCC-2 are also plotted in Figure J-4.3-4. Larger values of the sensitivity coefficient indicate greater importance of the respective model parameter in the model calibration. The sensitivity coefficients are computed directly in the inverse process by assessing how much the model predictions change in response to a change in the individual model parameters. As a result, the sensitivity coefficients are linear (assume a linear model), local (related to the current best estimate), and decoupled (do not account for how coupled changes in model parameters influence model predictions). As expected, parameters such as water fluxes and the chromium mass flux (during the period when chromium was used, cr1) are among the most important parameters.

The inverse model is also applied to compute the sensitivity of model parameters related to predicted concentrations of chromium and molybdenum at the top of the regional aquifer. The sensitivity coefficients are also listed in Tables J-4.3-1 through J-4.3-3; the sensitivity coefficients associated with SCC-2 and the concentrations reaching the aquifer are plotted in Figures J-4.3-5 and J-4.3-6. The sensitivity coefficients are computed directly in the inverse process by assessing how much the model predictions change in response to a change in the individual model parameters. The analysis demonstrates that not all the model parameters that are important in the overall calibration process are also important when estimating the concentration of chromium and molybdenum arriving at the top of the regional aquifer and vice versa (Tables J-4.3-1 through J-4.3-3).

To further investigate uncertainty in the model predicted concentration of chromium at the top of the regional aquifer, the inverse model is executed in predictive mode. In this case, the model is constrained to match the calibration data (observed water content and chromium and molybdenum concentrations along the boreholes), but it is also forced to maximize or minimize the predicted concentration of chromium at the top of the regional aquifer. In this process, the model parameters are also forced to stay within the specified uncertainty ranges (Table J-4.2-1). The best estimates of chromium concentrations circa 2007 at the bottom of the vadose zone (just above the regional water table) are listed in Table J-4.3-5. The best estimates for SCC-2, SCC-3 and SCC-4 correspond to the chromium profiles presented in Figures J-4.3-1 through J-4.3-3, respectively. Table J-4.3-5 also lists the minimum and maximum chromium concentrations arriving at the regional aquifer that the model can predict and still be consistent with the calibration data and the uncertainty ranges of model parameters. The predictive uncertainties represent 95% confidence intervals. For SCC-2, the model predicts that the chromium concentration arriving at the regional water table can be as low as 50 parts per billion (ppb), but the maximum concentration (8,500 ppb) is not substantially higher than the best estimate (6,000 ppb). The inverse model results associated with minimum and maximum predicted chromium concentrations at the bottom of the vadose zone near SCC-2 are plotted in Figures J-4.3-7 and J-4.3-8. The chromium concentrations at the bottom of the vadose zone near SCC-3 and SCC-4 are even better constrained; the minimum and maximum in the model predictions are not substantially different from the best estimate.

The model parameters associated with the maximum and minimum predictions (confidence level of 95%) of chromium concentrations at the bottom of the vadose zone near SCC-2 are listed in Table J-4.3-6. Most of the model parameters did not deviate substantially from their best estimates. Only a few parameters changed and appear to be important for obtaining the maximum and minimum in the model predictions; these parameters are marked in the table. It is important to note that the permeability and porosity uncertainties do not seem to substantial affect model predictions, except for perm_tf, por_tf and por_tpf. The uncertainty in the model predictions is influenced by uncertainties related to infiltration rates (q1 and q2), chromium mass flux (cr1 and cr2), adsorption in Cerro Toledo (kd_cr_ct), and vertical dispersivity (vz_disp).

J.4.4   Summary of 1-D Vadose Zone Simulations

Three inverse models are developed to analyze data collected along boreholes SCC-2, SCC-3, and SCC⁻4. The estimates of model parameters obtained using the three different inverse models are consistent. The inverse analysis results will be applied to address the uncertainty in the model parameters of the vadose zone in general. The results suggest that infiltration rates are spatially variable, high (potentially 1 to 6 m/yr), and probably time dependent. Chromium concentrations predicted at the base of the vadose zone are consistent with the concentrations predicted at the entry points based on the regional aquifer modeling. In this case, it is assumed that due to dilution the contaminant concentrations at the bottom of the vadose zone represent one-quarter to one-half the contaminant concentrations at the top of the regional aquifer.

J-5.0   REGIONAL AQUIFER MODELS

This section discusses regional aquifer models. In section J-5.1, the 2-D regional aquifer model LGM2D (see section J-3) is used to estimate the potential arrival locations for chromium entering the regional aquifer and detected in monitoring wells near Sandia and Mortandad Canyons. The analysis predicts current-day (circa 2007) chromium distributions in the regional aquifer that are consistent with the calibration targets presented in Appendix G. In section J-5.2, both analytical and numerical models (LGM3D, section J-3) are used to estimate the vertical extent of the chromium plume down gradient from R-28.

J-5.1   Identification of Potential Contaminant-Arrival Locations at the Top of the Regional Aquifer

Chromium is detected at monitoring wells R-28 and R-11 in the regional aquifer at concentrations above background levels. These detections may be associated with a chromium plume that arrives at a single or at multiple locations at the top of the regional aquifer. Both scenarios are considered below. No other chromium detections above background concentrations are observed at the other wells near Sandia Canyon, except potentially at R-15 (Appendix G). Observed chromium concentrations in the regional aquifer may be used to estimate the potential locations (entry points) where chromium arrives at the top of the regional aquifer. A brief discussion of the available techniques and the methods applied in this report to evaluate the location of the contaminant arrivals at the top of the regional aquifer is presented in section 3.

A map of average chromium concentrations at the monitoring wells is presented in Figure J-5.1-1. A visual inspection of the concentration map (Figure J-5.1-1) and the potential structure of the groundwater flow near Sandia Canyon (Figures J-5.1-2 and J-5.1-3) suggests that even without sophisticated modeling analyses, the location where chromium enters the regional aquifer may not be located very far (~1–2 km) upgradient of R-28. Approximate, potential contaminant-arrival areas causing the elevated chromium concentrations at R-28 and R-11 are marked in Figures J-5.1-2 and J-5.1-3. Inverse modeling analyses can provide a more accurate estimate.

Two conceptual models of the water table are shown in Figures J-5.1-2 and J-5.1-3. Water table conceptual models are discussed more fully in Appendix H. It should be noted that according to the first water table map (Figure J-5.1-2), the groundwater flow near R-28 has slightly more southern components than in the second water table map (Figure J-5.1-3). According to the first map, groundwater flow is affected by local recharge along the canyons. The first water table map also matches the observed water-level data more precisely (Appendix H).

The application of inverse modeling techniques requires the definition of calibration targets. Taking into account various uncertainties, it is estimated that if a numerical model predicts chromium concentrations within given ranges, it can be considered adequate (calibrated). The rationale for the calibration ranges is discussed in Appendix G. For example, the calibration range for the chromium concentration at R-28 is defined to be between 300 and 700 ppb. The calibration ranges are presented spatially in Figure J-5.1-4.

J-5.1.1 Methodology

To estimate chromium-arrival locations at the top of the regional aquifer, 573 potential locations (entry points) are considered (Figure J-5.1-5). These represent potential breakthrough locations at the top of the regional aquifer in the vicinity of Sandia and Mortandad Canyons for chromium that was released at the surface in Sandia Canyon (or possibly in Mortandad Canyon). Although chromium migrated by a combination of surface-water, alluvial-groundwater and vadose zone transport pathways to the regional aquifer, the exact pathways are not important for this analysis because the potential entry points at the regional aquifer are defined only by constraining the regional aquifer model such that it reproduces the currently observed chromium concentrations and relative distributions in the regional aquifer.

The potential entry points are uniformly spaced at 100-m intervals. The individual entry locations are assumed to have a relative small lateral size of 10×10 m^2. (The squares identifying the entry locations in Figure J-5.1-5 do not represent the size of the entry location; they are intended for visualization purposes only.) For each of these locations, a numerical inverse model is created to estimate the required characteristics of the chromium source upon its arrival at the top of the regional aquifer, so this source produces chromium concentrations that are consistent with the observations at the monitoring wells. Concentrations at all of the monitoring wells are considered, but only wells near Sandia Canyon effectively constrain the numerical model. In this way, 573 inverse models are solved—one solution for each entry location. The inverse analyses are constrained to produce models having parameters that are consistent with existing knowledge and data about the site. A summary of the existing uncertainty in the model parameters is presented in Appendix E of the previous chromium fate and transport modeling report (LANL 2007, 098938). The ranges for different model parameters are listed also in Table J-3.0-2 in this report. For some of the entry locations, the inverse model may estimate that it is impossible to create a numerical model that is consistent with all the existing data, and specifically with observed chromium concentrations. In these instances, the inverse models may be consistent with the chromium observations at some of the monitoring wells but not at all of them. Only the inverse models that are consistent with all the chromium observations are selected because in this way the model will be calibrated and will adequately represent the current site conditions. This methodology allows not only the development of numerical models that are calibrated and coherent with the existing data, but it also allows the estimation of the uncertainty in the model predictions. The chromium concentration predictions of all the numerical models are within the predefined calibration ranges. Most importantly, this approach allows potential contaminant-arrival locations at the top of the regional aquifer to be identified.

The methodology for identification of contaminant-arrival locations is general, and it can consider wide ranges of uncertainties related to conceptual models (e.g., alternative water table maps), model parameters, single and multiple arrival locations (simultaneously affecting regional aquifer concentrations), and transients in the contaminant mass arriving at the top of the regional aquifer. However, the analysis below is focused on the case of a constant-concentration source arriving at the top of the regional aquifer. The assumption that the concentration arriving at the regional aquifer is steady is somewhat consistent with the current observations of chromium concentration at the regional monitoring wells, which are also relatively steady (section 2.6). This situation is not expected to remain indefinitely because the original chromium source released to Sandia Canyon had a finite release period

(section 2.1). However, the assumption of a steady concentration can be applied as an approximation to evaluate the current distribution of the chromium mass in the regional aquifer.

The steady-concentration assumption is also supported by the relatively high estimates for the ambient groundwater velocities near R-28 (section 2.6). To estimate the groundwater velocities, the following parameters are considered: hydraulic gradient ~0.005 (Appendix H); permeability 20–40 m/d based on the R-11 and R-28 pumping test data (Kleinfelder 2004, 090048; Kleinfelder 2005, 090044); and effective transport porosity 0.1 based on literature data (cf., Freeze and Cherry 1979, 088742). As a result, the groundwater transport velocity in the regional aquifer near R-28 may be on the order of 365–730 m/yr. The chromium plume may have traveled for only 2 to 3 yr before it was detected at R-28 (if the source is within 1–2 km upgradient of R-28, as discussed above). The high ambient velocities will cause the recent concentrations at the contaminant entry point, rather than any past transients, to impact the observed current concentrations at the monitoring wells. As a result, it will be difficult to evaluate what the past chromium concentrations were when they arrived at the top of the regional aquifer because the data regarding past chromium concentrations in the regional aquifer are insufficient. Therefore, past (as well the future) chromium concentrations arriving at the top of the regional aquifer are best evaluated using the vadose zone model (see sections J-4 and J-6 in this appendix and section 4.1 of the report).

The high ambient fluxes will also cause the contaminant plume to quickly reach a relatively steady shape in the area near Sandia Canyon. Numerical simulations (not presented here) demonstrate that the steady plume may be achieved within 10 yr. It is important to note that in the case of a steady plume, the spatial distribution of contaminant concentrations (as well as the shape of the plume) depends only on the dispersivity and not on other hydrogeological parameters (permeability, porosity). Therefore the inverse analyses presented below only consider uncertainty in the dispersivity. The model predictions of the spatial distribution of chromium concentrations are insensitive to permeability and advective transport velocity.

The inverse analyses presented below are based on the LGM2D model (see section J-3). LMG2D is applied because it is more computationally efficient than the more complicated three-dimensional model LMG3D. Future work may focus on a smaller area having fewer number of potential entry locations than the area analyzed here (Figure J-5.1-5). This may allow the use of more sophisticated numerical models such as LMG3D.

The model parameters applied in the model are listed in Table J-3.0-2, except that in this analysis the permeability of Puye hydrostratigraphic units is increased to $10^{-10.5}$ [m^2] (~40 m/d) to match the estimated permeability at R-28. The inverse model also uses ranges for longitudinal (50–150 m) and transverse dispersivity (5–15 m). It is demonstrated in the literature (e.g., Neuman 1990, 090184) that the dispersivity is dependent on the distance of plume migration. Typically, the longitudinal and transverse dispersivities are assumed to be 1/10 and 1/100 of the distance, respectively. If the plume migrated shorter distances, the dispersivities are expected to be proportionally smaller as well. FEHM currently does not directly compute scale-dependent dispersivities. To reproduce the potential dispersion for different scales of migration, a series of model runs is executed with different dispersion coefficients. As a result, the inverse model cannot continuously vary the dispersivity values but can select between the predefined set of values. The current analysis uses three sets: (1) longitudinal dispersivity = 150 m, transverse dispersivity = 15 m; (2) longitudinal dispersivity = 100 m, transverse dispersivity = 10 m; and (3) longitudinal dispersivity = 50 m, transverse dispersivity = 5 m.

J-5.1.2 Results and Discussion

J-5.1.2.1 Identification of a Single Potential Entry Location

Initially in the inverse analyses, it is assumed that the observed concentrations at R-28 and R-11 are caused by a plume originating from a single entry location. In this way, the hypothesis that R-28 and R-11 show evidence of a contaminant plume originating from a single entry location is tested.

The first set of results presented below uses the water table map presented in Figure H-1 (also Figure J-5.1-2) as an initial boundary condition. The analysis also initially assumes fixed dispersivity coefficients: longitudinal dispersivity equal to 100 m; transverse dispersivity equal to 10 m. These values are based on literature data assuming that the distance of plume migration before reaching R-28 and R-11 is on the order of kilometers.

The inverse analysis is first applied taking into account the chromium concentrations observed at R-28. If all the 573 inverse models are solved in an attempt to match the calibration range at R-28, 500 of the models can actually be calibrated. The entry locations at the top of the regional aquifer that can produce acceptable chromium concentrations at R-28 are shown in Figure J-5.1-6. The rest of the entry points cannot reproduce this concentration range because most are downgradient of R-28. For each entry location, the inverse analysis also predicts the potential chromium concentration range arriving at the top of the regional aquifer to be consistent with the R-28 observations; these ranges reflect the uncertainty in the model predictions. The area outlined by the potential entry locations (Figure J-5.1-6) also approximately defines the detection area of monitoring well R-28. Contaminants that migrate by regional groundwater flow and are detected in R-28 likely originate somewhere within this detection area (although an area south of this is also possible but was not included in the analysis). This analysis can be repeated for any other monitoring well based on its calibration range (Appendix G); sample results are presented for R-11 and R-15 in Figures J-5.1-7 and J-5.1-8, respectively.

Next, the inverse analysis is performed to create models consistent with the calibration ranges of R-28 and R-11 simultaneously (Figure J-5.1-9). The analysis demonstrates that constraining the R-28 calibration results (Figure J-5.1-5) by adding the extra calibration target for R-11 substantially reduces the uncertainty in the model predictions and the number of potential chromium entry locations to 319. Incorporating R-15 calibration ranges further limits the uncertainty in the model predictions and the number of potential chromium entry locations to 49 (Figure J-5.1-10).

When calibration ranges at R-28, R-11, R-15, R-13, R-33, R-35, and R-36 are incorporated, the inverse model cannot find a possible solution. None of the entry points can produce concentrations consistent with the seven calibration ranges. No solution is obtained when calibration targets at all the wells are considered in the inverse analysis. The same result is also obtained when the second water table map (Figure J-5.1-3) is applied in the inverse model.

This conclusion suggests that the selected values for the model parameters may not adequately represent the existing hydrogeological conditions. In this case (the steady plume), the model parameters controlling the solution of the inverse problem are dispersivities. Additional inverse analyses (not presented here) demonstrate that increasing the dispersivity does not yield a solution. The only way the model can find a solution is to decrease dispersivity. If the longitudinal and transverse dispersivities equal 50 and 5 m, respectively, there are only two possible solutions of the inverse problem when calibrating to all of the wells (Figure J-5.1-11). This solution is for the case of the first water table map (Figure J-5.1-2). However, the numerical inverse model could not find any possible contaminant entry locations that satisfy the full set of calibration data for the case of the second water table map (Figure J-5.1-3). This finding suggests that if there is a single contaminant-arrival location causing chromium to be detected at R-28 and R-11, the first water table map gives a more probable representation of the actual flow conditions

than the second map. It should be noted that according to the first water table map (Figure J-5.1-2), flow near R-28 has slightly more southern components than in the second water table map (Figure J-5.1-3), and the structure of the water flow is affected by local recharge along the canyons. The first water table also more closely matches the observed water-level data (Appendix H).

The inverse solution presented in Figure J-5.1-11 shows that only two locations close to and upgradient of R-28 and R-11 can satisfy the calibration targets. If the resolution of the initial entry points considered in this analysis were finer (currently the locations are spaced by 100 m), a larger number of potential entry points could have been indentified. However, all of the new entry points are expected to be in close proximity to the currently identified locations (Figure J-5.1-11). Also, in this case, the entry locations are about 250–500 m upgradient of R-28/R-11, so the applied dispersivity coefficients (longitudinal/transverse dispersivities equal to 50 and 5 m) are consistent with the scale of lateral migration.

Figure J-5.1-12 presents the maximum chromium concentrations at the entry points at the top of regional aquifer that satisfy the calibration targets for all of the monitoring wells. In this case, the model predicts that the maximum concentrations are between 1400 and 1700 ppb. The minimum concentrations at the entry points at the top of regional are about 1300 ppb (not shown in Figure J-5.1-12). The source concentration ranges are applied to compute the potential chromium concentrations in the regional aquifer. In this case, all the potential entry locations are considered to be equally probable. The results are presented in section 4 of this report.

J-5.1.2.2 Identification of Two Potential Entry Locations

This analysis identified two potential entry locations that may cause the observed contaminant plume at R-28 and R-11. The first entry point is assumed to predominantly affect contaminant detections at R-28, and the second entry point is assumed to predominantly affect contaminant detections at R-11. It is assumed that an unknown fraction (up to 100%) of the R-11 chromium concentration results from chromium arriving at the location that is responsible for the R-28 detections and vice versa. The inverse analyses results are presented in Figures J-5.1-13 and J-5.1-14 for the two water table maps, respectively. The model longitudinal/transverse dispersivities are equal to 50 m and 5 m and are consistent with the scale of the problem. According to Figure J-5.1-13, the model suggests that the areas of the potential entry locations may almost overlap to the west or at least be located very close to each other. The shapes of the entry-location areas appear to be affected by the shape of the water table (Figure J-5.1-2). The results are also consistent with the prediction in Figure J-5.1-11 where a contaminant plume originating from a single entry point is considered. According to Figure J-5.1-14, the model estimates the entry point of the contaminants detected at R-28 may be next to R-28.

Figures J-5.1-15 and J-5.1-16 present the maximum chromium concentrations at the entry points at the top of regional aquifer, assuming two entry locations; the results correspond with the solutions presented in Figures J-5.1-13 and J-5.1-14, respectively. The model predicts the existence of two potential areas where the chromium may have arrived at the regional aquifer. The model predicts that the maximum concentrations at the entry points are between 40 and 100 ppb for the area associated with R-11 detections. The maximum concentration at the entry points are between 600 and 1200 ppb for the case of the R-28 contaminants. The entry concentration ranges are applied to compute the potential chromium concentrations in the regional aquifer. In this case, all the potential entry locations are considered to be equally probable. The results are presented in section 4 of this report.

J-5.1.2.3 Estimation of Contaminant Concentrations at Additional Contaminant-Arrival Locations

It is possible that multiple contaminant-arrival locations exist at the top of the regional aquifer. Based on the numerical-model analyses presented above, it is possible that one or two contaminant-arrival

locations can reproduce the observed concentrations at R-28, R-11, and the other wells near by. However, an additional contaminant-arrival location may cause a plume that is already established and has reached steady shape in the regional aquifer, but the measured chromium concentrations are within the background range, and therefore, the plume is not identified as potential contamination at the monitoring wells.

Background chromium concentrations are uncertain and are expected to vary in different hydrostratigraphic units. Background concentrations may be as high as 10 ppb, and vary between 3 and 7 ppb based on local geochemical conditions. As a result, an additional contaminant-arrival location that causes chromium concentrations at the monitoring wells as high as 1 ppb may not be distinguishable from background. Therefore, the inverse analysis can be performed for each of the potential 573 entry locations to estimate the maximum chromium concentration at each entry location that can produce 1 ppb concentrations at all the monitoring wells. The obtained results are presented in Figures J-5.1-17 and J-5.1-18 for the two water table maps, respectively. The maximum concentrations at the contaminant-arrival locations do not exceed 30 ppb, which is below the current water-quality standards (the U.S. Environmental Protection Agency maximum contaminant level for chromium is 100 ppb and the New Mexico Human Health Standard is 50 ppb). This conclusion suggests that even if there is an unknown contaminant-arrival location, the maximum concentration anywhere in the aquifer will be below 30 ppb. If there are two or more additional contaminant-arrival locations producing steady-shape plumes in the regional aquifer, the maximum concentration in the aquifer will be equal to or lower than the concentrations plotted in the figures because concentrations for all the additional plumes will have to be constrained to produce 1 ppb concentrations at all the monitoring wells. If more than two additional plumes are detected at a given monitoring well, the concentrations at the contaminant-arrival locations will need to be even lower than the values presented in Figures J-5.1-17 and J-5.1-18 to compensate for the additive effect.

Because the problem is linear, the results presented in Figures J-5.1-17 and J-5.1-18 can be used to estimate maximum concentrations at the entry points based on different concentrations at all the monitoring wells. For example, if 2 ppb is observed at all the wells, then the maximum concentration at each entry point will be 2 times higher.

Ultimately, this analysis also demonstrates the detection efficiency of the monitoring network. If the network were less efficient, there would be few constraints on the maximum concentration at the entry locations.

J-5.1.2.4 Estimation of Contaminant Mass Flux Entering the Regional Aquifer

The ambient flow velocities can also be applied to estimate the volume of groundwater and the chromium mass flux entering and flowing in the regional aquifer. Based on the hydrogeological parameters discussed above, the groundwater Darcy velocity in the regional aquifer near R-28 may be on the order of 36.5–73 m/yr. For a section of the aquifer with area of 10 × 10 m^2, this will amount to groundwater flux of 3650 to 7300 m^3/yr; in this case, the aquifer section is assumed to 10 m wide and 10 m deep below the water table. Taking into account an average chromium concentration of 400 ppb, 2 to 4 kg/yr of chromium may flow in close vicinity to R-28.

Similarly the maximum chromium concentrations at the potential entry points for the chromium detected by R-28 may vary between 600 and 1700 ppb (Figures J-5.1-12, J-5.1-15, and J-5.1-16). The individual entry locations are defined to have a lateral size of 10 × 10 m^2. As a result, the vertical cross-sectional area through which the contaminant flux occurs is 10 × 10 m^2. The contaminant mass flux needed to produce chromium concentrations between 600 and 1700 ppb at the entry points ranges between 3 and 18 kg/yr of chromium.

The estimated chromium mass flux can be compared to the mass of chromium naturally occurring in groundwater within the regional aquifer. The area presented in the figures (e.g., Figure J-5.1-18) is 44 km^2 (8.5 × 5 km). If the aquifer thickness is 30 m (the phreatic zone) and the effective porosity is 0.1, the total volume of groundwater is on the order of 0.1 km^3. For a background groundwater concentration of 5 ppb, the total mass of chromium in this area is about 660 kg. The current mass of chromium predicted by the model to be in the aquifer and originating from Sandia Canyon sources is less than 100 kg. It is also possible to compute how much chromium is naturally discharged by the groundwater flow in the area near the White Rock Canyon springs and Rio Grande. At the scale of Pajarito Plateau, the groundwater flux is on the order of 200 kg/s, which at a background concentration of 5 ppb, produces a mass flux on the order of 30 kg/yr of chromium.

J-5.1.3 Conclusions and Future Work

Only chromium-concentration and water-level data observed in the regional aquifer can be applied to effectively constrain the potential locations of contaminant arrival at the top of the regional aquifer. The available data are not sufficient to estimate whether there is a single or two entry points of the chromium plume that is detected by R-28 and R-11. The chromium-concentration and water-level data observed at the four new regional monitoring wells (R-42, R-43, R-44, and R-45) that are expected to be drilled by December 2008 will further reduce the uncertainty in the contaminant-arrival locations.

Uncertainty in the background chromium concentration data and measurement uncertainties allows for additional secondary contaminant entry points. However, the maximum concentrations in the regional aquifer that can be caused by secondary entry points are likely to be relatively low (below 30 ppb).

Uncertainties in the presented model predictions depend on the uncertainty in the plume dispersion. The plume dispersion is controlled by aquifer heterogeneity. Future work may address further what ranges of plume dispersion occur in the regional aquifer. New modeling tools may be needed to simulate the scale-dependency and non-Fickian behavior of dispersion during contaminant migration in heterogeneous aquifers (e.g., Gouze et al. 2008, 102462; Le Borgne and Gouze 2008, 102463). The data collected at the new regional monitoring wells may further reduce uncertainty in plume dispersion.

The results presented in this appendix are related to steady concentrations at the arrival locations. However, the developed methodology can also be applied for more general cases such as transient concentrations. In this way, it may be possible to evaluate the chromium mass that could have flowed through the regional aquifer before the existing monitoring wells were drilled.

J-5.2 Simulation of Vertical Dispersion of the Chromium Plume in the Regional Aquifer

The chromium plume in the regional aquifer detected at R-28 is expected to disperse not only laterally, as simulated in section J-5.1 of this appendix, but also vertically. To evaluate the vertical dispersion of the chromium plume in the aquifer, analytical and numerical techniques are applied. The analytical techniques have the capability to account for the expected increased dispersivity, which is typically proportional to the distance traveled. The numerical simulation allows for more accurate representation of groundwater flow conditions, particularly the decrease of groundwater heads with depth.

It is possible to analytically estimate the lateral and vertical dispersion of a plume migrating through the regional aquifer. In the analysis, it is assumed that (1) the groundwater fluxes downgradient from the source are similar to the fluxes near the source (uniform flow, i.e. there is no large-scale focusing/channeling of the groundwater flow), (2) the contaminant source originates from a point, and (3) the longitudinal, lateral (or horizontal) transverse, and vertical transverse dispersivities are on the order of 1/10, 1/100 and 1/1000 of the traveled distance, respectively. The smooth water-table map

presented in Figure H-2 is consistent with the first assumption; however, there is a focusing of groundwater flow to the east of R-28 in the water-table map in Figure H-1. The assumed dispersivity ratios are considered typical for the scale of simulated contamination transport and type of medium heterogeneity (Freeze and Cherry 1979, 088742, Chapter 9; Neuman 1990, 090184; Gelhar et al. 1992, 102465).

To estimate the size of the plume, a scaling parameter σ is computed:

$$\sigma = \frac{1}{3}\sqrt{2\lambda L}$$

where λ is dispersivity (longitudinal or transverse), and *L* is the distance of the center of the plume from the source location. The parameter σ defines the standard deviation of the spatial plume dispersion. Typically, it is considered that 68.3%, 95.4%, and 99.7% of the contaminant mass will be within 1σ, 2σ and 3σ distances from the center of the plume, respectively (Freeze and Cherry 1979, 088742, Chapter 9). This calculation is based on assumptions for an unbounded flow domain and a normal spatial distribution of the contaminant plume mass.

The calculated plume sizes due to longitudinal and transverse dispersion are presented in Table J-5.2-1. The plume sizes define the section that will contain a given fraction of the plume mass. In the computation, it is assumed that the flow domain is bounded by the water table (the regional contaminant flow is confined by the water table). The effect of vertical anisotropy in the medium on the potential vertical plume sizes is also estimated. The vertical spreading is diminished by increase of aquifer anisotropy (reduction of anisotropy ratios). However, it is important to note that the reduction in the vertical spreading due to medium anisotropy may increase the lateral spreading of the plume. Anisotropic ratios in the range of 0.1–0.001 are expected to be characteristic for some of the hydrostratigraphic formations in the study area (Puye and Santa Fe Group sediments).

R-13 is potentially downgradient of R-28, and the screen of R-13 is located about 40 m (120 ft) below the regional water table. The distance between R-28 and R13 is 750 m. If the chromium plume has migrated toward R-13, it can be expected that it has travelled at least 750 m. In this case, based on the analytical method, the vertical size of the plume might be on the order of 45 m for the isotropic case and between 0.05 and 4.5 m for the anisotropic case (Table J-5.2-1).

However, this analysis cannot account for potential vertical components of hydraulic gradients. In general, the hydraulic heads decrease with depth. At R-10/10a, the head difference is on the order of 30 ft between the screens that are 200 ft apart (Allen and Koch 2008, 101613), such that the vertical component of hydraulic gradient is 0.15. At R-35a/b, the head difference is on the order of 6 ft between screens that are 164 ft apart (LANL 2008, 102185), such that the vertical component of hydraulic gradient is 0.04.

To evaluate the impact of the hydraulic gradients on the vertical plume spread, simulations using LGM3D are performed. The aquifer is assumed to be uniform. The lateral flow structure in the model is constrained by the water table map presented in Figure H-2, and the vertical component of the hydraulic gradient is set to be equal to 0 (no vertical gradient), 0.05, and 0.15 to evaluate the model sensitivity. The longitudinal and lateral transverse dispersivity coefficients are fixed and equal to 50 m and 5 m, respectively, which are consistent with the results presented in section J-5.1 of this appendix. To evaluate sensitivity, the vertical transverse dispersivity is varied between 0.5 and 1.0 m. Typically, the vertical transverse dispersivity is expected to be lower (by about an order of magnitude) than the horizontal transverse dispersivity (Gelhar et al. 1992, 102465).

The results for the vertical spreading of the plume predicted using numerical simulations are listed in Table J-5.2-2. The numerical simulations appear to be affected by, but not very sensitive to, (1) the vertical transverse dispersivity coefficient and (2) the vertical component of the hydraulic gradient. These results are somewhat surprising. Furthermore, the numerical results for the case of no vertical gradients are substantially higher than the analytical results for the case of isotropic aquifer. Additional future work may address the accuracy of these results. Based on the results listed in Table J-5.2-2, the vertical size of the plume at R-13 (~750 m downgradient from R-28) may exceed 100 m, which is not observed.

In conclusion, the analytical method seems to provide more accurate representation of the potential vertical spreading of the plume. In the case of an isotropic aquifer, the vertical plume size is expected to be on the order of 45 m after the plume has migrated for about 750 m. This size is similar to the depth of the R-13 screen below the water table. Therefore, if the aquifer is uniform, it can be expected that the R-13 screen may be capable of observing contaminants detected at R-28. If the hydrostratigraphic units near the regional water-table are highly anisotropic (which is very likely), the vertical plume size may be much smaller than the depth of the R-13 screen. However, this analysis does not take into account the aquifer heterogeneity. If the aquifer is highly heterogeneous (as may be expected), the dispersion (lateral and vertical) of the contaminant plume is substantially underestimated in the analysis presented in this section.

J-6.0   3-D–COUPLED MODEL OF VADOSE ZONE AND REGIONAL AQUIFER

The simulations presented in section J-5.1 identify entry locations at the top of the regional aquifer to the south of Sandia Canyon as likely causing the distribution of chromium that is currently observed in the regional groundwater aquifer. Lateral diversion within the vadose zone could potentially lead to such entry locations, which are away from the axis of Sandia Canyon. The 3-D CRM (section J-3) is used to investigate the 3-D effects on vadose zone flow in the Sandia Canyon area. Particularly, simulations explore potential lateral diversion of groundwater along sloping geologic contacts between hydrostratigraphic units, as shown in Figures J-2.0-2 through J-2.0-5. They also explore the sensitivity of lateral diversion to the permeability of the Cerros del Rio basalt. The effects and the magnitude of mounding along the water table of the regional aquifer caused by recharge along Sandia Canyon are also discussed. These simulations are preliminary and are designed for hypothesis testing rather than to fully explore uncertainty in the model predictions.

J-6.1   Boundary Conditions for 3-D Model

An initial steady-state flow field is calculated by defining the upper boundary conditions as constant infiltration boundaries. Most of the top boundary is defined as having an infiltration rate of approximately 1 mm/yr (equivalent to a water flux of 1.08 kg/s over the entire model domain, which has an area of 34 km^2), which is a representative value of infiltration rates for mesa tops and dry canyons (Birdsell et al. 2005, 092048). The model areas representing the canyon bottoms in Sandia, Mortandad and Los Alamos/Pueblo Canyons (see Section J-2.0) are initiated with infiltration rates of approximately 50 mm/yr. The equivalent water sources for these conditions are given in Table J-6.1-1. The resulting steady-state flow field is then used as an initial condition for transient simulations that represent enhanced recharge in Sandia Canyon.

Transient upper boundary conditions are applied to three Sandia Canyon segments (S4, S5, and S6 in Figure J-3.0-2b) to represent long-term increased infiltration resulting from effluent discharges to the canyon. The period 1950 to 1991 has assumed lower discharge rates (150,000 gal/d) than the period 1992 to present (250,000 gal/d) because greater volumes of treated sanitary waste effluent was routed to Sandia Canyon starting in 1992 (section 2.1). The water distribution to the canyon segments for the more

recent period is within ranges estimated by the surface water and alluvial water balance information provided in Appendix C and by the vadose zone calibration runs discussed in section J-4. The equivalent water sources for these two time periods and three canyon segments are shown in Table J-6.1-2. A greater volume of water is assumed to reach S6 (the farthest downcanyon infiltration segment) when the discharge rate increases.

No-flow boundary conditions are used on the side boundaries, which are far enough from the area of interest (Sandia Canyon) to not affect vadose zone flow. Nodes along the water table and in the regional aquifer are fully saturated throughout the simulations, and a hydraulic gradient of zero is defined for the regional aquifer. Therefore, the aquifer behaves as a stagnant zone in the simulations. Future work will include the simulation of groundwater flow in the regional aquifer portion of the grid as well.

J-6.2   Hydrologic Properties

The simulations were run using unsaturated-zone hydrologic properties based on the van Genuchten formulation for the retention curve (Van Genuchten 1980, 063542). Mean values for the hydrologic properties were used, as presented in Appendix D of the previous flow and transport report (LANL 2007, 098938) and the permeability and porosity values used in these simulations is given in Table J-6.2-1. The Tshirege Member units of the Bandelier Tuff were lumped together for this study and given a common set of properties because those units have similar properties and the flow effects of interest (for the purpose of these simulations) are located below that horizon. The units capable of causing lateral diversion along with those units above and below are assigned their appropriate (mean value) properties. A series of simulations was run using stepwise increasing (one order of magnitude at a time) bulk permeability for the Cerros del Rio basalt from $10^{-14.5}$ to $10^{-11.5}$ m^2 (Table J-6.2-1) to determine the sensitivity of flow results to basalt permeability, especially related to lateral diversion. The lowest permeability represents a massive, low-permeability and low-porosity basalt, and the highest represents a fractured, high-permeability basalt with properties like those observed at the Los Alamos Canyon weir site (Stauffer and Stone 2005, 090037).

In addition to the bulk hydrologic properties of the units, another model input parameter is defined to capture the permeability reduction that occurs at some geologic boundaries because of the presence of fine-grained deposits (e.g., clay layers, silt layers or buried soils) (section 2.3). These structures may be too thin (on the order of a few cm) to include in a large-scale numerical grid but are often perching horizons that strongly influence vadose zone flow paths (Robinson et al. 2005, 091682). A numerical technique was developed and implemented within the FEHM code that considers perching horizons to be at the interfaces between hydrostratigraphic units (Robinson et al. 2005, 091682). An estimated thickness and permeability for a thin layer can be harmonically averaged with those of the surrounding units to come up with an interface reduction factor which effectively retards flow across a low-permeability interface. A simulation using interface reduction factors at the base of the Guaje Pumice Bed, and at the top, the base, and the internal interface (tholeiitic/alkalic) for the Cerros del Rio basalts was run to determine their effect on vadose zone flow, perching, and potential lateral flow. A value of 0.01 was used at each interface in that case, as presented below.

J-6.3   Lateral Diversion in the Vadose Zone and Mounding of the Water Table

Figures J-6.3-1a through J-6.3-1e show a series of model-predicted, vadose zone saturation profiles from the ground surface to below the water table and along a cross-section perpendicular to Sandia (on right) and Mortandad (on left) Canyons. The simulation results represent predictions of saturation circa 2007. The cross-section is along a plane 35-m west of gaging station E124 (Figures 1.0-1 and 2.0-1). These simulations use the boundary conditions and model parameters described above.

In the first four figures (J-6.3-1a through J-6.3-1d), the saturated permeability of the Cerros del Rio basalt is varied from $10^{-14.5}$ to $10^{-11.5}$ m^2, and no permeability reduction factor is used. In the final figure (Figure J-6.3-1e), the permeability value of $10^{-11.5}$ m^2 is used for the basalt, and permeability reduction is applied at the base of the Guaje Pumice Bed, and at the top, the base, and the internal interface for the Cerros del Rio basalts.

In Figures J-6.3-1a through J-6.3-1d, the basalt is assumed to be uniform with effectively no internal structure (heterogeneity), and water entering from Sandia Canyon raises the saturation in the basalt below Sandia Canyon as a single thick lens centered below the canyon. Lower basalt permeability produces a higher maximum saturation within the lens and greater saturations throughout the basalt, even extending to beneath Mortandad Canyon. This can be observed by analyzing the progression from Figures J-6.3-1a through J-6.3-1d, where the colors within the basalt range from purples and greens (saturations from approximately 0.6 to 0.9) [Figure J-6.3-1a] to greens, yellows and oranges (saturations from approximately 0.2 to 0.6) [Figure J-6.3-1d]. Although it appears that the basalt in these cases diverts flow laterally toward Mortandad Canyon, velocity vectors for the various cases show that the major flow path in these four simulations is predominantly vertically downward. The most spreading occurs on the top of the lowest permeability basalt (Figure J-6.3-1a), but from there the flow lines move generally downward. As the basalt permeability incrementally increases, the lateral spreading decreases further, and saturations within the Puye Formation (beneath the basalt) increase. The transient results show that the saturation front produced by the canyon-bottom recharge reaches the water table more quickly as the basalt permeability increases, as expected. In addition, these simulations apply a much lower infiltration rate along Mortandad Canyon than along Sandia Canyon, and the drier simulated conditions beneath Mortandad Canyon are apparent.

The saturation profile in Figure J-6.3-1e shows thinner lenses of increased saturation occurring along the three basalt interfaces below Sandia Canyon. These thinner lenses form because of the assigned permeability reduction and the high water flux from that canyon. Higher saturations spread laterally along these interfaces and extend to beneath Mortandad Canyon. Some spreading also occurs at the base of the Guaje Pumice Bed. However, it again appears that despite such diversion most flow is predominantly vertical because the highest saturation values above the water table are beneath Sandia Canyon and are centered beneath the canyon floor. Transient results show that for the two cases that use the highest basalt permeability and differ only in the use of the permeability reduction factors at interfaces (Figure J-6.3-1d vs. J-6.3-1e), the saturation front reaches the water table more quickly when no interface permeability reduction is present.

Figure J-6.3-2 shows the simulated saturation field for a 2-D cross-section down Sandia Canyon superimposed onto the hydrostratigraphy. This cross-section is equivalent to the conceptual cross-section (Figure 2.0-1). Here perched water occurs along the three basalt interfaces and higher saturations occur in some portions of the Guaje Pumice Bed. The perching horizons follow the dipping units and appear conceptually much like those depicted in the conceptual cross section. The three enhanced infiltration zones (S4, S5, S6 in Figure J-3.0-2b and Table J-6.1-2) produce discrete saturation fields in Figure J-6.3-2. That is, saturations beneath S4 predominantly range between 0.1 and 0.3 (orange to yellow), beneath S5 they range between 0.2 and 0.8 (yellow to blue), and beneath S6 they range between 0.3 and 0.9 (yellow to dark blue). These values are in line with the assumed increasing infiltration rates from S4 to S6 (Table J-6.1-2).

Figures J-6.3-3a through J-6.3-3c show 3-D depictions of the saturation field along three cross-sections in Sandia Canyon beneath infiltration area S5 (Figure J-3.0-2b). The cross-sections move from west to east down canyon; saturation values of 0.45 and higher are shown. The figures show a view westward up Sandia Canyon and show some structure to these saturation fields west of the respective cross-section as well as the hydrostratigraphic units, which follow the same color scheme used in Figure J-6.3-2. The

streamlines represent potential water flow paths (because the simulations are transient, the streamlines define the potential for the water to flow along the current snapshot of the flow field). These figures are for the case that uses permeability reduction factors at the four interfaces (Figure J-6.3-1e).

Saturation values greater than 0.45 occur predominantly beneath Sandia Canyon (the canyon on the right side of the figures) and are located in the tuff unit beneath the canyon floor, along the Guaje Pumice Bed, and at the top, middle and base of the Cerros del Rio basalt because of enhanced infiltration along the canyon. These bodies of relatively high saturation occur as lenses along the unit interfaces. Some are also present beneath Mortandad and Ten Site Canyons (the two canyons on the left side of the figures) along the same unit interfaces, although these have lower saturations and are of less volume than the lenses beneath Sandia Canyon. In each figure, the highest (in elevation) lens occurs in the Guaje Pumice Bed. The streamlines show that lateral diversion of flow occurs only along the base of the pumice in these simulations. In the western most location (Figure J-6.3-3a), 70% of the streamlines are diverted laterally along the pumice (potentially about 70% of the groundwater flow is also diverted). This percentage of diverted streamlines decreases for the other two cross-sections. Where diversion occurs along the pumice bed, the streamlines eventually divert downward as the lens thins and the saturation decreases so that lateral diversion is of limited spatial extent. Although the same permeability reduction factor is applied at the four interfaces, the permeability values for adjacent units also factor into the simulated permeability contrast. For this reason, the four interfaces do not divert water equally. The pumice permeability and some of its other hydrologic properties (e.g., the van Genuchten alpha parameter) differ significantly from the underlying Puye Formation, leading to lateral flow. In contrast, very little diversion in the flow lines occurs at the three basalt interfaces probably because the basalt permeability is high and does not differ much from the surrounding Puye Formation permeability in these simulations (Table J-6.2-1). Results for simulations that used a lower permeability value for the Puye Formation (not presented in this report) showed greater lateral diversion along and in the basalt.

Grid effects are apparent in all of the saturation fields shown in Figures J-6.3-1 through J-6.3-3. For example, in the Figures J-6.3-1a through Figures J-6.3-1d, the blocky stair-stepping slope at the base of the basalt is evident. In Figure J-6.3-1e, elevated saturations extend outward at the base and in the middle of the basalt along the interfaces beneath Sandia Canyon because of the reduced permeability (two lower blue lenses) in a stair-stepping fashion rather than along continuous slopes. The grid resolution is too coarse to capture the dips of the sloping units because they are of relatively small scales compared to the cell size and the vertical resolution of the grid. Simulations using a more refined grid that better captures the dips would probably yield even greater lateral diversion than these simulations predict. This is likely true even in the cases where the basalts have no internal structure. Grid effects are even more pronounced in Figure J-6.3-2 where the differing grid resolution along the section is evident. For example, the grid near SCC-1 is finer than near R-11, and the blocky high saturation (blue) areas are better defined and follow the hydrostratigraphy more closely near SCC-1 than near R-11.

The simulations presented here predict a slight groundwater mound (a few cm) beneath Sandia Canyon, as seen by the thin saturated zone above the water table in Figures J-6.3-1 and J-6.3-2. Previous simulations using a much lower permeability for the Puye Formation ($10^{-12.2}$ vs. $10^{-10.3}$ m^2) predicted mounding on the order of 10 to 20 m, which is unrealistically high based on water levels measured in the area. This prediction helps confirm that the large-scale permeability of the Puye Formation is potentially higher than the mean permeability listed in Table J-3.0-2. The permeability ranges presented in that table are based on single-hole pumping tests conducted at various monitoring wells on the Pajarito Plateau. However, the site specific data for the aquifer near Sandia Canyon suggest a higher permeability for the Puye deposits. Tests conducted at R-28, R-11, R-36b and R-15 suggest permeability values that are higher ($\sim 10^{-10.5}$ m^2) than the ranges listed in Table J-3.0-2. Future work will address the uncertainty in the Puye permeability.

J-6.4   Summary of 3-D Vadose Zone Simulations

The 3-D vadose zone simulations demonstrate that lateral diversion within the vadose zone from Sandia Canyon toward Mortandad Canyon might occur along dipping beds at the base of the Guaje Pumice Bed, and on the top, within, and at the base of Cerros del Rio basalts. Lateral diversion occurs in the simulations when basalt permeability is very low or when permeability reduction factors are applied at perching horizons. However, the lateral diversion is of limited spatial extent in all of the simulations, and the predominant pathways are vertically downward beneath Sandia Canyon. This scenario supports a hypothesis that directly beneath Sandia Canyon, high water fluxes may have flushed much of the chromium from the vadose zone, as observed in the SCC boreholes (section J-4) and predicted by the one-dimensional vadose zone simulations in this report (section J-4) and in the previous flow and transport report (LANL 2007, 098938). However, the fringe of the vadose zone plume that is not along the dominant flow path likely lags behind that center of the plume, which yields later arrival at the regional aquifer off the axis of Sandia Canyon. This effect seems to have occurred at the Los Alamos Canyon weir site during a bromide tracer test conducted in the canyon bottom and observed at a borehole located off the canyon axis (Stauffer and Stone 2005, 090037).

The use of permeability reduction factors is justified by frequent observations of perched water on top of or interspersed between fine-grained materials at these horizons in Los Alamos Canyon. The permeability reduction factors allow the simulations to capture thin perching horizons with a relatively coarse grid. Field observations of perching horizons and perched water in the vicinity of Sandia and Mortandad Canyons can help to define the interfaces where reduction factors might be used in future simulations and help to constrain their values.

Although lateral diversion is successfully demonstrated in these simulations, the coupled (vadose zone and regional aquifer) 3-D CRM has insufficient grid resolution to adequately capture the small-scale dip of the hydrostratigraphic units. The grid was designed to study larger-scale processes (fully coupled vadose zone and regional-aquifer transport) rather than vadose zone lateral diversion, so it is not a surprise that grid effects (Figures J-6.3-1 and J-6.3-2) are present. Chromium transport was not simulated with the 3-D CRM because of the insufficient grid resolution.

The 3-D modeling analysis demonstrates that recharge along Sandia Canyon may cause a mound at the water table that may affect the flow directions in the regional aquifer. The size and height of the mound are very sensitive to the recharge rate, the permeability of the Puye Formation, and the size of the recharge area at the top of the regional aquifer resulting from lateral dispersion of the wetting front as it moves through the vadose zone. If a permeability value is used in the model that is similar to that used in the analytic solution presented in Appendix I, then the predicted mound is of a similar height.

J-7.0   REFERENCES

The following list includes all documents cited in this appendix. Parenthetical information following each reference provides the author(s), publication date, and ER ID number. This information is also included in text citations. ER ID numbers are assigned by the Environmental Programs Directorate's Records Processing Facility (RPF) and are used to locate the document at the RPF and, where applicable, in the master reference set.

Copies of the master reference set are maintained at the NMED Hazardous Waste Bureau; the U.S. Department of Energy–Los Alamos Site Office; the U.S. Environmental Protection Agency, Region 6; and the Directorate. The set was developed to ensure that the administrative authority has all material needed to review this document, and it is updated with every document submitted to the administrative authority. Documents previously submitted to the administrative authority are not included.

Allen, S.P., and R.J. Koch, March 2008. "Groundwater Level Status Report for Fiscal Year 2007, Los Alamos National Laboratory," Los Alamos National Laboratory report LA-14358-PR, Los Alamos, New Mexico. (Allen and Koch 2008, 101613)

Birdsell, K.H., B.D. Newman, D.E. Broxton, and B.A. Robinson, 2005. "Conceptual Models of Vadose Zone Flow and Transport beneath the Pajarito Plateau, Los Alamos, New Mexico," *Vadose Zone Journal,* Vol. 4, pp. 620-636. (Birdsell et al. 2005, 092048)

Carey, W.J., and G. Cole, January 2002. "Description of the Cerro Grande Fire Laser-Altimetry (LIDAR) Data Set," Los Alamos National Laboratory report LA-13892-MS, Los Alamos, New Mexico. (Carey and Cole 2002, 073784)

Cole, G., J.W. Carey, L. Burnette, and T. Miller, 2006. "The 2005 Three-Dimensional Geologic Model of the Pajarito Plateau," Los Alamos National Laboratory document LA-UR-06-3060, Los Alamos, New Mexico. (Cole et al. 2006, 095079)

Freeze, R.A., and J.A. Cherry, January 1979. *Groundwater*, Prentice-Hall, Inc., Englewood Cliffs, New Jersey. (Freeze and Cherry 1979, 088742)

Gelhar, L.W., C. Welty, and K.R. Rehfeldt, July 1992. "A Critical Review of Data on Field-Scale Dispersion in Aquifers," *Water Resources Research,* Vol. 28, No. 7, pp. 1955–1974. (Gelhar et al. 1992, 102465)

Gouze, P., T. Le Borgne, R. Leprovost, G. Lods, T. Poidras, and P. Pezard, 2008. "Non-Fickian Dispersion in Porous Media: 1. Multicale Measurements Using Single-Well Injection Withdrawal Tracer Tests," *Water Resources Research,* Vol. 44, W06426, 15 pp. (Gouze et al. 2008, 102462)

Kleinfelder, April 28, 2004. "Final Well R-28 Completion Report," report prepared for Los Alamos National Laboratory, Project No. 37151/16.12, Albuquerque, New Mexico. (Kleinfelder 2004, 090048)

Kleinfelder, February 2005. "Final Completion Report, Characterization Well R-11," report prepared for Los Alamos National Laboratory, Project No. 37151, Albuquerque, New Mexico. (Kleinfelder 2005, 090044)

LANL (Los Alamos National Laboratory), November 2006. "Interim Measures Investigation Report for Chromium Contamination in Groundwater," Los Alamos National Laboratory document LA-UR-06-8372, Los Alamos, New Mexico. (LANL 2006, 094431)

LANL (Los Alamos National Laboratory), September 2007. "Fate and Transport Modeling Report for Chromium Contamination from Sandia Canyon," Los Alamos National Laboratory document LA-UR-07-6018, Los Alamos, New Mexico. (LANL 2007, 098938)

LANL (Los Alamos National Laboratory), April 2008. "Completion Report for Regional Aquifer Well R-36," Los Alamos National Laboratory document LA-UR-08-2610, Los Alamos, New Mexico. (LANL 2008, 102185)

Le Borgne, T., and P. Gouze, 2008. "Non-Fickian Dispersion in Porous Media: 2. Model Validation from Measurements at Different Scales," *Water Resources Research,* Vol. 44, W06427, 10 pp. (Le Borgne and Gouze 2008, 102463)

Miller, T.A., V.V. Vesselinov, P.H. Stauffer, K.H. Birdsell, and C.W. Gable, 2007. "Integration of Geologic Frameworks in Meshing and Setup of Computational Hydrogeologic Models, Pajarito Plateau, New Mexico," New Mexico Geological Society Guidebook: 58th Field Conference, Geology of the Jemez Mountains Region II, pp. 121–128. (Miller et al. 2007, 102466)

Neuman, S.P., August 1990. "Universal Scaling of Hydraulic Conductivities and Dispersivities in Geologic Media," *Water Resources Research,* Vol. 26, No. 8, pp. 1749-1758. (Neuman 1990, 090184)

Robinson, B.A., D.E. Broxton, and D.T. Vaniman, 2005. "Observations and Modeling of Deep Perched Water beneath the Pajarito Plateau," *Vadose Zone Journal,* Vol. 4, pp. 637-652. (Robinson et al. 2005, 091682)

Stauffer, P.H., and W.J. Stone, 2005. "Surface Water–Groundwater Connection at the Los Alamos Canyon Weir Site: Part 2. Modeling of Tracer Test Results," *Vadose Zone Journal,* Vol. 4, pp. 718–728. (Stauffer and Stone 2005, 090037)

Van Genuchten, M.T., 1980. "A Closed-Form Equation for Predicting the Hydraulic Conductivity of Unsaturated Soils," *Soil Science Society of America Journal,* Vol. 44, pp. 892-898. (van Genuchten 1980, 063542)

Vecchia, A.V., and R.L. Cooley, July 1987. "Simultaneous Confidence and Prediction Intervals for Nonlinear Regression Models with Application to a Groundwater Flow Model," *Water Resources Research,* Vol. 23, No. 7, pp. 1237–1250. (Vecchia and Cooley 1987, 102323)

Zyvoloski, G.A., B.A. Robinson, Z.V. Dash, and L.L. Trease, May 20, 1996. "Users Manual for the FEHMN Application," Rev. 1, Los Alamos National Laboratory document LA-UR-94-3788, Los Alamos, New Mexico. (Zyvoloski et al. 1996, 054421)

Zyvoloski, G.A., B.A. Robinson, Z.V. Dash, and L.L. Trease, July 1997. "Summary of the Models and Methods for the FEHM Application — A Finite-Element Heat- and Mass-Transfer Code," Los Alamos National Laboratory report LA-13307-MS, Los Alamos, New Mexico. (Zyvoloski et al. 1997, 070147)
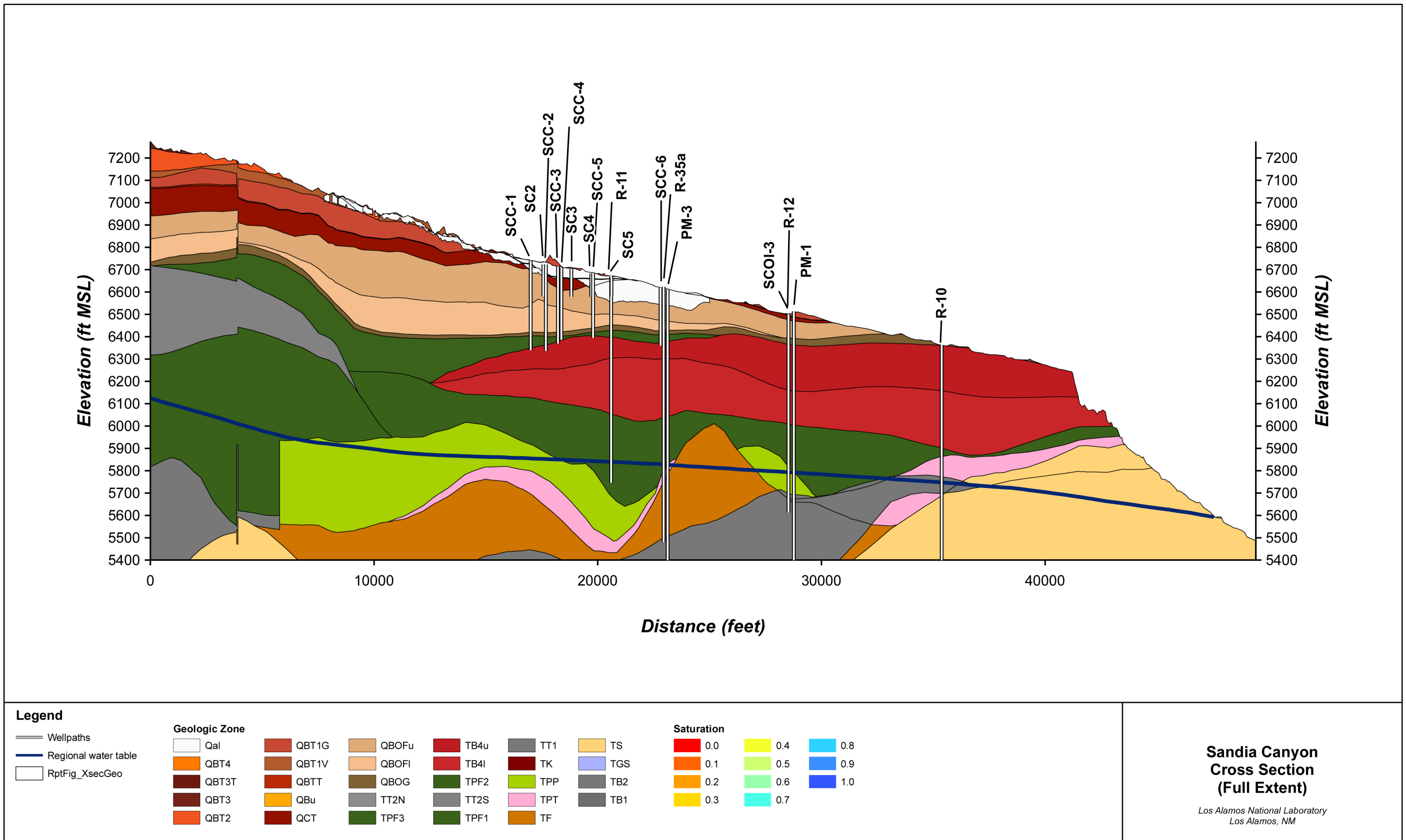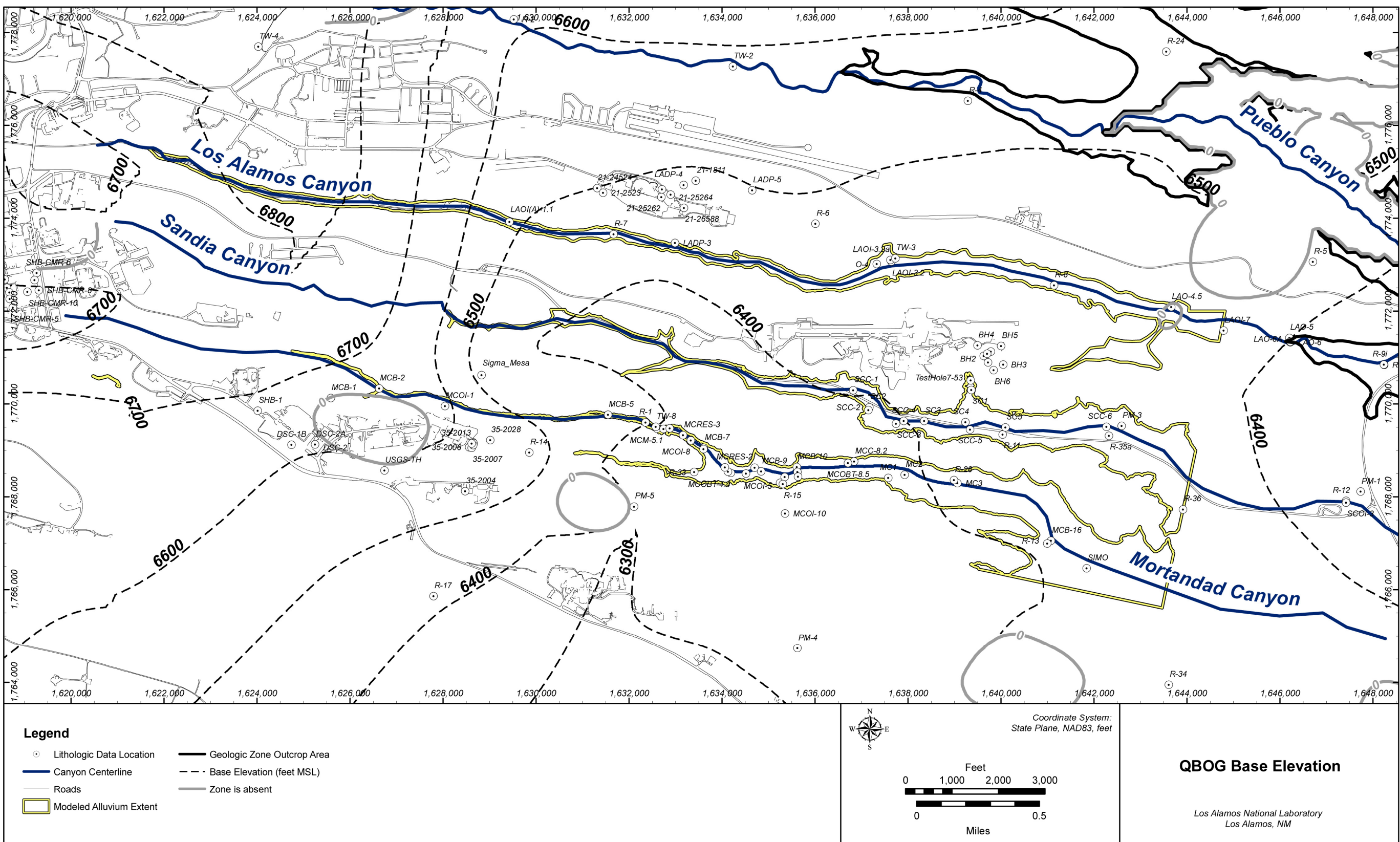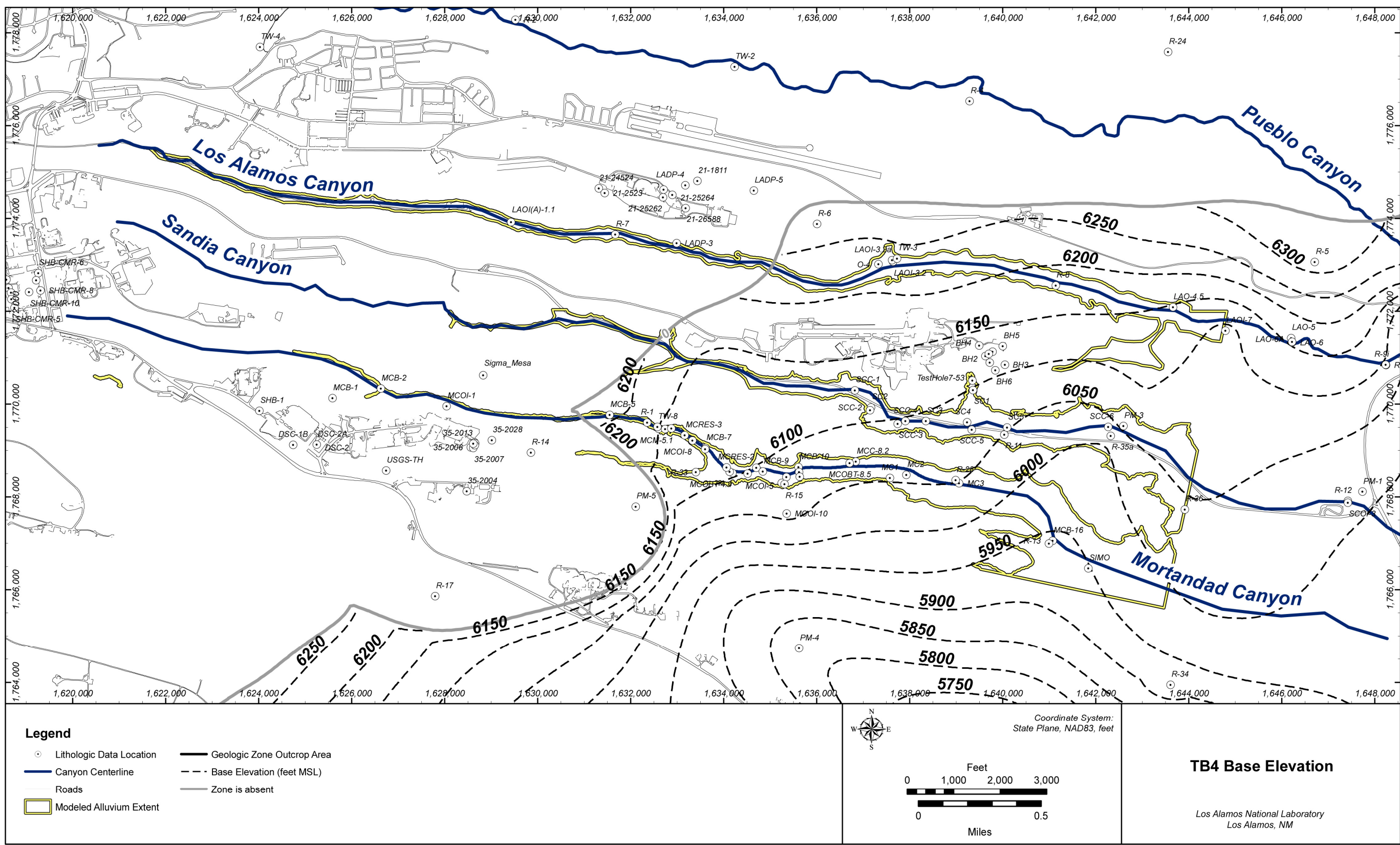
Figure J-2.0-1 Sandia cross section extracted from the WC08 geologic model, same view and vertical exaggeration as conceptual model Figure 2.0-1

Figure J-2.0-2 Elevation contours for the base of the Guaje Pumice Bed (Qbog) in the WC08 geologic model, chromium domain. Includes outline (in yellow) defined for canyon bottom alluvium (Qal)

Figure J-2.0-3 Elevation contours for the base of the Cerros del Rio basalt (Tb4) in the WC08 geologic model, chromium domain

Legend

- ⊙ Lithologic Data Location
- ── Canyon Centerline
- ── Roads
- ▭ Modeled Alluvium Extent
- ━━ Geologic Zone Outcrop Area
- ┄┄ Top Elevation (feet MSL)
- ━━ Zone is absent

Coordinate System:
State Plane, NAD83, feet

QBOF Internal Elevation

Los Alamos National Laboratory
Los Alamos, NM

C:\Projects\LANL\MCLA\WC08\QBOFltop.mxd
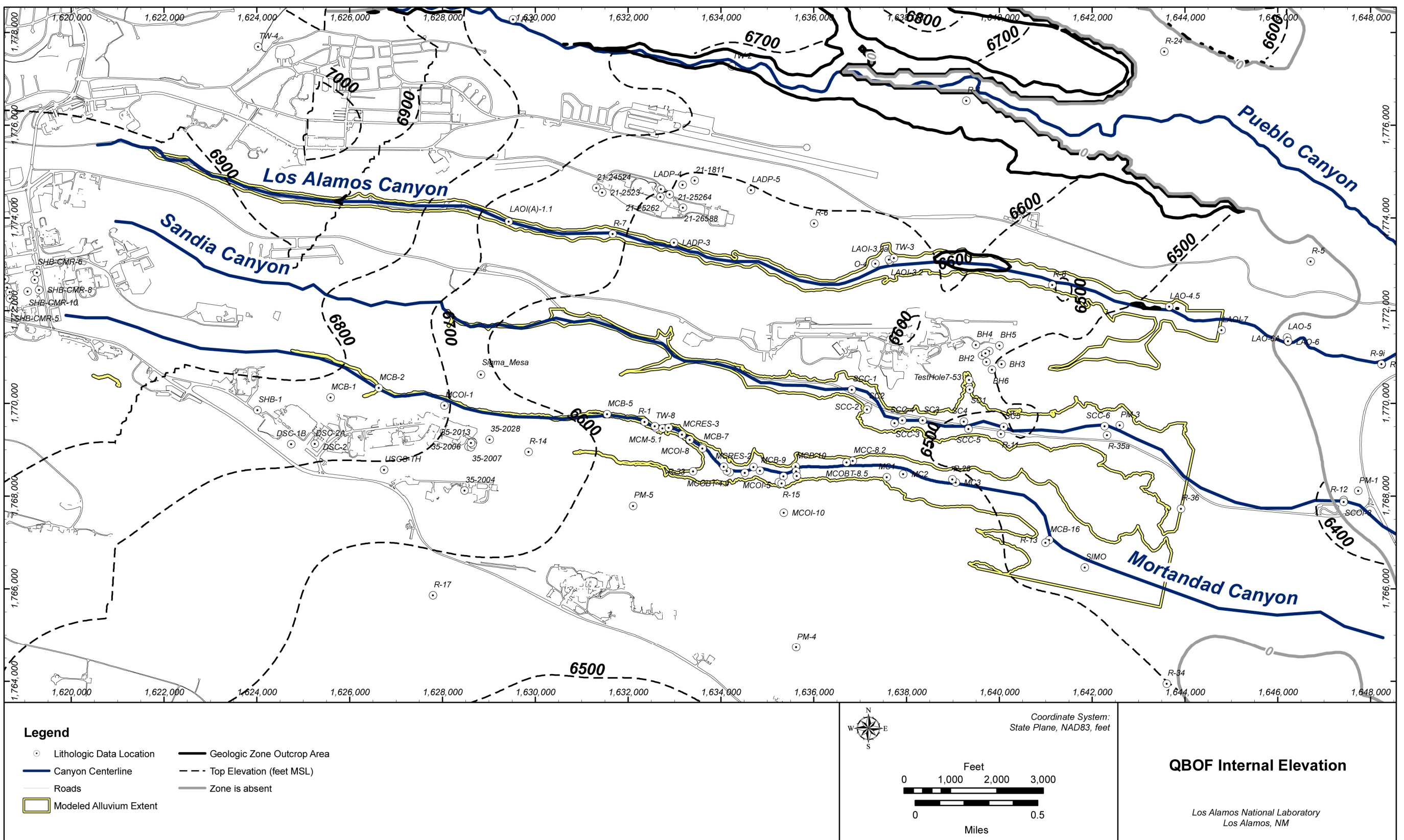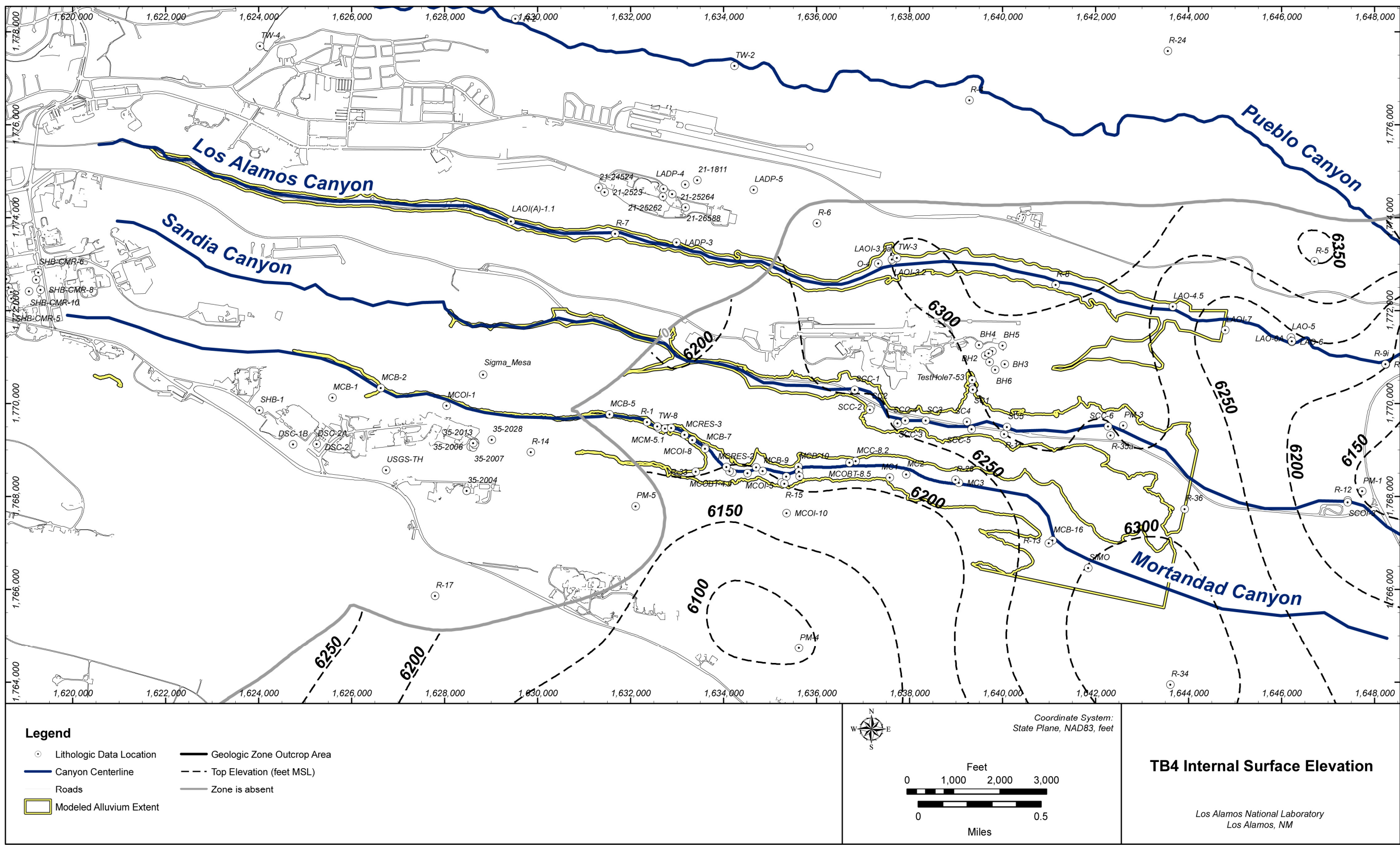
Figure J-2.0-4 Elevation contours for internal stratigraphic features of the Otowi Member (Qbof) in the WC08 geologic model, chromium domain

Figure J-2.0-5   Elevation contours for the internal stratigraphic features of the Cerros del Rio Basalt (Tb4) in the WC08 geologic model, chromium domain
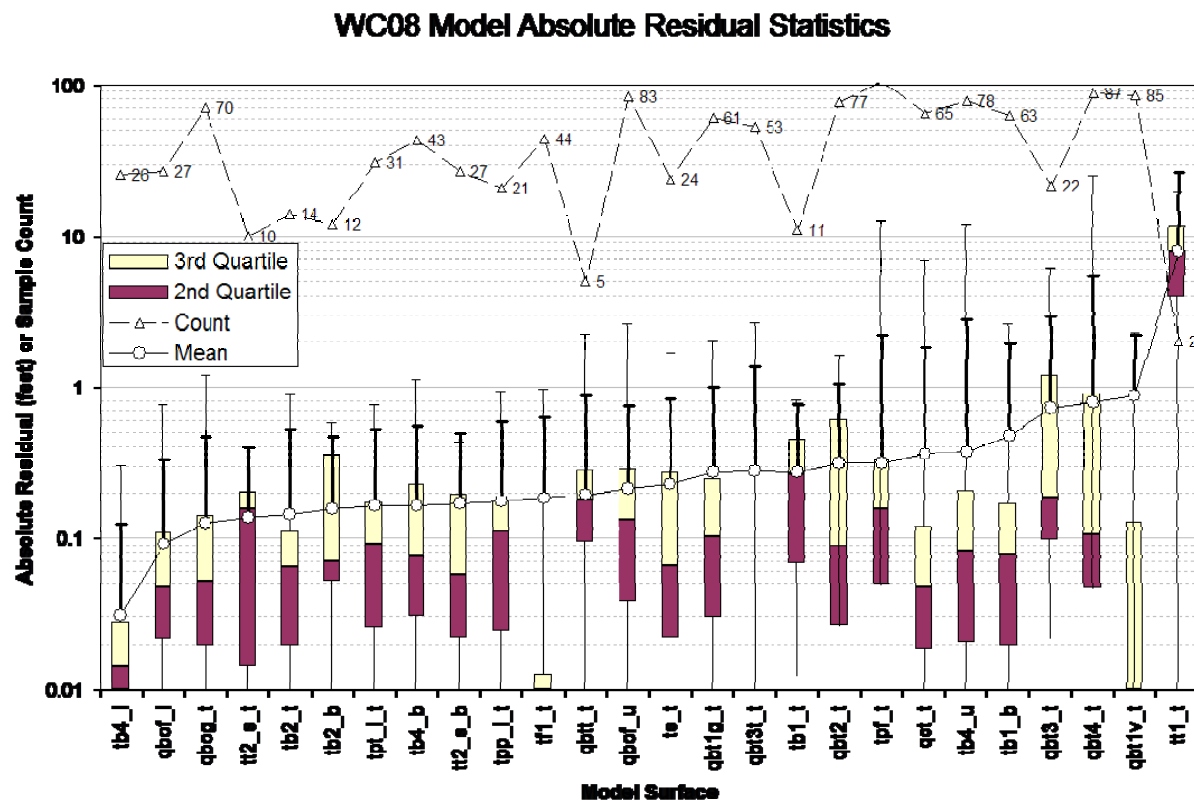
Figure J-2.0-6   Geologic framework model WC08 absolute residual statistics for modeled surfaces as compared to measured elevations
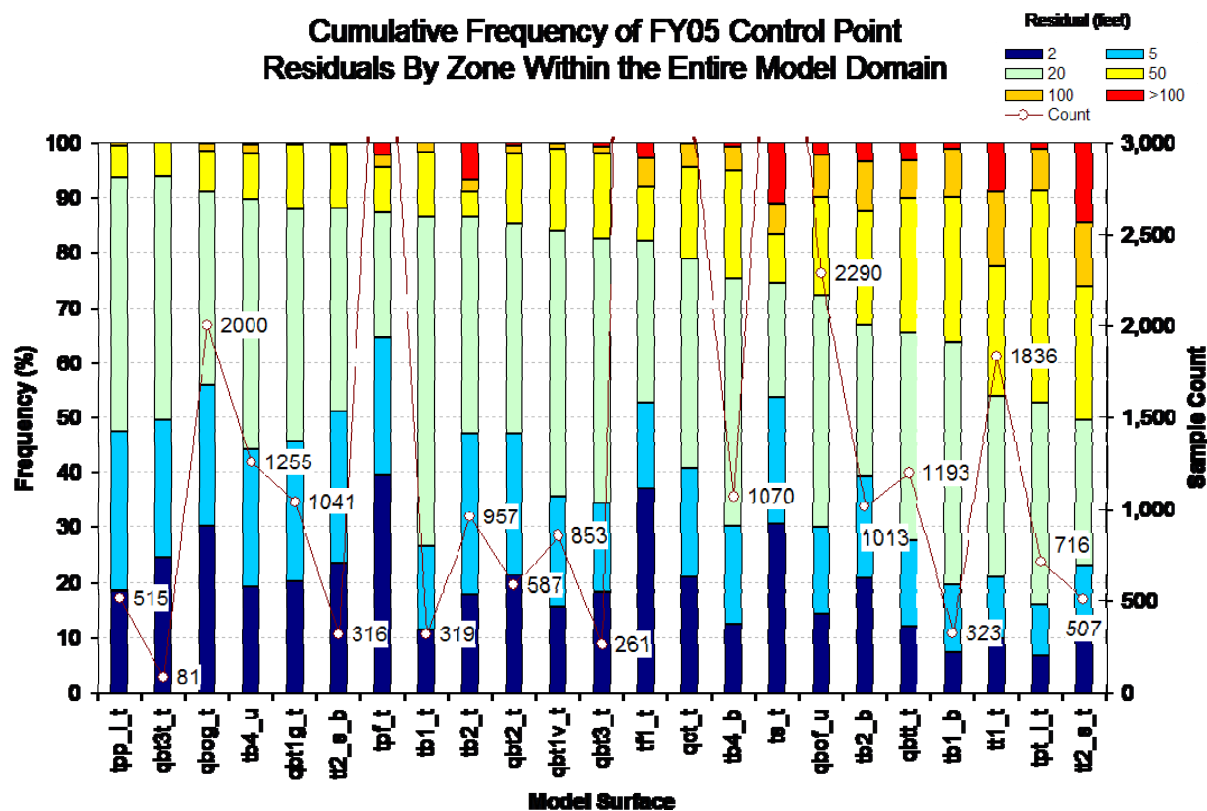
Figure J-2.0-7   Geologic framework model WC08 control point residual statistics by geologic unit (EarthVision zone) for modeled surfaces compared to the same points defined by the FY2005 GFM for the full model domain
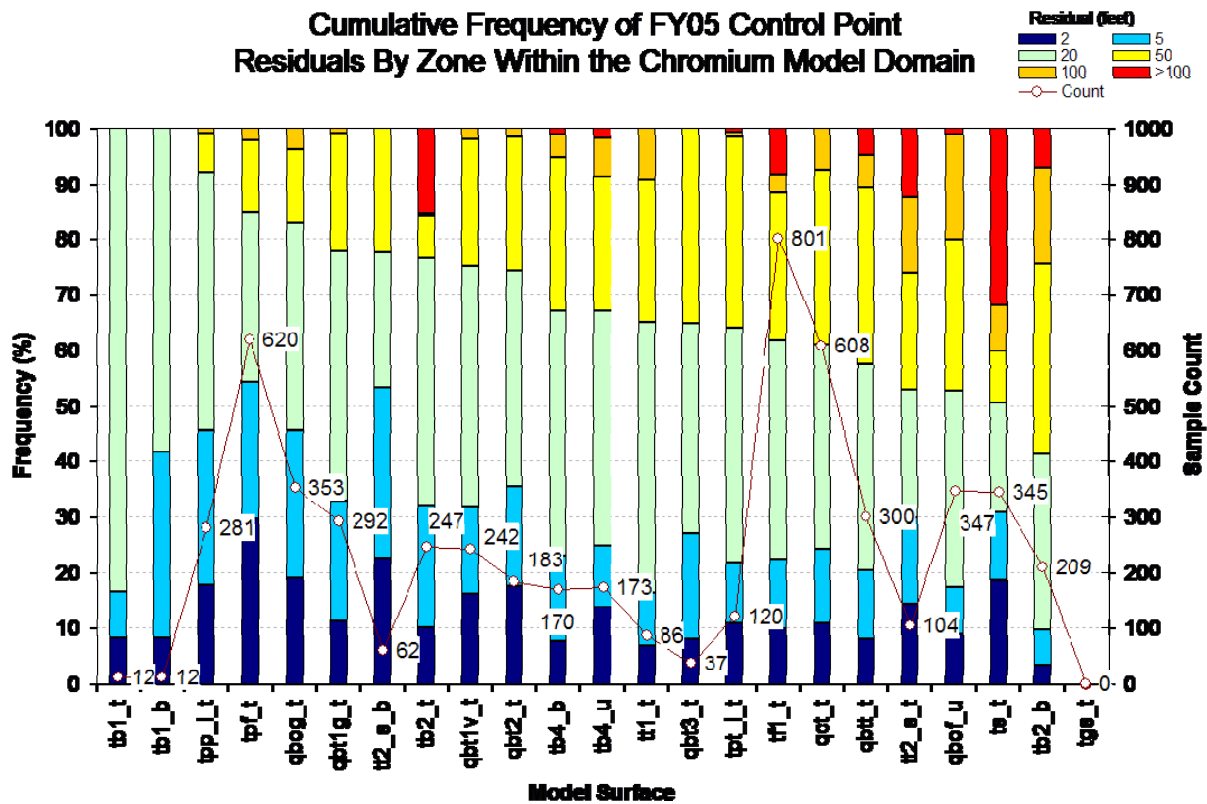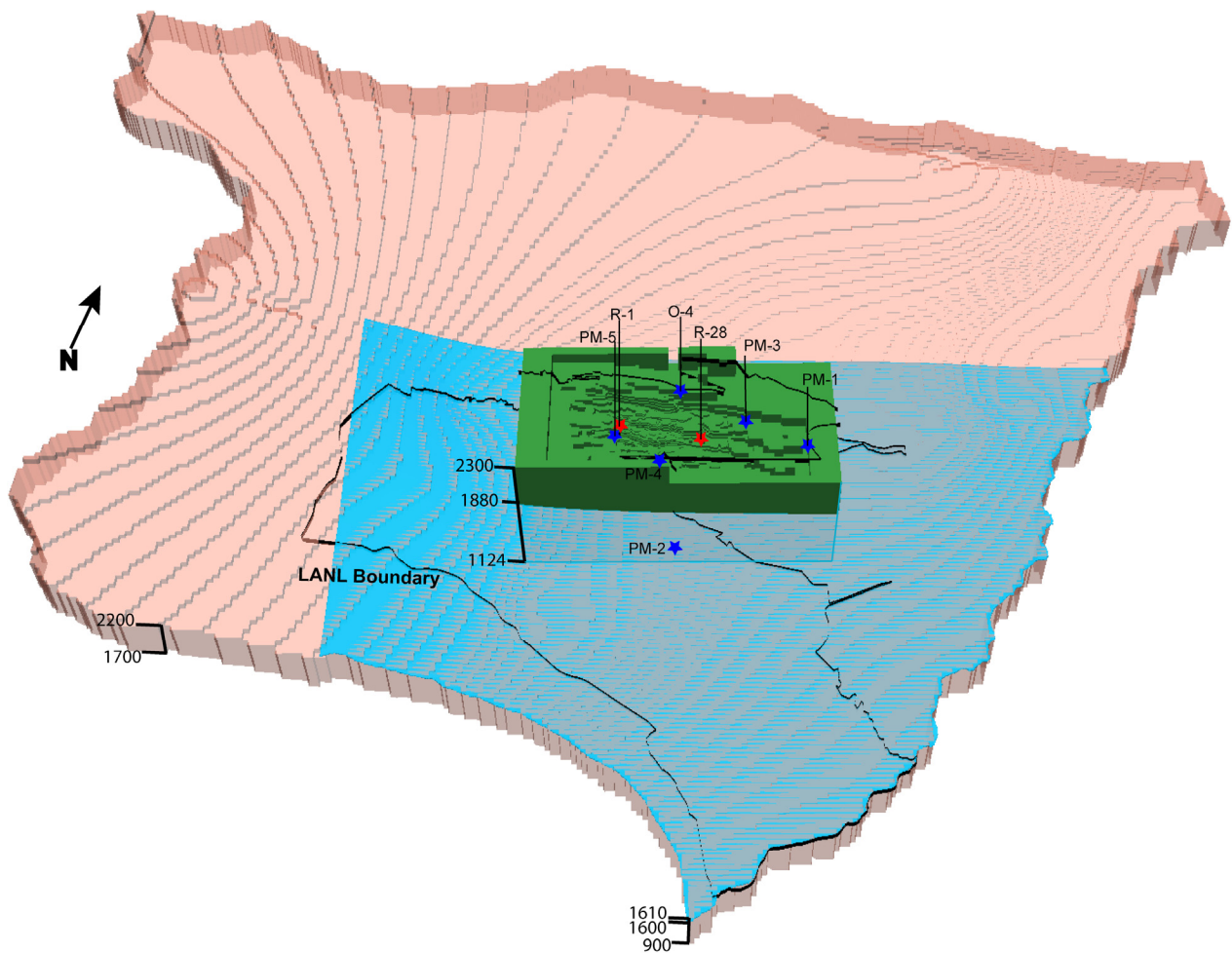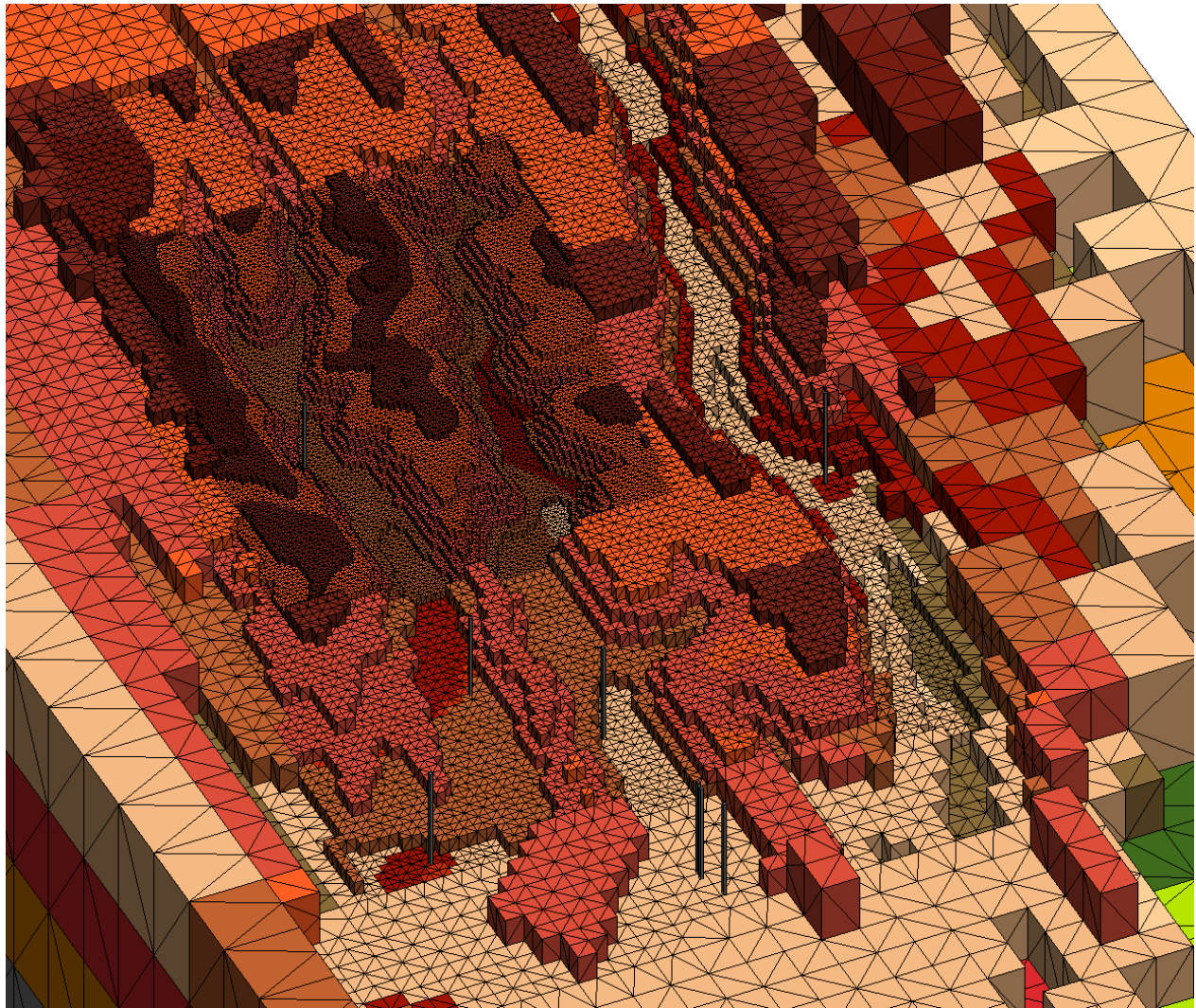
Figure J-2.0-8   Geologic framework model WC08 control point residual statistics by geologic unit (EarthVision zone) for modeled surfaces compared to the same points defined by the FY2005 GFM for the chromium model domain
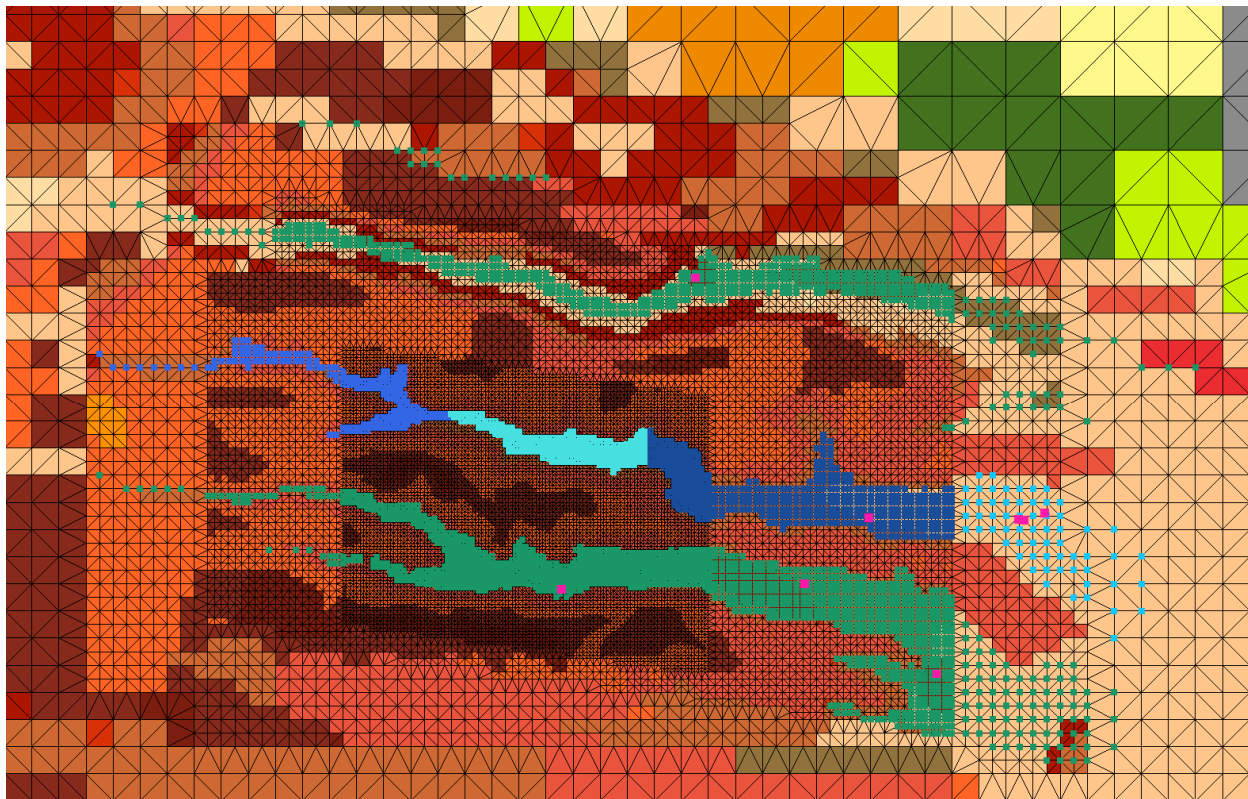
**Figure J-3.0-1   Domains of the models applied for simulation of chromium contamination
(1) CRM (green), (2) LGM2D (blue), and (3) LGM3D (pink). Grid thicknesses are in
meters.**
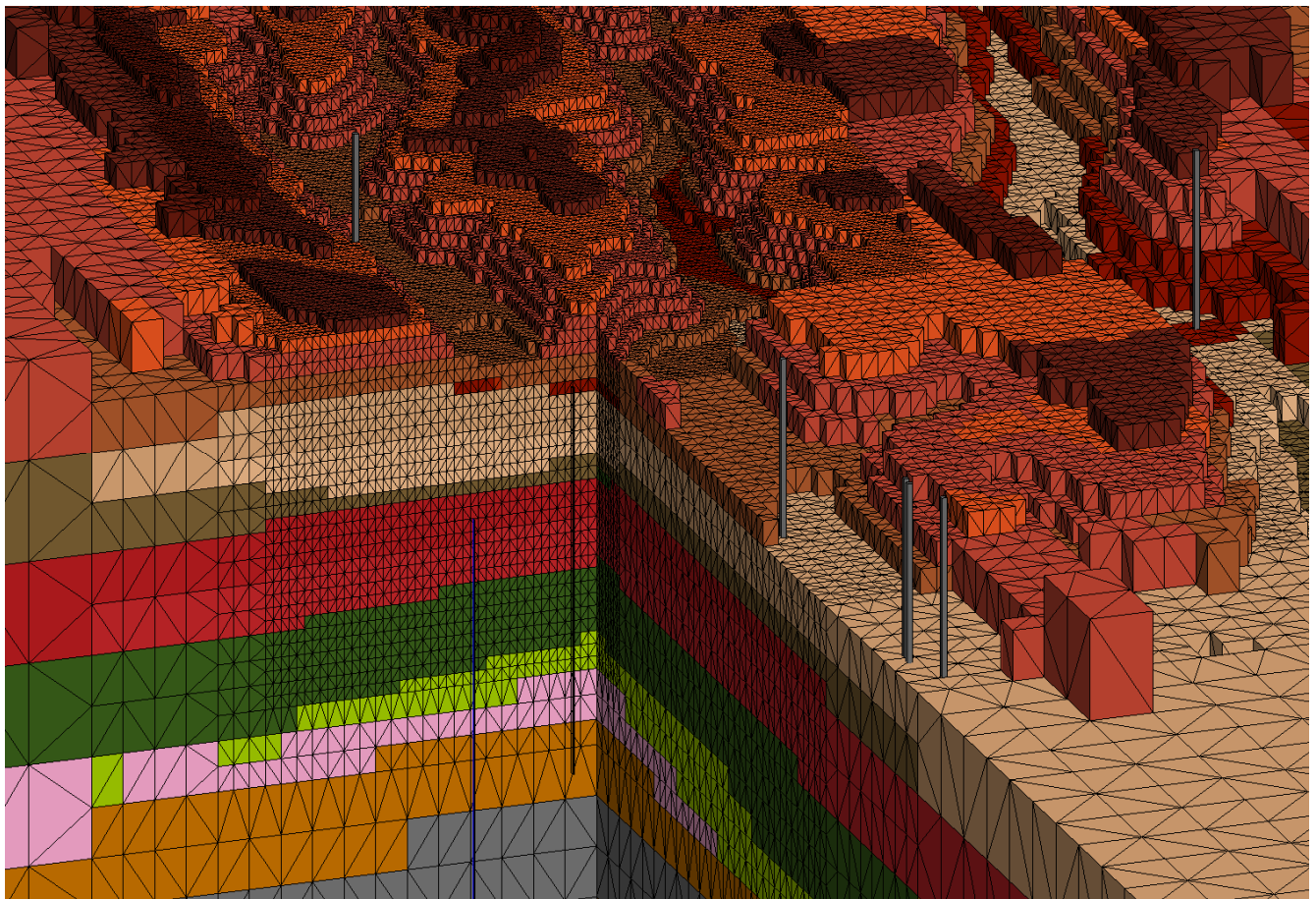
a.   Rotated close up view looking up Mortandad, Sandia, and Los Alamos Canyons (left to right). The locations of well group are shown (left to right) R-28, R-15, R-11, R-35a and R-35b, PM-3, and O-4.

Figure J-3.0-2   Close-up views of the refined site model grid CRM, (a) view up-canyon (b) top view with Qal nodes
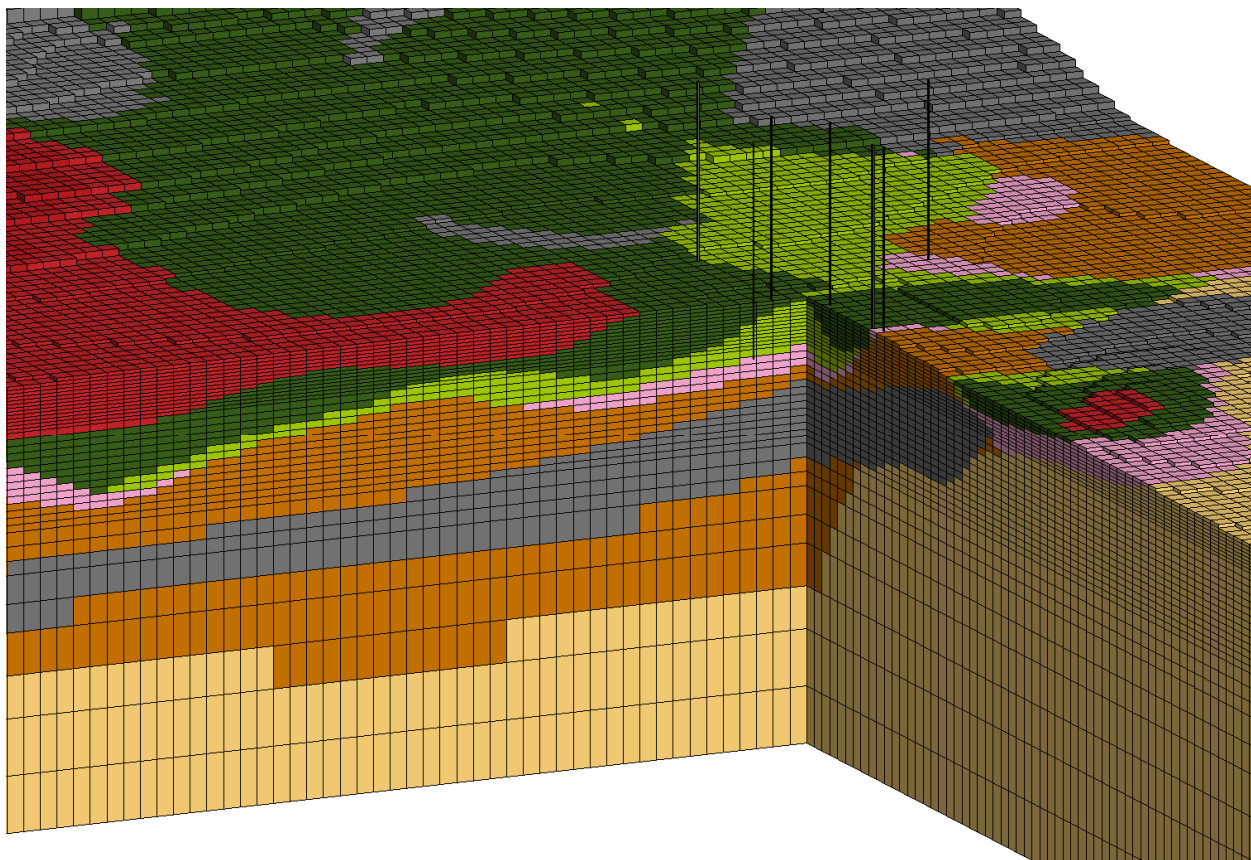
b.   Plan view of CRM showing horizontal spacing. Colors represent geologic units at top of grid as colored by the WC08 geologic framework. The nodes representing the alluvium zones are shown as green for Mortandad, Los Alamos, and part of Pueblo Canyons. The Sandia canyon zones are broken into four zones (blue). Sandia segments from left to right (west to east) are S4, S5, S6, and S7 (in the coarse part of the grid). The well group are pink dots (counterclockwise) R-15, R-28, R-13, PM-3, R-35a and R-35b, R-11, and O-4 in Los Alamos Canyon.

Figure J-3.0-2 (continued)   Close-up views of the refined site model grid CRM, (a) view up-canyon (b) top view with Qal nodes
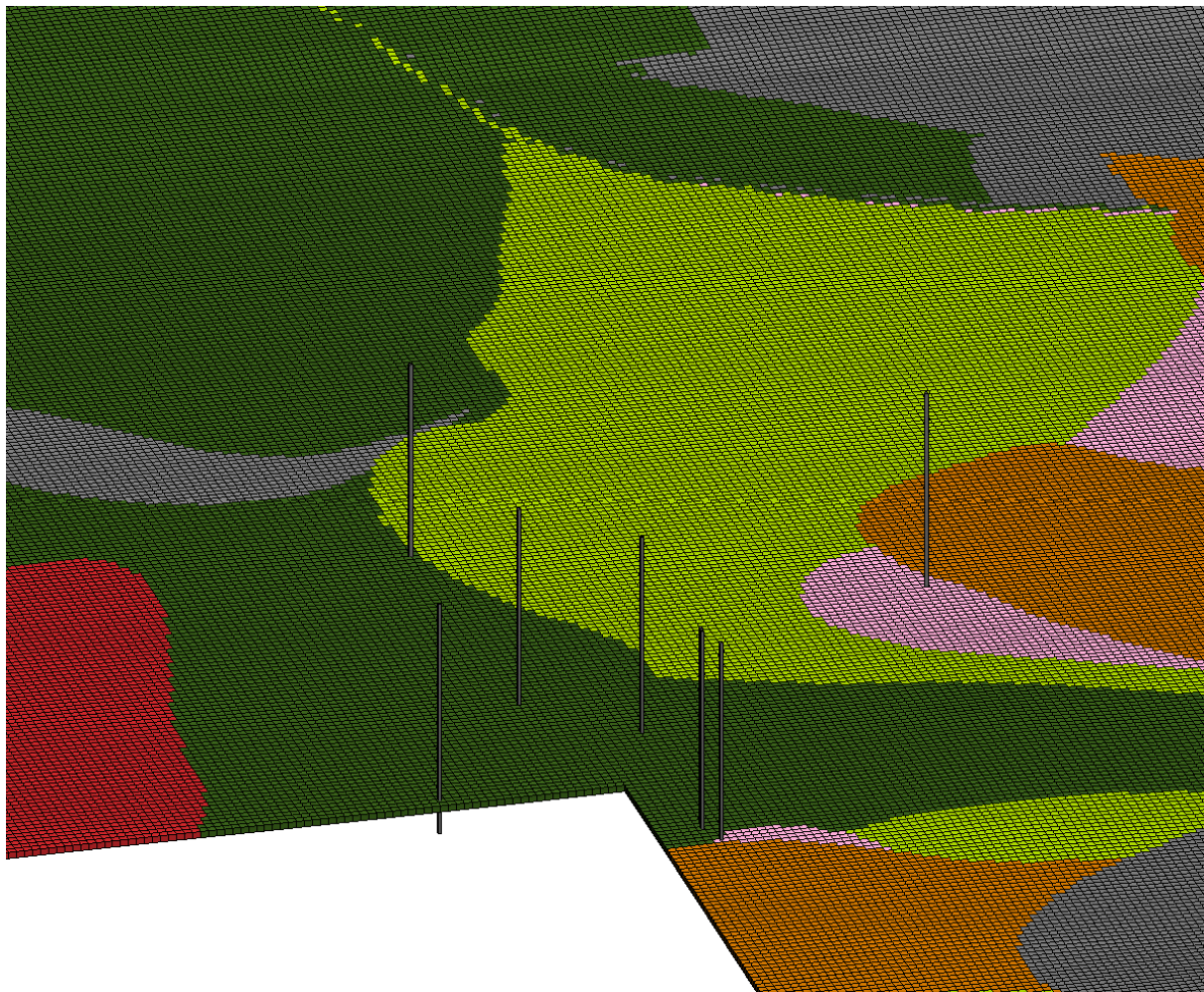
a.   CRM cut along and perpendicular to Sandia Canyon showing the finest grid resolution (horizonatally 15.62 and vertically 12.5 m) in the center of the figure; the size of the grid blocks increases by a factor of 2 to the outside the domain. Grid is truncated at ground surface and has the bottom below the water table at 1124 m.

Figure J-3.0-3   Computational grid resolution and representation of hydrostratigraphy in the numerical models: (a) CRM, (b) LGM3D, (c) LGM2D. The grids are cut perpendicular and along Sandia Canyon to show the internal resolution and unit colors. Visible larger units top to bottom are Tshireges (browns, oranges, pink), Cerro Toledo (burgundy), Otowi (tan), Otowi Guaje Pumice (olive), Cerros del Rio basalt (red), Puye fanglomerates (green), Pumiceous Puye, (light green), Totavi Lentil (pink), Sante Fe fanglomerates (orange), Older Basalts (gray), Santa Fe sandy (light yellow).

b.   LGM3D cut along and perpendicular to Sandia Canyon showing 125 m horizontal spacing and vertical resolution starting at 6.25 m near the top and increasing to 100 m at the bottom. The grid is truncated by the water table surface and has a flat bottom at elevation equal to 1000 m, more than 500 m below the water table.

Figure J-3.0-3 (continued)   Computational grid resolution and representation of hydrostratigraphy in the numerical models: (a) CRM, (b) LGM3D, (c) LGM2D The grids are cut perpendicular and along Sandia Canyon to show the internal resolution and unit colors. Visible larger units top to bottom are Tshireges (browns, oranges, pink), Cerro Toledo (burgundy), Otowi (tan), Otowi Guaje Pumice (olive), Cerros del Rio Basalt (red), Puye fanglomerates (green), Pumiceous Puye, (light green), Totavi Lentil (pink), Sante Fe fanglomerates (orange), Older Basalts (gray), Santa Fe sandy (light yellow).

c.   LGM2D cut along Sandia Canyon and well group showing 25 × 25 m uniform lateral spacing. Grid has top nodes set at elevation of the water table surface.

Figure J-3.0-3 (continued)   **Computational grid resolution and representation of hydrostratigraphy in the numerical models: (a) CRM, (b) LGM3D, (c) LGM2D The grids are cut perpendicular and along Sandia Canyon to show the internal resolution and unit colors. Visible larger units top to bottom are Tshireges (browns, oranges, pink), Cerro Toledo (burgundy), Otowi (tan), Otowi Guaje Pumice (olive), Cerros del Rio Basalt (red), Puye fanglomerates (green), Pumiceous Puye, (light green), Totavi Lentil (pink), Sante Fe fanglomerates (orange), Older Basalts (gray), Santa Fe sandy (light yellow).**
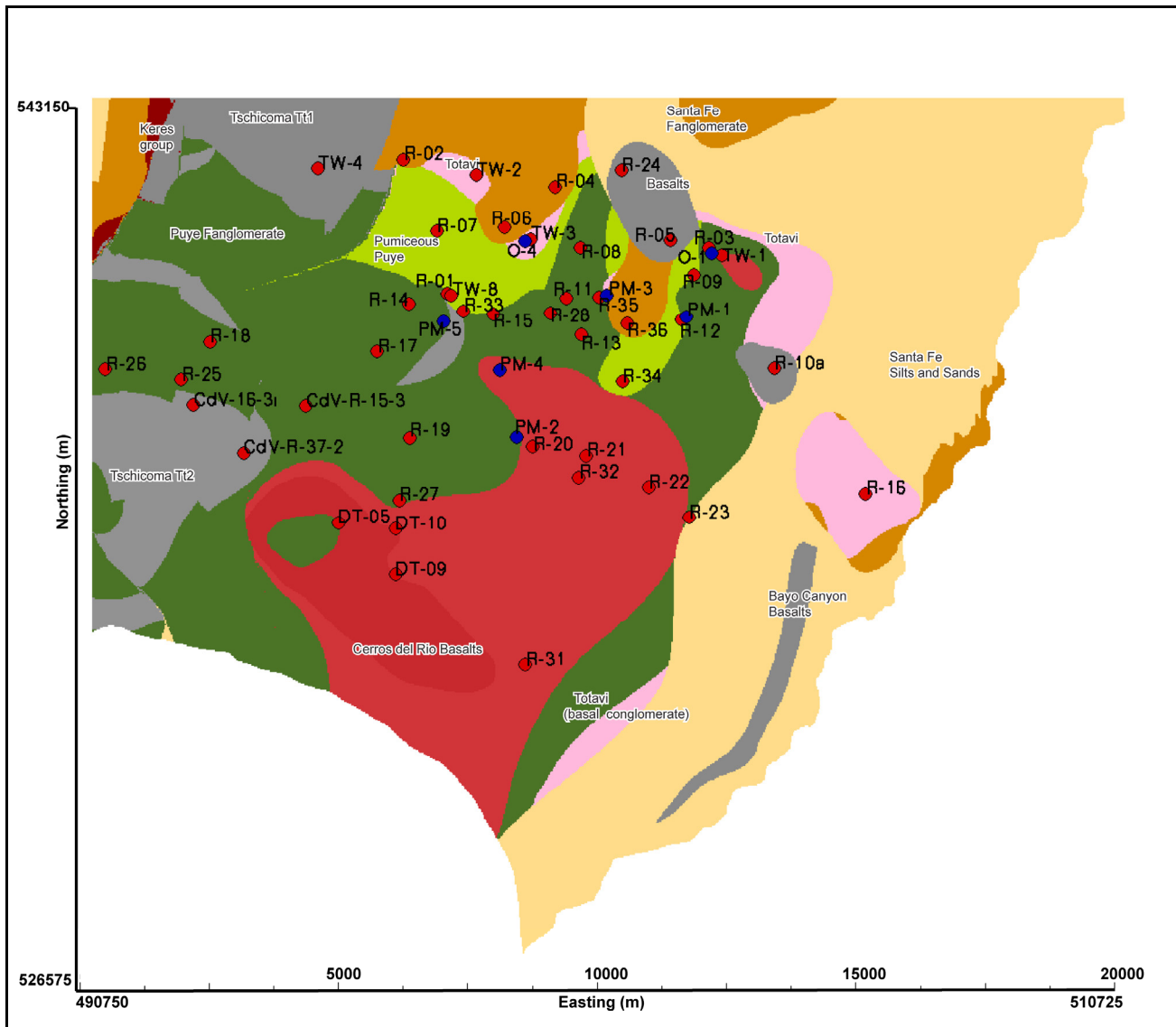
Figure J-3.0-4   LGM2D hydrostratigraphy along the water table
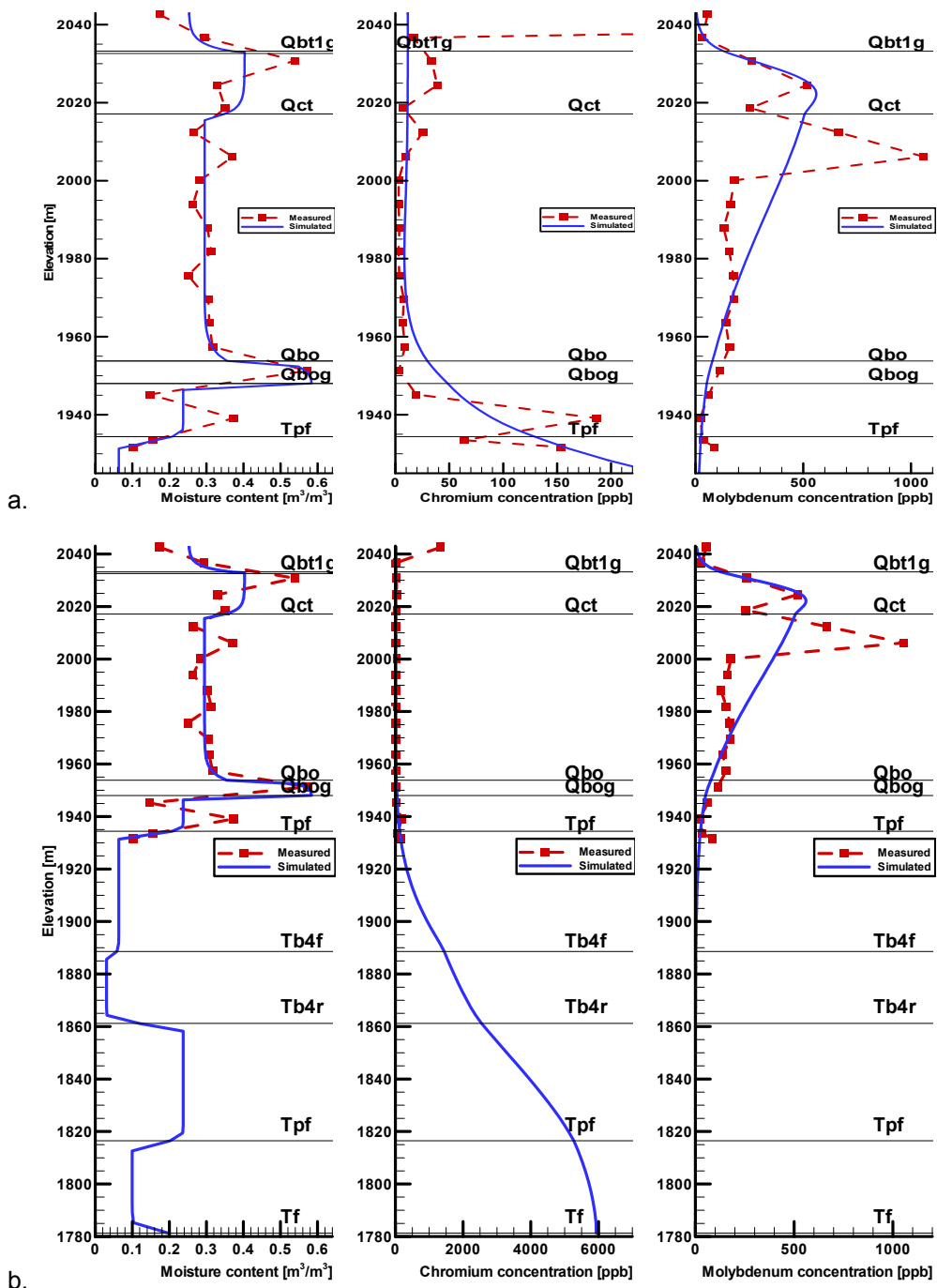
Figure J-4.3-1   Observed (red-dashed line) vs. simulated (blue solid line) data of moisture content and chromium and molybdenum concentrations at SCC-2. The model results represent the most probable predictions based on available data. The same data are shown on both plots. Plot (a) shows the depth over which borehole data are available; Plot (b) shows the entire vadose zone beneath Qal.
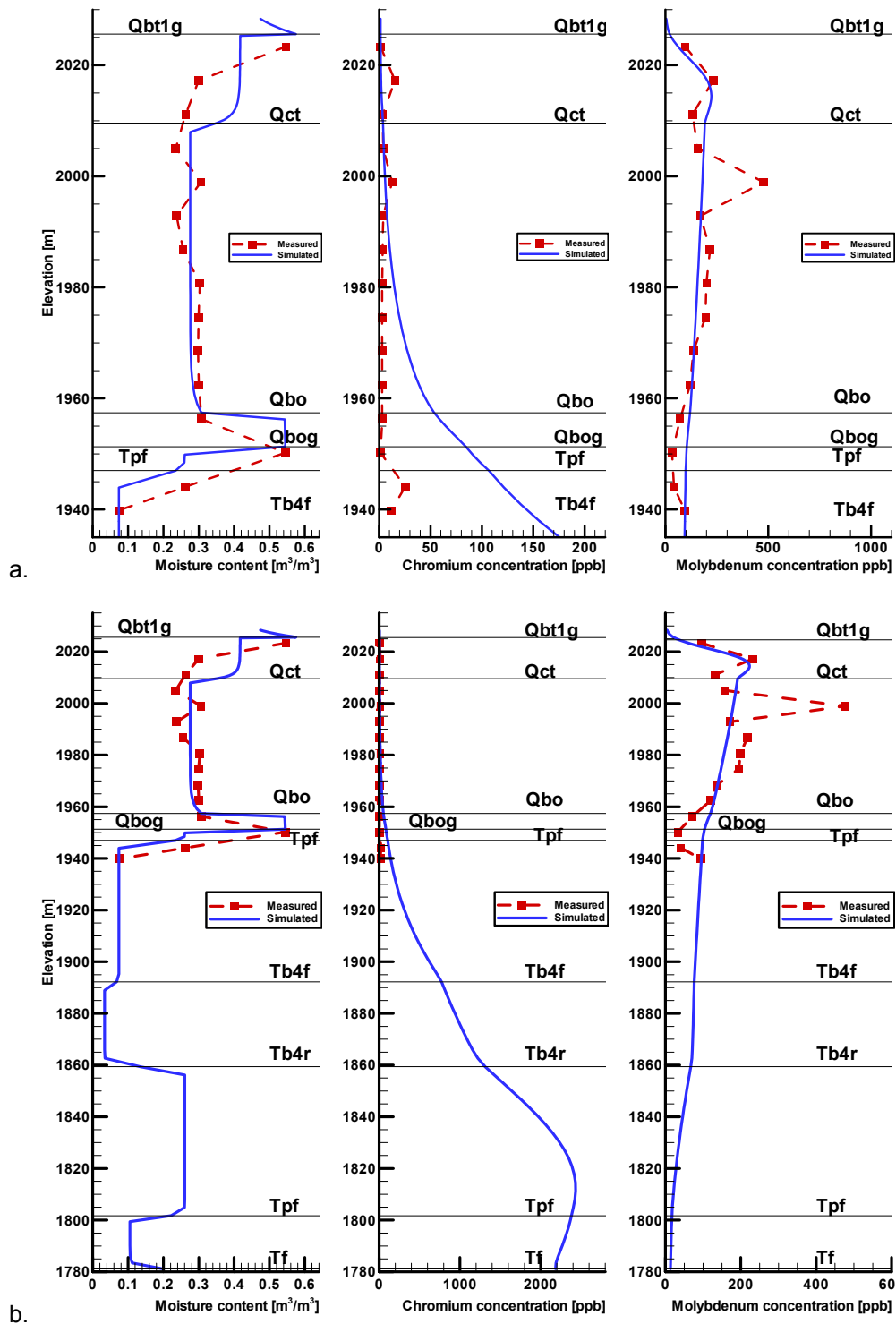
Figure J-4.3-2   Observed (red-dashed line) vs. simulated (blue solid line) data of moisture content and chromium and molybdenum concentrations at SCC-3. The model results represent the most probable predictions based on available data. The same data are shown on both plots. Plot (a) shows the depth over which borehole data are available; Plot (b) shows the entire vadose zone.
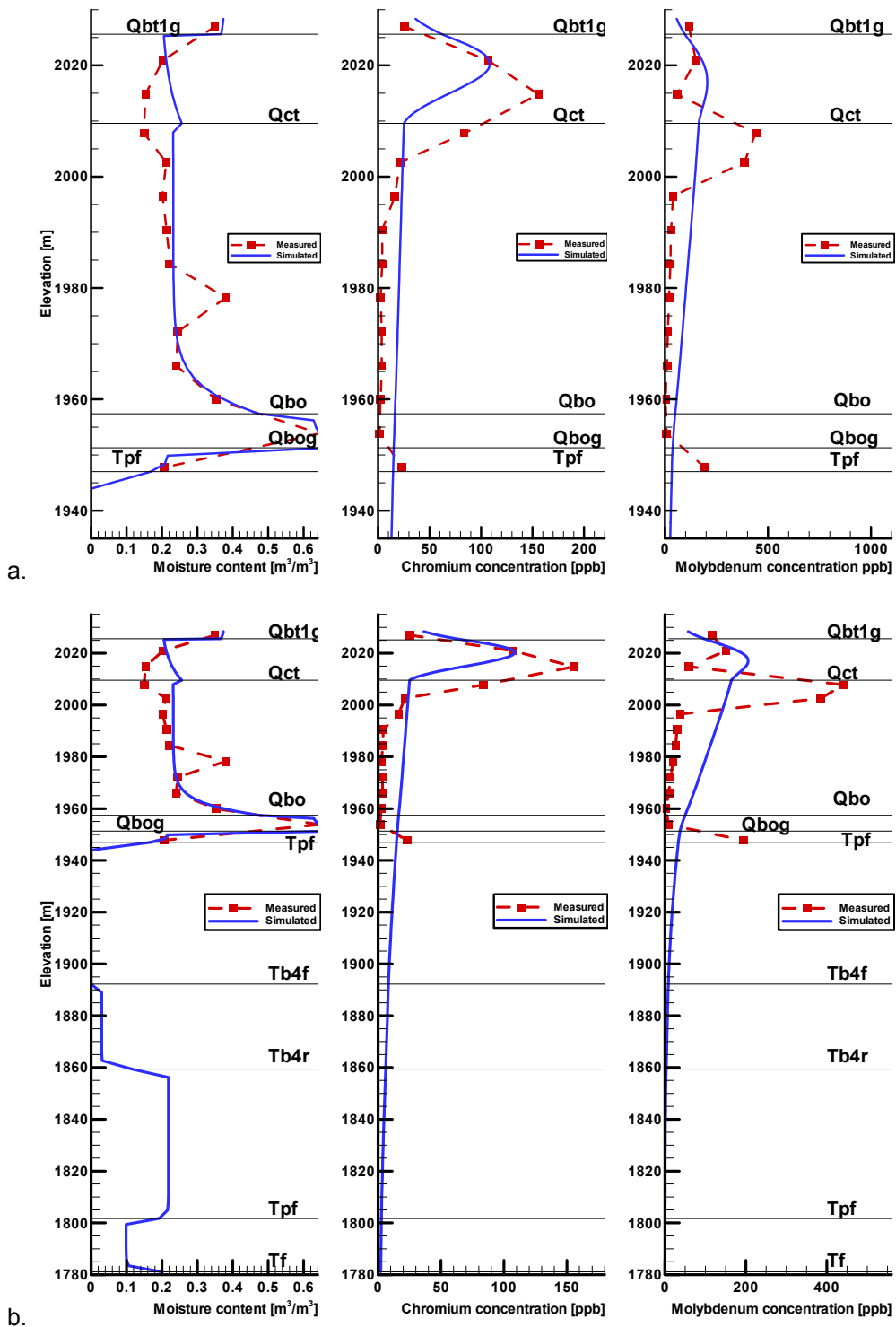
Figure J-4.3-3 Observed (red-dashed line) vs. simulated (blue solid line) data of moisture content and chromium and molybdenum concentrations at SCC-4. The model results represent the most probable predictions based on available data. The same data are shown on both plots. Plot (a) shows the depth over which borehole data are available; Plot (b) shows the entire vadose zone.
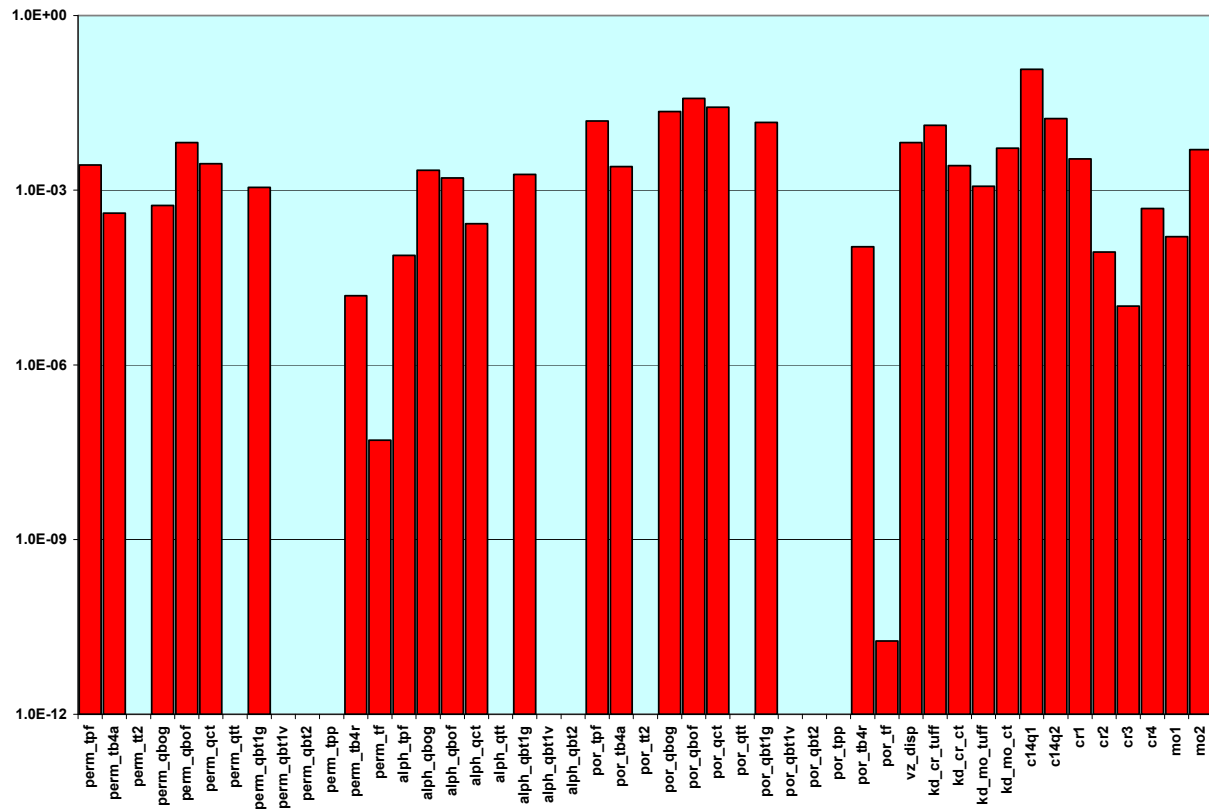
Figure J-4.3-4 **Linear point sensitivities of model parameters related to calibration data at SCC-2 (moisture content and chromium and molybdenum concentrations)**
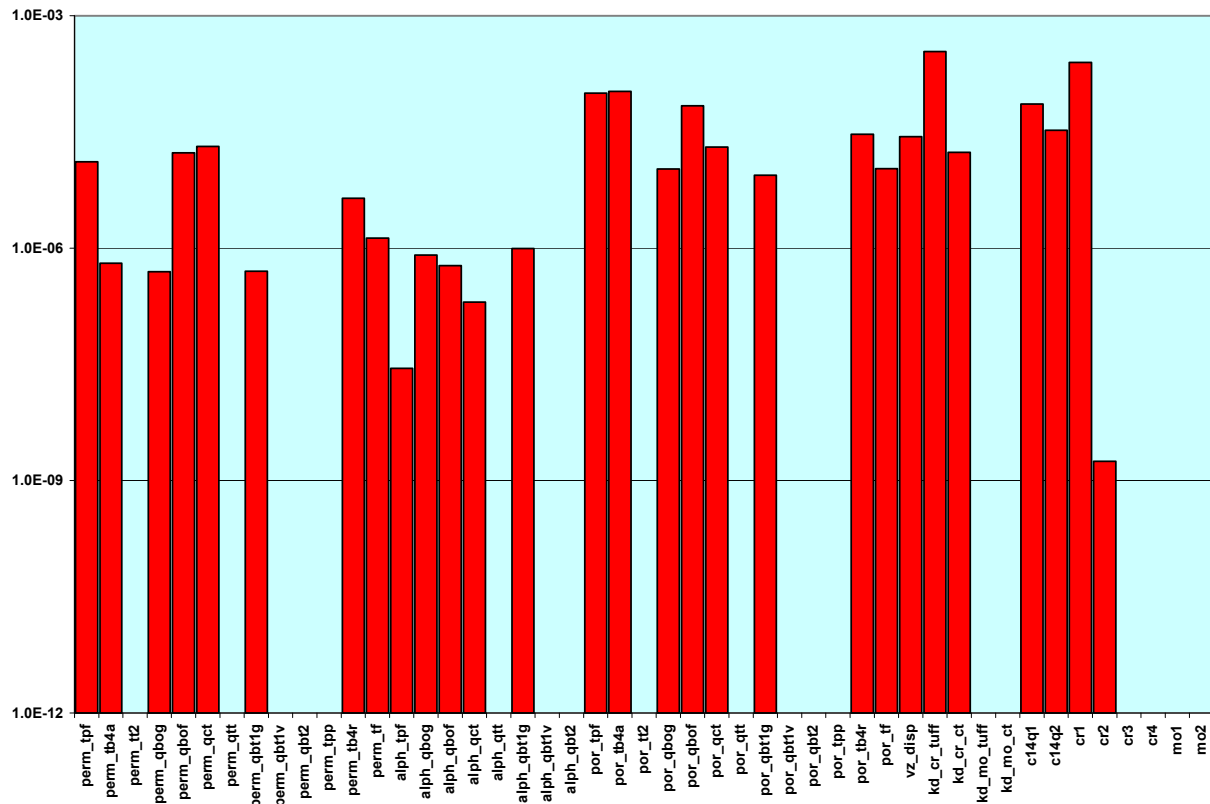
Figure J-4.3-5   Linear point sensitivities of model parameters related to model predicted chromium concentration at the top of the regional aquifer at SCC-2
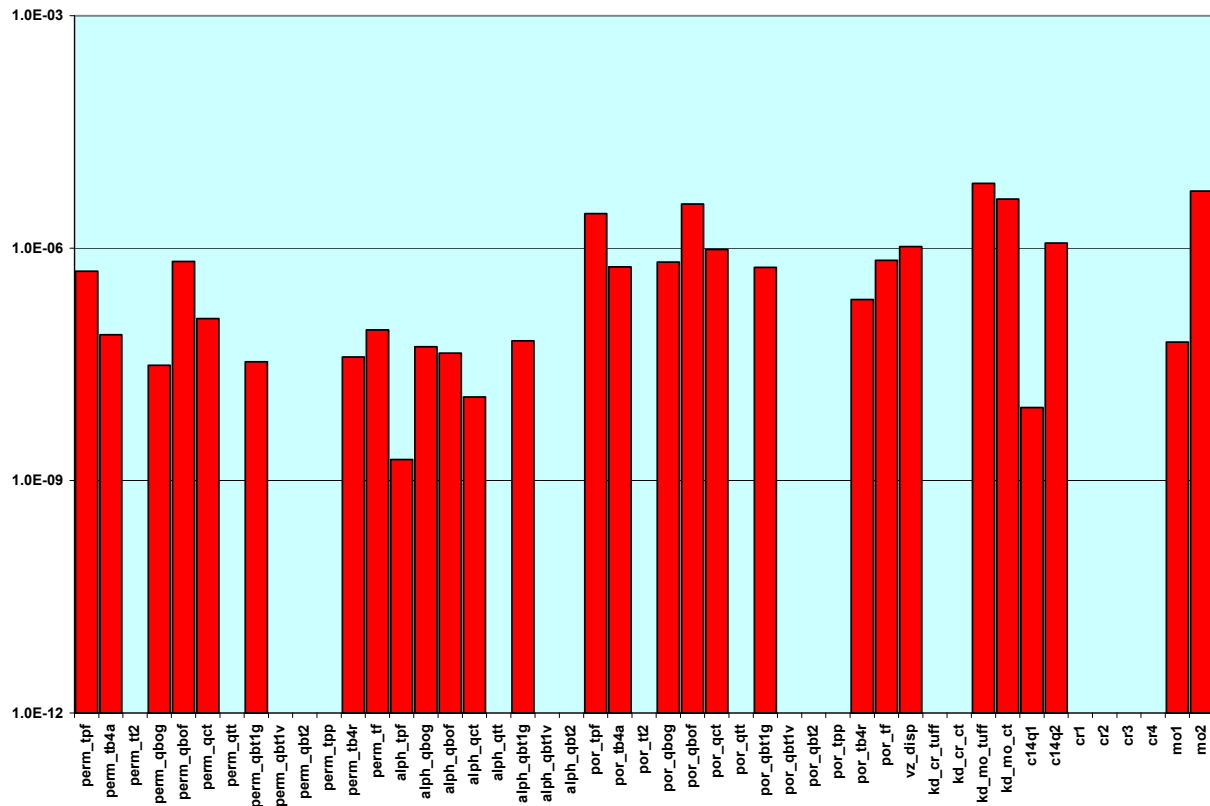
Figure J-4.3-6   Linear point sensitivities of model parameters related to model predicted molybdenum concentration at the top of the regional aquifer at SCC-2
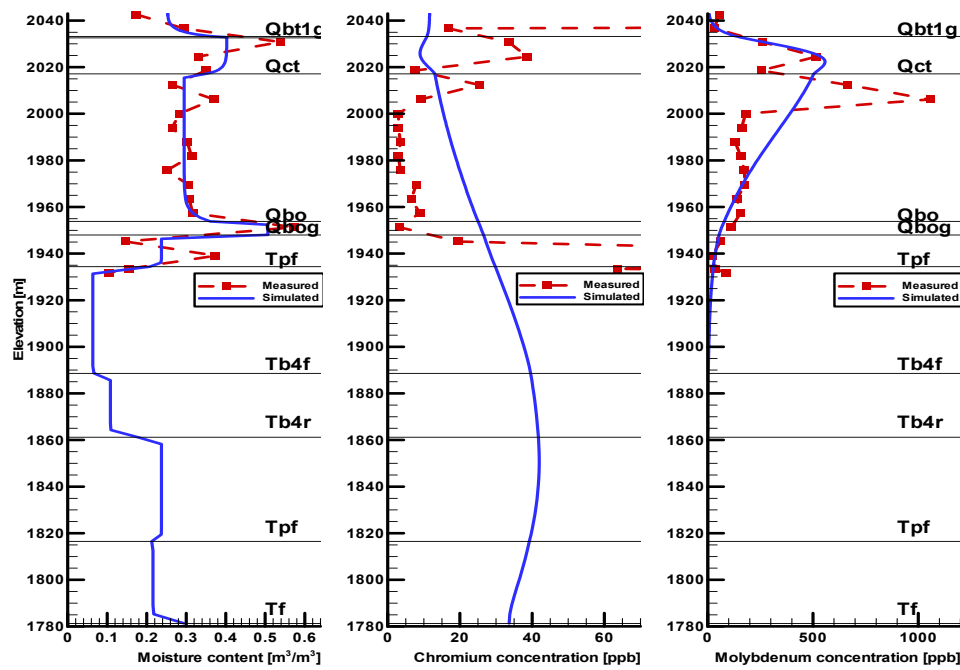
Figure J-4.3-7   **Observed (red-dashed line) vs. simulated (blue solid line) data of moisture content and chromium and molybdenum concentrations at SCC-2. The model results represent the minimum prediction (confidence level 95%) taking into account predictive uncertainty in the available data.**
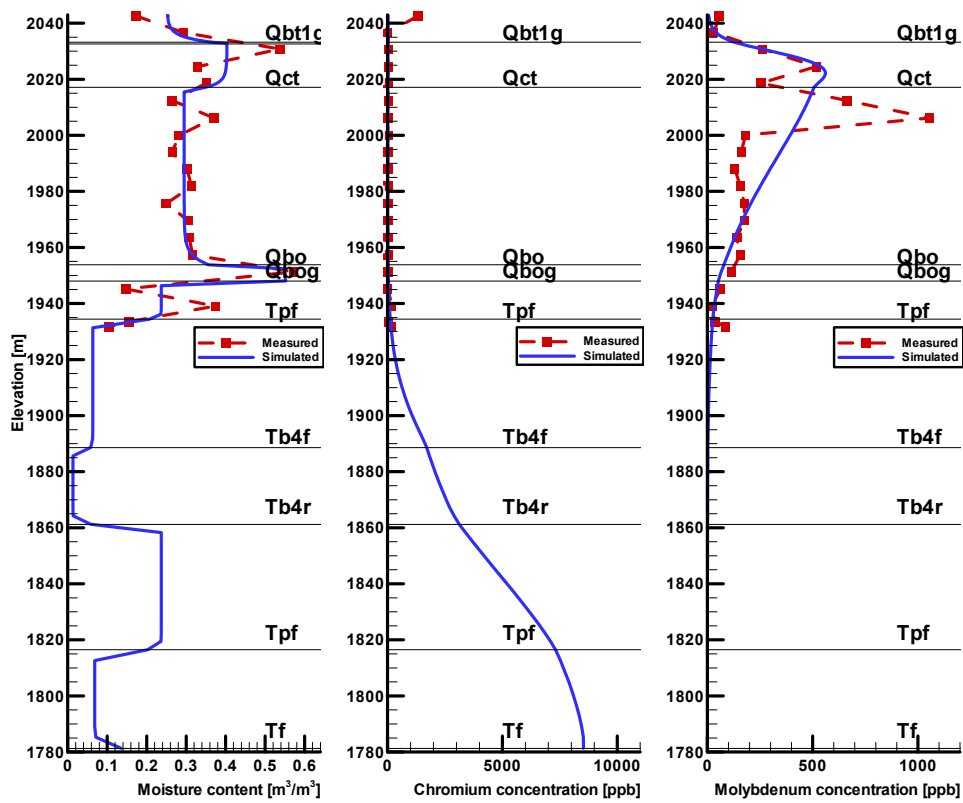
Figure J-4.3-8   Observed (red-dashed line) vs. simulated (blue solid line) data of moisture content and chromium and molybdenum concentrations at SCC-2. The model results represent the maximum prediction (confidence level 95%) taking into account predictive uncertainty in the available data.
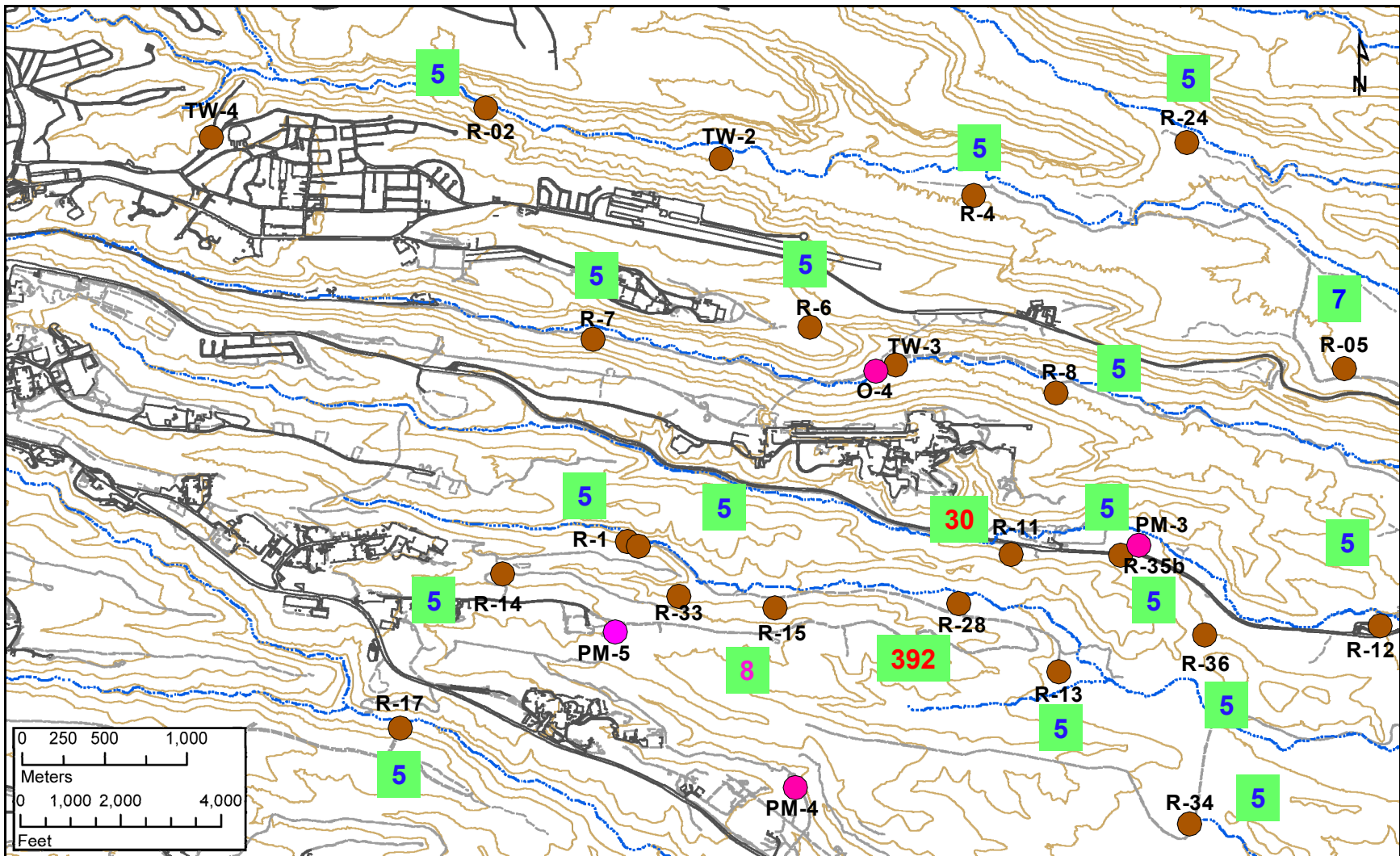
Figure J-5.1-1   Average chromium concentrations at the monitoring wells near Sandia Canyon
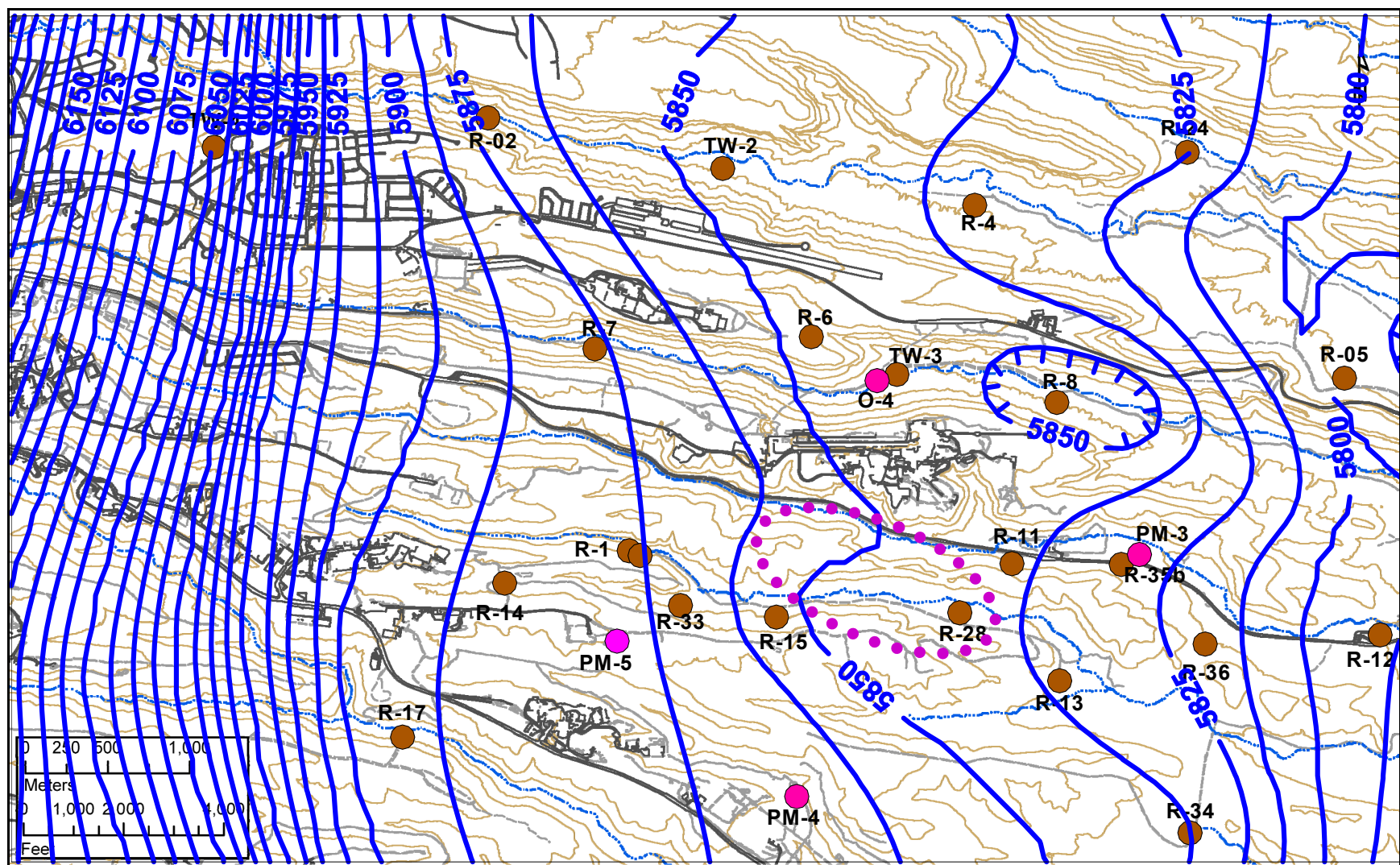
Figure J-5.1-2   Water-table map 1 near Sandia Canyon (based on Figure H-1). Water-level contours are labeled in feet. The pink dotted area defines an area where the chromium plume detected at R-28 may have arrived at the top of the regional aquifer.

Fate and Transport Update for Chromium from Sandia Canyon
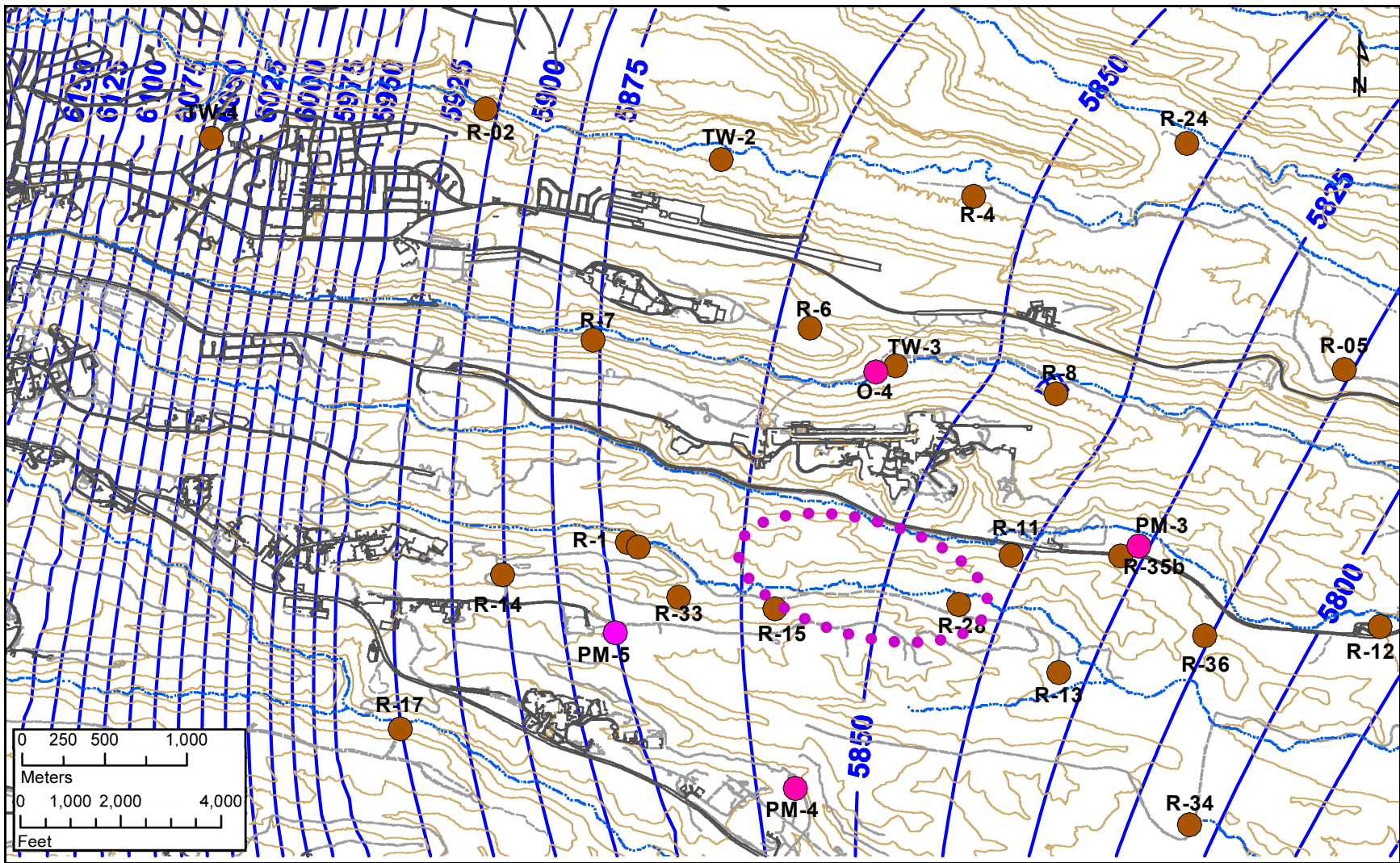
Figure J-5.1-3 **Water-table map 2 near Sandia Canyon (based on Figure H-2). Water-level contours are labeled in feet. The pink dotted area defines an area where the chromium plume detected at R-28 may have arrived at the top of the regional aquifer.**
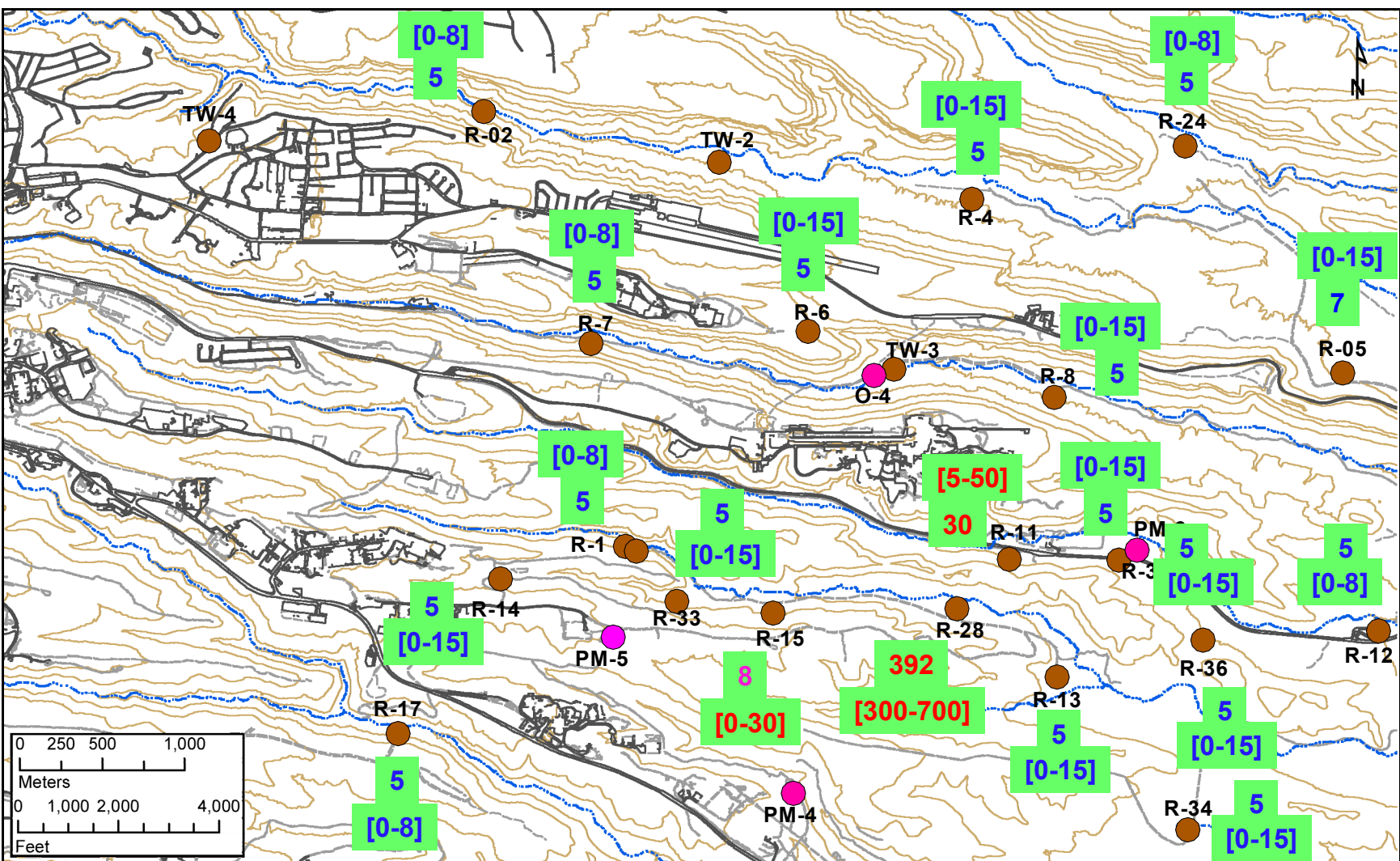
Figure J-5.1-4   Average chromium concentrations and calibration ranges at the monitoring wells near Sandia Canyon
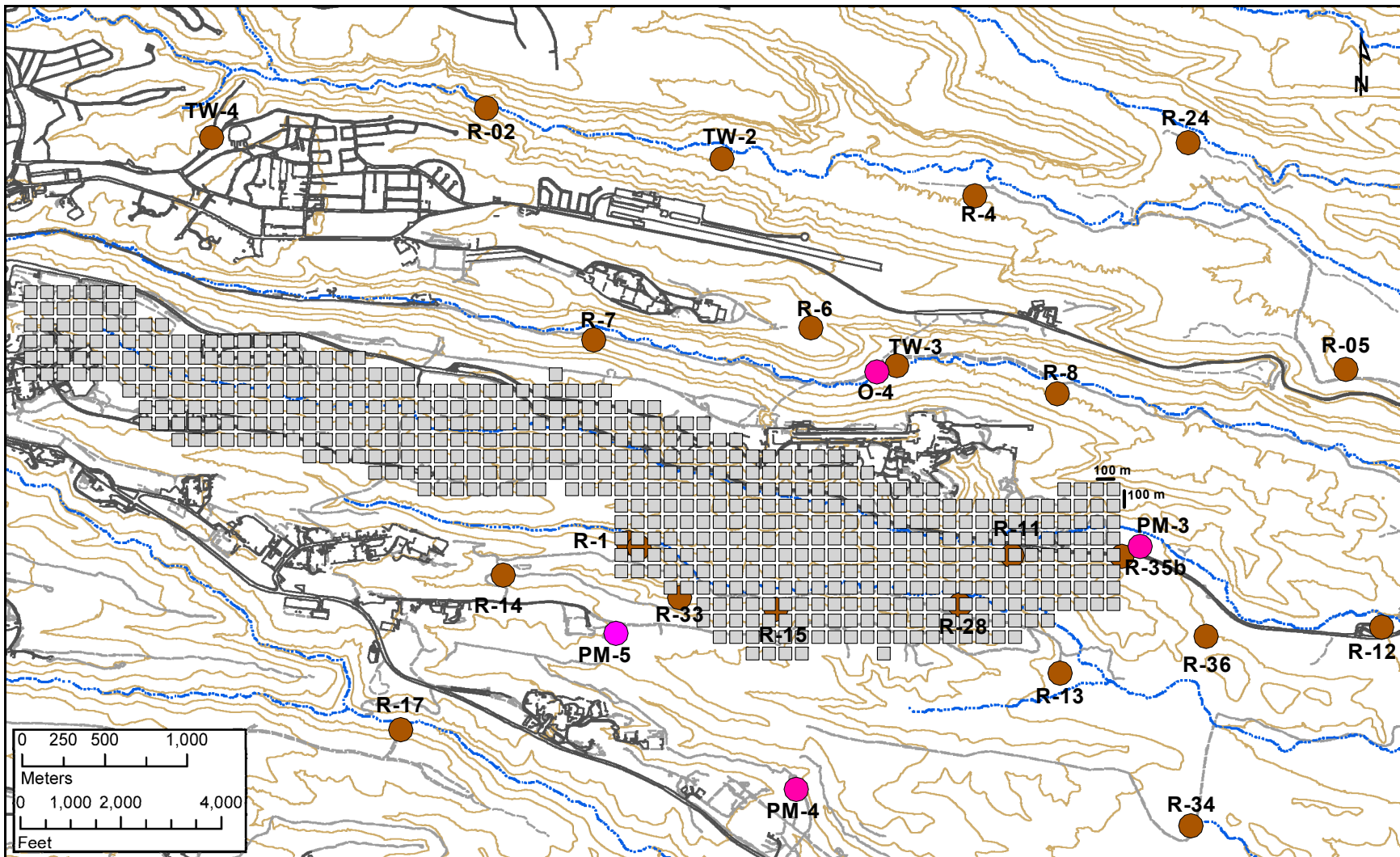
Figure J-5.1-5 **Potential locations of contaminant arrival at the top of the regional aquifer considered in the numerical inverse analyses. The 573 entry points are uniformly spaced laterally, with 100-m spacing. The individual entry locations have a lateral size of 10 × 10 m^2. The squares identifying the entry locations do not represent the size of the entry location; they are intended for visualization purposes only.**
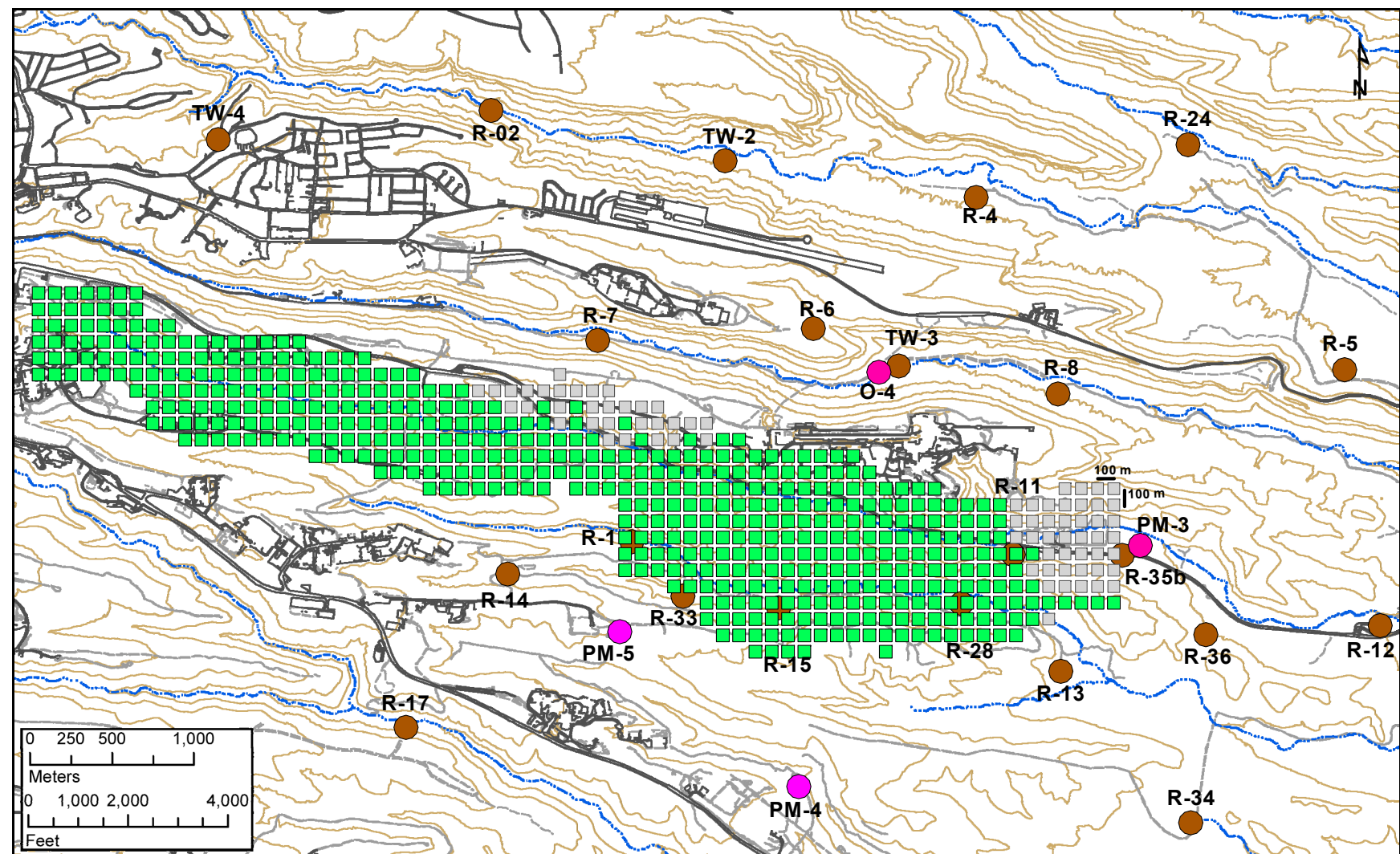
Figure J-5.1-6   **Potential locations of contaminant arrival at the top of the regional aquifer that can produce inverse numerical models consistent with R-28 calibration ranges (500 out of 573), assuming arrival at a single entry location. The model uses the water table map presented in Figure H-1 and longitudinal/transverse dispersivities equal to 100 and 10 m, respectively.**
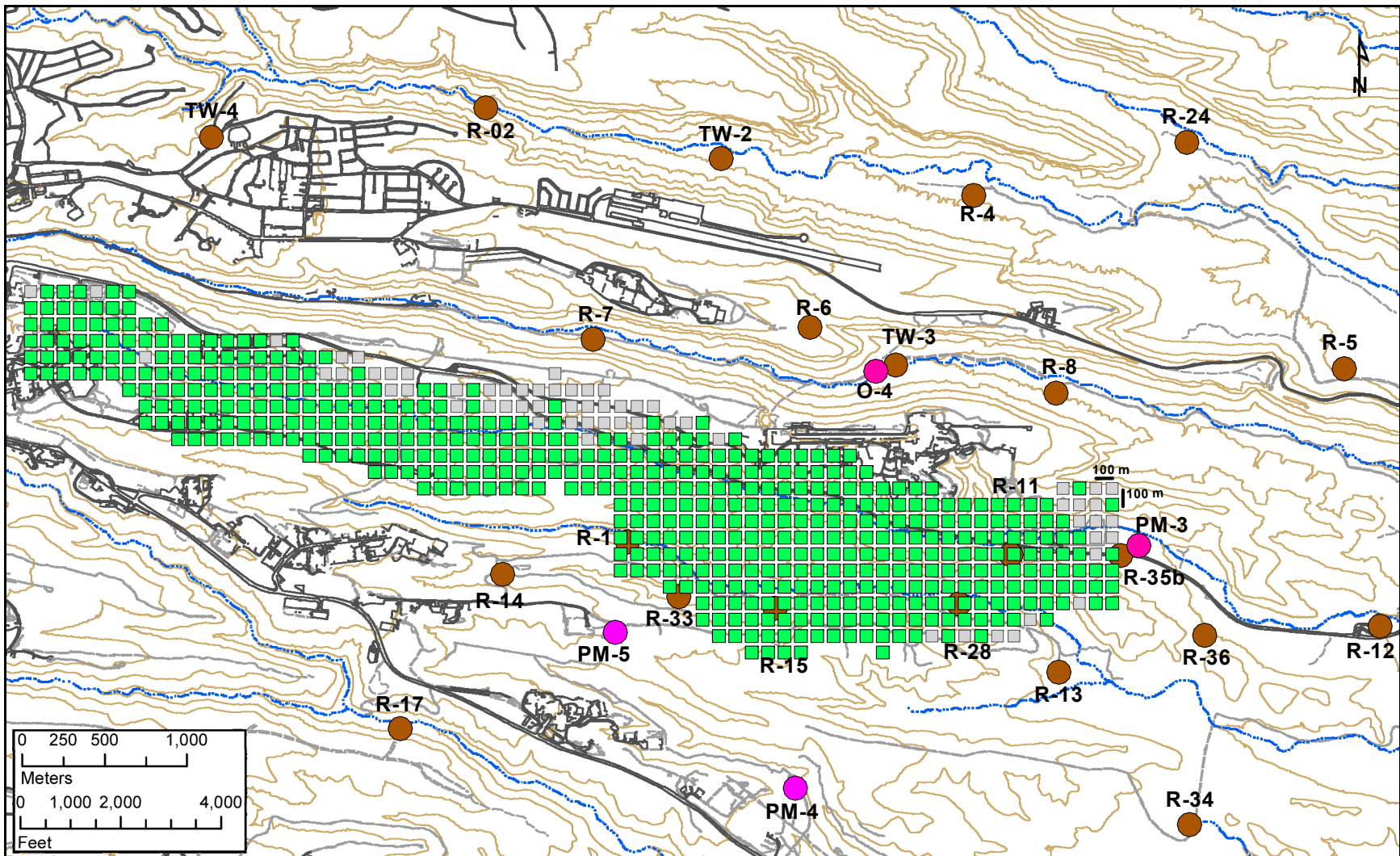
Figure J-5.1-7 **Potential locations of contaminant arrival at the top of the regional aquifer that can produce inverse numerical models consistent with R-11 calibration ranges (510 out of 573), assuming arrival at a single entry location. The model uses the water table map presented in Figure H-1 and longitudinal/transverse dispersivities equal to 100 and 10 m, respectively.**
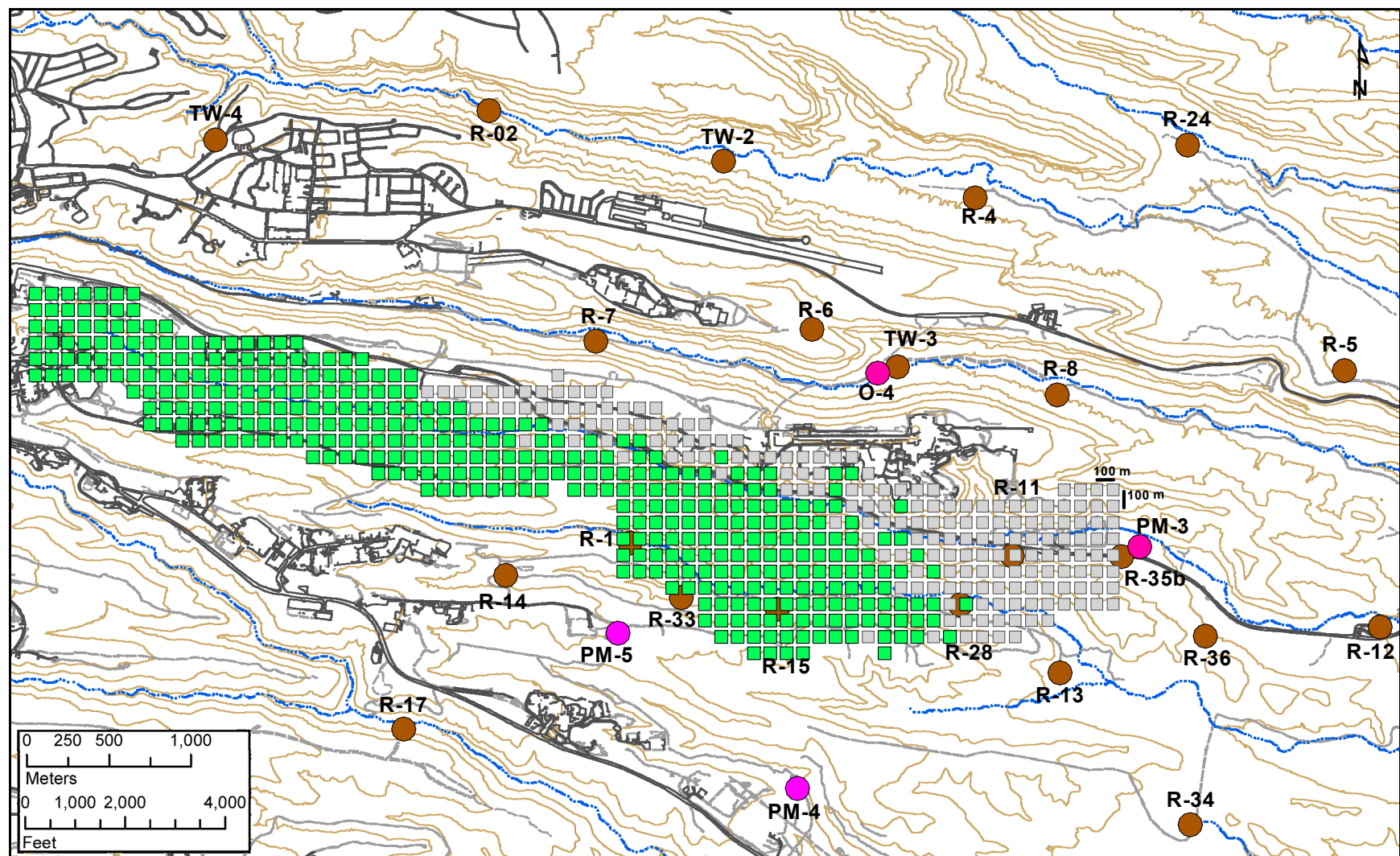
Figure J-5.1-8   Potential locations of contaminant arrival at the top of the regional aquifer that can produce inverse numerical models consistent with R-15 calibration ranges (389 out of 573), assuming arrival at a single entry location. The model uses the water table map presented in Figure H-1 and longitudinal/transverse dispersivities equal to 100 and 10 m, respectively.
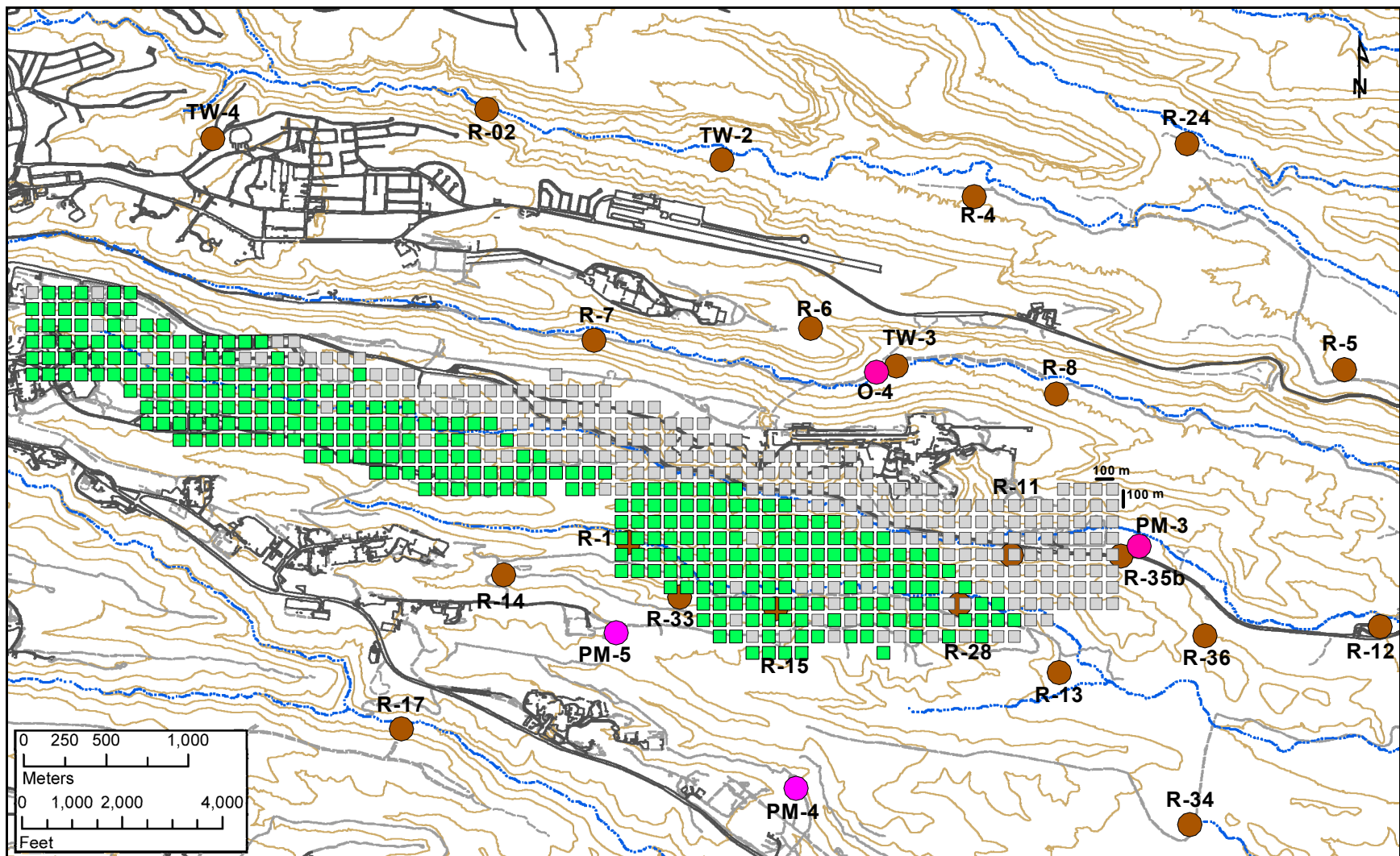
Figure J-5.1-9   Potential locations of contaminant arrival at the top of the regional aquifer that can produce inverse numerical models consistent with R-28 and R-11 calibration ranges simultaneously (319 out of 573), assuming arrival at a single entry location. The model uses the water table map presented in Figure H-1 and longitudinal/transverse dispersivities equal to 100 and 10 m, respectively.

Fate and Transport Update for Chromium from Sandia Canyon
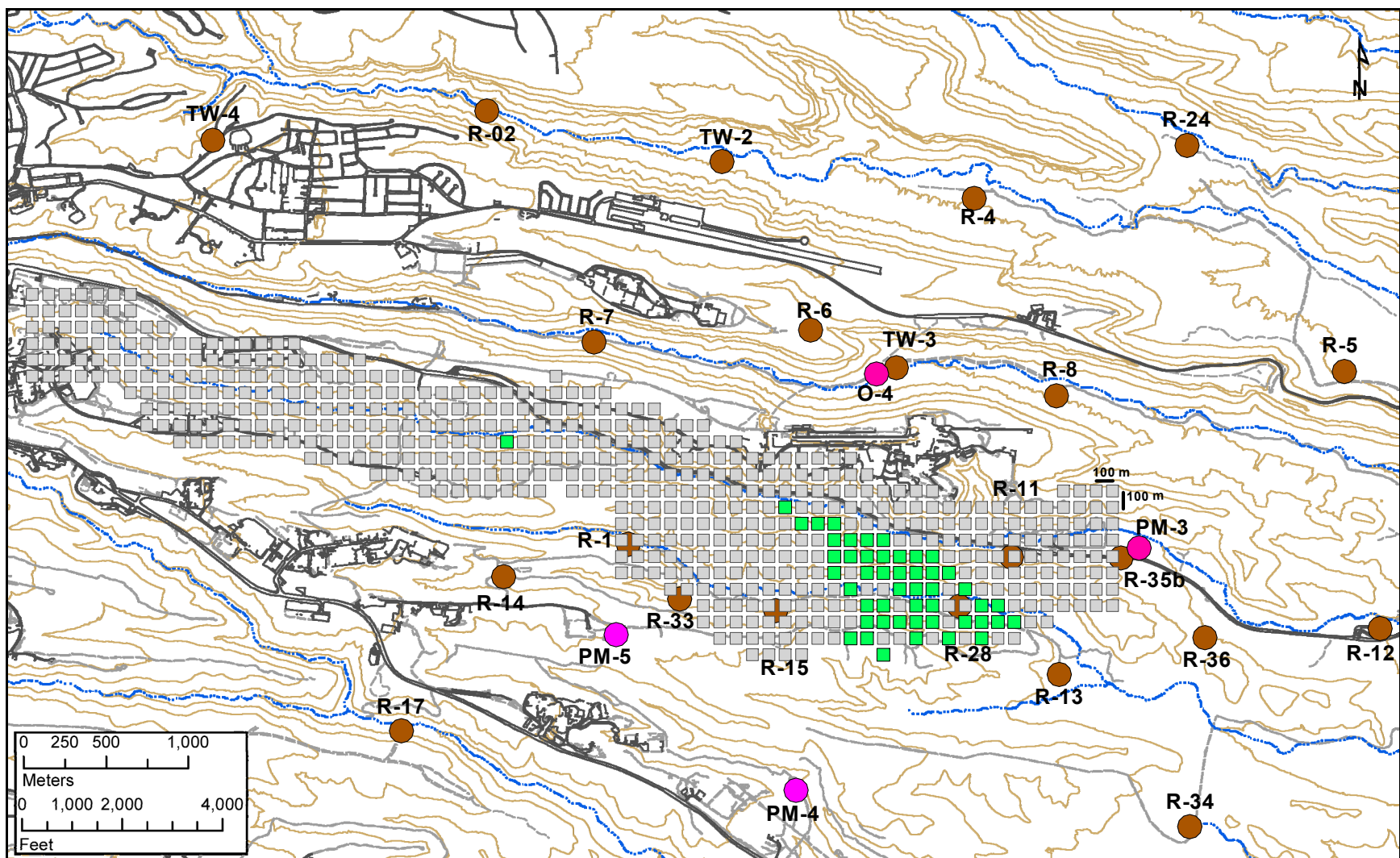
Figure J-5.1-10   Potential locations of contaminant arrival at the top of the regional aquifer that can produce inverse numerical models consistent with R-28, R-15 and R-11 calibration ranges simultaneously (49 out of 573), assuming arrival at a single entry location. The model uses the water table map presented in Figure H-1 and longitudinal/transverse dispersivities equal to 100 and 10 m, respectively.
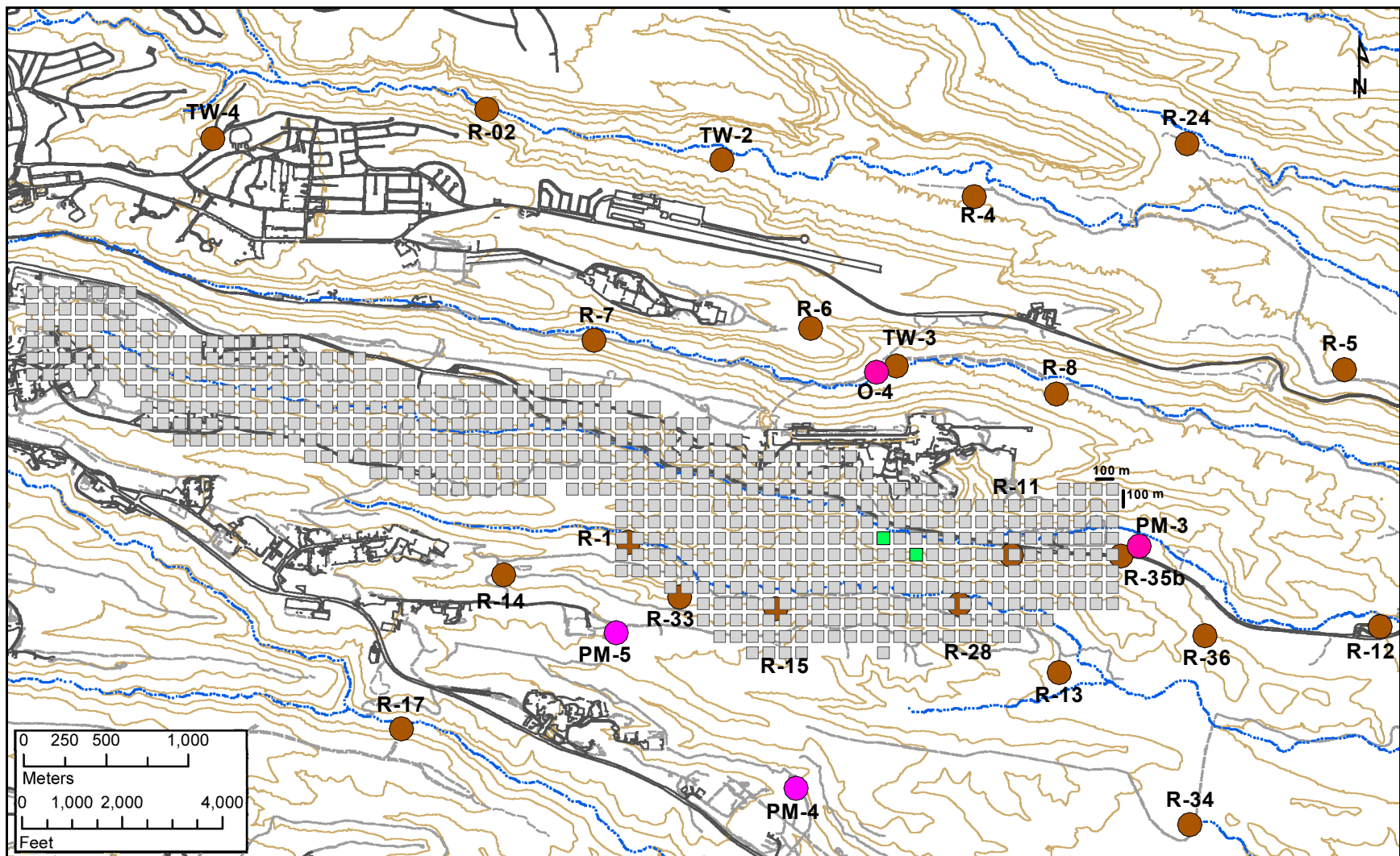
Figure J-5.1-11 **Potential locations of contaminant arrival at the top of the regional aquifer that can produce inverse numerical models consistent with calibration ranges at all the wells simultaneously (2 out of 573), assuming arrival at a single entry location. The model uses the water table map presented in Figure H-1 and longitudinal/transverse dispersivities equal to 50 and 5 m, respectively.**

Fate and Transport Update for Chromium from Sandia Canyon
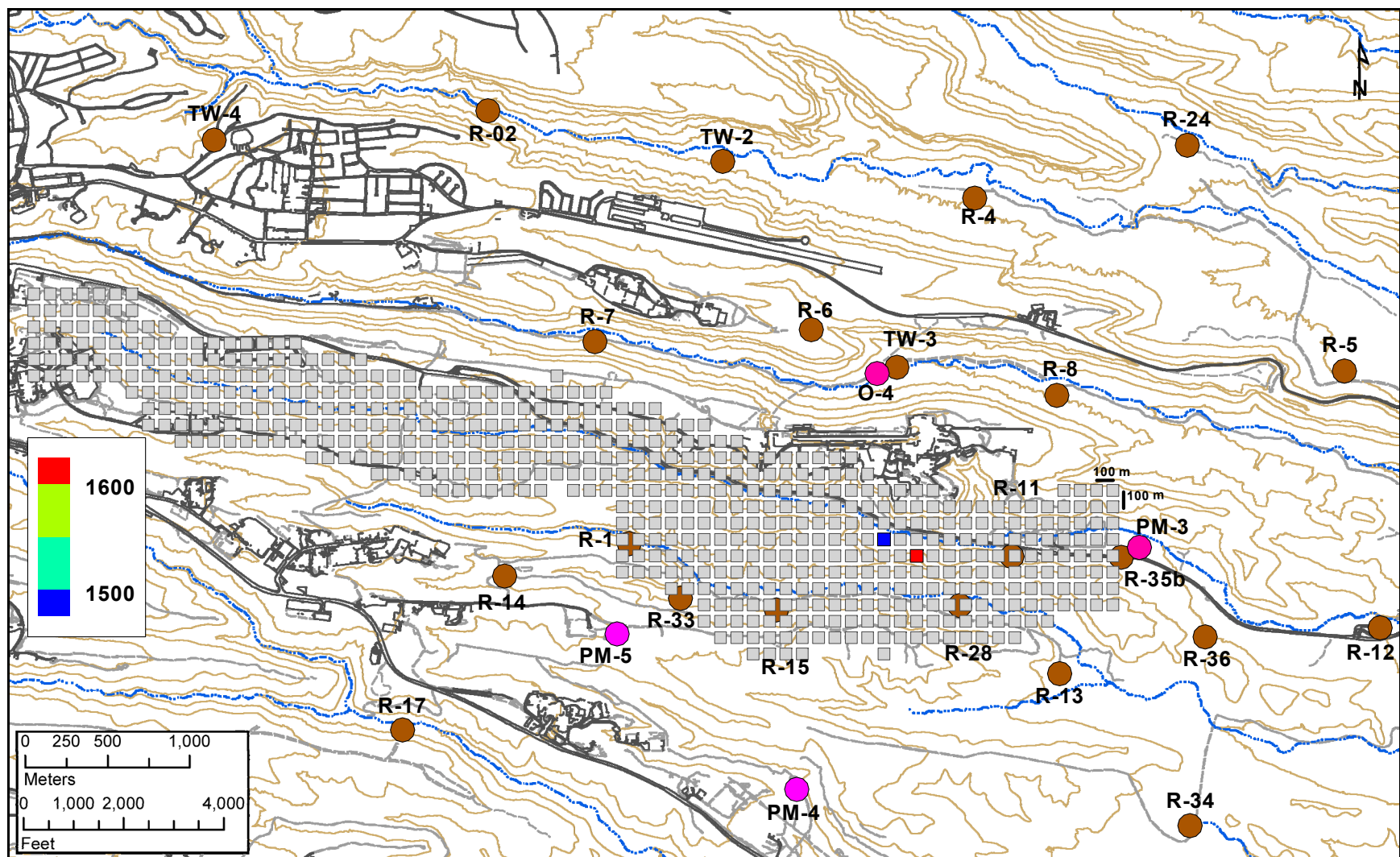
Figure J-5.1-12   Maximum concentrations at the entry points at the top of the regional aquifer that can produce inverse numerical models consistent with calibration ranges at all the wells simultaneously for the solution presented in Figure J-5.1-11. The model uses the water table map presented in Figure H-1 and longitudinal/transverse dispersivities equal to 50 and 5 m, respectively.

Fate and Transport Update for Chromium from Sandia Canyon
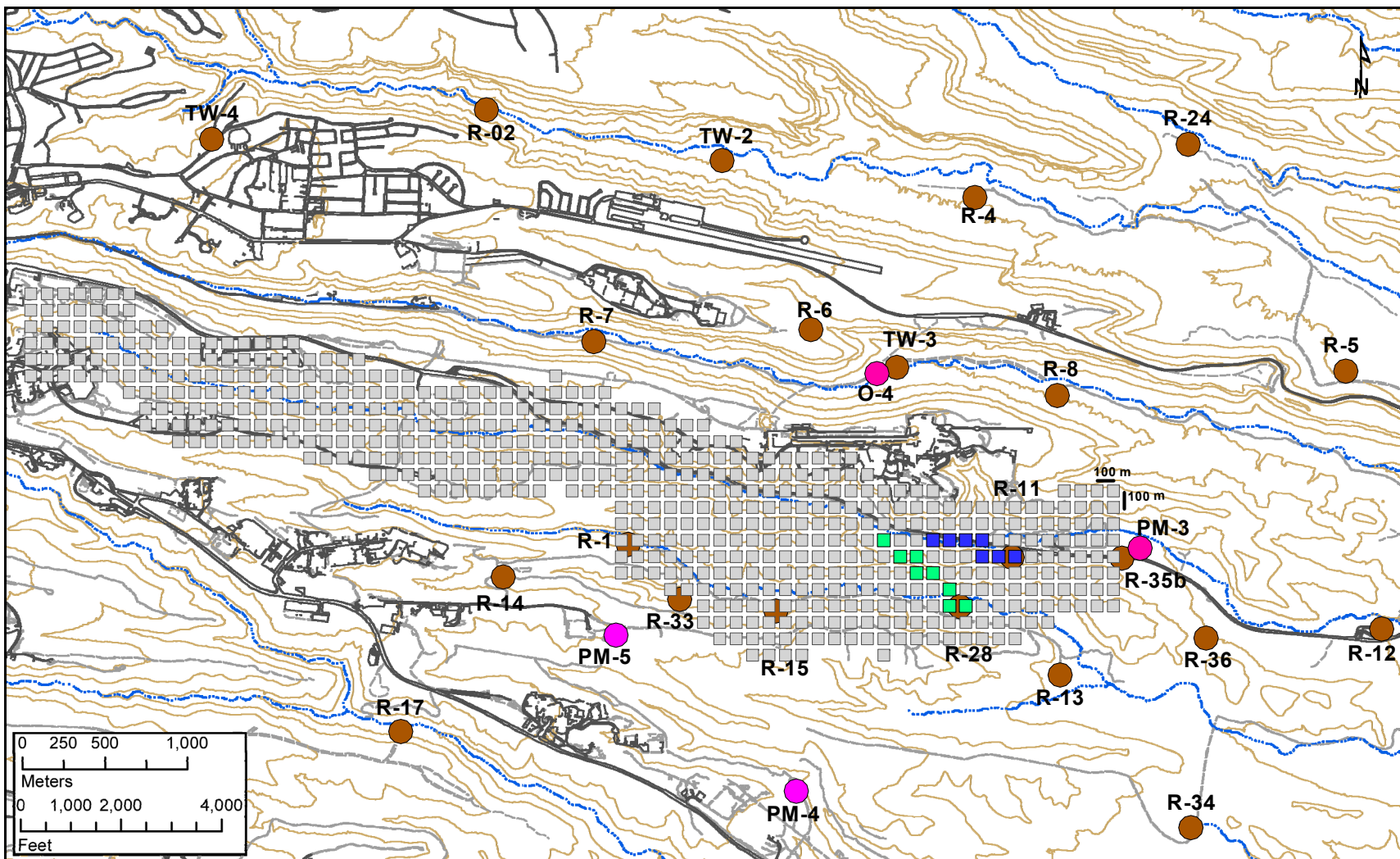
Figure J-5.1-13 **Potential locations of contaminant arrival at the top of the regional aquifer that can produce inverse numerical models consistent with calibration ranges at all the wells simultaneously. Two sets of potential entry locations are considered: potential entry locations are shown in green and blues for contaminants detected at R-28 and R-11, respectively. The model uses the water table map presented in Figure H-1 and longitudinal/transverse dispersivities equal to 50 and 5 m, respectively.**
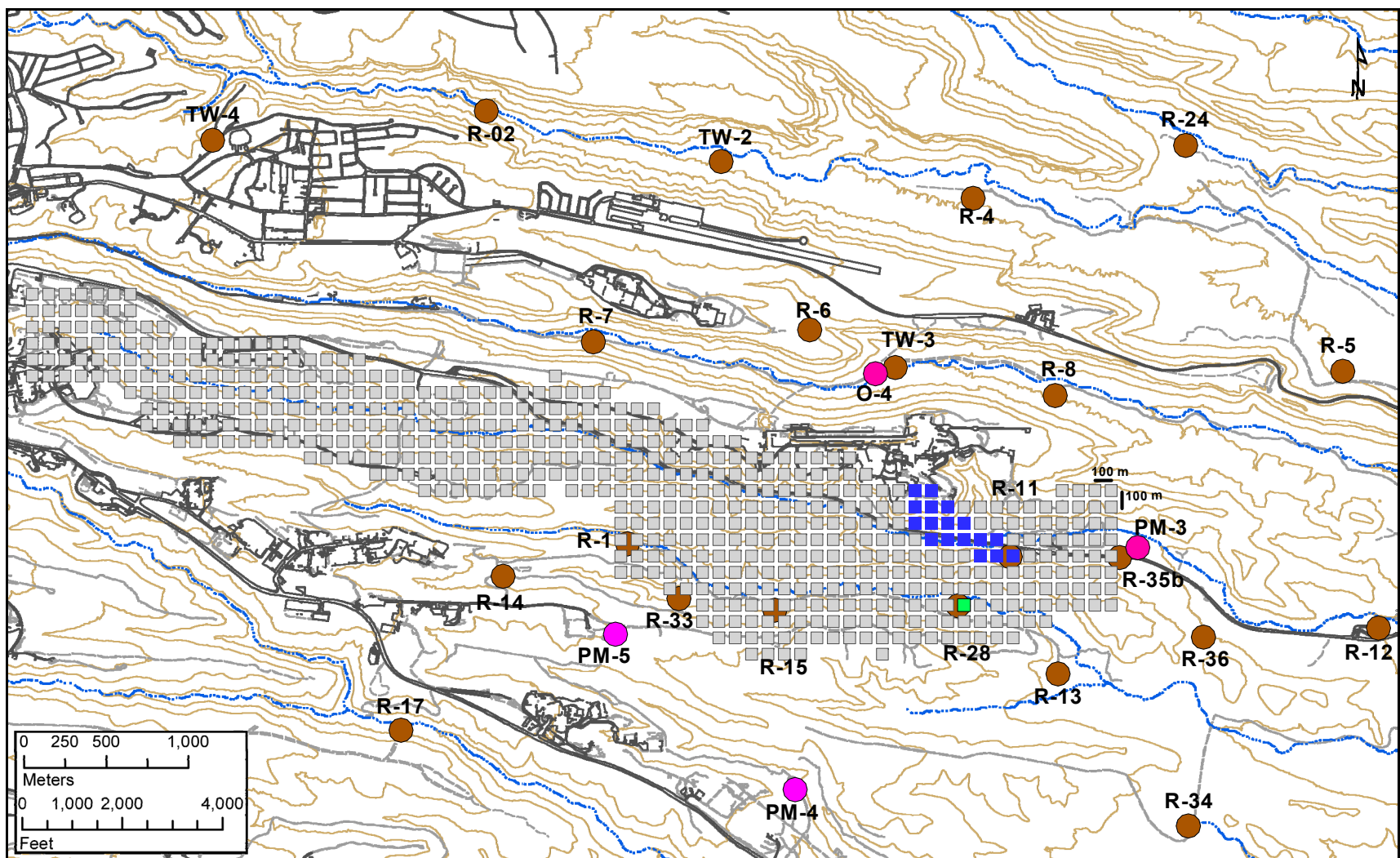
Figure J-5.1-14   Potential locations of contaminant arrival at the top of the regional aquifer that can produce inverse numerical models consistent with calibration ranges at all the wells simultaneously. Two sets of potential entry locations are considered: potential entry locations are shown in green and blues for contaminants detected at R-28 and R-11, respectively. The model uses the water table map presented in Figure H-2 and longitudinal/transverse dispersivities equal to 50 and 5 m, respectively.
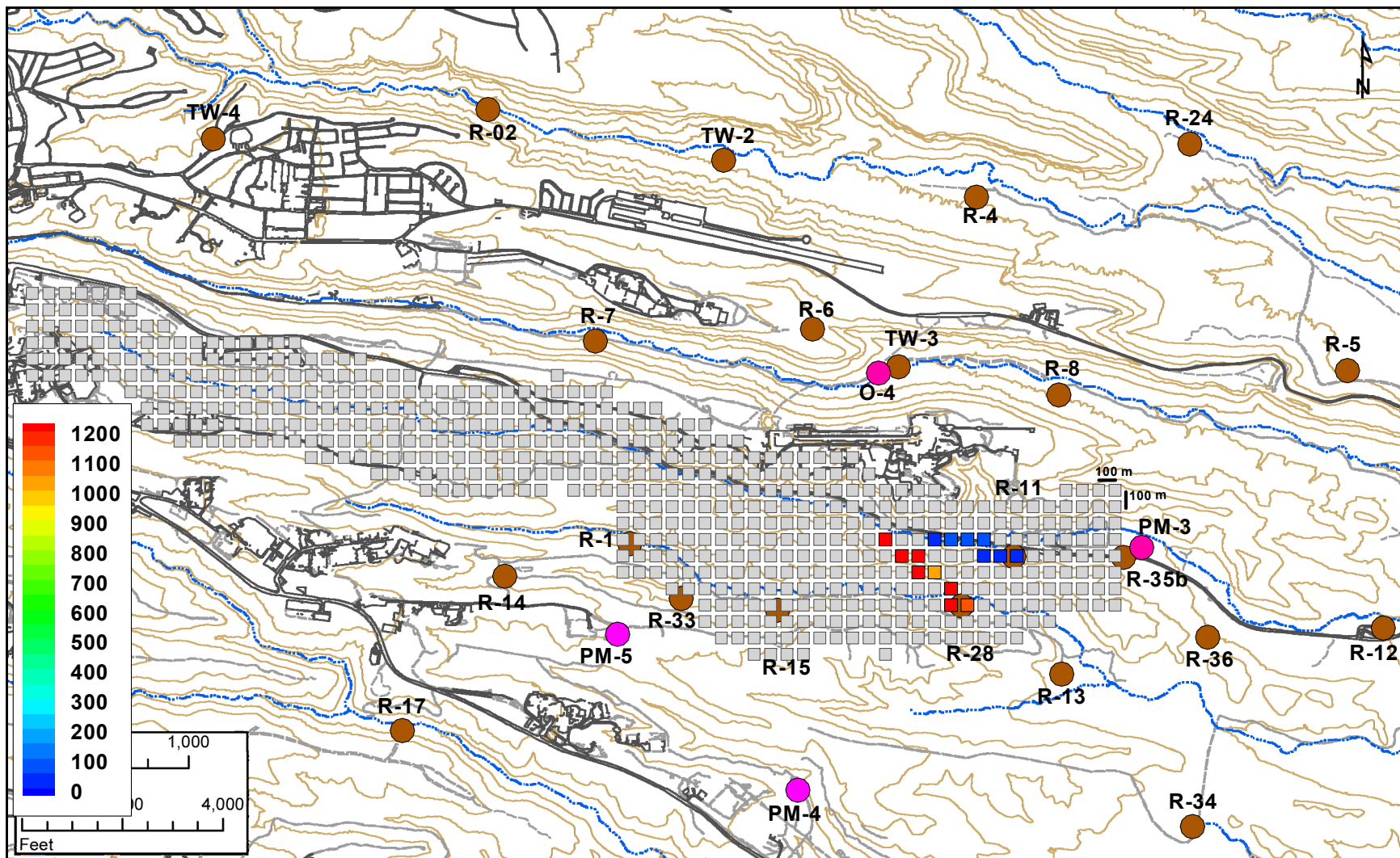
Figure J-5.1-15 **Maximum concentrations at the entry points at the top of regional aquifer that can produce inverse numerical models consistent with calibration ranges at all the wells simultaneously for the solution presented in Figure J-5.1-13. The model uses water table map presented in Figure H-1 and longitudinal/transverse dispersivities equal to 50 and 5 m, respectively.**
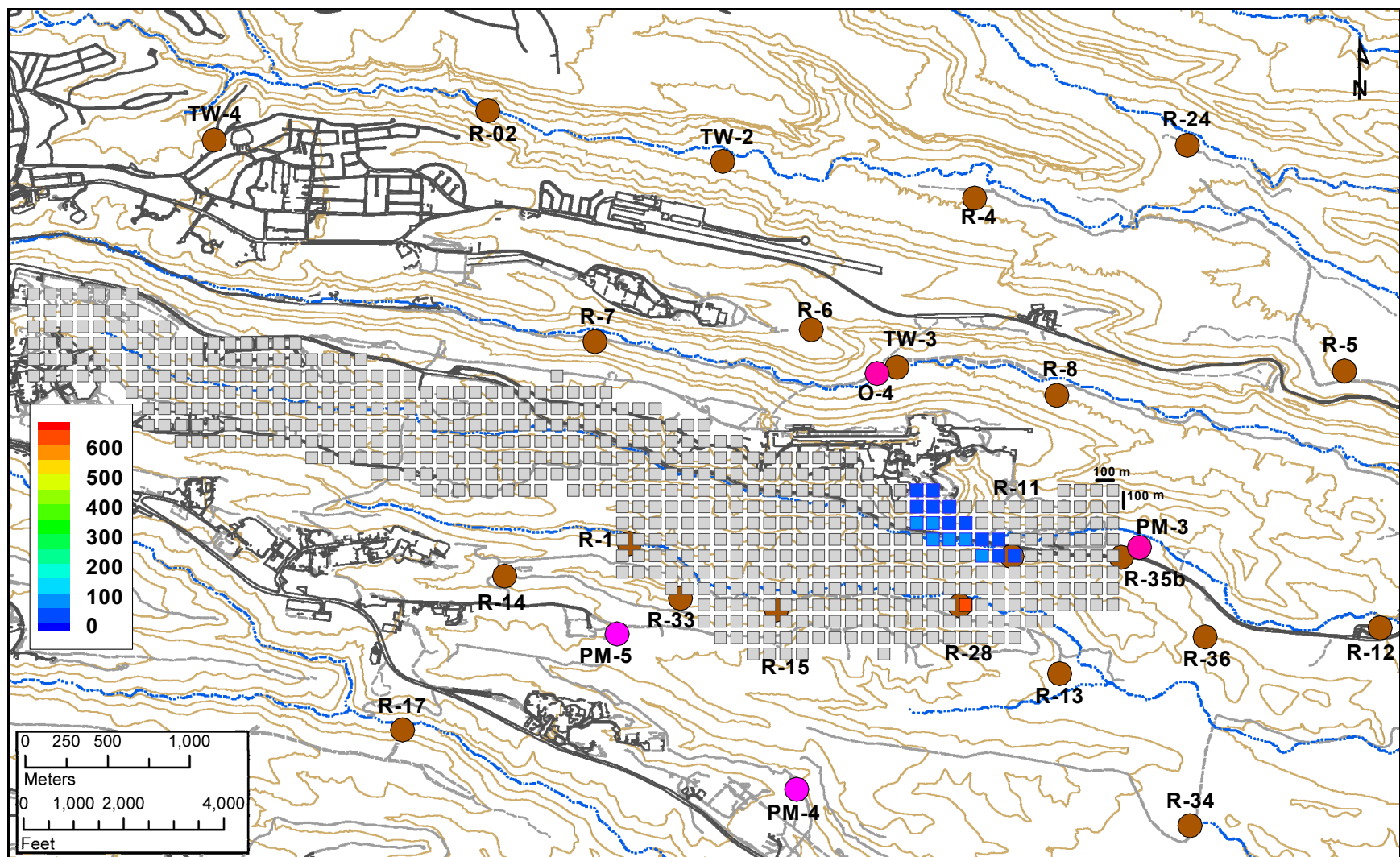
Figure J-5.1-16 **Maximum concentrations at the entry points at the top of regional aquifer that can produce inverse numerical models consistent with calibration ranges at all the wells simultaneously for the solution presented in Figure J-5.1-14. The model uses water table map presented in Figure H-2 and longitudinal/transverse dispersivities equal to 50 and 5 m, respectively.**

Fate and Transport Update for Chromium from Sandia Canyon
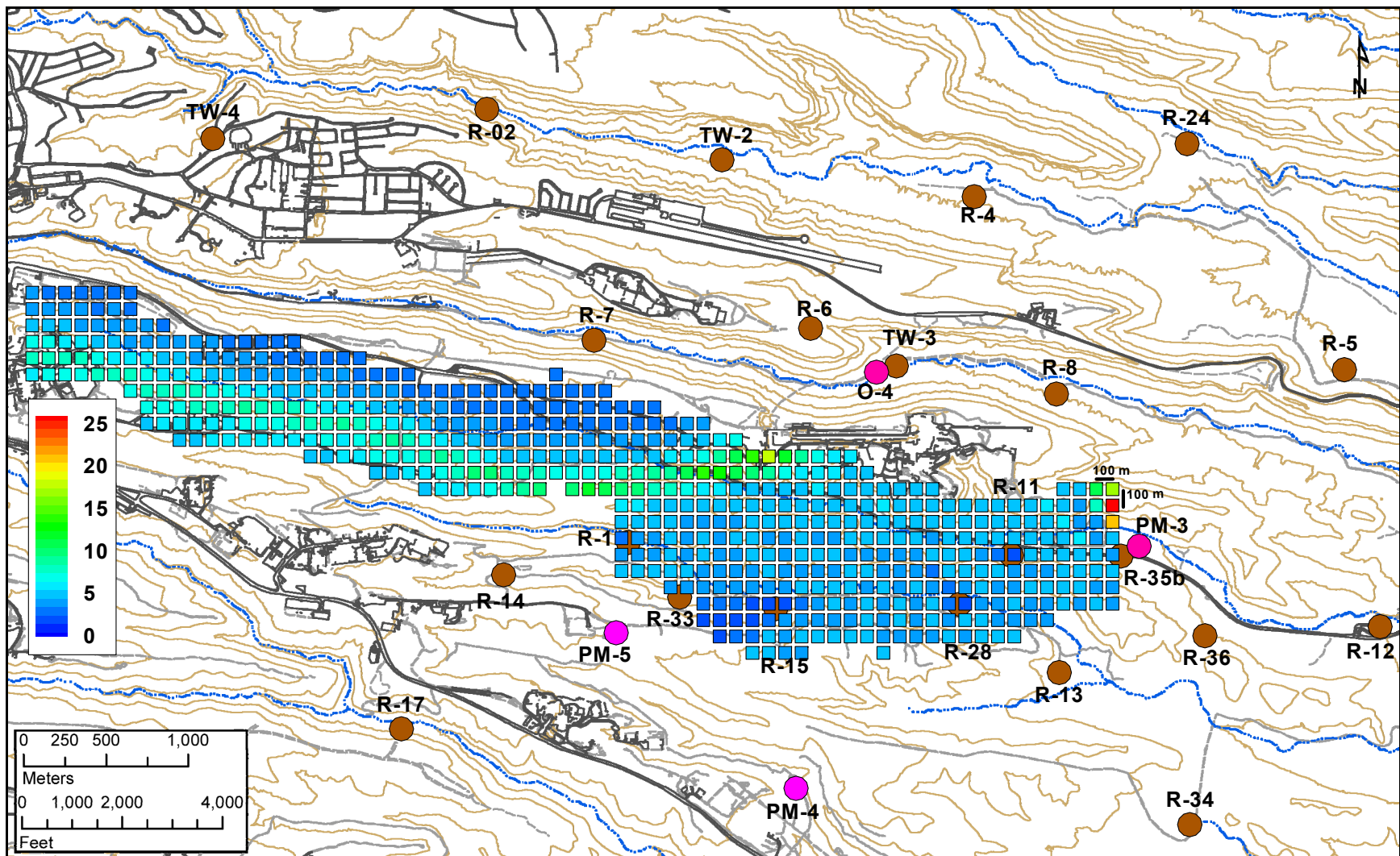
Figure J-5.1-17   Maximum concentrations at the entry points at the top of the regional aquifer that can produce inverse numerical models predicting 1 ppb at all the monitoring wells simultaneously. The model uses the water table map presented in Figure H-1 and longitudinal/transverse dispersivities equal to 100 and 10, respectively.
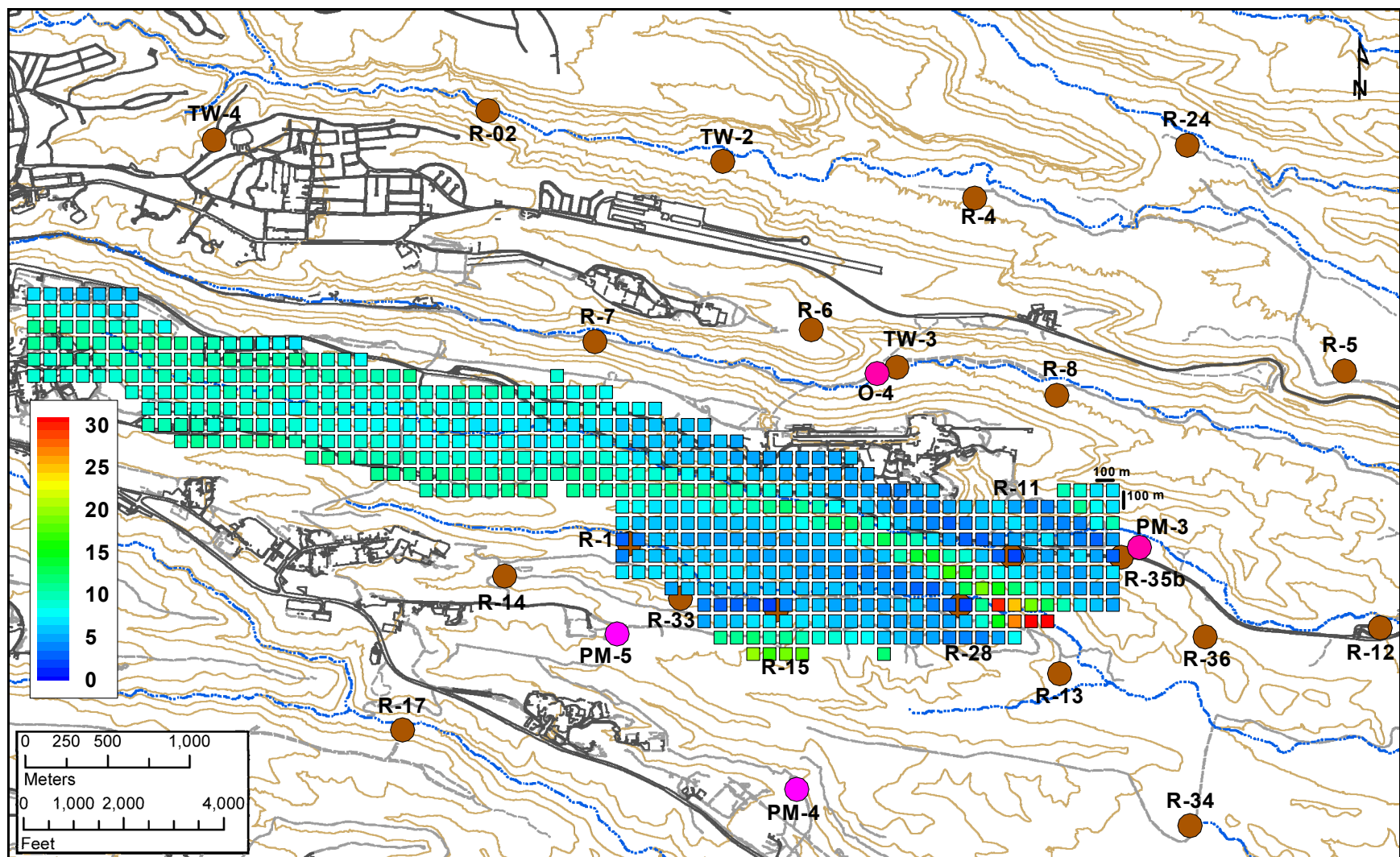
Figure J-5.1-18   Maximum concentrations at the entry points at the top of the regional aquifer that can produce inverse numerical models predicting 1 ppb at all the wells simultaneously. The model uses the water table map presented in Figure H-2 and longitudinal/transverse dispersivities equal to 100 and 10 m, respectively.
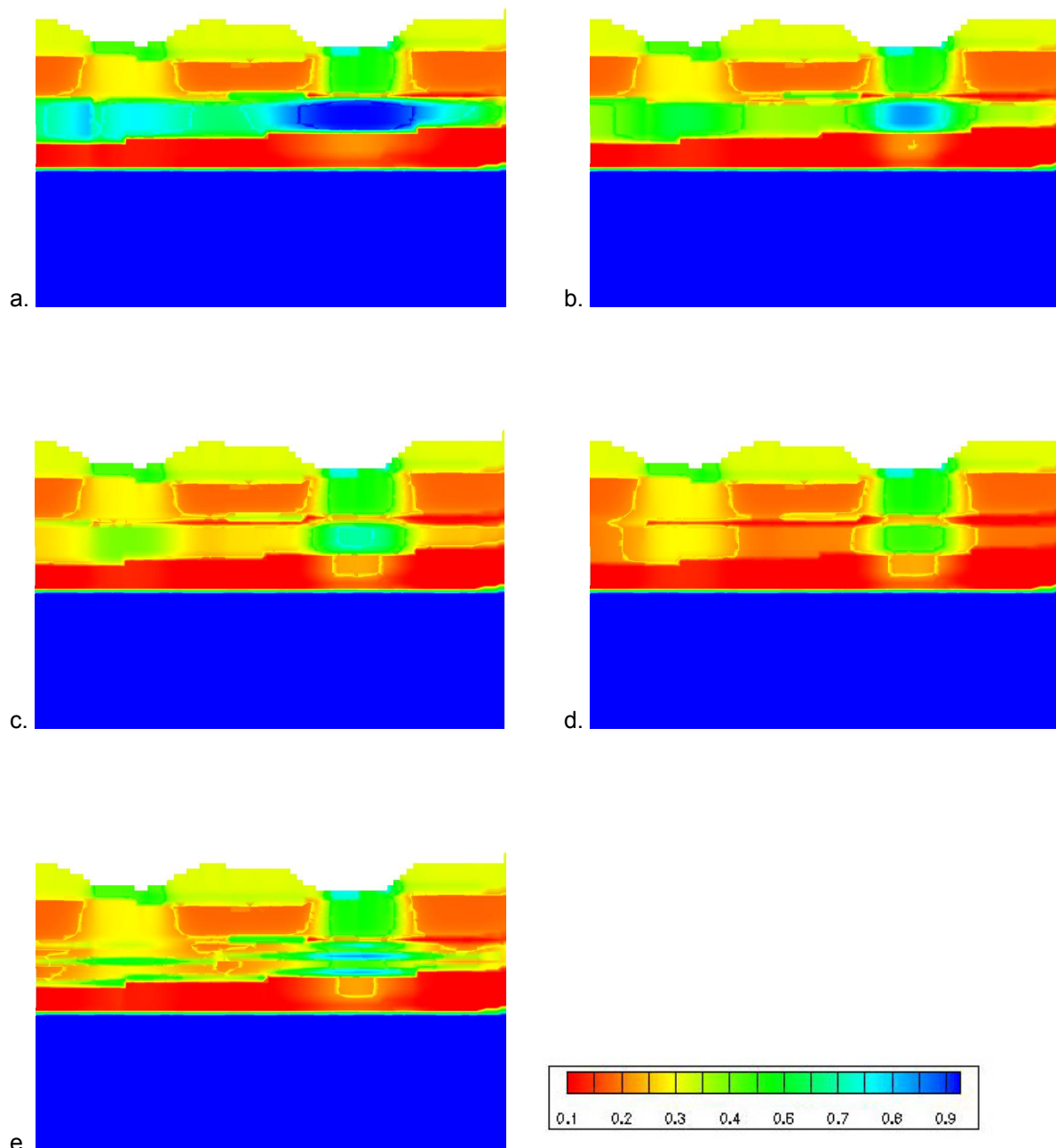
Figure J-6.3-1   Saturation profiles showing values from 0 to 1 through 3-D model (CRM) along 2-D cross-section A–A' (Figure 1.0-1) using different permeability values for the Cerros del Rio basalts : (a) $10^{-14.5}$ m^2, (b) $10^{-13.5}$ m^2, (c) $10^{-12.5}$ m^2, (d) $10^{-11.5}$ m^2, and (e) $10^{-11.5}$ m^2 and permeability reduction defined for base of the Guaje Pumice Bed and base, top, and internal interface for the Cerros del Rio basalts. Sandia Canyon is the depression on the right, and Mortandad Canyon is on the left.
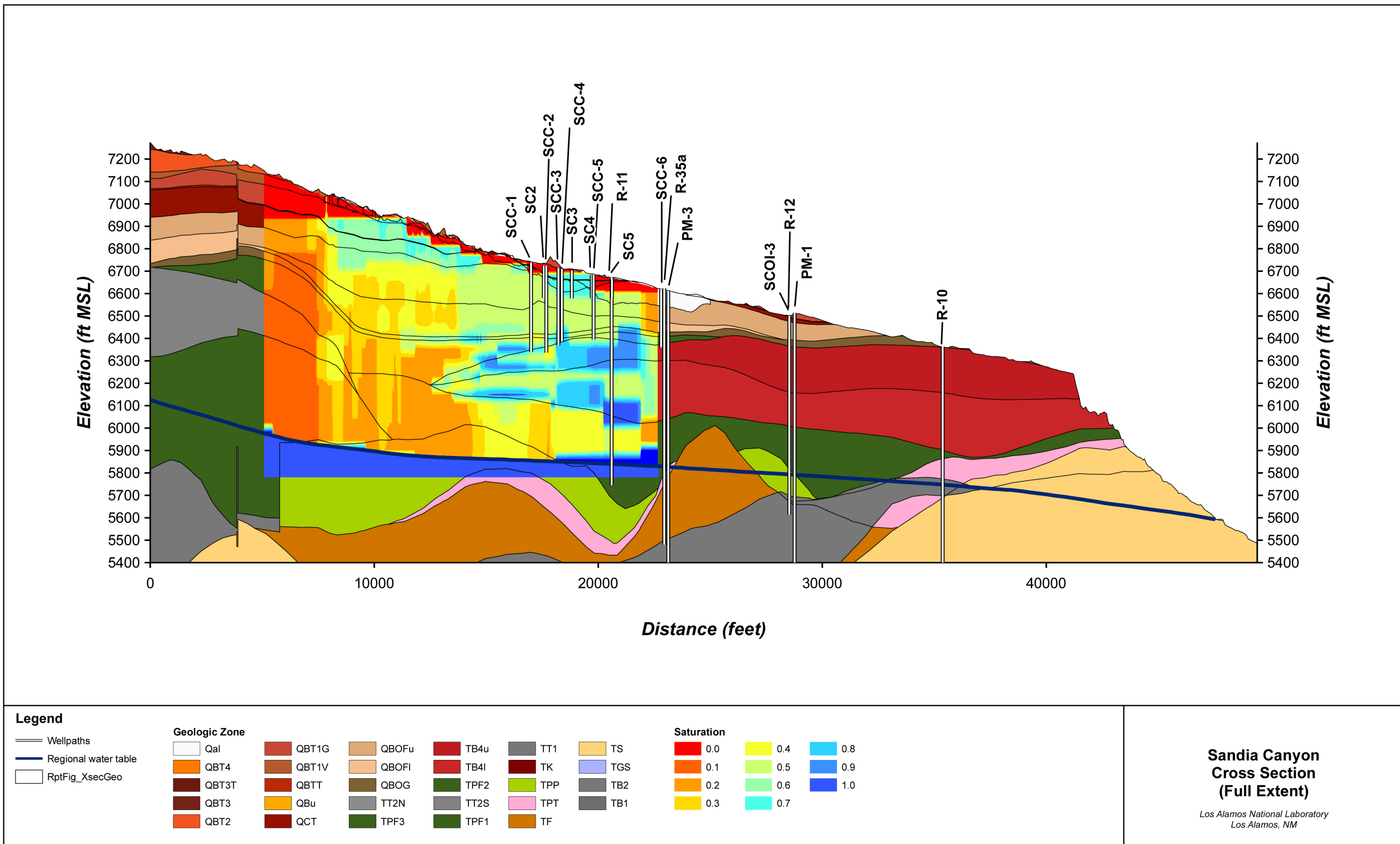
Figure J-6.3-2   Simulated saturation field for a 2-D cross-section down Sandia Canyon superimposed onto the hydrostratigraphy. This cross-section is equivalent to the conceptual cross-section (Figure 2.0-1).

a.
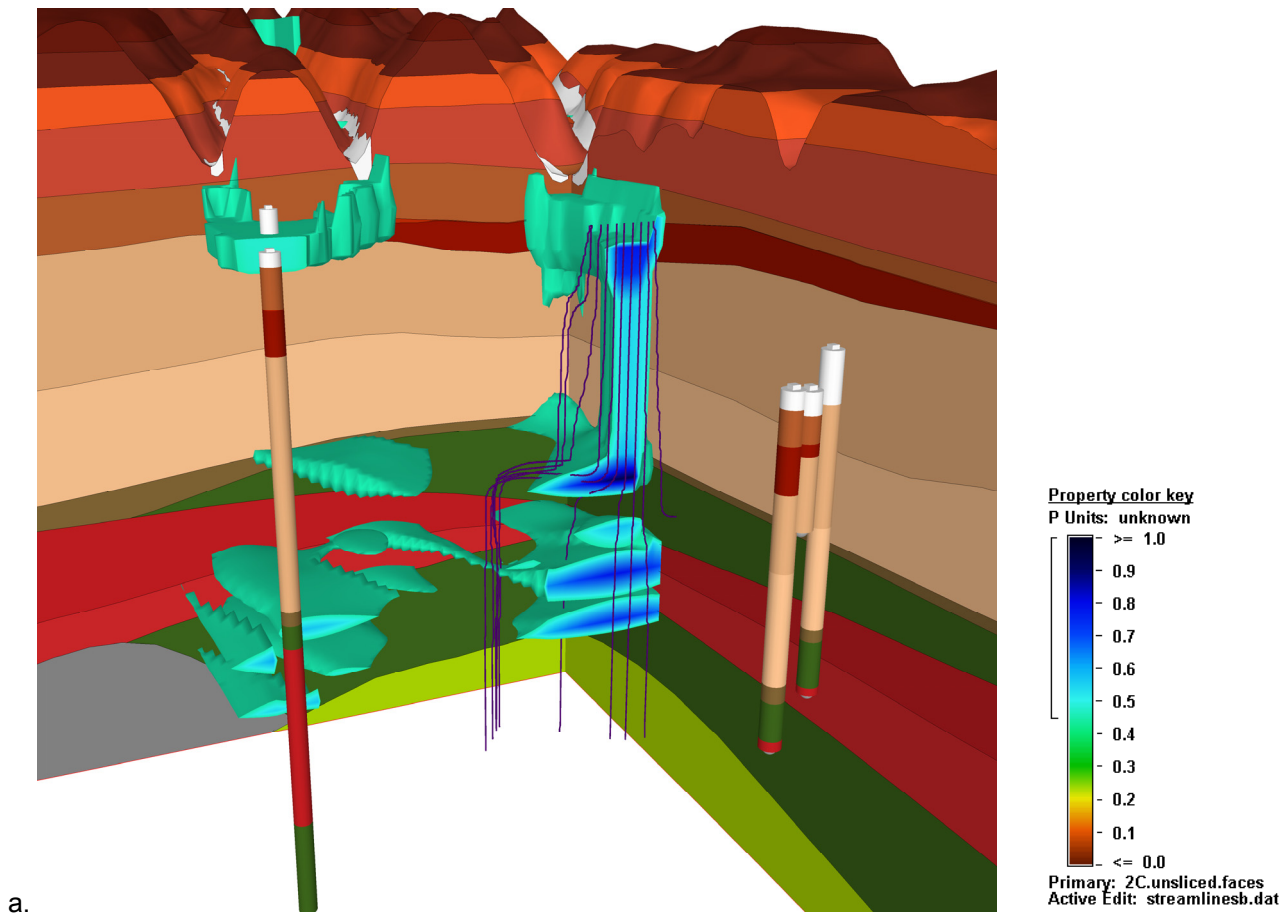
Figure J-6.3-3   3-D depictions of saturation values from 0.45 to 1.0 looking westward up Sandia Canyon. Also included are the hydrostratigraphic units (using color map given in Figure J-6.3-2) and streamlines, which represent potential water flow paths. Wells shown in figures are (clockwise from back left starting in Mortandad Canyon): MCOI-4 (only top of well shows), SCC-1, SC2, SCC-2, and R-15.

b.

Figure J-6.3-3 (continued) **3-D depictions of saturation values from 0.45 to 1.0 looking westward up Sandia Canyon. Also included are the hydrostratigraphic units (using color map given in Figure J-6.3-2) and streamlines, which represent potential water flow paths. Wells shown in figures are (clockwise from back left starting in Mortandad Canyon): MCOI-4 (only top of well shows), SCC-1, SC2, SCC-2, and R-15.**

c.

Figure J-6.3-3 (continued)   **3-D depictions of saturation values from 0.45 to 1.0 looking westward up Sandia Canyon. Also included are the hydrostratigraphic units (using color map given in Figure J-6.3-2) and streamlines, which represent potential water flow paths. Wells shown in figures are (clockwise from back left starting in Mortandad Canyon): MCOI-4 (only top of well shows), SCC-1, SC2, SCC-2, and R-15.**

Table J-3.0-1
Spatial Representation of Hydrostratigraphic Units Represented in the Three Models

Unit	Short Name	CRM Model 404,809 Nodes		LGM3D Model 520,664 Nodes		LGM2D Model 693,948 Nodes	
		Number of Nodes	Percentage in the Model	Number of Nodes	Percentage in the Model	Number of Nodes	Percentage in the Model
Tshirege	Qbt	59814	14.78 %	0	0.00 %	0	0.00 %
Cerro Toledo Interval	Qct	11066	2.73 %	0	0.00 %	0	0.00 %
Otowi	Qbof	74184	18.33 %	0	0.00 %	0	0.00 %
Otowi Guaje Pumice	Qbog	33842	8.36 %	0	0.00 %	0	0.00 %
Tschicoma	Tt	5622	1.39 %	27023	5.19 %	60739	8.75 %
Keres Group	Tk	0	0.00 %	397	0.08 %	1996	0.29 %
Cerros del Rio Basalt	Tb4	52010	12.85 %	25334	4.87 %	123188	17.75 %
Bayo Canyon Basalt	Tb2	6305	1.56 %	24203	4.65 %	19445	2.80 %
Older Basalts	Tb1	38	0.01 %	1652	0.32 %	0	0.00 %
Totavi Lentil	Tpt	11037	2.73 %	12358	2.37 %	29361	4.23 %
Pumiceous Puye	Tpp	47417	11.71 %	18686	3.59 %	27385	3.95 %
Puye Fanglomerate	Tpf	77516	19.15 %	65299	12.54 %	185810	26.78 %
Santa Fe Fanglomerate	Tf	20151	4.98 %	59820	11.49 %	41462	5.97 %
Santa Fe Silt and Sands*	Ts	5807	1.43 %	285892	54.91 %	204562	29.48 %

*Geologic units have been combined. Galisteo (Tgs) is combined with Santa Fe silt and sands.

Table J-3.0-2
Characteristics of Hydrostratigraphic Units Represented in the Model

Unit	Name	Permeability, log10[m²]			Porosity		
		Mean	Min	Max	Mean	Min	Max
Tshirege	Qbt	-12	-13.3	-11.4	0.53	0.48	0.56
Cerro Toledo Interval	Qct	-12.6	-13.2	-12.5	0.48	0.47	0.50
Otowi	Qbof	-12.2	-14	-11.1	0.48	0.31	0.54
Otowi Guaje Pumice	Qbog	-12.8	-13.8	-11.4	0.67	0.40	0.70
Tschicoma	Tt	-10.5	-10.5	0.50	1.E-05	1.E-05	1.E-02
Keres Group	Tk	-10.5	-10.5	0.50	1.E-05	1.E-05	1.E-02
Cerros del Rio Basalt	Tb4	-12.0	-12.0	1.00	1.E-02	1.E-05	1.E-01
Bayo Canyon Basalt	Tb2	-12.0	-12.0	1.00	1.E-05	1.E-05	1.E-01
Totavi Lentil	Tpt	-11.0	-11.0	0.33	1.E-02	1.E-02	2.E-01
Pumiceous Puye	Tpp	-12.5	-12.5	0.50	1.E-02	1.E-02	2.E-01
Puye Fanglomerate	Tpf	-12.5	-12.5	0.50	1.E-02	1.E-02	2.E-01
Santa Fe Fanglomerate	Tf	-12.5	-12.5	0.50	1.E-02	1.E-02	2.E-01
Santa Fe Silt and Sands	Ts	-12.5	-12.5	0.50	1.E-02	1.E-02	2.E-01

Note: Log_{10} permeability = -12 denotes that permeability = $10^{-12}\,m^2$.

Table J-4.1-1
Calibration Data for the SCC-2 Inverse Model

Elevation [m]	Node Number	Water Content [kg/kg]		Cr Concentration [kg/kg]		Mo Concentration [kg/kg]	
		Target	Weight	Target	Weight	Target	Weight
2042.6	5	0.174	1	2.56E-05	0	5.82E-07	1.0E+05
2036.6	25	0.294	1	3.24E-07	2.0E+05	3.26E-07	1.0E+05
2030.8	41	0.539	1	6.44E-07	2.0E+05	2.72E-06	1.0E+05
2024.5	51	0.330	1	7.44E-07	2.0E+05	5.38E-06	1.0E+05
2018.6	61	0.351	1	1.44E-07	2.0E+05	2.65E-06	1.0E+05
2012.4	66	0.265	1	4.87E-07	2.0E+05	6.91E-06	1.0E+05
2006.2	70	0.370	1	1.75E-07	2.0E+05	1.10E-05	1.0E+05
2000.1	74	0.283	1	5.77E-08	2.0E+05	1.88E-06	1.0E+05
1994.0	78	0.264	1	5.77E-08	2.0E+05	1.68E-06	1.0E+05
1987.9	82	0.302	1	6.73E-08	2.0E+05	1.36E-06	1.0E+05
1981.8	85	0.314	1	5.77E-08	2.0E+05	1.64E-06	1.0E+05
1975.7	89	0.250	1	6.73E-08	2.0E+05	1.82E-06	1.0E+05
1969.6	93	0.305	1	1.52E-07	2.0E+05	1.84E-06	1.0E+05
1963.5	97	0.308	1	1.26E-07	2.0E+05	1.45E-06	1.0E+05
1957.4	101	0.316	1	1.71E-07	2.0E+05	1.63E-06	1.0E+05
1951.3	105	0.572	1	6.31E-08	2.0E+05	1.17E-06	1.0E+05
1945.2	109	0.147	1	3.74E-07	2.0E+05	6.43E-07	1.0E+05
1939.1	112	0.374	1	3.59E-06	2.0E+05	2.25E-07	1.0E+05
1933.5	115	0.155	1	1.22E-06	2.0E+05	3.65E-07	1.0E+05
1931.7	116	0.103	1	2.95E-06	2.0E+05	9.19E-07	1.0E+05

Table J-4.1-2
Calibration Data for the SCC-3 Inverse Model

Elevation [m]	Node Number	Water Content [kg/kg]		Cr Concentration [kg/kg]		Mo Concentration [kg/kg]	
		Target	Weight	Target	Weight	Target	Weight
2023.3	12	0.546	1	2.88E-08	2.0E+05	1.01E-06	1.0E+05
2017.2	25	0.300	1	2.97E-07	2.0E+05	2.42E-06	1.0E+05
2011.2	38	0.263	1	6.73E-08	2.0E+05	1.37E-06	1.0E+05
2005.1	40	0.235	1	7.69E-08	2.0E+05	1.63E-06	1.0E+05
1999.0	43	0.306	1	2.44E-07	2.0E+05	4.97E-06	1.0E+05
1992.9	47	0.238	1	7.69E-08	2.0E+05	1.78E-06	1.0E+05
1986.8	51	0.256	1	6.73E-08	2.0E+05	2.27E-06	1.0E+05
1980.7	55	0.303	1	5.77E-08	2.0E+05	2.07E-06	1.0E+05
1974.6	58	0.299	1	5.77E-08	2.0E+05	2.02E-06	1.0E+05
1968.5	62	0.298	1	5.77E-08	2.0E+05	1.42E-06	1.0E+05
1962.4	66	0.300	1	5.77E-08	2.0E+05	1.25E-06	1.0E+05
1956.3	69	0.308	1	5.77E-08	2.0E+05	7.48E-07	1.0E+05
1950.2	72	0.544	1	2.88E-08	2.0E+05	3.42E-07	1.0E+05
1944.1	75	0.262	1	4.89E-07	2.0E+05	4.28E-07	1.0E+05
1939.8	78	0.074	1	2.31E-07	2.0E+05	9.82E-07	1.0E+05

Table J-4.1-3
Calibration Data for the SCC-4 Inverse Model

Elevation [m]	Node Number	Water Content [kg/kg]		Cr Concentration [kg/kg]		Mo Concentration [kg/kg]	
		Target	Weight	Target	Weight	Target	Weight
2027.0	12	0.350	1	4.90E-07	2.0E+05	1.21E-06	1.0E+05
2020.9	25	0.202	1	2.05E-06	2.0E+05	1.56E-06	1.0E+05
2014.8	38	0.153	1	2.99E-06	2.0E+05	6.12E-07	1.0E+05
2007.8	40	0.149	1	1.61E-06	2.0E+05	4.59E-06	1.0E+05
2002.6	43	0.212	1	4.11E-07	2.0E+05	4.02E-06	1.0E+05
1996.5	47	0.202	1	3.12E-07	2.0E+05	4.06E-07	1.0E+05
1990.4	51	0.213	1	7.69E-08	2.0E+05	3.11E-07	1.0E+05
1984.3	55	0.223	1	7.69E-08	2.0E+05	2.74E-07	1.0E+05
1978.2	58	0.380	1	4.81E-08	2.0E+05	2.08E-07	1.0E+05
1972.1	62	0.244	1	6.73E-08	2.0E+05	1.47E-07	1.0E+05
1966.0	66	0.241	1	6.73E-08	2.0E+05	9.77E-08	1.0E+05
1959.9	69	0.353	1	4.81E-08	2.0E+05	2.61E-08	1.0E+05
1953.9	72	0.645	1	2.88E-08	2.0E+05	9.00E-08	1.0E+05
1947.8	75	0.205	1	4.44E-07	2.0E+05	2.01E-06	1.0E+05

Table J-4.2-1
Input Model Parameters and Their Ranges for SCC Inverse Models

Parameter	Initial Estimate	Calibration Range		Group
		Min	Max	
perm_tpf	-13.20	-13.20	-11.00	perm
perm_tb4a	-12.16	-14.00	-9.00	perm
perm_qbog	-11.62	-13.80	-11.40	perm
perm_qbof	-11.45	-14.00	-11.10	perm
perm_qct	-13.20	-13.20	-11.00	perm
perm_qbt1g	-10.50	-13.30	-10.50	perm
perm_tb4r	-10.50	-12.00	-9.00	perm
perm_tf	-11.00	-12.20	-11.00	perm
alph_tpf	5.00	1.00	5.00	alpha
alph_qbog	0.02	0.01	1.00	alpha
alph_qbof	0.29	0.29	1.73	alpha
alph_qct	0.18	0.18	28.00	alpha
alph_qbt1g	0.49	0.05	23.10	alpha
por_tpf	0.30	0.02	0.30	por
por_tb4a	9.9E-02	1.0E-04	1.0E-01	por
por_qbog	0.55	0.40	0.70	por
por_qbof	0.54	0.31	0.54	por
por_qct	0.50	0.47	0.50	por
por_qbt1g	0.66	0.48	0.66	por
por_tb4r	0.20	0.10	0.30	por
por_tf	0.20	0.10	0.30	por
vz_disp	1.58	0.50	5.00	disp
kd_cr_tuff	1.4E-01	1.0E-05	3.0E-01	kd
kd_cr_ct	8.2E-01	1.0E-05	6.0E+01	kd
kd_mo_tuff	2.6E-03	1.0E-05	1.0E-01	kd
kd_mo_ct	2.8E+00	1.0E-05	5.0E+00	kd
q1	0.427988	0.1	2	watflux
q2	1.373001	0.2	3.5	watflux
cr1	4.2E-05	1.0E-06	1.4E-04	crflux
cr2	1.3E-08	1.0E-08	1.0E-06	crflux
cr3	1.1E-08	5.0E-10	1.0E-07	crflux
cr4	3.8E-08	5.0E-10	1.0E-07	crflux
mo1	8.2E-07	5.0E-10	1.0E-04	moflux
mo2	4.8E-06	5.0E-10	1.0E-04	moflux

Table J-4.3-1
Model Parameters, Their Best Estimates, and Their Sensitivity
to Calibration Data and Model Predictions Based on the SCC-2 Inverse Model

Parameter	Short Name	Best Estimate	Sensitivity to Calibration Data	Sensitivity to Cr Predictions	Sensitivity to Mo Predictions
Permeability [m²]	perm_tpf	-13.1	2.7E-03	1.3E-05	5.0E-07
	perm_tb4a	-11.8	4.0E-04	6.4E-07	7.6E-08
	perm_qbog	-12.8	5.5E-04	5.0E-07	3.1E-08
	perm_qbof	-11.8	6.6E-03	1.7E-05	6.7E-07
	perm_qct	-13.2	2.9E-03	2.1E-05	1.2E-07
	perm_qbt1g	-10.5	1.1E-03	5.0E-07	3.4E-08
	perm_tb4r	-10.5	1.5E-05	4.4E-06	3.9E-08
	perm_tf	-11.0	5.1E-08	1.3E-06	8.8E-08
Alpha [1/m]	alph_tpf	5.00	7.6E-05	2.8E-08	1.9E-09
	alph_qbog	0.09	2.2E-03	8.1E-07	5.3E-08
	alph_qbof	0.29	1.6E-03	6.0E-07	4.4E-08
	alph_qct	0.18	2.7E-04	2.0E-07	1.2E-08
	alph_qbt1g	1.27	1.9E-03	9.9E-07	6.4E-08
Porosity	por_tpf	0.3000	1.5E-02	1.0E-04	2.8E-06
	por_tb4a	0.1000	2.5E-03	1.1E-04	5.7E-07
	por_qbog	0.5868	2.2E-02	1.0E-05	6.6E-07
	por_qbof	0.5400	3.8E-02	6.9E-05	3.7E-06
	por_qct	0.5000	2.7E-02	2.0E-05	9.6E-07
	por_qbt1g	0.4800	1.5E-02	8.7E-06	5.7E-07
	por_tb4r	0.2020	1.1E-04	3.0E-05	2.2E-07
	por_tf	0.2010	1.8E-11	1.1E-05	6.9E-07
Dispersivty [m]	vz_disp	2.51	6.6E-03	2.8E-05	1.0E-06
Kd [mL/g]	kd_cr_tuff	0.30	1.3E-02	3.4E-04	
	kd_cr_ct	0.29	2.7E-03	1.7E-05	
	kd_mo_tuff	0.10	1.2E-03		6.8E-06
	kd_mo_ct	1.57	5.3E-03		4.3E-06
Water flux [kg/s]	q1	0.69	1.2E-01	7.2E-05	8.8E-09
	q2	0.45	1.7E-02	3.3E-05	1.2E-06
Cr flux [moles/s]	cr1	9.7E-05	3.5E-03	2.5E-04	
	cr2	3.4E-08	8.7E-05	1.8E-09	
	cr3	1.5E-08	1.0E-05		
	cr4	1.0E-07	4.8E-04		
Mo flux [moles/s]	mo1	1.0E-06	1.6E-04		6.1E-08
	mo2	4.1E-06	5.0E-03		5.4E-06

Note: Blank = parameter is insensitive.

Table J-4.3-2
Model Parameters, Their Best Estimates, and Their Sensitivity
to Calibration Data and Model Predictions Based on the SCC-3 Inverse Model

Parameter	Short Name	Best Estimate	Sensitivity to Calibration Data	Sensitivity to Cr Predictions	Sensitivity to Mo Predictions
Permeability [m^2]	perm_tpf	-13.2	2.1E-03	8.4E-06	1.7E-08
	perm_tb4a	-12.2	4.0E-04	1.4E-06	2.8E-09
	perm_qbog	-11.6	2.4E-04	5.0E-08	1.1E-10
	perm_qbof	-11.5	7.0E-03	7.9E-06	1.4E-08
	perm_qct	-13.2	2.7E-03	2.6E-06	8.9E-09
	perm_qbt1g	-10.5	1.8E-06	2.2E-08	5.0E-11
	perm_tb4r	-10.5	2.0E-08	8.0E-07	1.6E-09
	perm_tf	-11.0	8.7E-08	8.3E-07	1.7E-09
Alpha [1/m]	alph_tpf	5.00	6.4E-05	1.3E-08	2.6E-11
	alph_qbog	0.02	7.7E-05	2.8E-08	5.9E-11
	alph_qbof	0.29	4.8E-03	9.0E-07	1.4E-09
	alph_qct	0.18	1.3E-04	3.9E-07	1.0E-09
	alph_qbt1g	0.49	6.1E-05	7.1E-07	1.6E-09
Porosity	por_tpf	0.3000	1.3E-02	5.3E-05	1.0E-07
	por_tb4a	0.0988	3.6E-03	1.2E-05	2.5E-08
	por_qbog	0.5457	2.7E-02	1.0E-05	2.2E-08
	por_qbof	0.5400	4.4E-02	4.4E-05	9.3E-08
	por_qct	0.5000	2.9E-02	2.1E-05	8.1E-08
	por_qbt1g	0.6600	3.8E-04	4.5E-06	1.1E-08
	por_tb4r	0.2020	9.1E-08	4.3E-06	8.7E-09
	por_tf	0.2010	1.4E-07	6.4E-06	1.3E-08
Dispersivty [m]	vz_disp	1.58	2.4E-03	8.1E-06	1.6E-07
Kd [mL/g]	kd_cr_tuff	0.14	2.9E-03	6.5E-05	
	kd_cr_ct	0.82	5.9E-03	4.7E-05	
	kd_mo_tuff	0.00	1.3E-05		5.2E-09
	kd_mo_ct	2.82	3.9E-03		6.6E-07
Water flux [kg/s]	q1	0.43	7.4E-18		
	q2	1.37	6.5E-18		
Cr flux [moles/s]	cr1	4.2E-05	7.2E-18		
	cr2	1.3E-08	2.1E-17		
	cr3	1.1E-08	7.4E-18		
	cr4	3.8E-08	1.8E-18		
Mo flux [moles/s]	mo1	8.2E-07	9.1E-18		
	mo2	4.8E-06			

Note: Blank = parameter is insensitive.

Table J-4.3-3
Model Parameters, Their Best Estimates, and Their Sensitivity
to Calibration Data and Model Predictions Based on the SCC-4 Inverse Model

Parameter	Short Name	Best Estimate	Sensitivity to Calibration Data	Sensitivity to Cr Predictions	Sensitivity to Mo Predictions
Permeability [m^2]	perm_tpf	-13.2	2.1E-03	2.9E-08	1.1E-07
	perm_tb4a	-9.0	8.6E-05	1.6E-08	8.3E-10
	perm_qbog	-13.8	6.9E-03	2.5E-08	4.0E-08
	perm_qbof	-11.3	5.7E-03	6.0E-09	7.7E-08
	perm_qct	-11.0	1.1E-03	2.0E-08	3.1E-09
	perm_qbt1g	-12.4	5.7E-04	3.1E-11	8.2E-10
	perm_tb4r	-10.5	9.6E-06	3.1E-09	1.1E-08
	perm_tf	-11.0	1.4E-07	7.4E-10	1.2E-08
Alpha [1/m]	alph_tpf	1.00	1.1E-03	1.3E-07	4.4E-09
	alph_qbog	0.28	3.5E-03	6.0E-08	6.0E-09
	alph_qbof	0.29	6.4E-03	1.4E-07	3.4E-08
	alph_qct	0.18	4.4E-03	6.4E-08	5.4E-09
	alph_qbt1g	0.07	2.7E-03	6.4E-08	4.7E-09
	alph_qbt1v	0.50			
Porosity	por_tpf	0.2698	1.1E-02	6.5E-08	6.0E-07
	por_tb4a	0.0001	1.2E-08	3.8E-12	6.7E-11
	por_tt2	0.0010			
	por_qbog	0.7000	3.4E-02	4.3E-07	1.7E-07
	por_qbof	0.5229	4.0E-02	1.1E-06	5.4E-07
	por_qct	0.4700	1.7E-02	1.2E-06	3.8E-08
	por_qbt1g	0.4800	1.9E-02	2.1E-07	3.2E-08
	por_tb4r	0.2020	1.4E-09	3.1E-09	5.8E-08
	por_tf	0.2010	2.1E-09	5.8E-09	9.4E-08
Dispersivty [m]	vz_disp	5.00	1.5E-02	3.2E-07	6.9E-07
Kd [mL/g]	kd_cr_tuff	0.30	1.1E-03	2.3E-07	
	kd_cr_ct	50.59	4.0E-02	1.6E-06	
	kd_mo_tuff	0.10	3.8E-03		1.5E-06
	kd_mo_ct	2.91	3.4E-02		8.9E-07
Water flux [kg/s]	q1	2.00	1.8E-02	4.5E-07	4.6E-10
	q2	0.88	2.7E-02	1.1E-07	5.5E-07
Cr flux [moles/s]	cr1	2.8E-05	1.5E-02	9.7E-08	
	cr2	1.0E-08	6.3E-06		
	cr3	5.0E-10	4.6E-08		
	cr4	5.0E-10	1.7E-06		
Mo flux [moles/s]	mo1	5.0E-10	3.2E-07		2.0E-11
	mo2	4.6E-06	2.5E-02		2.8E-06

Note: Blank = parameter is insensitive.

Table J-4.3-4
Best Estimate Equivalent Infiltration Rates Based on Flux Estimates

Well	Infiltration rate, 1950–1991 [m/yr]	Infiltration rate, 1992–2007 [m/yr]
SCC-2	4.3	2.8
SCC-3	1.3	4.2
SCC-4	6.2	2.7

Table J-4.3-5
Best Estimate and Uncertainty Ranges of Predicted Chromium Concentrations (ppb)

Well	Best Estimate	Min	Max
SCC-2	6000	50	8500
SCC-3	2200	2000	2400
SCC-4	5	2	50

Note: Confidence level of 95%. Circa 2007 at the bottom of the vadose zone just above the regional water table.

Table J-4.3-6
Parameters Associated with the Best Estimate and
Maximum and Minimum in Predictive (Confidence Level of 95%)
Uncertainty in Simulated Cr Concentrations [ppb] Circa 2007 at the
Bottom of the Vadose Zone at SCC-2 (Just above the Regional Water Table)

Parameter	Best Estimate	Minimum Estimate	Maximum Estimate
perm_tpf	-13.12	-13.13	-13.20
perm_tb4a	-11.79	-11.78	-11.40
perm_qbog	-12.77	-12.89	-12.49
perm_qbof	-11.81	-11.82	-11.66
perm_qct	-13.20	-13.20	-13.20
perm_qbt1g	-10.50	-10.50	-10.50
perm_tb4r	-10.50	-10.50	-10.50
perm_tf	-11.00	-12.20	-11.00
alph_tpf	5.00	5.00	5.00
alph_qbog	0.09	0.02	0.06
alph_qbof	0.29	0.29	0.29
alph_qct	0.18	0.18	0.18
alph_qbt1g	1.27	1.26	1.54
por_tpf	0.30	0.30	0.05
por_tb4a	0.10	0.10	0.10
por_qbog	0.59	0.51	0.56
por_qbof	0.54	0.54	0.54
por_qct	0.50	0.50	0.50
por_qbt1g	0.48	0.48	0.48
por_tb4r	0.20	0.30	0.30
por_tf	0.20	0.30	0.17
vz_disp	2.51	2.62	0.50
kd_cr_tuff	0.30	0.30	0.30
kd_cr_ct	0.29	5.00	0.00
kd_mo_tuff	0.10	0.10	0.10
kd_mo_ct	1.57	1.57	1.57
q1	0.69	0.91	0.60
q2	0.45	0.45	0.63
cr1	9.7E-05	1.18E-06	1.40E-04
cr2	3.4E-08	1.24E-08	2.45E-08
cr3	1.5E-08	1.51E-08	1.51E-08
cr4	1.0E-07	1.00E-07	1.00E-07
mo1	1.0E-06	1.05E-06	1.05E-06
mo2	4.1E-06	4.11E-06	4.11E-06

Note: Sensitive Model parameters related to this model prediction are marked in gray.

Table J-5.2-1
Approximate Longitudinal, Transverse Lateral, and Transverse Vertical
Plume Sizes for Different Model Parameters Estimated Using an Analytical Method

Distance from the Source [m]	Longitudinal Dispersivity [m]	Transverse Lateral Dispersivity [m]	Transverse Vertical Dispersivity [m]	Isotropic Aquifer						Anisotropic Aquifer		
				6 Sigma (~99% of the mass)			4 Sigma (~70% of the mass)			Vertical Transverse Plume Size [m] (~99% of the mass) for Different Vertical Anisotropic Ratios		
				Longitudinal Plume Size [m]	Transverse Lateral Plume Size [m]	Transverse Vertical Plume Size [m]	Longitudinal Plume Size [m]	Transverse Lateral Plume Size [m]	Transverse Vertical Plume Size [m]	0.1	0.01	0.001
50	5.0	0.5	0.05	30.0	9.4	3.0	15.0	4.7	1.5	0.3	0.03	0.003
100	10.0	1.0	0.1	60.0	19.0	6.0	30.0	9.4	3.0	0.6	0.06	0.006
200	20.0	2.0	0.2	120.0	38.0	12.0	60.0	19.0	6.0	1.2	0.12	0.012
500	50.0	5.0	0.5	300.0	94.0	30.0	150.0	47.0	15.0	3.0	0.30	0.030
750	75.0	7.5	0.8	450.0	140.0	45.0	220.0	71.0	22.0	4.5	0.45	0.045
1000	100.0	10.0	1.0	600.0	190.0	60.0	300.0	94.0	30.0	6.0	0.60	0.060

Table J-5.2-2
Approximate Vertical Plume Sizes for
Different Model Parameters Estimated Using a Numerical Model

Distance from the source [m]	Vertical Transverse Dispersivity = 0.5			Vertical Transverse Dispersivity = 1.0		
	Approximate Vertical Plume Size [m] (~99% of the mass) for Different Values of the Vertical Component of the Pressure Gradient			Approximate Vertical Plume Size [m] (~99% of the mass) for Different Values of the Vertical Component of the Pressure Gradient		
	0	0.05	0.15	0	0.05	0.15
50	49	48	50	92	98	100
100	54	59	60	99	103	105
200	57	60	70	105	107	110
500	85	91	100	120	125	133
750	98	102	110	146	158	154
1000	105	115	120	151	160	184

Table J-6.1-1
Initial Water Fluxes Used in Canyon Bottoms to Establish a Steady-State Flow Field

Canyon Segment	Los Alamos /Pueblo	Mortandad	Sandia – S4	Sandia – S5	Sandia – S6
Approximate Segment Area [m^2]	750,000	900,000	100,000	130,000	290,000
Water source equivalent to 50 mm/yr infiltration rate [kg/s]	1.2	1.4	0.16	0.20	0.45

Table J-6.1-2
Increased Water Fluxes to Three Lower Sandia Canyon Segments Due to Effluent Releases

Time Period	Assumed Total Water Reaching S4 to S6 [kg/s, (gal/day)]	Sandia – S4 [kg/s, (gal/day)]	Sandia – S5 [kg/s, (gal/day)]	Sandia – S6 [kg/s, (gal/day)]
1950–1991	6.6 (150,000)	1.1 (25,000)	2.4 (55,000)	3.1 (70,000)
1992–present	11.0 (250,000)	1.5 (35,000)	2.9 (65,000)	6.6 (150,000)

Table J-6.2-1
Permeability and Porosity Used for the CRM Domain Three-Dimensional Simulations

Unit	Abbreviated Name	Properties Used	Log ks [m²]	Porosity
Tshirege Member	Qbt	Qbt 1g	-12	0.53
Cerro Toledo Interval	Qct	Qbt 1g	-12.6	0.48
Otowi Member	Qbof	Qbof	-12.2	0.48
Otowi Guaje Pumice	Qbog	Qbog	-12.8	0.67
Tschicoma	Tt	Tb 4	-11.3	0.01
Cerros del Rio Basalt	Tb4	Tb 4	Varied for simulations -14.5, -13.5, -12.5, -11.5	0.01
Pumiceous Puye	Tpp	TTpp	-10.3	0.20
Puye Fanglomerate	Tpf	Tpf	-10.3 below Tb 4; -11 elsewhere	0.06
All others	Ts, Tf, Tpt, Tb 1		-11.5	0.01

Note: Log ks = -12 denotes that ks = 10^{-12} m².

Appendix K

Hexavalent Chromium Attenuation on
Vadose Zone and Regional Aquifer Materials:
Application of X-ray Absorption Near-Edge Spectroscopy

K-1.0   INTRODUCTION

Geochemical characterization and remediation of sites contaminated by chromium (Cr) require knowledge of chromium oxidation states including Cr(III) and/or Cr(VI) present in the vadose zone and regional aquifer at Los Alamos National Laboratory (LANL). Geochemical processes controlling the movement of chromium in surface and subsurface environments include adsorption and precipitation onto solid material. Laboratory experiments using various rock types present beneath Sandia Canyon were conducted to quantify adsorption and precipitation of Cr(III, VI) in contact with core samples collected from the Cerros del Rio basalt, Puye Formation, and Santa Fe Group. As part of x-ray absorption fine structure (XAFS), x-ray absorption near-edge structure (XANES) spectroscopy was used in this study to identify resulting chromium oxidation state(s) and to quantify the ratio of Cr(III)/Cr(VI) for rock samples exposed to solutions containing Cr(VI). The preliminary spectroscopic results for chromium are presented in this appendix.

K-2.0   MATERIALS AND METHODS

K-2.1   Materials

K-2.1.1   Chromium Compounds

For Cr(VI), hybridization of the p-d electron orbitals due to a 1s to 3d electronic transition gives rise to a well-defined peak (called the pre-edge peak) below the main absorption edge in x-ray absorption spectra, indicating a transition to a bound state, which is allowed in tetrahedral compounds containing Cr(VI). For octahedral Cr(III), the pre-edge peak is much smaller. Consequently, the Cr(VI)/Cr(III) ratio for a sample in which chromium is present in unknown, oxidation states can be determined from the normalized pre-edge peak height. The pre-edge peak height calibration spectra were obtained in this study using Cr(III) and Cr(VI) compounds. The Cr(III) compound used for XANES pre-edge height calibration is Cr_2O_3 with 99.995% purity. The Cr(VI) compound used for XANES pre-edge height calibration and also for adsorption of Cr(VI) onto the various rock samples consisted of K_2CrO_4 of analytical reagent quality.

K-2.1.2   Rock Sample Descriptions

Sample LAOI-7, 83.3–85.6-ft depth. The sample from LAOI-7 represents a rubble zone in the upper part of the tholeiitic lava series in this core. The flow-top rubble in this core contains abundant smectite and lesser amounts of carbonate minerals (possibly pedogenic) coating the basaltic rubble. When LAOI-7 was drilled, perched groundwater was observed at a depth of 26 ft within the Otowi Member of the Bandelier Tuff. This perched zone probably extends through the lower Otowi Member, the Guaje Pumice Bed, and Puye Formation sediments to the very top of the Cerros del Rio lavas at 75 ft depth. The sample selected for study, at 83.3–85.6-ft depth, is from a dry interval and represents the type of material that can support perched zones immediately above Cerros del Rio lavas (Tb 4). Available data for the tholeiitic Cerros del Rio lavas indicate that even in clay-bearing rubble zones the basaltic substrate can retain considerable ferrous iron (generally more than ~50% FeO/Fe_2O_3 by weight), principally in readily altered mesostasis (groundmass), olivine, magnetite, and ilmenite. Specific petrologic and chemical analysis of the LAOI-7 sample will be conducted at a later date.

Sample R-9, 183.0–183.7-ft depth. The sample from R-9 represents an interval (180- to ~225–236-ft depth) that hosts a very productive perched interval within the lower Cerros del Rio lava (Tb 4) series. A transition from upper tholeiitic lavas to underlying alkalic lavas occurs at 180-ft depth in R-9; perched water is localized in the upper alkalic lavas (more evolved lavas at 180–206-ft depth), and the uppermost

part of the lower alkalic lavas (more primitive compositions, from 206- to 282-ft depth). The upper alkalic lavas are highly fractured and contain abundant clay; the deeper alkalic lavas are more fractured at the top but have a central dense zone that probably forms the aquitard below the perched interval. Although differing from the tholeiitic lava sample at LAOI-7 in many respects (alkalic lavas have lower Si, higher Sr, and higher Mg), the overall mineralogy, clay content and FeO/Fe_2O_3 relations are similar. The primary distinction between these two samples is that the LAOI-7 specimen represents a perching horizon and the R-9 specimen is from within a perched interval. Specific petrologic and chemical analysis of the R-9 sample will be obtained at a later date.

Sample R-35b, 840–845-ft depth. The sample from R-35b represents the upper zone of regional saturation, within the Puye Formation (Tpf). The first significant water production at R-35b occurred at this depth, and the sample is typical of the lower part of the screened interval in the well. The sediments returned at 840–845 ft depth consisted of angular gravels from a variety of intermediate volcanic sources. Volcanic clasts within the Puye Formation are typically slightly altered and may retain a significant amount of ferrous iron, although total iron content is much lower than in the basaltic Cerros del Rio (2–3 wt% Fe versus ~7.5 wt% Fe). Specific petrologic and chemical analysis of the R-35b sample will be conducted at a later date.

Sample R-35a, 1060–1065-ft depth. The sample from R-35a consists of tuffaceous sands and gravels of the Santa Fe Group (Tch). A significant amount of volcaniclastic versus Precambrian components indicates this sample is of the Hernandez Member of the Chamita Formation. A significant increase in water production at R-35a occurred at this depth, and the sample is typical of the lower part of the screened interval in well R-35a. Although containing a significant amount of intermediate volcanic detritus, the Santa Fe Group sands and gravels have a much greater transport distance and most of the ferrous iron originally present has likely altered to ferric iron in the form of ferric oxide-hydroxide. Specific petrologic and chemical analysis of the R-35a sample will be obtained at a later date.

K-2.1.3 Groundwater

The groundwater collected from Los Alamos Canyon intermediate well LAOI-7 was used for experiments conducted using rock samples from LAOI-7 and R-9, and the groundwater collected from Sandia Canyon regional well R-35a was used for experiments conducted using rock samples from R-35a and R-35b.

Groundwater within the Cerros del Rio lavas at LAOI-7 is relatively oxidizing characterized by measurable dissolved oxygen (DO), nitrate-nitrite(N), and sulfate. Concentrations of DO range from 4.5 to 7.3 mg/L confirm that the groundwater is oxic at LAOI-7. Concentrations of total organic carbon (TOC) range from 0.4 to 1.7 mgC/L at the well, suggesting that groundwater is not reducing with respect to organic carbon. Inorganic carbon, in the form of bicarbonate, dominates in groundwater at LAOI-7 and all other wells drilled in the Los Alamos area. Dissolved concentrations of iron and manganese are less than 50 and 6 μg/L, respectively, suggesting that reductive dissolution of Fe(III) and Mn(IV) solids is not extensive. Dissolved concentrations of Cr(III,VI) range from 1 to 2 μg/L, suggesting that dissolved Cr(III, VI) species are controlled by either adsorption or precipitation processes. It is hypothesized that dissolved chromium concentrations at LAOI-7, mainly occurring as Cr(III) hydrolysis species, are controlled by $Cr(OH)_3$, a reactive solid stable under a wide range of Eh-pH conditions. The same hydrochemical conditions occur in this perched intermediate zone encountered at R-9, located east of LAOI-7 within Los Alamos Canyon.

Groundwater within the Puye Formation (R-35b) and Santa Fe Group (R-35a) is relatively oxidizing characterized by measurable DO, nitrate-nitrite(N), and sulfate. Concentrations of DO measured at R-35a range from 3.0 to 5.2 mg/L. Concentrations of TOC range from 0.4 to 1.2 mgC/L at R-35a. Dissolved concentrations of iron and manganese at R-35a range from 32 to 315 μg/L and from 3 to 20 μg/L,

respectively, suggesting reductive dissolution of Fe(III) solids is possible in the absence of Fe(III) colloids smaller than 0.45 micrometers; however, Mn(IV) solids have not undergone extensive dissolution. Dissolved concentrations of Cr(III, VI) at R-35a range from 2 to 6 μg/L, suggesting that dissolved Cr(III, VI) species are controlled by either adsorption or precipitation processes. Concentrations of DO measured at R-35b range from 4.8 to 5.5 mg/L. Concentrations of TOC range from 0.4 to 1.0 mgC/L at R-35b. Dissolved concentrations of iron and manganese at R-35b range from 39 to 118 μg/L and from 6 to 16 μg/L, respectively, also suggesting reductive dissolution of Fe(III) solids is possible in the absence of Fe(III) colloids smaller than 0.45 micrometers; however, Mn(IV) solids have not undergone extensive dissolution. Dissolved concentrations of Cr(III, VI) at R-35b range from 4 to 7 μg/L, suggesting that dissolved Cr(III, VI) species are controlled either by adsorption or by precipitation processes.

K-2.2 Methods

K-2.2.1 XANES Specimen Preparation

Batch adsorption experiments were carried out by weighing approximately 0.3 g of solid sample into a weighed and cleaned polyethylene tube (denoted as tube 1) with a cap, adding ~35 mL of noncontaminated groundwater containing 1 part per million (ppm) of Cr(VI) to the tube, shaking the mixture, and placing the tube in a shaker to be agitated at a speed of approximately 120 revolutions per minute (rpm). After 1 d, the sample was removed from the shaker and centrifuged for 30 min at approximately 1200 rpm. A portion of the liquid phase (the top 30 mL) was pipetted to a clean polyethylene tube (denoted as tube 2) and capped. Approximately 30 mL more noncontaminated groundwater containing 1 ppm of Cr(VI) was added to the residue in tube 1, and the mixture was shaken and again placed in the tube in a shaker to be agitated at a speed of approximately 120 rpm. This procedure was repeated until the chromium concentration in the solution removed from tube 1 remained constant, indicating adsorption of chromium onto the solid sample had reached a maximum. About 100 mg of the residual solid material from tube 1 was transferred to a sample holder and sealed with Kapton tape for XANES measurement. Solutions from tube 2 were subsequently analyzed for chromium content by inductively coupled plasma mass spectrometry (ICPMS) to determine total dissolved concentrations of chromium.

K-2.2.2 XANES Data Collection and Analysis

The XANES spectra were collected at ambient laboratory conditions at beam line 11 of the Stanford Synchrotron Radiation Laboratory.

K-3.0 PRELIMINARY RESULTS AND DISCUSSIONS

K-3.1 XANES for Chromium (III)/(VI) Compounds

To use the chromium XANES pre-edge peak in determining both the oxidation state of Cr(III, VI) and the Cr(III)/Cr(VI) content in a sample, XANES spectra of the two chromium calibration compounds (Cr_2O_3 and K_2CrO_4) were measured. Figure K-3.1-1 presents the normalized pre-edge region of both Cr_2O_3 and K_2CrO_4. As shown in Figure K-3.1-1, increasing normalized pre-edge height reflects an increasing proportional of Cr(VI) content.

K-3.2 XANES for Chromium Adsorption onto Various Rock Samples

Figure K-3.2-1 presents the XANES measurements of chromium adsorbed or precipitated onto the four rock samples. A tabulation (Table K-3.2-1) of the resulting Cr(III)/Cr(VI) contents calculated by XANES fitting shows that Cr(III) adsorbed onto the samples from R-9, LAOI-7, and R-35b (no pre-edge feature of Cr[VI]). These spectra indicate that reduction of Cr(VI) to Cr(III) occurred after the solution was exposed to the three rock materials, although concentrations of Cr(III) in contact with R-35b and LAOI-7 were very dilute. The fitting result for adsorbed/precipitated chromium in contact with R-35a material suggests that 50% Cr(VI) and 50% Cr(III) coexist on the sample (Table K-3.2-1). The specific attenuation process (adsorption versus precipitation) for chromium associated with the sample will be investigated at a later date.
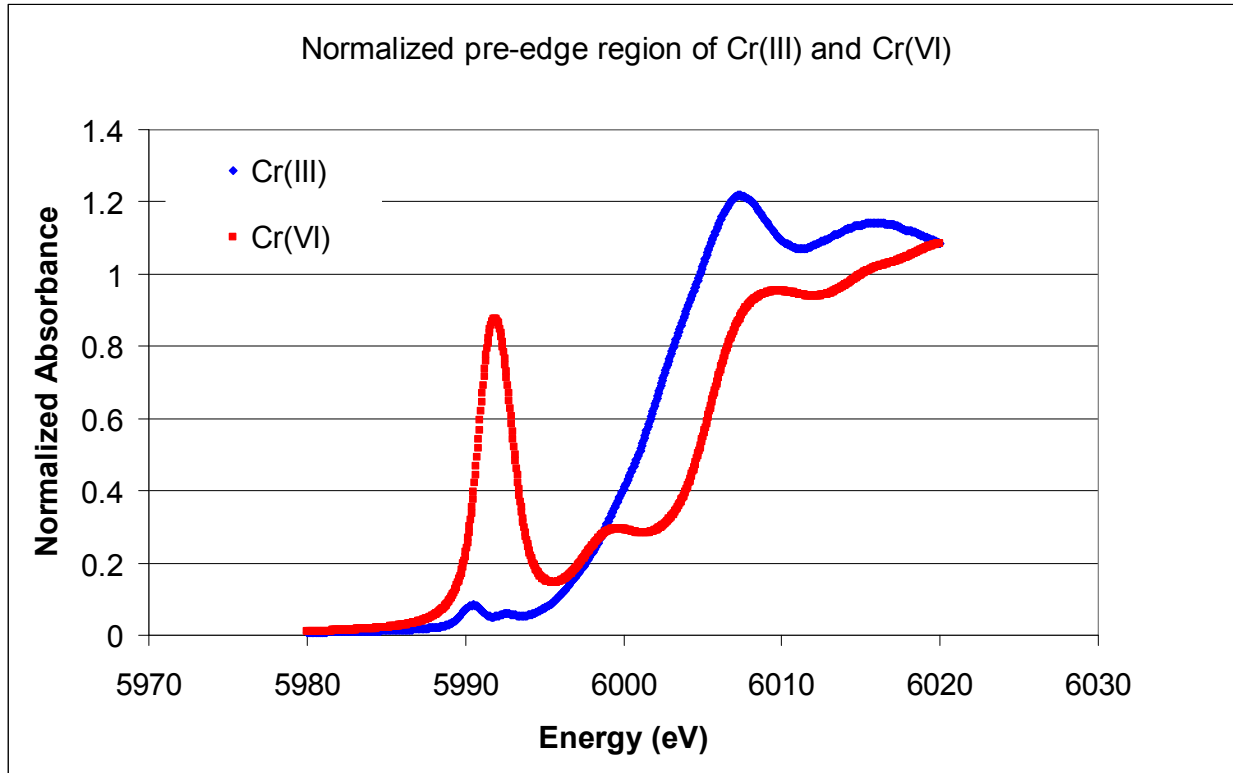
Figure K-3.1-1 Normalized pre-edge region of Cr₂O₃ and K₂CrO₄
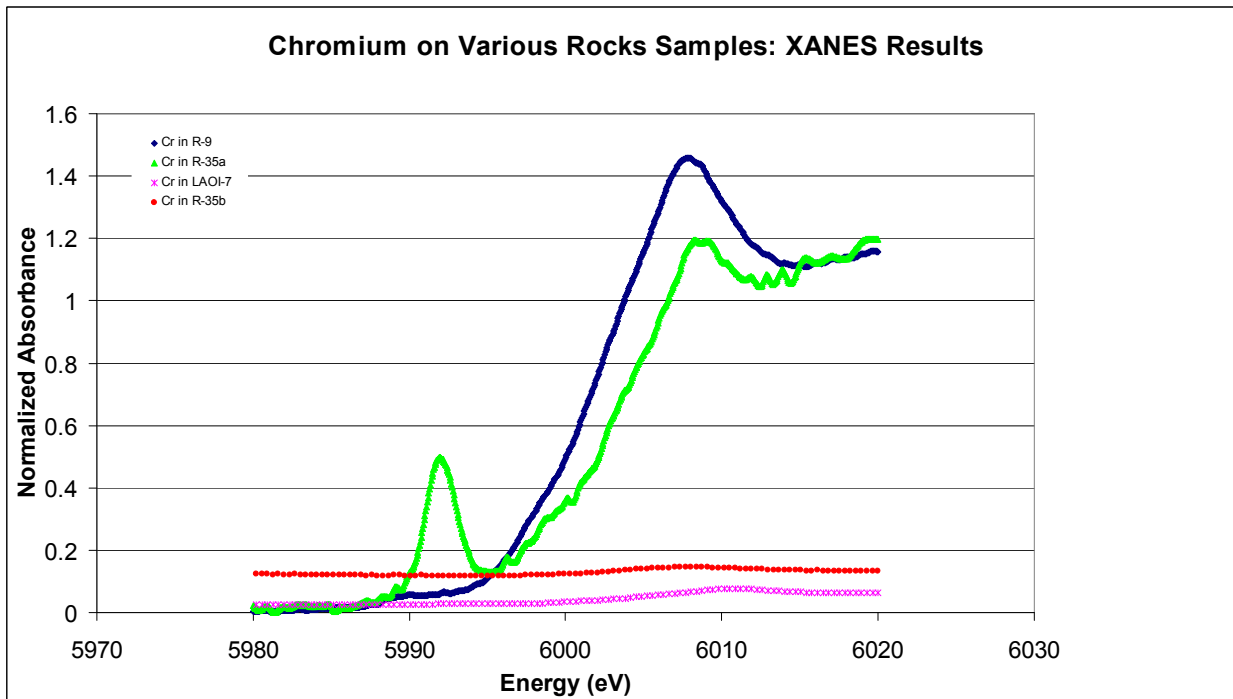
Figure K-3.2-1 XANES results for adsorbed/precipitated chromium on various rocks

Table K-3.2-1
Cr(III)/Cr(VI) Content Relative to
Total Chromium Calculated by XANES Fitting

Rock Sample	Cr(III) /Cr(VI) (%) by XANES Fitting
R-9 (Tb 4)	100% Cr(III)
LAOI-7 (Tb 4)	100 % Cr(III)
R-35a (Tch)	50% Cr(III), 50% Cr(VI)
R-35b (Tpf)	100% Cr(III)

Appendix L

Status Summary of
Sandia Canyon Wetland Dewatering Experiments

L-1.0   STATUS SUMMARY OF SANDIA CANYON WETLAND DEWATERING EXPERIMENTS (APRIL–JUNE 2008)

L-1.1   Introduction

This section provides a status report for chromium-leaching experiments conducted by Los Alamos National Laboratory's (the Laboratory's) Earth and Environmental Sciences Group 6 (EES-6) from April to June 2008, using sediment samples collected from the Sandia wetland. A more detailed discussion of the experimental results will be proved in a future report. Leaching experiments were conducted to evaluate and quantify the potential for insoluble Cr(III) reoxidizing to soluble Cr(VI) by reacting with deionized water and Technical Area 03 (TA-03) treated effluent following various periods of drying. Reoxidation of Cr(III) may potentially occur if the organic material concentrated in the Sandia wetland dries out and decomposes. Sample preparation and experimental procedures using the Sandia wetland samples are provided at the end of this section.

L-1.2   Sampling Location and Experimental Design

Sediment samples were collected from eight locations within the Sandia wetland including

- along the bank of the channel upstream of the currently active wetland (one sample, 600108);

- within the central portion of the active wetland (two samples, 600905 and 600906);

- within the dewatered, western portion of the wetland (two samples, 600110 and 600112);

- at the headcut located at the eastern end of the wetland (two samples, 600113A and 600113B); and

- within the dry bank east of the wetland containing relic cattails (one sample, 600115).

Aliquots of homogenized Sandia wetland samples were either dried in a vacuum oven at 25°C to prevent the presence of any atmospheric oxygen or dried in a fume head at room temperature or an oven at 40°C in the presence of atmospheric oxygen. The samples placed in the vacuum oven required varying amounts of time to dry completely, depending on initial moisture content. Sediment samples were dried in the oven for 2 d. Aliquots of other Sandia wetland samples collected from the eight locations were allowed to dry in a fume hood at room temperature for extended periods of time including 1, 2, 4, and 6 mo (the 4 and 6 mo experiments are still in progress). After drying, the aliquots of the wetland samples were leached with either deionized water or TA-03 treated effluent collected from the Solid Waste System Consolidation (SWSC) plant for 48 hr. The leachates were filtered through 0.22 micrometer membranes and analyzed for total dissolved Cr, Cr(VI), and other solutes.

L-1.3   Results

Analytical results for the Sandia wetland leachates including total dissolved chromium and Cr(VI) are provided in Table L-1.3-1. Detectable concentrations of total dissolved chromium and Cr(VI) in the leachates range from 0.005 to 1.69 parts per million (ppm) (5 to 1690 parts per billion [ppb]) and from 0.00006 to 0.01449 ppm (0.06 to 14.49 ppb), respectively. Most of the chromium in the leachates probably occurs as Cr(III), based on much smaller concentrations of Cr(VI) in comparison to total dissolved Cr (Table L-1.3-1). Samples (600115) collected from the dry bank east of the Sandia wetland, leached with both deionized water and the SWSC treated effluent, contain the highest concentrations of total dissolved chromium (ranging from 1.36 to 1.69 ppm). One sample (600108) collected from the bank

upstream from the active wetland, leached with both deionized water and the SWSC treated effluent, contain the highest concentrations of dissolved Cr(VI) (ranging from 0.00287 to 0.01449 ppm).

Higher concentrations of total dissolved chromium and/or Cr(VI) were leached from wetland samples dried in the oven and fume hood in the presence of atmospheric oxygen, depending on sample location (Table L-1.3-1). These include samples collected from the bank upstream of the active wetland (sample 600108), within the western portion of the dewatered wetland (samples 600110 and 600112), within the headcut at the eastern end of the wetland (sample 600113B), and within the active portion of the wetland (samples 600905 and 600906). It appears that atmospheric oxygen can be an important component enhancing the leaching of chromium from the wetland samples.

Higher concentrations of total dissolved Cr typically were measured in both the vacuum oven and oven dried samples using the SWSC treated effluent than in those using deionized water (Table L-1.3-1). Three hypotheses are proposed to explain how the SWSC-treated effluent leaches chromium from the Sandia wetland samples.

- Cations, including calcium, sodium, and magnesium concentrated in the SWSC-treated effluent, may enhance desorption of Cr(III) through cation exchange reactions from the wetland samples.

- Complexing of Cr(III) with dissolved organic carbon, in the forms of humate and fulvate ligands (anions), may also enhance desorption of Cr(III) from the organic-rich solids concentrated within the Sandia wetland.

- Colloids (smaller than 0.22 micrometers in size) consisting of Fe(III) (as $Fe(OH)_3$)and Cr(III) may be mobilized through the leaching process. Chromium(III) may occur as cations adsorbed onto $Fe(OH)_3$ and/or as $Cr(OH)_3$.

Leaching of both total dissolved chromium and Cr(VI) from the wetland samples appears to approach steady-state conditions within 48 hr. Prolonged drying of the wetland samples for a period of 2 mo results in continued leaching of chromium (Table L-1.3-1).

Monitoring of surface water upstream and downstream of the Sandia wetland shows small concentrations of chromium (between 4 and 32 ppb or 4 and 32 μg/L) were leached from the Sandia wetland during 2006 and 2007. Concentrations of total dissolved Cr in the leachates overlap but may be higher than field analytical results. This difference probably results from completely drying the wetland samples before it is leached with SWSC-treated effluent and deionized water.

L-1.4   Summary

Monitoring of surface water upstream and downstream of the Sandia wetland shows that small concentrations of chromium (between 4 and 32 ppb or 4 and 32 μg/L) were leached from the Sandia wetland during 2006 and 2007. Concentrations of total dissolved Cr in the leachates overlap but may be higher than field analytical results. This difference probably results from completely drying the wetland samples before it is leached with SWSC-treated effluent and deionized water. Analytical results obtained from the leaching experiments conducted from April to June 2008 show that up to 1.69 ppm of chromium, most likely stable as Cr(III), is leached from wetland samples. Samples collected from the dry bank east of the active wetland leached the highest concentrations of total dissolved chromium. Detectable concentrations of total dissolved chromium and Cr(VI) in the leachates range from 0.005 to 1.69 ppm (5 to 1690 ppb) and from 0.00006 to 0.01449 ppm (0.06 to 14.49 ppb), respectively. Higher concentrations of total dissolved chromium were leached from samples collected from dried sections of the Sandia wetland. Cr(VI) release appears to peak at approximately 1 mo, although longer-term experiments continue.

L-2.0   STABILITY OF CHROMIUM WITHIN THE SANDIA WETLAND, PRESENT-DAY CONDITIONS

This section provides a summary of calculations performed to evaluate the stability of Cr(III) within the Sandia wetland under present-day conditions. Concentrations of total chromium, Cr(VI), Fe(II), and Mn(IV) in the wetland samples were used in the calculations. The two most important reductants concentrated within the Sandia wetland include dissolved organic carbon and Fe(II) for maintaining the stability of Cr(III). Oxidants including Mn(IV) in the form of MnO_2 and atmospheric and dissolved oxygen, however, have the ability to reoxidize Cr(III) to Cr(VI). In addition, reoxidation of Cr(III) may occur if the organic material in the Sandia wetland dries out, decomposes, and oxidizes to inorganic carbon.

Concentrations of Fe(II), total iron, total chromium, and Cr(VI) associated with wetland sediments were previously reported by in a Laboratory report (LANL 2007, 098127). Concentrations of Cr(III) were determined by subtracting the amount of Cr(VI) from total chromium present in the sediment samples. Manganese(IV) extractions were conducted at the EES-6 analytical laboratory by reacting 0.5 g of dry soil with 25 mL of hydroxylamine hydrochloride solution for a period of 30 min on a mechanical shaker at ambient laboratory temperature (Chao 1972, 102495). With respect to Cr(III), only analytical results for samples denoted by "J" values and those without qualifiers were used for this evaluation of the stability of the Sandia wetland under present-day conditions.

Concentrations of solid organic carbon were not included in these calculations because the composition and molecular weight of organic carbon, in the form of humic and fulvic acids, present in the Sandia wetland are not known. These data are required to determine mole concentrations of solid organic carbon. The calculations only involving Fe(II) as a reductant are conservative, if the mass of this reductant alone is sufficient to maintain the stability of Cr(III) within the wetland.
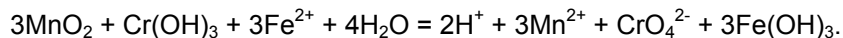
Redox reactions involving chromium are controlled by both abiotic and biotic processes in which microbial populations serve as a catalyst enhancing reaction rates. Oxidation-reduction processes with chromium have been experimentally investigated by Rai et al. (1987, 091684), showing that reduction of Cr(VI) to Cr(III) by Fe(II) follows first-order kinetics. Experimental results provided by Rai et al. (1987, 091684) show that the half-life of Cr(VI) reduction varies from 1 to 10 mo between pH values ranging from 4.2 to 6.5. More time (several years) is required for Cr(VI) reduction under circumneutral pH conditions in the presence of Fe(II), because the stability of Cr(VI) species expands in terms of decreasing oxidation-reduction potential (Eh). The reduction rate is also controlled by the strength and type of the reductant (for example, sulfide, Fe[II], lactic acid, calcium poly sulfide). Rai et al. (1987, 091684) report that the length of time required to remove Cr(VI) from solution by Fe(II) is strongly dependent on the reactivity of this reductant. For example, iron sulfides, magnetite, and Fe(II) particles require 15 min to 6 hr, acidic pH conditions, and in some instances elevated temperatures under experimental conditions to increase the rate and concentration of Fe(II) available to reduce Cr(VI). Highly soluble salts including hydrated ferrous sulfate provided higher concentrations of Fe(II) to solution resulting faster rates for Cr(VI) (Rai et al. 1987, 091684).

Site-specific data on the kinetics of Cr(III) oxidation and Cr(VI) reduction for the Sandia wetland are not known with the available data. This important aspect of chromium redox chemistry will be addressed in detail in the upcoming Sandia Canyon Investigation Report. The rate of reoxidation of Cr(III) to Cr(VI) under saturated conditions is most likely limited based on chromium concentrations (<10 μg/L) measured in oxygenated surface water within and downstream of the wetland. Under relatively reducing conditions characteristic of the Sandia wetland, dissolved Cr(III) species dominate in pore water in the presence of Fe(II) and dissolved organic carbon, also limiting rapid reoxidation of this metal.

Analytical results for chromium, iron, and manganese determined from either acid digestion or selective extraction are provided in Table L-2.0-1. Concentrations of extractable Cr(IV) and total chromium range

from 0.04 to 2.01 mg/kg and from 11.8 to 3740 mg/kg, respectively, confirming that Cr(III) is the dominant form of chromium within the Sandia wetland (Table L-2.0-1). Concentrations of extractable Mn(IV) and Fe(II) range from 18.9 to 294 mg/kg and from 100 to 6540 mg/kg, respectively. Ratios of Fe(II) to Mn(IV) range from 2.31 to 67.63 for 11 wetland samples (Table L-2.0-1). Mole ratios of Fe(II) to Cr(III) range from 0.49 to 167 for the samples (Table L-2.0-1).

Manganese(IV) serves as an electron acceptor (oxidant for Cr(III)) and Fe(II) serve as an electron donor [reductant for Cr(VI)]. One overall oxidation-reduction reaction involving Cr(III,VI), Mn(II,IV), and Fe(II,III) is

$$3MnO_2 + Cr(OH)_3 + 3Fe^{2+} + 4H_2O = 2H^+ + 3Mn^{2+} + CrO_4^{2-} + 3Fe(OH)_3.$$

Ferrous iron is much more abundant than Mn^{4+} (Table L-2.0-1) that the oxidizing effect of Mn(IV) is not taken into account in these initial calculations but will be considered, along with the reducing capacity of organic carbon, in future calculations. According to this reaction, 3 moles of Fe^{2+} are required to prevent oxidation of 1 mole of $Cr(OH)_3$ to CrO_4^{2-}. Seven of the 11 wetland samples (64%) contain enough Fe(II) to potentially limit reoxidation of Cr(III) to Cr(VI). Four samples (CASA-07-634, CASA-07-637, CASA-07-638, and CASA-07-640) with molar ratios of Fe(II): Cr(III) less than 3 do not contain enough reductant (Fe^{2+}) to prevent oxidation of Cr(III) as $Cr(OH)_3$ to Cr(VI). These calculations, however, are conservative because they do not consider the abundance of solid organic carbon, an excellent reductant enhancing the long-term stability of Cr(III) within the active (water saturated) Sandia wetland.

L-3.0 SUPPLEMENTAL MATERIAL

L-3.1 Sample Methods and Procedures

- Sandia Canyon wetland samples collected from the eight locations were individually stored in two to four 2-gal. high-density polyethylene (HDPE) bottles before the sample was prepared. Each container was sealed and stored in an EES-6 refrigerator until it was needed for sample preparation. The sediment samples were allowed to thaw for approximately 4 hr before the sample was prepared.

- If a Sandia wetland sample had interstitial water (IW), then an aliquot of the sample was filtered with a small-mesh size sieve into a collection beaker. Both pH and oxidation-reduction potential (ORP) measurements where taken for each water sample and the water sample was transferred to an appropriate size storage HDPE bottle. If the sample did not have IW, then a slurry consisting of equal proportions of deionized (DI) water and solid sample was made, and pH and ORP were measured.

- Aliquot trays/pans and moisture content jars were preweighed and measurements were recorded before the sample was added. All sample containers were labeled with the name of sample and list of analytes.

L-3.2 Homogenization of Sandia Wetland Samples

- An aliquot of each wetland sample was transferred from a HDPE bottle to a large plastic tub for homogenizing that took place within a glove box. Each sample was stirred using a spoon and macro-sized material (plant material and rocks larger then approximately 2 cm) was removed and placed in ziplock bags. Each sample was then transferred to five vials for homogenization check and to a moisture content jar for determining moisture content. The samples collected from each

location were then placed in 12 aliquot trays/pans labeled "baseline," "control," and "Mn spike" sample groups. The "Mn Spike" results evaluate potential oxidation of Cr(III) by MnO_2.

- The glove box was sealed, the chamber evacuated with an inert gas (argon, nitrogen, or helium) for at least 5 min and checked for leaks.

- Gloves were used to remove each sample from its container and the residual macros picked out and placed in a ziplock bag. Hand sieved material was then placed in a preweighed tub and occasionally stirred to start the homogenization process.

- Once all of the 2-gal. sample bottles were emptied, each sample was thoroughly stirred and homogenized to find residual macros.

- Once homogenized, the moisture content jar were filled, the 5 homogenization vials and 12 aliquot trays/pans were checked. The "control" and "Mn spikes" trays/pans were filled completely, so no air pockets remained. All sealable containers were checked to ensure they were properly resealed.

- The remaining sample in the tub was taken out of glove box to fill remaining aliquot trays/pans because mobility in glove box is limited. Aliquot trays/pans where filled with approximately equal amounts of sample. A small amount of sample was placed in a grain-size pan and placed in a drying oven heated to 110°C.

- The aliquot trays/pans and moisture content jars were weighed and the outside of each jar was checked to ensure it was clean of excess sample). Initial weights ranged between 200 and 400 g for the "baseline," "air-dried" and "oven dried" aliquot trays/pans. Weights ranged between 300 and 700 g for the completely filled "control" and "Mn spike" aliquot trays/pans. Each "baseline," "control," and "Mn spike" sample aliquot trays/pans was sealed with electrical tape and placed in separate ziplock bags. Each "baseline" sample was then placed in the vacuum oven and the "control" and "Mn spike" aliquot trays/pans where stored on counter top. All the "air-dried" aliquot trays/pans where placed in fume hoods with lids off for the determined duration (1, 2, 4, and 6 mo) before they were leached. The "oven dried" aliquot trays/pans were placed in the oven for 2 d at 40°C. Each moisture content jar was placed in the oven at 110°C for 1 d. (Moisture content is calculated in two ways: weight lost/wet sample weight and weight lost/dry sample weight.) The 5 vials for checking homogenization were sent to the EES-6 analytical lab for U.S. Environmental Protection Agency (EPA) Method 3050 digestion.

- The glove box and all equipment were cleaned before each sample was homogenized.

L-3.3 Vacuum Oven Operation

- The level and quality of vacuum oven oil and o-rings/seals were checked before use. (EES-6 technicians initially used just the vacuum oven and pump and then switched to a vacuum line so a water trap could be added to the system.)

- The sample aliquot trays/pans were placed without lids on the oven sample rack, which holds a maximum of 12 trays/pans. The water trap was checked and emptied if needed. The door was closed and sealed, vacuum pump and pressure sensors were turned on and the oven temperature set to 25°C. The oven chamber was slowly evacuated. Oven chamber remained at 2 to 10 torr when in use. (Differences in pressure occurred from decreasing moisture content as the samples dried.) The integrity of seals was checked.

- Samples where allowed to dry until water trap showed little to no water and oven chamber held a low pressure. To confirm samples were completely dry, these samples were weighed and their

moisture content checked against the results of the moisture content jar containing a sample that was oven dried at 110°C for 1 d.

- To open vacuum oven, the oven chamber was slowly sealed off from pump and vent chamber, to ensure no pressure sensors were subject to high pressures. The vacuum pump was turned off and isolated and the water trap was emptied, if necessary. Samples and containers where sealed with electrical tape and placed in ziplock bags when not in the vacuum oven.

- All "baseline" samples where allowed to completely dry before they were leached in groups.

L-3.4 Sample Leaching Process

- TA-03 SWSC-treated effluent or DI water, depending on the specific leaching test required, was added to the dry samples at a ratio of 3:2, respectively. A solid sample weight of 200 g was most desired, but sometimes this was not achieved because the quantity of the sample was not sufficient.

- Each sample flask containing sediment and DI water/TA-03 SWSC-treated effluent was then placed on a shaker table for 48 hr and covered with parafilm. The flasks where hand-swirled each morning and evening.

- After 48 hr of shaking, fluid was extracted from each flask and ORP and pH were measured. A nonfiltered aliquot (30 mL) was extracted from each flask and total alkalinity was measured. The remaining sample was delivered to the EES-6 analytical laboratory for centrifuging, filtering (0.22-micrometer membranes), sample preparation (nitric acid for metal analyses), and chemical analyses.

- Part of solid aliquot was crushed for total carbon and total organic carbon (TOC) analysis performed in the EES-6 isotope ratio mass spectrometry (IRMS) analytical laboratory.

L-3.5 Analytical Methods

Chemical analyses of the sediment-leachate samples were performed at the EES-6 laboratory. Groundwater samples were analyzed by EES-6 using techniques specified in the EPA SW-846 manual. Total carbonate alkalinity was measured using standard titration techniques. Ion chromatography was the analytical method for chloride, phosphate, Cr(VI), and sulfate. Inductively coupled (argon) plasma optical emission spectroscopy (ICPOES) was used for analyses of calcium, iron, magnesium, potassium, and sodium. Arsenic, chromium, manganese, and zinc were analyzed by inductively coupled (argon) plasma mass spectrometry (ICPMS). The precision limits (analytical error) for major ions and trace elements were generally less than ±10% using ICPOES and ICPMS. Dissolved organic carbon and TOC were measured using a total carbon-organic carbon analyzer.

L-4.0 REFERENCES

The following list includes all documents cited in this appendix. Parenthetical information following each reference provides the author(s), publication date, and ER ID number. This information is also included in text citations. ER ID numbers are assigned by the Environmental Programs Directorate's Records Processing Facility (RPF) and are used to locate the document at the RPF and, where applicable, in the master reference set.

Copies of the master reference set are maintained at the NMED Hazardous Waste Bureau; the U.S. Department of Energy–Los Alamos Site Office; the U.S. Environmental Protection Agency, Region 6;

and the Directorate. The set was developed to ensure that the administrative authority has all material needed to review this document, and it is updated with every document submitted to the administrative authority. Documents previously submitted to the administrative authority are not included.

Chao, T.T., 1972. "Selective Dissolution of Manganese Oxides from Soils and Sediments with Acidified Hydroxylamine Hydrochloride," *Soil Science Society of America Proceedings,* Vol. 36, pp. 764–768. (Chao 1972, 102495)

LANL (Los Alamos National Laboratory), September 2007. "Summary of Sandia Canyon Phase 1 Sediment Investigations," Los Alamos National Laboratory document LA-UR-07-6019, Los Alamos, New Mexico. (LANL 2007, 098127)

Rai, D., J.M. Zachara, L.E. Eary, D.C. Girvin, D.A. Moore, C.T. Resch, B.M. Sass, and R.L. Schmidt, August 1987. "Inorganic and Organic Constituents in Fossil Fuel Combustion Residues, Volume 1: A Critical Review," report prepared by Battelle, Pacific Northwest Laboratories for the Electric Power Research Institute, interim report EA-5176, Richland, Washington. (Rai et al. 1987, 091684)

Table L-1.3-1
Analytical Results for the Sandia Wetland Leachates

Sample ID	ER ID #	Date Received	Description	Sample Content	Depth Range (cm)	Moisture Content (%)	Cr rslt (ppm)	Stdev (cr)	Cr 6+ rslt (mg/L)	Cr 6+ (u)
600108 Init.	—	—	Initial sample. Measurements made in a 1:1 slurry	River sand/gravel, little to no organics	20.0–108.0	—*	—	—	—	—
600108	1	—	Moisture content jar. Oven dried @ 110°C	—	20.0–108.0	7.48	—	—	—	—
600108-BL-DI	7	5/14/2008	Vacuum dried @ 25°C until dry, leached w/ DI water	—	20.0–108.0	—	0.006	0.000	0.00325	—
600108-BL-OF24	8a	5/13/2008	Vacuum dried @ 25°C until dry, leached w/ Outflow water, Cr 6+ check @ 24hrs	—	20.0–108.0	—	—	—	0.00287	—
600108-BL-OF48	8b	5/14/2008	Vacuum dried @ 25°C until dry, leached w/ Outflow water	—	20.0–108.0	—	0.017	0.000	0.00294	—
600108-DRY-DI	21	4/17/2008	Oven dried @ 40°C for 2 days, Leached w/ DI water	—	20.0–108.0	—	0.009	0.000	0.00531	—
600108-DRY-OF	22	4/17/2008	Oven dried @ 40°C for 2 days, Leached w/ Outflow water	—	20.0–108.0	—	0.020	0.000	0.00586	—
600108-DRY-DIG	23	—	Oven dried @ 40°C for 2 days	—	20.0–108.0	—	—	—	—	—
600108-1MON-DI	24	5/15/2008	Dried in fume hood for 1 month, leached w/ DI water	—	—	—	0.017	0.000	0.01449	—
600108-1MON-OF	25	5/15/2008	Dried in fume hood for 1 month, leached w/ Outflow water	—	—	—	0.025	0.000	0.01146	—
600108-1MON-DIG	26	—	—	—	—	—	—	—	—	—
600108-2MON-DI	27	6/16/2008	Dried in fume hood for 2 month, leached w/ DI water	—	20.0–108.0	—	0.013	0.000	0.00823	—
600108-2MON-OF	28	6/16/2008	Dried in fume hood for 2 month, leached w/ Outflow water	—	20.0–108.0	—	0.023	0.001	0.00647	—
600110 Init.	—	—	Initial sample. Measurements made in a 1:1 slurry	Sample was frozen	26.0–42.0	—	—	—	—	—

Table L-1.3-1 (continued)

Sample ID	ER ID #	Date Received	Description	Sample Content	Depth Range (cm)	Moisture Content (%)	Cr rslt (ppm)	Stdev (cr)	Cr 6+ rslt (mg/L)	Cr 6+ (u)
600110	1	—	Moisture content jar. Oven dried @ 110°C	Clumps of clay and plant roots	26.0–42.0	22.73	—	—	—	—
600110-BL-DI	7	5/14/2008	Vacuum dried @ 25°C until dry, leached w/ DI water	—	26.0–42.0	—	0.009	0.000	0.00026	—
600110-BL-OF24	8a	5/13/2008	Vacuum dried @ 25°C until dry, leached w/ Outflow water, Cr 6+ check @ 24hrs	—	26.0–42.0	—	—	—	0.00020	—
600110-BL-OF48	8b	5/14/2008	Vacuum dried @ 25°C until dry, leached w/ Outflow water	—	26.0–42.0	—	0.020	0.001	0.00015	—
600110-DRY-DI	21	4/17/2008	Oven dried @ 40°C for 2 days, Leached w/ DI water	—	26.0–42.0	—	0.012	0.000	0.00199	—
600110-DRY-OF	22	4/17/2008	Oven dried @ 40°C for 2 days, Leached w/ Outflow water	—	26.0–42.0	—	0.020	0.001	0.00084	—
600110-DRY-DIG	23	—	Oven dried @ 40°C for 2 days	—	26.0–42.0	—	—	—	—	—
600110-1MON-OF	24	5/15/2008	Dried in fume hood for 1 month, leached w/ DI water	—	—	—	0.014	0.000	0.00050	—
600110-1MON-DI	25	5/15/2008	Dried in fume hood for 1 month, leached w/ Outflow water	—	—	—	0.025	0.001	0.00171	—
600110-1MON-DIG	26	—		—	—	—	—	—	—	—
600110-2MON-DI	27	6/16/2008	Dried in fume hood for 2 month, leached w/ DI water	—	26.0–42.0	—	0.026	0.000	0.00017	
600110-2MON-OF	28	6/16/2008	Dried in fume hood for 2 month, leached w/ Outflow water	—	26.0–42.0	—	0.017	0.000	0.00005	U
600112 Init.	—	—	Initial sample. Measurements made in a 1:1 slurry	Many arthropods found alive	0.0–41.0	—	—	—	—	—
600112	1	—	Moisture content jar. Oven dried @ 110°C	Found some growing green grass	0.0–41.0	14.69	—	—	—	—

Table L-1.3-1 (continued)

Sample ID	ER ID #	Date Received	Description	Sample Content	Depth Range (cm)	Moisture Content (%)	Cr rslt (ppm)	Stdev (cr)	Cr 6+ rslt (mg/L)	Cr 6+ (u)
600112-BL-DI	7	5/14/2008	Vacuum dried @ 25°C until dry, leached w/ DI water	—	0.0–41.0	—	0.005	0.000	0.00055	—
600112-BL-OF24	8a	5/13/2008	Vacuum dried @ 25°C until dry, leached w/ Outflow water, Cr 6+ check @ 24hrs	—	0.0–41.0	—	—	—	0.00013	—
600112-BL-OF48	8b	5/14/2008	Vacuum dried @ 25°C until dry, leached w/ Outflow water	—	0.0–41.0	—	0.017	0.000	0.00024	—
600112-DRY-DI	21	4/17/2008	Oven dried @ 40°C for 2 days, Leached w/ DI water	—	0.0–41.0	—	0.005	0.000	0.00097	—
600112-DRY-OF	22	4/17/2008	Oven dried @ 40°C for 2 days, Leached w/ Outflow water	—	0.0–41.0	—	0.018	0.000	0.00057	—
600112-DRY-DIG	23	—	Oven dried @ 40°C for 2 days	—	0.0–41.0	—	—	—	—	—
600112-1MON-DI	24	5/15/2008	Dried in fume hood for 1 month, leached w/ DI water	—	—	—	0.011	0.000	0.00069	—
600112-1MON-OF	25	5/15/2008	Dried in fume hood for 1 month, leached w/ Outflow water	—	—	—	0.020	0.000	0.00100	—
600112-1MON-DIG	26	—	—	—	—	—	—	—	—	—
600112-2MON-DI	27	6/16/2008	Dried in fume hood for 2 month, leached w/ DI water	—	0.0–41.0	—	0.009	0.000	0.00017	—
600112-2MON-OF	28	6/16/2008	Dried in fume hood for 2 month, leached w/ Outflow water	—	0.0–41.0	—	0.023	0.000	0.00006	—
600113A Init.	—	—	Initial interstitial water sample	Very wet. Mold growing on surface	9.0–71.0	—	—	—	—	—
600113A	—	—	Moisture content jar. Oven dried @ 110°C	Moderate plant content (some growing)	9.0–71.0	52.92	—	—	—	—
600113A-BL-DI	7	5/14/2008	Vacuum dried @ 25°C until dry, leached w/ DI water	—	9.0–71.0	—	0.065	0.001	0.00005	U

Table L-1.3-1 (continued)

Sample ID	ER ID #	Date Received	Description	Sample Content	Depth Range (cm)	Moisture Content (%)	Cr rslt (ppm)	Stdev (cr)	Cr 6+ rslt (mg/L)	Cr 6+ (u)
600113A-BL-OF24	8a	5/13/2008	Vacuum dried @ 25°C until dry, leached w/ Outflow water, Cr 6+ check @ 24hrs	—	9.0–71.0	—	—	—	0.00005	U
600113A-BL-OF48	8b	5/14/2008	Vacuum dried @ 25°C until dry, leached w/ Outflow water	—	9.0–71.0	—	0.113	0.003	0.00005	U
600113A-BL-IW	10	4/3/2008	Interstitial water collected before homogenization	—	9.0–71.0	—	0.018	0.000	0.00005	U
600113A-DRY-DI	21	4/17/2008	Oven dried @ 40°C for 2 days, Leached w/ DI water	—	9.0–71.0	—	0.039	0.001	0.00005	U
600113A-DRY-OF	22	4/17/2008	Oven dried @ 40°C for 2 days, Leached w/ Outflow water	—	9.0–71.0	—	0.045	0.000	0.00021	—
600113A-DRY-DIG	23	—	Oven dried @ 40°C for 2 days	—	9.0–71.0	—	—	—	—	—
600113A-1MON-DI	24	5/15/2008	Dried in fume hood for 1 month, leached w/ DI water	—	—	—	0.049	0.000	0.00033	—
600113A-1MON-OF	25	5/15/2008	Dried in fume hood for 1 month, leached w/ Outflow water	—	—	—	0.053	0.001	0.00027	—
60113A-1MON-DIG	26	—	—	—	—	—	—	—	—	—
600113A-2MON-DI	27	6/16/2008	Dried in fume hood for 2 month, leached w/ DI water	—	9.0–71.0	—	0.054	0.000	0.00005	U
600113A-2MON-OF	28	6/16/2008	Dried in fume hood for 2 month, leached w/ Outflow water	—	9.0–71.0	—	0.068	0.001	0.00006	—
600113B Init.	—	—	Initial interstitial water sample	Not many macros	71.0–101.0	—	—	—	—	—
600113B	1	—	Moisture content jar. Oven dried @ 110°C	—	71.0–101.0	34.55	—	—	—	—
600113B-BL-DI	7	5/14/2008	Vacuum dried @ 25°C until dry, leached w/ DI water	—	71.0–101.0	—	0.010	0.000	0.00005	U
600113B-BL-OF24	8a	5/13/2008	Vacuum dried @ 25°C until dry, leached w/ Outflow water, Cr 6+ check @ 24hrs	—	71.0–101.0	—	—	—	0.00012	—

Table L-1.3-1 (continued)

Sample ID	ER ID #	Date Received	Description	Sample Content	Depth Range (cm)	Moisture Content (%)	Cr rslt (ppm)	Stdev (cr)	Cr 6+ rslt (mg/L)	Cr 6+ (u)
600113B-BL-OF48	8b	5/14/2008	Vacuum dried @ 25°C until dry, leached w/ Outflow water	—	71.0–101.0	—	0.015	0.000	0.00005	U
600113B-BL-IW	10	4/8/2008	Interstitial water collected before homogenization	—	71.0–101.0	—	0.008	0.000	0.00005	U
600113B-DRY-DI	21	4/17/2008	Oven dried @ 40°C for 2 days, Leached w/ DI water	—	71.0–101.0	—	0.011	0.000	0.00016	—
600113B-DRY-OF	22	4/17/2008	Oven dried @ 40°C for 2 days, Leached w/ Outflow water	—	71.0–101.0	—	0.018	0.000	0.00015	—
600113B-DRY-DIG	23	—	Oven dried @ 40°C for 2 days	—	71.0–101.0	—	—	—	—	—
600113B-1MON-DI	24	5/15/2008	Dried in fume hood for 1 month, leached w/ DI water	—	—	—	0.015	0.000	0.00011	—
600113B-1MON-OF	25	5/15/2008	Dried in fume hood for 1 month, leached w/ Outflow water	—	—	—	0.023	0.000	0.00022	—
600113B-1MON-DIG	26	—	—	—	—	—	—	—	—	—
600113B-2MON-DI	27	6/17/2008	Dried in fume hood for 2 month, leached w/ DI water	—	71.0–101.0	—	0.020	0.001	0.00006	—
600113B-2MON-OF	28	6/17/2008	Dried in fume hood for 2 month, leached w/ Outflow water	—	71.0–101.0	—	0.017	0.001	0.00009	—
600115 Init.	—	—	Initial sample. Measurements made in a 1:1 slurry	Sand grains in mud	0.0–30.0	—	—	—	—	—
600115	1	—	Moisture content jar. Oven dried @ 110°C	—	0.0–30.0	33.04	—	—	—	—
600115-BL-DI	7	5/14/2008	Vacuum dried @ 25°C until dry, leached w/ DI water	—	0.0–30.0	—	1.50	0.01	0.00005	U
600115-BL-OF24	8a	5/13/2008	Vacuum dried @ 25°C until dry, leached w/ Outflow water, Cr 6+ check @ 24hrs	—	0.0–30.0	—	—	—	0.00005	U
600115-BL-OF48	8b	5/14/2008	Vacuum dried @ 25°C until dry, leached w/ Outflow water	—	0.0–30.0	—	1.50	0.00	0.00005	U

Table L-1.3-1 (continued)

Sample ID	ER ID #	Date Received	Description	Sample Content	Depth Range (cm)	Moisture Content (%)	Cr rslt (ppm)	Stdev (cr)	Cr 6+ rslt (mg/L)	Cr 6+ (u)
600115-DRY-DI	21	4/17/2008	Oven dried @ 40°C for 2 days, Leached w/ DI water	—	0.0–30.0	—	1.36	0.02	0.00045	—
600115-DRY-OF	22	4/17/2008	Oven dried @ 40°C for 2 days, Leached w/ Outflow water	—	0.0–30.0	—	1.46	0.01	0.00019	—
600115-DRY-DIG	23	—	Oven dried @ 40°C for 2 days	—	0.0–30.0	—	—	—	—	—
600115-1MON-DI	24	5/15/2008	Dried in fume hood for 1 month, leached w/ DI water	—	—	—	1.49	0.00	0.00005	U
600115-1MON-OF	25	5/15/2008	Dried in fume hood for 1 month, leached w/ Outflow water	—	—	—	1.51	0.01	0.00005	U
600115-1MON-DIG	26	—	—	—	—	—	—	—	—	—
600115-2MON-DI	27	6/17/2008	Dried in fume hood for 2 month, leached w/ DI water	—	0.0–30.0	—	1.69	0.05	0.00005	U
600115-2MON-OF	28	6/17/2008	Dried in fume hood for 2 month, leached w/ Outflow water	—	0.0–30.0	—	1.66	0.03	0.00005	U
600905 Init.	—	—	Initial interstitial water sample	Very wet. Approx. half plant material	0.0–15.0	—	—	—	—	—
600905	1	—	Moisture content jar. Oven dried @ 110°C	—	0.0–15.0	47.02	—	—	—	—
600905-BL-DI	7	5/14/2008	Vacuum dried @ 25°C until dry, leached w/ DI water	—	0.0–15.0	—	0.009	0.000	0.00005	U
600905-BL-OF24	8a	5/13/2008	Vacuum dried @ 25°C until dry, leached w/ Outflow water, Cr 6+ check @ 24hrs	—	0.0–15.0	—	—	—	0.00005	U
600905-BL-OF48	8b	5/14/2008	Vacuum dried @ 25°C until dry, leached w/ Outflow water	—	0.0–15.0	—	0.011	0.000	0.00005	U
600905-BL-IW	10	4/8/2008	Interstitial water collected before homogenization	—	0.0–15.0	—	0.016	0.000	0.00005	U
600905-DRY-DI	21	4/17/2008	Oven dried @ 40°C for 2 days, Leached w/ DI water	—	0.0–15.0	—	0.014	0.000	0.00010	—

Table L-1.3-1 (continued)

Sample ID	ER ID #	Date Received	Description	Sample Content	Depth Range (cm)	Moisture Content (%)	Cr rslt (ppm)	Stdev (cr)	Cr 6+ rslt (mg/L)	Cr 6+ (u)
600905-DRY-OF	22	4/17/2008	Oven dried @ 40°C for 2 days, Leached w/ Outflow water	—	0.0–15.0	—	0.019	0.000	0.00007	—
600905-DRY-DIG	23	—	Oven dried @ 40°C for 2 days	—	0.0–15.0	—	—	—	—	—
600905-1MON-DI	24	5/15/2008	Dried in fume hood for 1 month, leached w/ DI water	—	—	—	0.015	0.000	0.00017	—
600905-1MON-OF	25	— 5/15/2008	Dried in fume hood for 1 month, leached w/ Outflow water	—	—	—	0.023	0.000	0.00007	—
600905-1MON-DIG	26	—	—	—	—	—	—	—	—	—
600905-2MON-DI	27	6/17/2008	Dried in fume hood for 2 month, leached w/ DI water	—	0.0–15.0	—	0.016	0.000	0.00005	U
600905-2MON-OF	28	6/17/2008	Dried in fume hood for 2 month, leached w/ Outflow water	—	0.0–15.0	—	0.024	0.000	0.00005	U
600906 Init.	—	—	Initial interstitial water sample	High plant material (mostly roots)	0.0–15.0	—	—	—	—	—
600906	1	—	Moisture content jar. Oven dried @ 110°C	—	0.0–15.0	45.19	—	—	—	—
600906-BL-DI	7	5/14/2008	Vacuum dried @ 25°C until dry, leached w/ DI water	—	0.0–15.0	—	0.004	0.000	0.00007	—
600906-BL-OF24	8a	5/13/2008	Vacuum dried @ 25°C until dry, leached w/ Outflow water, Cr 6+ check @ 24hrs	—	0.0–15.0	—	—	—	0.00040	—
600906-BL-OF48	8b	5/14/2008	Vacuum dried @ 25°C until dry, leached w/ Outflow water	—	0.0–15.0	—	0.011	0.000	0.00005	U
600906-BL-IW	10	4/9/2008	Interstitial water collected before homogenization	—	0.0–15.0	—	0.012	0.000	0.00005	U
600906-DRY-DI	21	4/17/2008	Oven dried @ 40°C for 2 days, Leached w/ DI water	—	0.0–15.0	—	0.008	0.000	0.00012	—
600906-DRY-OF	22	4/17/2008	Oven dried @ 40°C for 2 days, Leached w/ Outflow water	—	0.0–15.0	—	0.013	0.000	0.00007	—

Table L-1.3-1 (continued)

Sample ID	ER ID #	Date Received	Description	Sample Content	Depth Range (cm)	Moisture Content (%)	Cr rslt (ppm)	Stdev (cr)	Cr 6+ rslt (mg/L)	Cr 6+ (u)
600906-DRY-DIG	23	—	Oven dried @ 40°C for 2 days	—	0.0–15.0	—	—	—	—	—
600906-1MON-DI	24	5/15/2008	Dried in fume hood for 1 month, leached w/ DI water	—	—	—	0.008	0.000	0.00030	—
600906-1MON-OF	25	5/15/2008	Dried in fume hood for 1 month, leached w/ Outflow water	—	—	—	0.016	0.000	0.00020	—
600906-1MON-DIG	26	—	—	—	—	—	—	—	—	—
600906-2MON-DI	27	6/17/2008	Dried in fume hood for 2 month, leached w/ DI water	—	0.0–15.0	—	0.010	0.000	0.00005	U
600906-2MON-OF	28	6/17/2008	Dried in fume hood for 2 month, leached w/ Outflow water	—	0.0–15.0	—	0.016	0.001	0.00008	—
BLANK-1	B-1	4/17/2008	—	—	—	—	0.001	—	0.00005	U
BLANK-2	B-2	4/17/2008	—	—	—	—	0.001	—	0.00005	U
BLANK-3	B-3	4/17/2008	—	—	—	—	0.001	—	0.00005	U
BLANK-4	B-4	6/17/2008	—	—	—	—	0.001	—	—	—
BLANK-5	B-5	6/17/2008	—	—	—	—	0.001	—	—	—
BLANK-6	B-6	6/17/2008	—	—	—	—	0.001	—	—	—
BLANK-7	B-7	6/17/2008	—	—	—	—		—	—	—
BLANK-8	B-8	6/17/2008	—	—	—	—		—	0.00005	U
BLANK-9	B-9	6/17/2008	—	—	—	—	—	—	0.00005	U

Note: — = Not available or not applicable. Data and sample analyses are pending.

Table L-2.0-1

Analytical Results for Chromium, Iron, and Manganese Determined from Either Acid Digestion or Selective Extraction

Sample ID	Date Analyzed	Matrix	Qualifier	ER Request Number with (sample location)	Solid Concentration Cr (mg/kg)	Solid Concentration Cr(VI) (mg/kg)	uMoles Cr(III)/g soil	uMoles Cr(VI)/g soil	uMoles Mn(IV)/g soil	uMolesMn(IV)/uMolesCr(III)	Fe (mg/kg) 3050 dig.	Total Fe (mg/kg) (Huffman)	Fe(II) (mg/kg) (Huffman)	uMoles Fe(II)/g soil	uMolesFe(II)/g soil/ uMolesCr(III)/g soil	Potential for Cr(III) to remain reduced good, poor
casa-07-4012	8/14/2007	solid	J-	07-236 (wetland)	21.5	0.05	0.41	0.001	0.43	1.05	5870	1410	1400	25.07	61.15	good
casa-07-4014	8/14/2007	solid	J-	07-236 (wetland)	36.5	0.07	0.7	0.001	1.73	2.47	6040	6560	6540	117	167.14	good
casa-07-4016	8/14/2007	solid	UJ	07-236 (wetland)	19.0	0.29	0.36	0.006	3.62	10.06	3460	4270	4270	76.5		
casa-07-4018	8/14/2007	solid	J-	07-236 (wetland)	114.0	0.07	2.19	0.001	3.09	1.41	14400	6380	6360	114	52.05	good
casa-07-632	8/14/2007	solid	J+	07-92 (wetland)	11.8	0.16	0.22	0.003	0.48	2.19	11400	600	100	1.79	8.14	good
casa-07-633	8/14/2007	solid	U	07-92 (wetland)	137.0	0.77	2.62	0.015	0.8	0.31	10200	5070	860	15.4		
casa-07-634	8/14/2007	solid	J+	07-92 (wetland)	112.0	0.14	2.15	0.003	1.57	0.73	12300	1380	320	5.73	2.67	poor
casa-07-635	8/14/2007	solid	J+	07-92 (wetland)	51.3	0.04	0.99	0.001	0.72	0.73	10600	1200	210	3.76	3.8	good
casa-07-636	8/14/2007	solid	J+	07-92 (wetland)	16.9	0.12	0.32	0.002	0.97	3.03	9500	1110	210	3.76	11.75	good
casa-07-637	8/14/2007	solid	J+	07-92 (wetland)	3580.0	2.01	68.81	0.039	5.35	0.08	7980	5970	2660	47.6	0.69	poor
casa-07-638	8/14/2007	solid	J+	07-92 (wetland)	601.0	1.06	11.54	0.020	3	0.26	18200	3510	1250	22.4	1.94	poor
casa-07-639	8/14/2007	solid	U	07-92 (wetland)	3740.0	0.69	71.91	0.013	0.72	0.01	18000	10160	620	11.1		
casa-07-640	8/14/2007	solid	J+	07-92 (wetland)	592.0	0.31	11.38	0.006	2.4	0.21	12100	4140	310	5.55	0.49	poor
casa-07-641	8/14/2007	solid	J+	07-92 (wetland)	18.5	0.28	0.35	0.005	0.34	0.97	5070	970	230	4.12	11.77	good

Appendix M

A Geochemical Conceptual Model for Fate and Transport of Chromium at Los Alamos National Laboratory

This section summarizes a geochemical conceptual model for the mobility of chromium (Cr) contamination at Los Alamos National Laboratory (LANL). This conceptual model focuses on speciation, adsorption, and precipitation, which influence the fate and transport of chromium in the environment. Developing and refining a geochemical conceptual model for chromium is essential for characterizing nature and extent of chromium contamination and for evaluating remediation options and technologies, including monitored natural attenuation.
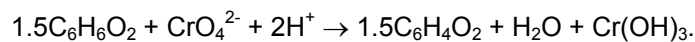
A conceptual geochemical cross section showing potential chromium transport pathways and geochemical reactions influencing fate and transport of chromium in surface and subsurface environments at Los Alamos is shown in Figure M-1. This conceptual cross-section complements the physical system conceptual model for chromium transport in Sandia Canyon presented in section 2 of this report. The assumption in Figure M-1 is that the potassium dichromate ($K_2Cr_2O_7$) releases from the Technical Area 03 (TA-03) power plant cooling towers (see section 2) are the predominant Cr(VI) source (as CrO_4^{2-}) in the environment. Potassium dichromate was released from the TA-03 power plant between approximately June 1956 and April 1972 (LANL 2006, 094431).

Natural sources of chromium occur at Los Alamos in soils and in vadose zone and aquifer materials consisting of the Bandelier Tuff, Cerros del Rio basalt, Tschicoma Formation, Puye Formation, and Santa Fe Group sediments. Chromium is concentrated within iron-rich minerals and amorphous solids, including hematite, magnetite, biotite, amphiboles, pyroxenes, ferric (oxy)hydroxide, smectite, and volcanic glass. At Los Alamos, mean background concentrations of chromium in weak acid leachates are 10.5 and 19.3 mg/kg within sediments and soil horizons, respectively (LANL 1998, 059730).

Chromium is stable in the III and VI oxidation states in aqueous solution (Rai et al. 1986, 091686). Under relatively reducing conditions, Cr(III) is stable as Cr^{3+}, $CrOH^{2+}$, $Cr(OH)_2^+$, $Cr(OH)_3^0$, and $Cr(OH)_4^-$ with hydrolysis species dominating above pH 3. Under relatively oxidizing conditions, Cr(VI) is stable as bichromate ($HCrO_4^-$) and chromate (CrO_4^{2-}) (Rai et al. 1986, 091686). At pH 6.5 and 25°C, $HCrO_4^-$ and CrO_4^{2-} are present in equal concentrations in solution under oxidizing conditions (Rai et al. 1986, 091686).

Background concentrations of total dissolved chromium range between 0.39 and 7.31 μg/L within perched intermediate-depth groundwater and the regional aquifer (LANL 2007, 095817). Dissolved concentrations of natural chromium are controlled by equilibrium between crystalline $Cr(OH)_3$ and dissolved Cr(VI) species, based on simulation results using the computer program PHREEQC2.2 (Parkhurst and Appelo 1999, 095402). Below an oxidation-reduction potential (Eh) of 500 millivolts at pH 7, amorphous and crystalline forms of $Cr(OH)_3$ are stable.
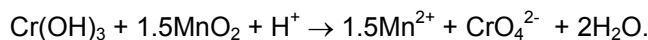
Since 1951, releases of water into Sandia Canyon created a wetland that has expanded over the years. This wetland contains between 5700 and 27,000 kg of Cr(III), with a median mass of 15,000 kg of total chromium (LANL 2007, 098938). Chromium(VI) is removed from surface water through chemical-biochemical reduction, enhancing adsorption and/or precipitation of Cr(III) solids. Solid organic matter present in the Sandia wetland is considered to be the dominant reductant for immobilizing chromium (Figure M-1). One example reaction describing the reduction of Cr(VI) to Cr(III) in the presence of solid organic matter, containing hydroquinone ($C_6H_6O_2$) that provides the reduction capacity (McBride 1994, 058947) is:

$$1.5C_6H_6O_2 + CrO_4^{2-} + 2H^+ \rightarrow 1.5C_6H_4O_2 + H_2O + Cr(OH)_3.$$

According to this reaction, 1.5 moles of $C_6H_6O_2$ are required to reduce 1.0 mole of CrO_4^2. This is easily accomplished with the abundant solid organic matter present within the Sandia Canyon wetland (Figure M-1). 1.5 moles of $C_6H_6O_2$ oxidize to form 1.5 moles of quinone ($C_6H_4O_2$) with the release of

two electrons. Evidence for this reaction occurring within the Sandia Canyon wetland is based on elevated concentrations of chromium in the organic-rich sediments (>1000 mg/kg) and concentrations of total dissolved chromium less than 20 µg/L (LANL 2006, 094431). Following reduction, dissolved Cr(III) species can either adsorb onto sediments or precipitate as amorphous $Cr(OH)_3$. Chromium(III) also coprecipitates with ferric iron forming $(Fe_xCr_{1-x})(OH)_3$ (Rai et al. 1986, 091686). Solid organic matter present in wetlands is characterized by a net-negative surface charge above pH 4.8, produced from aliphatic carboxylates (R-COO$^-$). This surface-active functional group provides numerous binding sites for adsorption of cationic Cr(III) species, including Cr^{3+}, $CrOH^{2+}$, and $Cr(OH)_2^+$ (Figure M-1).
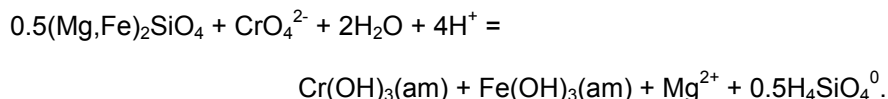
Amorphous and crystalline $Cr(OH)_3$, however, can reoxidize to soluble Cr(VI) species in the presence of Mn(III, IV) solids (Rai et al. 1986, 091686). During the reoxidation of Cr(III), Mn(III, IV) solids become reduced and dissolve to form Mn(II) aqueous species. One example of this oxidation-reduction process is shown by the following reaction:

$$Cr(OH)_3 + 1.5MnO_2 + H^+ \rightarrow 1.5Mn^{2+} + CrO_4^{2-} + 2H_2O.$$

This re-oxidation depends on the abundance, reactivity, and availability of MnO_2 (Rai et al. 1986, 091686). Concentrations of elemental Mn range from 186 to 1552 mg/kg in soils at the Laboratory (Longmire et al. 1995, 048818), suggesting possible oxidation of Cr(III) in Mn-rich soils. Ferrous iron concentrated in the Sandia wetland, however, is an excellent reductant for chromium and the majority of Cr(III) will be stable (see Appendix L). Concentrations of Fe(II) exceed those of Mn(IV) within the wetland and only a fraction of Cr(III) is expected to oxidize to Cr(VI).

Surface water in Los Alamos, Sandia, and Mortandad Canyons provides a source of recharge to alluvial groundwater, which in turn, provides recharge to perched intermediate-depth groundwater, and ultimately, to the regional aquifer (Figure M-1). As Cr(VI) migrates through the vadose zone to the regional water table, a small fraction of Cr(VI) potentially adsorbs onto ferric (oxy)hydroxide under basic pH conditions. This adsorbent has a large specific surface area of 600 m^2/g and is characterized by a net-positive surface charge below pH 6.7 (Langmuir 1997, 056037). Partial adsorption of Cr(VI) onto ferric (oxy)hydroxide under basic pH conditions may account for residual Cr(VI) observed within the vadose zone beneath the Sandia watershed (LANL 2006, 094431). Dissolved concentrations of chromium in pore water range from 3 to 1329 µg/L, suggesting that residual Cr(VI) is present in the upper 122 m of the vadose zone beneath Sandia Canyon (LANL 2006, 094431).

An unquantified mass of Cr(VI) has migrated to perched intermediate-depth groundwater and the regional aquifer beneath Sandia and Mortandad canyons (Figure M-1). Total dissolved concentrations of chromium have ranged from 16.7 to 58.2 µg/L at wells MCOBT-4.4, MCOI-4, and MCOI-6 between 2002 and 2006 (LANL 2006, 094431). These Mortandad Canyon wells are completed in perched intermediate-depth groundwater within the Cerros del Rio basalt and/or Puye Formation and pumiceous sediments (Figure M-1). The groundwater standard for total chromium promulgated by the New Mexico Environment Department is 50 µg/L. Ferrous iron (Fe^{2+}) is a natural reductant concentrated within the Cerros del Rio basalt that is capable of reducing Cr(VI) to Cr(III) (Figure M-1). An example of a generalized oxidation-reduction reaction describing the reduction of CrO_4^{2-} to amorphous $Cr(OH)_3$ by alteration of olivine within the Cerros del Rio basalt is

$$0.5(Mg,Fe)_2SiO_4 + CrO_4^{2-} + 2H_2O + 4H^+ =$$

$$Cr(OH)_3(am) + Fe(OH)_3(am) + Mg^{2+} + 0.5H_4SiO_4^0.$$

Coprecipitation of Cr(III) and Fe(III) as $(Cr_xFe_{1-x})(OH)_3$ is considered to be an additional process contributing to chromium removal from groundwater within the basalt. Reduction of soluble Cr(VI) to

$Cr(OH)_3$ results in lower concentrations of dissolved chromium within perched intermediate-depth groundwater than concentrations observed within the regional aquifer at well R-28 in Mortandad Canyon (Figure M-1).

Stable isotopes of chromium (^{52}Cr and ^{53}Cr) have application to quantifying the amount of Cr(VI) reduction to Cr(III) in aqueous systems. Stable isotopes of chromium (^{52}Cr and ^{53}Cr, $\delta^{53}Cr$) undergo fractionation as dissolved Cr(VI) species become reduced to Cr(III) species in the presence of solid organic matter, dissolved organic carbon, ferrous iron [Fe(II)], and hydrogen sulfide. During this reduction process, Cr(III) precipitates from solution as relatively insoluble $Cr(OH)_3$ and concentrations of total dissolved chromium can substantially decrease to less than 50 µg/L between pH 6 and 9 at 25°C. During chemical reduction of Cr(VI) to Cr(III), residual dissolved Cr(VI) becomes enriched in the heavier isotope ^{53}Cr, and Cr(III) solid and dissolved Cr(III) become depleted in this isotope. Chromium(III) species contain a higher abundance of ^{52}Cr as the reduction process takes place. The ratio of $^{53}Cr/^{52}Cr$ or $\delta^{53}Cr$ in a given water sample can be evaluated to quantify the amount or degree of chemical reduction of residual aqueous Cr(VI) (see Appendix D for more discussion on chromium isotopes).

Not all of the chromium is sequestered within the Cerros del Rio basalt through precipitation and adsorption processes. An unknown amount of chromium has reached the regional water table beneath Sandia and Mortandad canyons. During 2005 and 2006, concentrations of total chromium ranged from 375 to 413 µg/L and from 389 to 416 µg/L in filtered and nonfiltered samples, respectively, in regional aquifer groundwater at R-28 (LANL 2006, 094431). Speciation analyses showed that concentrations of Cr(VI) ranged from 380 to 405 µg/L and from 403 to 423 µg/L in filtered and nonfiltered samples, respectively, at R-28. Analytical error associated with all chromium measurements is ±10 percent. Water-supply wells O-4, PM-1, and PM-3 contained concentrations of total dissolved chromium ranging from 3.4 to 4.2 µg/L (LANL 2006, 094431), which are within the range of background chromium concentrations (LANL 2007, 095817). Regional aquifer wells R-11 in Sandia Canyon and R-15 in Mortandad Canyon contained total dissolved concentrations of chromium ranging from 7 to 29 µg/L (LANL 2006, 094431).

Geochemical modeling was performed to quantitatively evaluate speciation of dissolved chromium, precipitation reactions involving Cr(III), and adsorption of Cr(VI) onto hydrous ferric oxide (HFO). Results of simulations using PHREEQC2.2 (Parkhurst and Appelo 1999, 095402) and analytical results from R-28 (LANL 2006, 094431) suggest that 99.8% of dissolved chromium is stable as CrO_4^{2-} and only 0.2% occurs as $Cr(OH)_3^0$. Dissolved and total concentrations of chromium in filtered and nonfiltered samples are very similar, confirming very little chromium has adsorbed onto suspended particles.

Chromate (CrO_4^{2-}) is predicted to have a mobility similar to that of sulfate (SO_4^{2-}), considering that both molecules have tetrahedral coordination and a –II charge. Distribution coefficients (K_d) for both CrO_4^{2-} and SO_4^{2-} are estimated to range between 0 and 1, especially under the basic pH conditions encountered at R-28 (LANL 2006, 094431). The maximum retardation factor (R_f) for CrO_4^{2-} is estimated to be less than five, assuming an average bulk rock density of 1.2 g/cm^3 and an effective porosity of 0.25 for the Puye Formation. Simulations were conducted using the computer code MINTEQA2 (Allison et al. 1991, 049930) to quantify the extent of CrO_4^{2-} adsorption onto HFO present in aquifer material. Results showed that CrO_4^{2-} does not adsorb onto HFO at R-28. This is consistent with very similar concentrations of chromium measured in filtered and nonfiltered samples at R-28.

REFERENCES

The following list includes all documents cited in this appendix. Parenthetical information following each reference provides the author(s), publication date, and ER ID number. This information is also included in text citations. ER ID numbers are assigned by the Environmental Programs Directorate's Records

Processing Facility (RPF) and are used to locate the document at the RPF and, where applicable, in the master reference set.

Copies of the master reference set are maintained at the NMED Hazardous Waste Bureau; the U.S. Department of Energy–Los Alamos Site Office; the U.S. Environmental Protection Agency, Region 6; and the Directorate. The set was developed to ensure that the administrative authority has all material needed to review this document, and it is updated with every document submitted to the administrative authority. Documents previously submitted to the administrative authority are not included.

Allison, J.D., D.S. Brown, and K.J. Novo-Gradac, March 1991. "MINTEQA2/PRODEFA2, A Geochemical Assessment Model for Environmental Systems: Version 3.0 User's Manual," EPA/600/3-91/021, Office of Research and Development, Athens, Georgia. (Allison et al. 1991, 049930)

Langmuir, D., 1997. *Aqueous Environmental Geochemistry*, Prentice Hall, Inc., Upper Saddle River, New Jersey. (Langmuir 1997, 056037)

LANL (Los Alamos National Laboratory), September 22, 1998. "Inorganic and Radionuclide Background Data for Soils, Canyon Sediments, and Bandelier Tuff at Los Alamos National Laboratory," Los Alamos National Laboratory document LA-UR-98-4847, Los Alamos, New Mexico. (LANL 1998, 059730)

LANL (Los Alamos National Laboratory), November 2006. "Interim Measures Investigation Report for Chromium Contamination in Groundwater," Los Alamos National Laboratory document LA-UR-06-8372, Los Alamos, New Mexico. (LANL 2006, 094431)

LANL (Los Alamos National Laboratory), May 2007. "Groundwater Background Investigation Report, Revision 3," Los Alamos National Laboratory document LA-UR-07-2853, Los Alamos, New Mexico. (LANL 2007, 095817)

LANL (Los Alamos National Laboratory), September 2007. "Fate and Transport Modeling Report for Chromium Contamination from Sandia Canyon," Los Alamos National Laboratory document LA-UR-07-6018, Los Alamos, New Mexico. (LANL 2007, 098938)

Longmire, P.A., S.L. Reneau, P.M. Watt, L. McFadden, J.N. Gardner, C. Duffy, and R.T. Ryti, January 1995. "Natural Background Geochemistry, Geomorphology, and Pedogenesis of Selected Soil Profiles and Bandelier Tuff, Los Alamos, New Mexico, 1995," Draft, Los Alamos National Laboratory report LA-12913-MS, Los Alamos, New Mexico. (Longmire et al. 1995, 048818)

McBride, M., January 1, 1994. "Trace and Toxic Elements in Soils," in *Environmental Chemistry of Soils*, Oxford University Press, New York, New York. (McBride 1994, 058947)

Parkhurst, D.L., and C.A.J. Appelo, 1999. "User's Guide to PHREEQC (Version 2)—A Computer Program for Speciation, Batch-Reaction, One-Dimensional Transport, and Inverse Geochemical Calculations," U.S. Geological Survey Water-Resources Investigations Report 99-4259, Denver, Colorado. (Parkhurst and Appelo 1999, 095402)

Rai, D., C.C. Ainsworth, L.E. Eary, S.V. Mattigod, and D.R. Jackson, May 1986. "Geochemical Behavior of Chromium Species," report prepared by Battelle, Pacific Northwest Laboratories for the Electric Power Research Institute, interim report EA-4544, Richland, Washington. (Rai et al. 1986, 091686)
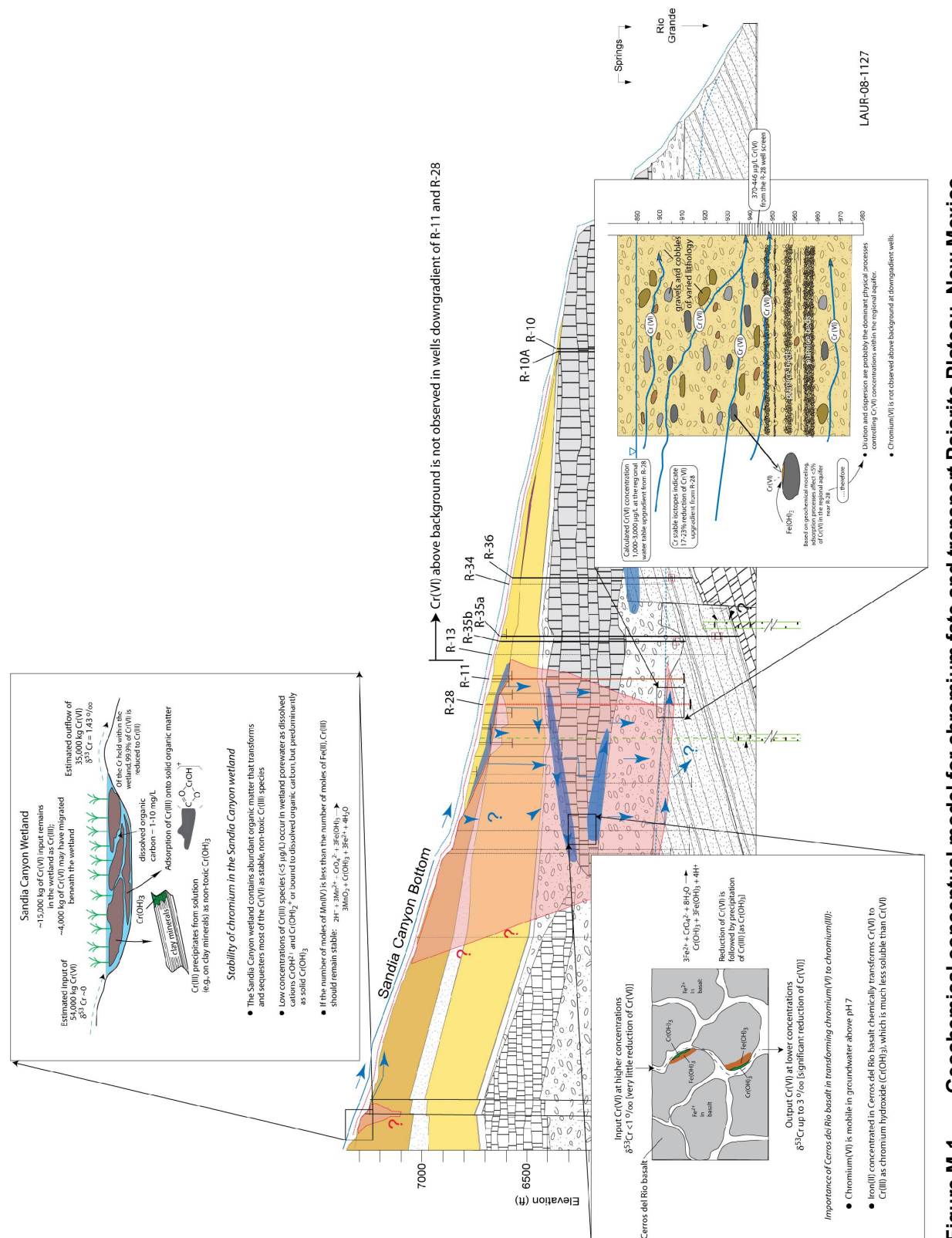
Figure M-1   Geochemical conceptual model for chromium fate and transport Pajarito Plateau, New Mexico